Birgit Stapf

Heavy Higgs Hunting

A search for a heavy Higgs boson decaying to a pair of Z bosons with the ATLAS detector

Heavy Higgs Hunting

A search for a heavy Higgs boson decaying to a pair of Z bosons with the ATLAS detector

Birgit Stapf

ISBN 978-94-6421-256-3

Heavy Higgs Hunting - A search for a heavy Higgs boson decaying to a pair of Z bosons with the ATLAS detector
Thesis, Universiteit van Amsterdam

Cover images by Wolfgang Stapf and "Diana of Versailles" by Eric Gaba under CC BY-SA 2.5
Printed by Ipskamp Printing

This work is part of the research programme of the Foundation for Fundamental Research on Matter (FOM), which is part of the Dutch Research Council (NWO) and has been performed at the National Institute for Subatomic Physics (Nikhef).

Heavy Higgs Hunting

A search for a heavy Higgs boson decaying to a pair of Z bosons with the ATLAS detector

ACADEMISCH PROEFSCHRIFT

ter verkrijging van de graad van doctor
aan de Universiteit van Amsterdam
op gezag van de Rector Magnificus
prof. dr. ir. K.I.J. Maex
ten overstaan van een door het College voor Promoties ingestelde commissie,
in het openbaar te verdedigen in de Agnietenkapel
op vrijdag 19 maart 2021, te 10.00 uur

door Birgit Sylvia Stapf
geboren te Aachen

Promotiecommissie

Promotor:	prof. dr. W. Verkerke	Universiteit van Amsterdam
Copromotor:	dr. ir. P.M. Kluit	Nikhef
Overige leden:	dr. I.B. van Vulpen	Universiteit van Amsterdam
	prof. dr. R. Fleischer	Vrije Universiteit Amsterdam
	dr. H.L. Snoek	Universiteit van Amsterdam
	prof. dr. M.P. Decowski	Universiteit van Amsterdam
	prof. dr. E.L.M.P. Laenen	Universiteit van Amsterdam
	prof. dr. H.G. Raven	Vrije Universiteit Amsterdam
	dr. Y. Wu	University of Science and Technology of China

Faculteit der Natuurwetenschappen, Wiskunde en Informatica

Contents

Introduction

Particle physics addresses fundamental questions about the universe that have accompanied humankind throughout the ages, such as "What is all that we see around us actually made of?". For this particular question, the *Standard Model* (SM), a mathematical model summarizing all our current knowledge of the world of elementary particles, is able to provide an answer at the deepest level: matter is made of atoms, atoms consist of nucleons and electrons and nucleons are made out of quarks. According to our current understanding, electrons and quarks are elementary particles with no substructure and they are considered to be point-like. Despite their minuscule size, studying elementary particles helps us answer big questions: understanding their interactions - happening at the microscopic scale - sheds light on how the universe came to be and how it functions at the most fundamental level. To be able to make what happens at such small scales "visible", extremely high energies are needed, achieved for example at particle accelerators such as the *Large Hadron Collider* (LHC) [1]. Experiments performed at the LHC allow us to probe predictions made by models like the SM, as well as to search for new physics processes not yet described by the SM, the discovery of which may lead to completely new fundamental theories. Since its inception and formulation during the second half of the previous century, the SM has proven to be immensely successful, making many predictions later confirmed by experiment. Its latest success story was the discovery of the Higgs boson in the LHC data by the ATLAS [2] and CMS [3] collaborations in 2012.

Although the Higgs boson discovery formally completes the SM, it is not an end to all questions, but rather a new beginning. There are many phenomena and observations the SM tells us nothing about, such as gravity, the nature of dark matter or why the universe primarily consists of matter, rather than anti-matter. At present, there are multiple ways forward to a possible understanding of particle physics *beyond the Standard Model* (BSM) and we do not currently know which one is the most likely to be successful. Many BSM theories are able to provide answers to the open questions, constituting many different avenues for experiments to explore. One promising avenue is to search for the existence of additional Higgs bosons, as an extended Higgs sector - with multiple Higgs bosons - is a common feature of many BSM models. Even though the already discovered Higgs boson seems to behave like a SM Higgs boson within the current limited experimental precision [4], the question whether it the only one of its kind is not yet answered.

This thesis presents a direct search for an additional heavy Higgs boson decaying to a pair of Z bosons, using the pp-collision data at a centre-of-mass energy of $\sqrt{s}$ = 13 TeV recorded with ATLAS during the LHC's second run throughout 2015 to 2018. Aside from its mass and decay width, the heavy Higgs boson is assumed to have the same properties as the SM Higgs, i.e. it is assumed to be a CP-even, electrically neutral scalar. The main focus of this thesis is the search in the $H \to ZZ \to \ell\ell\nu\nu$ channel, where one Z boson decays to two charged, light leptons - i.e.

electrons or muons - and the other to two neutrinos. In the publication of the ATLAS result, which is described in this thesis, the $\ell\ell\nu\nu$ channel is combined with the $\ell\ell\ell\ell$ channel. These two channels offer distinct advantages: Although the $\ell\ell\ell\ell$ channel offers a very clean signature with small backgrounds and an excellent invariant mass resolution, it is a rare process and therefore it has low numbers of events and correspondingly large statistical uncertainties. In contrast, the invariant mass of the $\ell\ell\nu\nu$ channel cannot be fully reconstructed due to the neutrinos, resulting in a worse mass resolution, but it has a higher branching ratio, more events and therefore smaller statistical uncertainties. This complementarity leads to the $\ell\ell\ell\ell$ channel dominating the search sensitivity at lower masses (below $\approx$ 700 GeV), while the $\ell\ell\nu\nu$ channel is more sensitive in the high mass range.

Two versions of the $\ell\ell\nu\nu$ search using the $\sqrt{s}$ = 13 TeV data are presented in this thesis: The first, published in [5], uses a partial dataset of $\mathscr{L}$ = 36.1fb^{-1} recorded in 2015+16 and the second, published in [6], employs the full run II datset of $\mathscr{L}$ = 139fb^{-1} recorded in 2015-18. Previously, a $H \to ZZ$ heavy Higgs search involving all decay channels of the Z boson pair - also including the hadronic $\ell\ell qq$ and $\nu\nu qq$ in addition to the fermionic $\ell\ell\nu\nu$ and $\ell\ell\ell\ell$ channels - using the LHC run I data from 2012 with a centre-of-mass energy of $\sqrt{s}$ = 8 TeV was published in [7]. In the run I analysis the $\ell\ell\nu\nu$ channel was found to perform similarly well as the combination of the two hadronic channels. Whereas the $\sqrt{s}$ = 8 TeV analysis searched for heavy Higgs bosons with a mass up to 1 TeV, the $\sqrt{s}$ = 13 TeV analyses presented here are able to extend the mass range up to 2 TeV when using the full run II data.

This thesis is organized as follows:

Chapter 1 introduces relevant concepts of the SM and BSM theory, providing theoretical background to and motiviation for the search.

Chapter 2 gives an overview of the experimental situation, describing the LHC, ATLAS and how pp-collision events are reconstructed.

Chapter 3 dives deeper into the muon reconstruction at ATLAS, proposing an alternative fit model for the dimuon invariant mass spectrum and studying the muon momentum scale and resolution. The work presented in this chapter is my own, building on to the initial studies of the fit model in [8].

Chapter 4 introduces the analysis concepts common to the heavy Higgs search in $H \to ZZ \to \ell\ell\nu\nu$. The modelling of signals, backgrounds and the interference between them is described and the general search strategy as well as the main statistical analysis concepts are outlined. Here, the signal-to-signal reweighting for large-width signals as well as the $H-h$ interference modelling were implemented by me, while the fit model for the $H-B$ interference was provided by others, using inputs prepared by me. The studies of the total impact of the interference and

the preparation of inputs to the statistical analysis were also done by me. Furthermore, I provided the comparison of generators for the ZZ and WZ backgrounds in the signal region.

Chapter 5 documents the $H \to ZZ \to \ell\ell\nu\nu$ heavy Higgs search using the 2015+16 dataset. Here I contributed to the interference modelling studies for the large-width analysis as described above.

Chapter 6 describes the $H \to ZZ \to \ell\ell\nu\nu$ search using the full 2015-18 dataset, including the $\ell\ell\nu\nu + \ell\ell\ell\ell$ combined results, where several improvements over the 2015+16 dataset analysis are made. The full run II $\ell\ell\nu\nu$ analysis constitutes the major part of my work: I studied the performance of the PFLOW-based missing transverse energy ($E_{\mathrm{T}}^{\mathrm{miss}}$) reconstruction in the phase space of this analysis, as well as the (re)-optimization of the event selection, which introduces the object-based $E_{\mathrm{T}}^{\mathrm{miss}}$ as a selection variable. In addition, I performed the studies optimizing the binning of the transverse mass observable in the ggF category. Moreover, I developed the software framework used for implementing the signal region selection of the $\ell\ell\nu\nu$ analysis and for producing the simulation based inputs - including experimental systematics - to the statistical analysis. The latter was also performed by me - I extracted the upper limits on the narrow- and large-width heavy Higgs production in the $\ell\ell\nu\nu$ channel and provided the corresponding workspaces as inputs to the $\ell\ell\nu\nu + \ell\ell\ell\ell$ combination. For this purpose, I implemented the different interpolation techniques used to obtain $\ell\ell\nu\nu$ results with a fine mass granularity. Furthermore, I studied the impact of systematics on the $\ell\ell\nu\nu$ results and worked on the interference modelling for the large-width analysis in this context. Finally, I was the main editor of the ATLAS internal documentation of the $\ell\ell\nu\nu$ heavy Higgs search using the 2015-18 dataset, given in [9].

The thesis concludes with a chapter that summarizes the results of the presented analyses as well as puts them into context in the bigger picture of BSM Higgs searches, and provides a brief outlook for future heavy Higgs searches in the $H \to ZZ$ channel. The discussion of prospects for the $H \to ZZ \to \ell\ell\nu\nu$ analysis is based on results obtained by me.

1 Theory

Particle physics studies the fundamental components of matter - the elementary particles - and the forces acting upon them, aiming to explain the inner workings of the universe as we observe it. To that end, theoretical particle physics employs mathematical models describing the building blocks of reality. Our current best understanding of particle physics is summarised in the *Standard Model* (SM), described in Chapter 1.1. Throughout the last century, the SM has proven to be a success story, bringing order into the observed "particle zoo" and supplying precise predictions, later confirmed by experiment. The discovery of the Higgs boson by ATLAS [2] and CMS [3] in 2012 is the latest of such successes, confirming the *Higgs mechanism*, outlined in Chapter 1.1.5. Although with the Higgs boson observed the SM is considered self-consistent, open questions remain - for example on the nature of dark matter and the several other questions summarized in Chapter 1.2.1. As further detailed in Chapter 1.2 answers are proposed by *Beyond the Standard Model* (BSM) theories, which in turn often predict the existence of additional BSM particles. This is the motivation for the search for a heavy, BSM Higgs boson decaying as $H \to ZZ \to \ell\ell\nu\nu$ presented in this work. Finally, this chapter concludes with a summary of theory predictions for heavy Higgs bosons that guide the strategy of the $H \to ZZ \to \ell\ell\nu\nu$ search, in Chapter 1.3.

1.1 The Standard Model

In the following, the basic concepts of the Standard Model that are most relevant to the work presented in this thesis are briefly outlined, starting from a phenomenological description of the SM particles and their interactions and then moving to a more formal summary of its mathematical formulation. The focus here is mostly on the concepts, and their physical implications. More exhaustive expositions of the Standard Model in all its formal detail and elegance can be found in a wide range of literature, such as textbooks [10], lectures [11], [12] or review articles [13], [14].

1.1.1 Particles and interactions

In the SM, all (currently known) elementary particles are categorized into two groups according to their intrinsic angular momentum, quantified by the quantum number of *spin*: Firstly, all matter is made of particles carrying half-integer spin, the so-called *fermions*. All interactions between the fermions, on the other hand, are mediated by particles of integer spin, which are referred to as *bosons*. The SM provides a description of three of the four fundamental forces observed in nature: the electromagnetic, weak and strong interaction. Only a description gravity, which is

negligible at subatomic scales, is not included. Whether a particle participates in a given interaction is determined by its respective quantum number, referred to as a *charge*. While all electrically charged particles are subject to the electromagnetic interaction, the weak interaction couples to the charge called *weak isospin*. The charge of the strong interaction is called the *colour charge*. Figure 1.1 presents an overview of all SM particles, their masses and electromagnetic charges in units of the elementary charge e[1]. For each particle listed, an anti-particle with the same mass, but opposite charges exists[2].

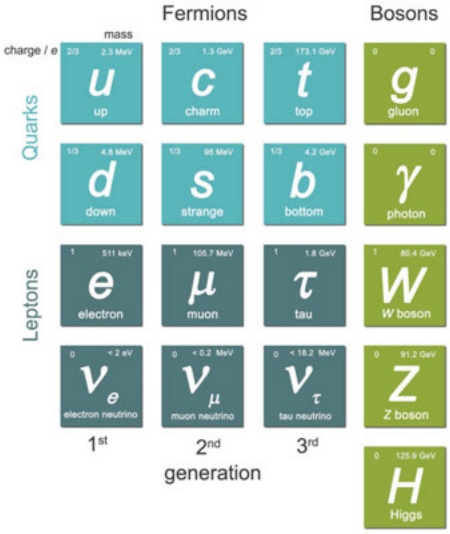

Figure 1.1: Overview of Standard Model particles and their properties [15].

Fermions are distinguished into *leptons* and *quarks*: Quarks carry a colour charge and thus are subject to the strong interaction, but leptons are not. Each group further consists of three *generations*, ordering fermions in groups with identical quantum numbers by increasing mass. A generation includes two quarks and two leptons with different electromagnetic charges. Only the quarks and leptons of the first generation are stable and are the constituents of all ordinary matter, such as nucleons and atoms. For example, a proton consists of two up- and one down-quark, and a hydrogen atom consists of one proton and one electron). *Exotic* matter composed of higher generation fermions is produced in particle physics experiments such as colliders, and in the universe, but eventually decays into the stable particles of the first generation.

There are three types or *flavours* of leptons carrying non-zero electromagnetic charge as well as

[1] $e = 1.602 \times 10^{-19}\,\mathrm{C}$

[2] In this thesis, anti-particles are denoted either by a bar above the particle's symbol, e.g. $\bar{t}$ refers to an anti-top-quark, or by explicitly stating the electromagnetic charge, e.g. e^+ refers to a positron.

weak isospin: electrons, muons and τ-leptons. These three participate in the electromagnetic and weak interaction. For each lepton flavour, a corresponding neutrino exists, which is electromagnetically neutral but has non-zero weak isospin and is therefore subject only to the weak interaction.

All quarks participate in the electromagnetic, weak and strong interactions. They are also distinguished by their weak isospin and electromagnetic charge: Quarks of the *up-type* have a weak isospin of $+\frac{1}{2}$ (as in pointing *up*wards) and an electromagnetic charge of $+\frac{2}{3}e$, whereas *down-type* quarks carry a weak isospin of $-\frac{1}{2}$ (as in pointing *down*wards) and an electromagnetic charge of $-\frac{1}{3}e$. The up- and down-quarks are commonly referred to as *light flavour*, with the heavier charm, strange, top and bottom quarks referred to as *heavy flavour*. Each quark carries one out of three possible colour charges, coupling to the strong interaction.

Each of the three interactions described by the SM is imparted by an exchange of different kinds of bosons between fermions. The photon mediates the electromagnetic interaction, coupling to the electromagnetic charge. Since the photon is massless (and electrically neutral) the range of the electromagnetic interaction is infinite. In contrast, the weak interaction is mediated by the massive W boson and Z boson, making it very short-ranged. Collectively, the (electrically) neutral Z boson and the charged W boson, are often referred to as the *vector bosons* and denoted as V[3]. While the physics of the electromagnetic interaction can be described by *quantum electrodynamics* (QED), in the SM the electromagnetic and weak interaction are unified and jointly described by *electroweak theory*.

The gluon acts as the mediator of the strong interaction. Although the gluon is massless, the range of the strong interaction is short, of the order of femtometers. The reason is that the gluons themselves carry colour charge, leading to self-interactions around a free colour charge, which enhance the effective charge with increasing distance. This effect is referred to as *anti-screening* and it also is the cause of the *confinement* of quarks (and gluons). Free colour charges cannot be observed, instead each free quark and gluon forms colour-neutral hadrons, by the process of *hadronization*, as this is energetically favourable at increasing distance[4]. The theory of strong interactions is called *quantum chromodynamics* (QCD), in reference to the colour charge.

Finally, the Higgs boson is introduced by the (Brout–Englert–)Higgs mechanism of electroweak symmetry breaking, which explains how the heavy Z boson and W boson acquire their masses. It is electrically neutral and a scalar (i.e. it has spin 0).

1.1.2 SM symmetries and formalism

At the heart of the SM is *quantum field theory* (QFT), which describes the universe using all-permeating *quantum fields*, combining quantum mechanics and special relativity. Elementary particles are then viewed as quantised excitations of a corresponding quantum field. In particular, particles with spin 0 are represented by *scalar* fields, whereas spin 1 particles are described by *vector* fields and spin 1/2 particles, the fermions, are expressed as *spinor* fields. The Higgs

[3] Although technically the photon and gluon are also vector bosons, in the meaning that they carry a spin of 1.
[4] Chapter 2.3.3 describes the experimental consequences of hadronization.

field Φ is the only scalar field in the SM. In contrast, four vector fields - W_μ^1, W_μ^2, W_μ^3 and B_μ- describe the physics of electroweak (EW) interactions [5] and one gluon field G_μ describes the strong interaction. Finally, the spinor fields ψ account for the fermions.

The dynamics of the SM particles and their interactions - quantified by an equation of motion - are fully determined by the Lagrangian density[6] $\mathscr{L}$. For example, the Dirac equation (cf. e.g. [10]), describing massive fermions at relativistic energies on the quantum level, follows from the Lagrangian

$$\mathscr{L}_{\text{Dirac}} = i\bar{\psi}\gamma_\mu\partial^\mu\psi - m\bar{\psi}\psi \tag{1.1}$$

where ψ refers to the fermion field and $\bar{\psi}$ to its adjoint $\bar{\psi} = \psi^\dagger\gamma_0$ and m is the fermion mass (cf. [11]). The Lagrangian density is derived from the *symmetries* of the system it describes. In QFT, symmetries are represented by groups (of transformations) and a symmetry exists, if the Lagrangian is invariant under transformations belonging to the group. Furthermore, according to Noether's theorem [16] every symmetry implies a conservation law. Continuing with the earlier example, the full Lagrangian of QED can be derived from the Dirac Lagrangian by requiring invariance under *local transformations* (i.e. transformations dependent on the space-time coordinate x) of the form:

$$\psi(x) \to \psi'(x) = e^{i\alpha(x)}\psi(x) \tag{1.2}$$

Such transformations belong to the group $U(1)$, which consists of unitary matrices of dimension one and represents changes to the complex phase of a field. The Dirac Lagrangian is not invariant under such transformations, as it contains derivative terms which transform as:

$$\partial_\mu\psi(x) \to \partial_\mu\psi'(x) = e^{i\alpha(x)}\left[\partial_\mu\psi(x) + i\partial_\mu\alpha(x) + i\psi(x)\right] \tag{1.3}$$

However, if the derivative ∂_μ is replaced by the so-called *gauge covariant derivative* D_μ, defined as

$$D_\mu = \partial_\mu + iqA_\mu(x) \tag{1.4}$$

where q is a constant and A_μ is a new vector field, also called *gauge field*, that is required to transform as

$$A_\mu(x) \to A'_\mu(x) = A_\mu(x) - \frac{1}{q}\partial_\mu\alpha(x) \tag{1.5}$$

the invariance under local phase transformation of Equation 1.2 - also called a *gauge transformation* - is restored, as:

$$D_\mu\psi(x) \to D'_\mu\psi'(x) = e^{i\alpha(x)}D_\mu\psi(x) \tag{1.6}$$

The modified Dirac Lagrangian then reads

$$\mathscr{L}^{\text{inv}}_{\text{Dirac}} = i\bar{\psi}\gamma_\mu\partial^\mu\psi - m\bar{\psi}\psi - q\bar{\psi}\gamma_\mu\psi A^\mu \tag{1.7}$$

where the last term, $q\bar{\psi}\gamma_\mu\psi A^\mu$, describes an interaction between the fermion field ψ and the vector field A_μ with a coupling strength of q. Identifying the field A_μ with the electromagnetic vector

[5] With the EW bosons γ, W and Z arising as mixed states of these fields

[6] The classical Lagrangian is defined as the difference of kinetic and potential energy of a system and a Lagrangian density is a function of fields, rather than generalized coordinates.

field and q with the electric charge, this term describes the interaction of a charged fermion with a photon. Furthermore, the apparent gauge symmetry under $U(1)$ transformations implies the conservation of the electric charge. The concept of bosons as the mediators of interactions between particles thus follows naturally from the imposition of gauge invariance and the imposed structure of the symmetry dictates the type of interactions that can take place.

To construct the full QED Lagrangian the free term of the EM field needs to be included as well, leading to:

$$\mathscr{L}_{\text{QED}} = i\bar{\psi}\gamma_\mu\partial^\mu\psi - m\bar{\psi}\psi - q\bar{\psi}\gamma_\mu\psi A^\mu - \frac{1}{4}F_{\mu\nu}F^{\mu\nu} \tag{1.8}$$

with the electromagnetic field strength tensor $F_{\mu\nu}$ defined as $F_{\mu\nu} = \partial_\mu A_\nu - \partial_\mu A_\mu$. It is not possible to include a mass term for the gauge field (i.e. of the form $m_\gamma^2 A_\mu A^\mu$) in this framework, as it would break the gauge invariance. The photon, as the mediator of the EM interaction, must therefore be massless.

The derivation of the QED Lagrangian is the simplest example to demonstrate how imposing certain gauge symmetries gives rise to additional fields associated with gauge bosons that impart a certain interaction by coupling to an intrinsic charge. While the formulation of the full SM formalism follows the same principles, it is much more complex. Specifically, the full gauge symmetry group of the SM is

$$SU(3)_C \times SU(2)_L \times U(1)_Y \tag{1.9}$$

where $SU(3)_C$ is the symmetry group describing the strong interaction that couples to the colour charge C and the combination of symmetry groups $SU(2)_L \times U(1)_Y$ yields the unified description of the electroweak interactions, where only *left-handed* particles participate in the weak interaction (hence the subscript L) and the *hypercharge* Y combines the electric charge and the weak isospin into one quantum number.

To be able to make predictions that can be probed experimentally, observable quantities need to be calculated from the Lagrangian formalism. In particle physics, predictions are commonly made on the *cross-section* of a given process, i.e. the probability for the process to occur. Here *process* refers to the transition of a certain initial state into a certain final state, e.g. the production of a new particle X from the collision of two protons. The cross-section is determined by the probability amplitude of this transition, also called the *matrix element*, and the integral over the available phase space (cf. [10], *Fermi's Golden Rule*). The matrix element encodes all dynamics of the interaction and can be derived from a set of *Feynman rules*, which in turn are derived from the Lagrangian. *Feynman diagrams* are graphical representations of these rules, where the point of interaction between different particles (drawn as lines) is represented by a *vertex*. For each kind of vertex, a vertex factor can be inferred from the corresponding Lagrangian, which accounts for the fact that the strength of the interaction is proportional to the respective coupling constant. To compute the full matrix element from the Feynman diagrams, a *perturbative* approach is commonly taken: The main contribution is assumed to come from the *leading order* diagram, representing the simplest way for the transition to happen (i.e. involving the minimum number of vertices necessary and therefore at the lowest order of the coupling constant). Higher order contributions in terms of diagrams featuring more vertices (e.g. because of virtual particle loops appearing in the transition, or incoming or outgoing particles emitting radiation) are added

on top (as "corrections"). However, some higher order contributions containing loops of virtual particles are divergent, as the particles in the loop could have any energy and momentum, leading to an infinite phase space integral. In the SM, this is solved by *renormalisation*, i.e. redefining the coupling constant involved to absorb the divergent part of the integrals. The renormalized coupling constant is then dependent on the energy scale at which the process happens. This is referred to as a *running coupling constant*. For the QED example this running coupling can be understood to take into account the effects of *vacuum polarisation*: a free charge constantly emits photons, which split into electron-positron pairs, and effectively "screen" the charge. At lower energies (equivalent to larger distances) the effective EM charge therefore decreases. Hence, in QED, a perturbation series of fixed order Feynman diagrams commonly converges (quickly) to a precise prediction on the cross-section.

1.1.3 Quantum chromodynamics

Quantum chromodynamics (QCD) is the theory modelling strong interactions between quarks and gluons, based on imposing local gauge symmetry under the $SU(3)_C$ group. The $SU(3)_C$ has eight generators, representing the eight possible, linearly independent combinations of the three colours the three anti-colours (and formalised by eight 3x3 matrices called the *Gell-Mann matrices* [17]). Hence there are eight gluons, each carrying a certain combination of one colour and one anti-colour charge. The colour charges are named red, green and blue - r, g, b with anti-colour charges $\bar{r}, \bar{g}, \bar{b}$. A colour neutral state can be achieved by e.g. either combining quarks of all three (anti-)colours (e.g. rgb) or by the combination of a colour and its anti-colour charge (e.g. $\bar{r}r$). In this framework, quarks, that have one color charge r, g or b, transform as triplets under the $SU(3)_C$ symmetry, i.e. they are represented by three-component vectors of fermion fields for each quark flavour.

QCD is underlying all processes probed at the LHC, as it is the theory that describes pp-interactions. However, for the work presented here, it is not necessary to understand the subtleties of its formalism in detail. Hence, rather than using the mathematical framework briefly introduced above to derive the QCD Lagrangian (as is done in e.g. [12]), the following describes the key concepts of QCD which have the most impact on the experimental study of pp-collisions. As mentioned before, the fact that gluons carry colour-charge and therefore self-interact, means that the strong coupling constant α_s decreases with increasing energy, but diverges at low energies (equivalent to large distance, cf. [15] on quantum chromodynamics). This lies behind two behind main features of QCD: Free colour charges such as single quarks and gluons are not observable, as they form colourless hadrons once they reach low energy scales. This is called *confinement*. The consequence of confinement is that all quarks and gluons produced at the LHC are detected as collimated beams of hadrons (and other particles) called *jets* (cf. Chapter 2.3.3). In contrast, at high energies the single quarks and gluons behave like free particles. This is called *asymptotic freedom*. Confinement and asymptotic freedom are two sides of the same coin, namely the running of the strong coupling constant α_s. In other words, at high energies QCD processes can be well described by perturbation theory. However, for low energy QCD processes this approach breaks down - due to the rising α_s a perturbation series cannot converge. Instead, empirical

considerations need to be used to model such processes. How this is relevant for the study of pp-collisions at the LHC as presented here is detailed in Chapter 2.4.

1.1.4 Electroweak theory

The theory of electroweak interactions, initially formulated by Glashow [18], Weinberg [19] and Salam [20], is relevant to the work presented here in two aspects: First, it describes the physics of the Z boson, one of the main protagonists of the $H \to ZZ \to \ell\ell\nu\nu$ analyses presented in Chapters 5 and 6. Second, it is the foundation of the electroweak symmetry mechanism, the theory of which introduces the Higgs boson - another key player in this thesis. Electroweak theory is a *chiral* theory (as parity is not conserved in weak interactions) meaning that it distinguishes between left- and right-handed fermion fields, defined as

$$\begin{aligned} \psi_L &= P_L\psi = \frac{1}{2}(1-\gamma^5)\psi \\ \psi_R &= P_R\psi = \frac{1}{2}(1+\gamma^5)\psi \end{aligned} \tag{1.10}$$

where $P_{L,R}$ are the respective projection operators and $\gamma^5 = i\gamma^0\gamma^1\gamma^2\gamma^3$. The handedness then defines how a fermion field transforms under the $SU(2)_L \times U(1)_Y$ group: right-handed fermion fields transform as singlets and left-handed fields as doublets. Hence, the fermions of the SM are represented by

$$\begin{aligned} \psi_L^{\text{leptons}} &= \begin{pmatrix}\nu_e\\ e\end{pmatrix}_L, \begin{pmatrix}\nu_\mu\\ \mu\end{pmatrix}_L, \begin{pmatrix}\nu_\tau\\ \tau\end{pmatrix}_L \\ \psi_L^{\text{quarks}} &= \begin{pmatrix}u\\ d\end{pmatrix}_L, \begin{pmatrix}c\\ s\end{pmatrix}_L, \begin{pmatrix}t\\ b\end{pmatrix}_L \\ \psi_R^{\text{leptons}} &= e_R, \mu_R, \tau_R \\ \psi_R^{\text{quarks}} &= u_R, c_R, t_R, d_R, s_R, b_R, t_R \end{aligned} \tag{1.11}$$

In this formalism, local transformations take the form

$$\begin{aligned} \psi_L(x) \to \psi'_L(x) &= e^{i\beta(x)Y + \frac{i}{2}\alpha(x)\sigma}\psi_L(x) \\ \psi_R(x) \to \psi'_R(x) &= e^{i\beta(x)Y}\psi_R(x) \end{aligned} \tag{1.12}$$

where σ are the Pauli matrices (cf. e.g. [10]) - three 2x2 matrices that also define the generators of the $SU(2)_L$ group. Moreover, Y denotes the weak hypercharge (and generator of the $U(1)_Y$ group), defined as

$$Y = 2(Q - I_3) \tag{1.13}$$

, combining the electric charge Q and the third component of the weak isospin, I_3. To preserve invariance under such local transformations, four gauge fields - three W_μ^i from the $SU(2)_L \times U(1)_Y$

group and one B_μ from the $U(1)_Y$ group need to be introduced. The covariant derivative is then defined as

$$D_\mu = \partial_\mu + i\frac{g}{2}\vec{\sigma}\vec{W}_\mu(x) + i\frac{g'}{2}YB_\mu(x) \tag{1.14}$$

where g and g' denote the coupling strengths of the $SU(2)_L$ and $U(1)_Y$, respectively. The gauge invariant EW Lagrangian consists of a fermion term and a term involving only the gauge fields. They read as

$$\begin{aligned}\mathscr{L}_\psi &= i\bar{\psi}\gamma_\mu\partial^\mu\psi - \frac{g'}{2}Y\bar{\psi}\gamma_\mu B_\mu\psi - \frac{g}{2}\bar{\psi}_L\gamma_\mu\vec{\sigma}\vec{W}_\mu\psi_L \\ \mathscr{L}_{\text{gauge}} &= -\frac{1}{4}F_{\mu\nu}F^{\mu\nu} - \frac{1}{4}B_{\mu\nu}B^{\mu\nu}\end{aligned} \tag{1.15}$$

where $F_{\mu\nu}$ and $B_{\mu\nu}$ denote the field strength tensors:

$$\begin{aligned}\vec{F_{\mu\nu}} &= \partial_\mu\vec{W}_\nu - \partial_\mu\vec{W}_\mu + g\vec{W}_\mu \times \vec{W}_\nu \\ B_{\mu\nu} &= \partial_\mu B_\nu - \partial_\mu B_\mu\end{aligned} \tag{1.16}$$

The unphysical fields $W_\mu^{1,2,3}$ and B_μ relate to the physical EW fields in the following way: The field corresponding to the charged W bosons, $W^\pm$, is defined as

$$W^\pm = \frac{1}{2}\left(W_\mu^1 \mp iW_\mu^2\right) \tag{1.17}$$

whereas the fields associated with the photon, A_μ, and the neutral Z boson, Z_μ, follow from a rotation of the unphysical fields as:

$$\begin{aligned}Z_\mu &= \cos\sigma_W W_\mu^3 - \sin\sigma_W B_\mu \\ A_\mu &= \cos\sigma_W W_\mu^3 + \sin\sigma_W B_\mu\end{aligned} \tag{1.18}$$

Here, the *weak mixing angle*, or Weinberg angle, σ_W is given by:

$$\tan\sigma_W = \frac{g'}{g} \tag{1.19}$$

The EW Langrangian cannot contain mass terms for neither the fermions (of the form $\frac{1}{2}m_\psi(\bar{\psi}_L\psi_R + \bar{\psi}_R\psi_L)$) nor for the gauge fields (e.g. of the form $\frac{1}{2}m_W W_\mu W^\mu$), as they are not invariant under the respective gauge transformation. Both are in contradiction with experiment, showing that fermions and the EW bosons Z and W are massive. The introduction an additional complex, scalar field - the Higgs field - and the associated spontaneous breaking of the EW symmetry, resolves these inconsistencies.

1.1.5 The Higgs mechanism

Based on the ideas of Brout, Englert and Higgs [21, 22, 23] and others [24], the SM is completed by adding a complex, scalar field with a specific potential that introduces *spontaneous symmetry*

breaking into the EW physics model. With the addition of this field the full Lagrangian stays invariant under the $SU(2)_L \times U(1)_Y$ group, but the vacuum state is then no longer invariant under this symmetry group. The Higgs sector is responsible for the masses of the gauge bosons, and additionally predicts the existence of a massive scalar boson, called the Higgs boson.

The simplest, minimal form to introduce spontaneous symmetry breaking is to add a new doublet of complex, scalar fields

$$\Phi = \begin{pmatrix} \phi^+ \\ \phi^0 \end{pmatrix} \tag{1.20}$$

with $\phi^+ = \frac{1}{2}(\phi_1 + i\phi_2)$ and $\phi^0 = \frac{1}{2}(\phi_3 + i\phi_4)$, where the ϕ_i are real fields. The new field has to be an isospin doublet to preserve the $SU(2)_L$ invariance and it needs to carry one unit of hypercharge Y, as well as a weak isospin of $I = \frac{1}{2}$. Generally, the additional term in the Lagrangian arising from this new field - the Higgs term $\mathscr{L}_{\text{Higgs}}$- can be written as

$$\mathscr{L}_{\text{Higgs}} = (D^\mu \Phi)^\dagger (D_\mu \Phi) - V(\Phi) \tag{1.21}$$

where D_μ is the covariant derivative of Equation 1.14 and $V(\Phi)$ denotes the *Higgs potential*, chosen to be of the form:

$$\begin{aligned} V(\Phi) &= \mu^2(\Phi^\dagger\Phi) + \lambda(\Phi^\dagger\Phi)^2 \\ &= \mu^2|\Phi|^2 + \lambda|\Phi|^4 \end{aligned} \tag{1.22}$$

It is this particular choice of potential, and its dependence on the parameters μ^2 and λ that introduces the spontaneous symmetry breaking. While $\lambda > 0$ is required to bound the potential from below (i.e. guaranteeing that a ground state exists, cf. [25]), the shape of the potential depends on the sign of the parameter μ^2, as illustrated in Figure 1.2.

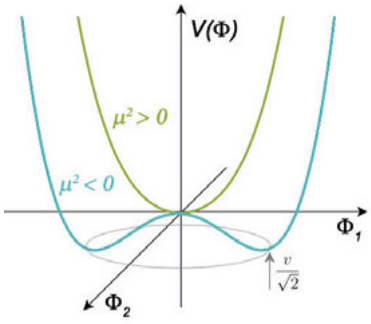

Figure 1.2: Illustration of the Higgs potential $V(\Phi)$ for different signs of the parameter μ^2.

If $\mu^2 > 0$ the potential exhibits a unique minimum at $< \Phi >_0 = 0$ and the symmetry is conserved. The minimum of the potential is the ground state of the system, or what we call the vacuum.

In contrast, when $\mu^2 < 0$ the potential minima are degenerate - an infinite number of possible minima exist, all satisfying the equation

$$|\Phi|^2 = -\frac{\mu^2}{2\lambda} = \frac{v^2}{2} \tag{1.23}$$

where $v = \sqrt{\frac{-\mu^2}{\lambda}}$ is the *vacuum expectation value* of the field Φ. As indicated in Figure 1.2 the minima lie on a circle of radius $\frac{v}{\sqrt{2}}$. Choosing a particular one of these degenerate minima breaks the original symmetry. When perturbatively calculating the corresponding Lagrangian, by expanding the potential around this particular minimum this symmetry is hidden and mass terms for the gauge fields appear. Specifically, the minimum can be chosen as

$$< \Phi >_0 = \frac{v}{\sqrt{2}} \begin{pmatrix} 0 \\ 1 \end{pmatrix} \tag{1.24}$$

encoding the fact that the vacuum should be electrically neutral (hence $\phi^+ = 0$). The field Φ around this minimum can then be expressed as an expansion using shifted fields $\eta_{1,2,3}$ and h:

$$\Phi(x) = \begin{pmatrix} \eta_1(x) + i\eta_2(x) \\ \frac{1}{\sqrt{2}}(v + h(x)) - i\eta_3(x) \end{pmatrix} = e^{\frac{i}{v}\vec{\eta}(x)\vec{\sigma}} \begin{pmatrix} 0 \\ \frac{1}{\sqrt{2}}(v + h(x)) \end{pmatrix} \tag{1.25}$$

While the fields $\eta_{1,2,3}$ correspond to unphysical, massless *Goldstone bosons* [26], h gives rise to the physical, massive Higgs boson. By transforming the field Φ as

$$\Phi(x) \rightarrow \Phi'(x) = e^{-i\vec{\eta}(x)\vec{\sigma}}\Phi(x) \tag{1.26}$$

the degrees of freedom introduced by the fields $\eta_{1,2,3}$ are *rotated away*. This is also called the unitary gauge and entering these relations into the covariant derivative term $D_\mu \Phi$ to expand the full Lagrangian (as is done for example in [13], [27] and [11]) results in mass terms for the gauge and fermion fields. Using the definitions of the physical fields W^+_μ, Z_μ and A_μ given in Equations 1.17 and 1.18, the mass terms for the gauge bosons read:

$$\begin{aligned} \mathscr{L}^W_{\text{mass}} &= \left(\frac{vg}{2}\right)^2 W^+_\mu W^{-\mu} = m^2_W W^+_\mu W^{-\mu} \\ \mathscr{L}^Z_{\text{mass}} &= \frac{v^2}{8}\left(g^2 + g'^2\right) Z_\mu Z^\mu = \frac{1}{2} m^2_Z Z_\mu Z^\mu \\ \mathscr{L}^\gamma_{\text{mass}} &= 0 \end{aligned} \tag{1.27}$$

Hence, the weak gauge bosons W and Z have each acquired a mass (proportional to the vacuum expectation value) due to the spontaneous symmetry breaking, while the photon remains massless. Furthermore, the ratio of the W and Z boson masses is given by the Weinberg angle as:

$$\frac{m_W}{m_Z} = \cos\sigma_W \tag{1.28}$$

Following the same principles also the fermion masses are generated through so-called *Yukawa* interactions with the Higgs field (cf. e.g. [27]). The Full SM Lagrangian, including the Higgs sector, then also contains a mass term for the Higgs itself (with $m_h = \sqrt{2\lambda v}$) and several interaction terms of the SM bosons, namely [13]:

- A three-point interaction of the form hVV, representing the coupling of a Higgs boson and two vector bosons with coupling strength $g_{hVV} \propto 2\frac{M_V^2}{v}$. This describes for example the decay of a (neutral) Higgs boson to two Z bosons, as studied here.
- A four-point interaction of the form $hhVV$ with coupling strength $g_{hhVV} \propto 2\frac{M_V^2}{v^2}$.
- A three-point self-interaction of the form hhh with coupling strength $g_{hhh} \propto 3\frac{m_h^2}{v}$.
- A four-point self-interaction of the form $hhhh$ with coupling strength $g_{hhhh} \propto 3\frac{m_h^2}{v^2}$.

It should be emphasized that while the mass of the SM Higgs boson h is not predicted by the theory (as the parameter λ is unknown)[7], predictions for all its couplings to gauge bosons exist (and also for the fermion couplings, though not discussed here). Probing these couplings, i.e. measuring the production and decay rates of the Higgs boson very precisely, is therefore one way to evaluate whether the Higgs boson discovered in 2012 really fulfills all its SM roles. Another way to test the consistency of the Higgs sector with the SM - and the one followed in this thesis - is to search for signs of additional Higgs bosons that are heavier than the SM one with its mass of $m_h \approx 125\,\text{GeV}$, as motivated from a theoretical standpoint in the following.

1.2 Beyond the Standard Model theories

The Standard Model offers a precise description of all physical phenomena within its domain, as described above. However, there are phenomena it does not describe as well as questions it does not answer. Chapter 1.2.1 outlines these limitations, which motivate the formulation of beyond the Standard Model (BSM) theories. The SM may be just one specific case of a more fundamental big picture, like Newtonian mechanics is an approximation - valid at low speeds - of relativistic mechanics. In the formulation of an extended theory that aims to address the shortcomings of the SM, it is often natural to extend the SMs Higgs sector, leading to the prediction of additional Higgs bosons in such BSM theories. The analyses presented in this thesis search for such an additional Higgs boson, specifically one that is heavier than the SM Higgs boson. The search is designed to be as model-independent as possible, in principle looking only for a scalar resonance of a certain mass and width, but an interpretation of the results in terms of a specific two Higgs doublet model (2HDM) is also given (cf. Chapter 6.5.3). Hence, 2HDMs are covered in some detail in Chapter 1.2.2, while other BSM theories with an extended Higgs sector are introduced only briefly in Chapter 1.2.3.

1.2.1 Limitations of the Standard Model

The following gives an overview of some of the main points that the SM is unable to explain. The list should not be considered complete and follows no particular order.

[7] Which explains why it took nearly 60 years to find it.

Gravity The SM describes three out of the four fundamental forces but does not include gravity. Theories of quantum gravity [28] hypothesize that like the other forces gravity is mediated by an elementary particle called the *graviton* (e.g. [29]). The graviton is a BSM particle that is not yet observed.

Dark matter and dark energy There is conclusive and abundant evidence from various astrophysical observations that as much as 95% of the universe consists of dark matter and dark energy [30] - the SM hence only describes 5% of the universe. Dark matter refers to a kind of matter that does not interact with the electromagnetic force, but is subject to gravity. The particle content of dark matter is unknown. Much of the evidence for dark matter comes from observing stronger gravitational effects than expected from the known, luminous matter. Examples are the rotation curves of galaxies as measured by Rubin and Ford [31] and more recently the effect of gravitational lensing in the *bullet cluster* [32]. Weakly interacting neutrinos are not a viable candidate to explain all of the observed dark matter distribution, but for example so-called WIMPs, i.e. Weakly Interacting Massive Particles, as predicted by BSM theories such as supersymmetry (cf. Chapter 1.2.3), are. A comprehensive overview of the observational evidence of and the candidates for dark matter can be found in e.g. [30].

Neutrino masses In the formalism of the SM neutrinos are massless. However, the observation of neutrino flavour oscillation [33] [34] implies that in reality they have non-zero mass. Constraints on the neutrino masses can be derived from experiment - for example by studying the kinematics of weak decays involving neutrinos - and these constraints are quoted in Figure 1.1. It is possible to integrate neutrino masses in the SM theory, but which exact mechanism is responsible for generating neutrino masses is still unknown. A detailed review of the neutrino mass problem is given in [15] (in section "Neutrino masses, mixing and oscillations").

Asymmetry of matter and antimatter We observe that the universe almost exclusively contains only matter and (almost) no antimatter. The CP-violating nature of the weak interaction in the quark sector (as represented in the CKM-matrix, cf. e.g. [10]) is unable to explain this observed asymmetry. Although weak CP-violation in the lepton sector and strong CP-violation are in principle also predicted by the SM and may be able to account for the rest of it, they remain unconfirmed by experiment so far and it is unclear whether they are the whole story. Thus the matter-antimatter asymmetry is an open question.

The hierarchy problem Moving to a more theoretical perspective, the hierarchy problem refers to an aspect of the SM itself that is often considered unsatisfactory: While the scale of the EW interaction is of $\mathcal{O}(100\,\text{GeV})$, the Planck scale, above which gravity becomes relevant and the SM is thus no longer sufficient, is of $\mathcal{O}(1 \times 10^{19}\,\text{GeV})$. The SM offers no explanation why this gap should be so large, leading to the idea that there could be a more fundamental theory behind the SM. This concern is motivated by the concept of *naturalness* - the principle that natural theories,

i.e. theories in which the ratio between free parameters is of the order of one, are preferable.[8] Along the same lines, it is also unexplained why the SM Higgs boson mass should be as small as observed. Assuming that the SM describes all phenomena up to an energy scale Λ, the observable Higgs mass can be expressed as the sum of a "bare" Higgs mass term and a correction term, arising from loop contributions, that is proportional to the square of the scale Λ. If this scale is large, e.g. it is indeed the Planck scale as often assumed, the parameters of the SM need to be *fine-tuned* in order to cancel out the dominant corrections and leaving only the observed, much smaller Higgs mass of 125 GeV. Such fine-tuning is considered unnatural.

Aside from these short-comings, it should be noted that the SM is an excellent model of all current experimental observations, but it does not provide answers *why* things are the way we observe them. For example, it does not explain the origin of the mass hierarchy of quarks and leptons, or why there should be three generations of each to begin with. Similarly, electroweak symmetry breaking is added "by hand" into the theory, by choosing a specific form of the potential, which of course does not address why this potential should be what it is. Some of the BSM theories described in the following give more in-depth answers to these questions.

1.2.2 Two Higgs Doublet Models

In the SM, the Higgs sector is *minimal*, meaning that only one complex Higgs doublet is included in the theory. This is the simplest form to introduce electroweak symmetry breaking. However, the Higgs sector may also be more complicated, i.e. *extended* by including more additional fields than just the one Higgs doublet. As the name suggests, *Two Higgs Doublet Models* (2HDMs) are a class of models that include two Higgs doublets that postulate the existence of multiple Higgs bosons. The original motivation behind 2HDMs was to introduce additional sources of CP-violation, able to explain the observed matter-antimatter asymmetry [35]. Already on their own, 2HDMs may hold the answer to this question. Another motivation is that some broader BSM frameworks require at least two Higgs doublets. The best known example are supersymmetric theories, in which an even number of Higgs doublets are needed to generate masses for all fermions. Supersymmetric theories are able to provide a solution for the naturalness problem and predict viable DM candidates (cf. Chapter 1.2.3). Moreover, axion models that explain why CP-violation in the strong sector seems to be suppressed in nature also require two Higgs doublets [36] [37]. Thus, there is a clear incentive to explore the parameter space and rich phenomenology of 2HDMs. Detailed overviews of different types of 2HDMs and their implications can be found in [38], [39] and [40]. Here, the specific 2HDM in terms of which the $H \rightarrow ZZ$ search results are interpreted conserves CP-symmetry in the Higgs sector and predicts in total five Higgs bosons:

[8] There is in principle no known reason to demand naturalness, and alternative attempts to explain why the fundamental constants of the universe as we know it arise from considerations such as the anthropic principle, in combination with multiverse theories. If we consider constants of nature of the form as we observe them to be a necessity for sentient life to exist and there is a large ensemble of universes, it should not be surprising that we live in the one where the constants are exactly right for us to exist and measure them. Such hypotheses are however impossible to test experimentally (as far as we currently know) and thus more of a philosophical nature.

- Two CP-even and neutral Higgs bosons, denoted as h and H. As the theory allows for one of these to be much lighter than the other, here it is assumed that h is the SM Higgs boson with a mass of 125 GeV and H is the significantly heavier object of the $H \to ZZ$ search.
- One CP-odd and neutral Higgs boson, usually referred to as A.
- Two charged Higgs bosons, denoted as $H^{\pm}$.

The masses of the Higgs bosons, m_h, m_H, m_A and $m_{H^{\pm}}$ are free parameters of the model. In its most general form, the potential in terms of the two Higgs doublets Φ_1 and Φ_2, can be written as

$$\begin{aligned} V(\Phi_1,\Phi_2) = {} & m_{11}^2\Phi_1^\dagger\Phi_1 + m_{22}^2\Phi_2^\dagger\Phi_2 - [m_{12}^2\Phi_1^\dagger\Phi_2 + \text{h.c.}] \\ & + \frac{1}{2}\lambda_2(\Phi_2^\dagger\Phi_2) + \lambda_3(\Phi_1^\dagger\Phi_1)(\Phi_2^\dagger\Phi_2) \\ & + \lambda_4(\Phi_1^\dagger\Phi_2)(\Phi_2^\dagger\Phi_1) + [\frac{1}{2}\lambda_5(\Phi_1^\dagger\Phi_2)^2 + \text{h.c.}] \end{aligned} \tag{1.29}$$

where in the CP conserving 2HDM all parameters are real. Each doublet has its own vacuum expectation value

$$<\Phi_a>_0 = \frac{1}{\sqrt{2}}\begin{pmatrix} 0 \\ v_a \end{pmatrix} \text{with } a = 1,2 \tag{1.30}$$

and the two doublets contain eight scalar fields in total:

$$\Phi_a = \frac{1}{\sqrt{2}}\begin{pmatrix} \phi_a^+ \\ v_a + \rho_a + i\eta_a \end{pmatrix} \text{with } a = 1,2 \tag{1.31}$$

Out of these eight fields, three are required to give mass to the W and Z bosons, while the remaining five give rise to the five Higgs bosons described above. The mass eigenstates of the neutral, CP-even Higgs bosons h and H, and the charged Higgs bosons $H^{\pm}$, are given by diagonalizing the respective mass matrices with angles α and β, respectively. Moreover, $\tan\beta$ gives the ratio of the vacuum expectation values:

$$\tan\beta = \frac{v_2}{v_1} \tag{1.32}$$

To summarize, the 2HDM considered here has seven free parameters: m_h, m_H, m_A, $m_{H^{\pm}}$, α, $\tan\beta$ and the mixing parameter m_{12}^2. The couplings of the two CP-even, neutral Higgs bosons to vector bosons can then be expressed as

$$\begin{aligned} g_{\text{2HDM}}^{hVV} &= \sin(\beta-\alpha) g_{\text{SM}}^{hVV} \\ g_{\text{2HDM}}^{HVV} &= \cos(\beta-\alpha) g_{\text{SM}}^{hVV} \end{aligned} \tag{1.33}$$

where the g_{SM}^{hVV} gives the coupling between the SM Higgs bosons and the vector bosons. In the case that $\cos(\beta-\alpha) = 0$, the heavy Higgs boson H does not couple to vector bosons and furthermore the couplings of the SM Higgs boson h agree exactly with the SM prediction[9]. This is called the *alignment limit*. The implication is that the alignment limit cannot excluded by direct

[9] This is true for bosons, as obvious from Equation 1.33, and fermions, cf. e.g. [40]

searches for additional Higgs bosons decaying to vector bosons, such as the $H \to ZZ$ search presented here, nor by precision measurements of the SM Higgs couplings. The region of 2HDM of parameter space in which the alignment limit holds and all Higgs masses are above the EW scale is called the *decoupling limit* and studied in detail in e.g. [41]. A problem with the general 2HDM formalism is that it introduces flavour changing neutral currents at tree level, which are observed to be highly suppressed in nature. This can be solved by requiring that each type of fermion (classified by electric charge) couples to only one of the Higgs doublets [42] [43]. Imposing the corresponding symmetries leads to four different *types* of 2HDMs:

Type I In type I models, only one of the doublets - Φ_2- couples to all fermions, i.e. to quarks and leptons. The other one only couples to gauge bosons. This type is also referred to as *fermiophobic*.

Type II In type II models, Φ_1 couples to down-type quarks and leptons, whereas Φ_2 couples to up-type quarks. This type is also called MSSM-like, because it features in the *Minimal Supersymmetric Model*.

Flipped Similar to type II, but flipped: In this type of models Φ_1 couples to down-type quarks, while Φ_2 couples to up-type quarks and leptons.

Lepton specific Finally, in lepton specific models, Φ_1 couples to leptons and Φ_2 to quarks.

As in this thesis the heavy Higgs boson decay to Z boson bosons is studied, only type I and type II models are relevant - the different coupling between Higgs bosons and fermions in the different types only plays a role for the Higgs production in this search. It should be noted that in each type of 2HDM the mass and width of the heavy Higgs boson are not predicted, but are dependent on the other free parameters.

1.2.3 Other BSM theories with an extended Higgs sector

Supersymmetry Supersymmetry (SUSY) is probably the most well-known BSM theory. In supersymmetric models, a superpartner for each SM particle exists, with the spin modified by half a unit but otherwise the same quantum numbers. The superpartners of bosons are fermions and vice versa. The fact that such superpartners with the same mass as the SM particles have not been observed implies that SUSY is a broken symmetry. SUSY models provide explanations for several of the questions the SM is unable to answer. For example, loop corrections to the Higgs mass involving the superpartners cancel those of the SM particles, solving the hierarchy problem (see e.g. [44], [45]). Furthermore, if the superpartners carry a new quantum number that is conserved, the so-called *R-parity*, the lightest supersymmetric particle is stable, i.e. it cannot decay to any SM particle despite potentially being very massive, and thus poses a viable dark

matter candidate (see e.g. [46] [47]). Finally, SUSY predicts a unification of the electromagnetic, weak and strong forces at high energies, and it is even possible to integrate gravity into some SUSY theories (see e.g. [48]). The downside of SUSY is that it contains many free parameters - leading to a wide range of models - and thus making exact predictions that can be excluded is difficult. Good overviews of the SUSY formalism in general are given in e.g. [49], [50] and [51]. A particular, simplified SUSY model is the *Minimal Supersymmetric Standard Model* - reviewed in detail in e.g. [52]. The Higgs sector of the MSSM is a (type II) 2HDM, as in SUSY a single Higgs doublet cannot couple to both up- and down-type quarks because the scalar fields are represented by chiral multiplets while their complex conjugates have opposite chirality. Hence, the MSSM predicts the five Higgs bosons as described in the previous section, one of which is the neutral and CP-even additional Higgs boson searched for in this thesis.

Electroweak singlet A simpler extension of the SM than 2HDMs are *electroweak singlet models*, which include one additional (real or complex) scalar field that transforms as a singlet under the SM symmetry group. Such models present the simplest, minimal BSM solution to the question why there is a matter-antimatter asymmetry and what could be a viable DM candidate [40]. If a real field X is added, the modified, gauge-invariant Higgs potential reads

$$V(\Phi, X) = \mu_1^2 \Phi^\dagger \Phi - \mu_2^2 X^2 + \lambda_1 (\Phi^\dagger \Phi)^2 + \lambda_2 X^4 + \lambda_3 \Phi^\dagger \Phi X^2 \tag{1.34}$$

where the μ_i^2 as well as λ_1 and λ_2 need to be positive and λ_3 needs to satisfy $\lambda_3 > -2\sqrt{\lambda_1 \lambda_2}$ for the potential to be bounded from below. The model then predicts two mass eigenstates with mixing angle α in the Higgs sector. If the mass eigenstates are not degenerate, they could correspond to the SM Higgs and a heavier neutral Higgs as searched for in this thesis. The coupling of this additional heavy Higgs to vector bosons is modified by a factor $\sin\alpha$ with respect to the SM couplings in these models. A more in-depth overview of EWS models can be found in [40] [39].

Composite Higgs Whereas in the SM the Higgs boson is an elementary particle, in composite Higgs models it is a bound state of a new strong interaction, i.e. the composite Higgs is not point-like but made of smaller components, held together by this new force. If f denotes the energy scale at which the components of the composite Higgs become relevant - just like e.g. quarks only become "visible" if protons are scattered at high energies - and v the vacuum expectation value of the Higgs field, in such a model the couplings of the Higgs boson to vector bosons are modified by a factor $\sqrt{1 - \frac{v^2}{f^2}}$ with respect to the SM [53]. Heavy Higgs bosons could then occur as higher energy excitations of the composite Higgs, similar to excited hadrons, where several states of different mass exist. The key motivation behind composite Higgs models is that they provide a solution for the hierarchy problem. Recent reviews of composite Higgs models and their compatibility with LHC data can be found in [53] [54].

1.3 How to find a heavy Higgs boson?

The high mass $H \to ZZ$ analyses presented in this thesis search for a neutral heavy Higgs boson - so the H in the 2HDM notation, assuming that the other neutral, CP-even Higgs boson, the h, is the already observed SM Higgs boson. Although generally this search strives to be as model independent as possible - i.e. it looks only for a scalar resonance of a certain mass and width - some assumptions on the production and decay modes, as well as the mass and width hypothesis, are needed to guide where it is worth to look exactly, and why[10]. These assumptions can be based on what we know about the SM Higgs boson - which is very similar in properties to the H - or on certain BSM benchmark scenarios (cf. e.g [40]), as outlined in the following.

Production modes The first thing to know when searching for a heavy Higgs boson in ATLAS data is how it would likely be produced in the LHC's pp-collisions. Figure 1.3 shows the cross-sections of different production modes of the SM Higgs boson as a function of its mass.

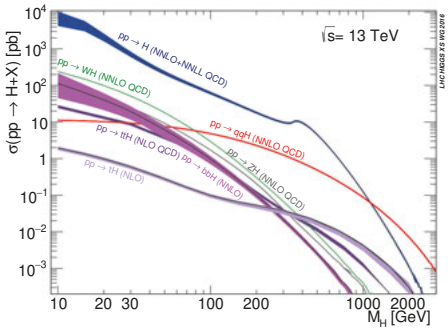

Figure 1.3: SM prediction for the Higgs boson production cross-sections as a function of the Higgs mass. From [56].

The dominant production mode of the SM Higgs boson at the LHC - for Higgs masses up to around 1.5 TeV - is **gluon-gluon fusion** (ggF). As illustrated in Figure 1.4(a), a single Higgs boson is produced through two gluons fusing into a virtual quark loop. Since the Higgs coupling to fermions is proportional to the fermion mass, the most likely quark to appear in this loop is the top quark.

[10] An alternative approach to such theory motivated direct searches for specific signatures are general searches such as [55].

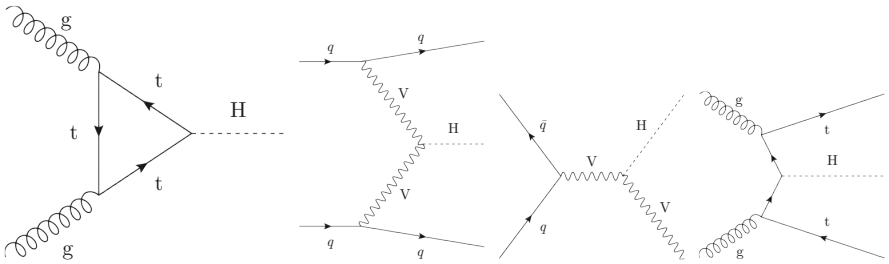

(a) ggF production (b) VBF production (c) VH production (d) ttH production

Figure 1.4: Leading order Feynman diagrams of different productions modes of the Higgs bosons in pp-collisions.

Another production mode of interest is **vector boson fusion** (VBF). This mode is the second most likely for SM-like Higgs bosons between 100 GeV and 1.5 TeV, and it becomes dominant for Higgs masses above 1.5 TeV. Its main advantage is a very characteristic signature - the Higgs is produced by two vector bosons that were radiated off two quarks, as shown in Figure 1.4(b). The two quarks (as remnants of the colliding protons) can be detected as two energetic jets (cf. Chapter 2.3.3) in the forward region.

The associated production of a Higgs boson with a vector boson, called the **Higgs-strahlung** process, also exhibits a characteristic signature of a massive vector boson recoiling against a Higgs boson, as shown in Figure 1.4(c). Although it is the third most likely mode for SM Higgs bosons with a mass of 125 GeV, its cross-section is strongly reduced with increasing mass.

Last, the Higgs boson can be produced in association with one or more quarks. As an example, Figure 1.4(d) shows the ttH production, where the Higgs is produced alongside a pair of top quarks. However, such modes also contribute little to heavy Higgs production.

The $H \to ZZ$ search presented here thus assumes that the heavy Higgs boson is produced in the ggF and VBF production mode. To stay model independent, the ratio of these two modes is left as a free parameter.

Decay channels and width Since the Higgs boson is not a stable particle, but has a very short lifetime - predicted to be $\mathcal{O}(10^{-22}\,\text{s})$ for the SM Higgs boson - it can only be reconstructed using its decay products. For a direct search as presented here, it is therefore important to know how likely it is to decay with the chosen signature, such as $H \to ZZ$. This is quantified by the *branching ratio* (BR), which for decay products X_1 is defined is

$$\text{BR}(H \to X_1) = \frac{\Gamma_1(H \to X_1)}{\sum_i \Gamma_i(H \to X_i)} \tag{1.35}$$

where Γ_1 is the partial width of the decay in X_1 and the Γ_i are the partial widths of all possible decay modes of the Higgs boson, the denominator hence giving its total decay width. Figure 1.5(a)

shows the branching ratios into different particles for an SM-like Higgs boson with masses up to 1 TeV.

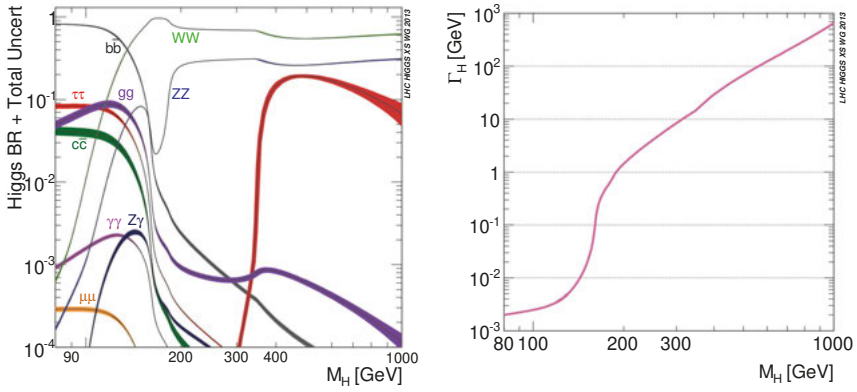

(a) (b)

Figure 1.5: SM predictions for (a) the braching ratios of different decay channels and (b) the total width of the Higgs boson as a function of the Higgs mass. From [56].

Above the threshold of two Z boson masses, $2m_Z \approx 182\,\text{GeV}$, where the two Z bosons produced in the decay can be on-shell, the BR($H \to ZZ$) channel is the second highest. However, this does not necessarily hold for heavy Higgs bosons postulated by BSM theories: for example near the alignment limit of the 2HDM the coupling of the heavy neutral Higgs boson to vector bosons is very small. Nonetheless the $H \to ZZ$ decay, especially with the Z boson pair further decaying into four leptons, is a good channel to study from an experimental standpoint: Both the $\ell\ell\nu\nu$ channel, that is the main focus of this thesis, and the $\ell\ell\ell\ell$ channel with which the $\ell\ell\nu\nu$ results are combined, have a clear experimental signature with multiple leptons which are generally well measured and simple to trigger on.

Another consideration in Higgs phenomenology is the total decay width of the heavy Higgs boson. A concrete prediction for the width is needed in the MC simulation of signal events, as described in Chapter 4.1, which are then compared to data, as explained in Chapter 4.5. Figure 1.5(b) shows the SM prediction of the total width of the Higgs, Γ_H, as a function of mass. Again, the threshold where the decay to two on-shell vector bosons becomes energetically possible is clearly visible. Although the total width of a SM-like Higgs is very small at low masses[11], it becomes sizeable at high masses. For example, a SM-like Higgs boson with a mass of 600 GeV would have a width of around 100 GeV - roughly 16% of its mass. The $H \to ZZ$ analysis therefore

[11] In fact, with only a few MeV the predicted width of the SM Higgs boson is smaller than the detector resolution, and thus can only be measured indirectly through studying off-shell Higgs production at ATLAS, as done in the $h \to ZZ \to \ell\ell\nu\nu$ channel in [57].

looks for Higgs bosons with a large width, equivalent to a certain fraction of its mass. Chapter 4.1.2 gives the precise details.

However, the large-width analysis (LWA) is only one part of the $H \to ZZ$ search. In many BSM theories, the heavy Higgs boson is assumed to have negligible width (compared to its mass), just like the SM Higgs boson at 125 GeV. As an example, Figure 1.6 shows the relative width of a heavy Higgs with two different masses in the parameter space of the specific 2HDM described in Chapter 1.2.2.

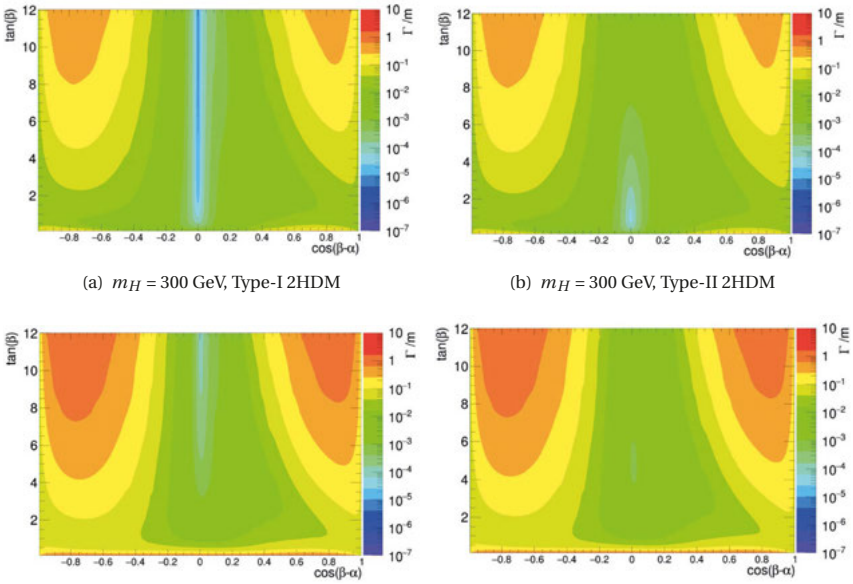

(a) m_H = 300 GeV, Type-I 2HDM

(b) m_H = 300 GeV, Type-II 2HDM

(c) m_H = 400 GeV, Type-I 2HDM

(d) m_H = 400 GeV, Type-II 2HDM

Figure 1.6: Contours of the relative width of the heavy Higgs with respect to its mass, Γ/m, as a function of the 2HDM parameters $\cos(\alpha-\beta)$ and $\tan\beta$ for type I and type II models and two different heavy Higgs masses. From [58].

Especially for the lower mass scenario of 300 GeV and in particular near the alignment limit of $\cos(\beta-\alpha) \approx 0$ the relative width of the heavy Higgs could be very small, of the order of 0.1% of its mass or less. Thus, in a large fraction of 2HDM parameter space the narrow width approximation (NWA) can be used. In fact, the NWA analysis is the key part of the $H \to ZZ$ search, for the simple reason that it is a less complex analysis than the LWA, since the interference effects described in Chapter 4.3 can be neglected in the NWA.

Mass range Finally, it should be stressed again that there are no exact predictions for the mass of a heavy BSM Higgs boson. The mass range studied in the $H \to ZZ$ search is therefore chosen for two practical reasons. First, the minimum mass searched for should be above the $2m_Z$ threshold, to exploit the higher $H \to ZZ$ branching ratio once the Z bosons become on-shell and to use the characteristic signature of an on-shell Z boson decay to identify possible signal events. Second, the upper bound of the mass range is determined by whether sufficient events in that energy range are expected to occur at the LHC. With these two criteria in mind, the $H \to ZZ \to \ell\ell\nu\nu$ analysis presented here searches for heavy Higgs bosons in the range from 300 GeV to 2 TeV. The addition of the results from the $H \to ZZ \to \ell\ell\ell\ell$ channel extends this range down to 200 GeV.

All of the above arguments are based on assumptions relying on specific models. In principle none of this needs to be true for a BSM Higgs, as there may be a kind of new physics behind it that no theory has imagined so far. Nevertheless, as long as this BSM Higgs boson decays to Z bosons and lies within the mass and width range studied, the $H \to ZZ$ search should still be able to find traces of it.

2 Experiment

In this thesis proton-proton(pp)-collision data recorded with the ATLAS detector [59] is analysed. The ATLAS detector is one of the four main experiments at the *Large Hadron Collider* (LHC), which is (currently) the most powerful particle accelerator in the world. This chapter describes first the LHC, as well as relevant properties of the pp-collision collision events and machine performance, then the setup and functionality of the ATLAS detector is detailed. The last part of the chapter focusses on the particle reconstruction algorithms as well as event simulation techniques employed at ATLAS.

2.1 The LHC

The LHC is a synchrotron-type particle accelerator located at the CERN site in Geneva, Switzerland. It consists of two (storage) rings of 27 km circumference, in which beams of protons (or heavy ions) are accelerated to nearly the speed of light and circulate in opposite directions, so they can be collided. It is housed in the tunnel originally built for the LEP collider [60], at depths of around 70-140 m underground.

2.1.1 The accelerator complex

Figure 2.1 shows a schematic overview of the LHC accelerator complex. Protons are extracted from hydrogen gas by using electric fields and then pass through an injection chain of multiple boosters before entering the LHC. First they enter the Linac 2, where they reach a momentum of 50 MeV. Next, they are accelerated to 1.4 GeV in the BOOSTER, to 25 GeV in the Proton Synchrotron (PS) and to 450 GeV in the Super Proton Synchrotron (SPS). Finally, the protons are injected into the LHC beam pipes. After all bunches of the LHC have been filled by the SPS, acceleration to 6.5 TeV takes around 20 minutes.

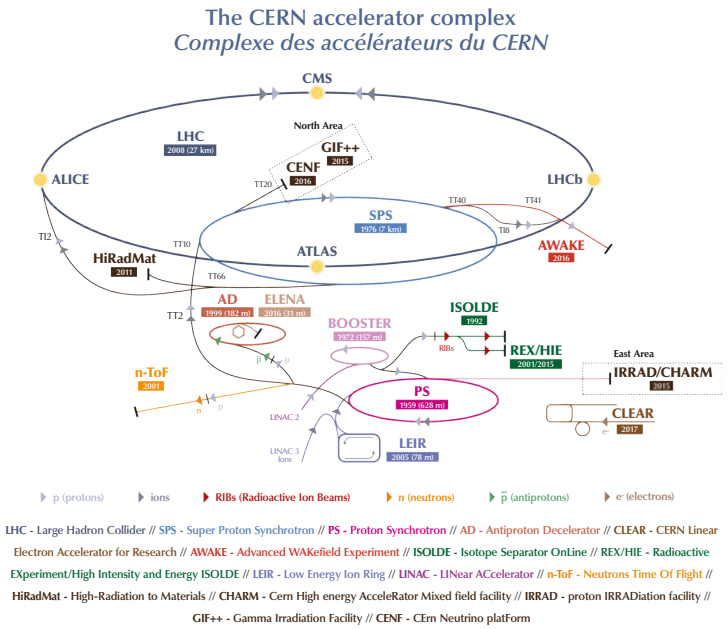

Figure 2.1: Scheme of the LHC accelerator complex. From [61].

The LHC consists of eight short straight sections, alternated with eight longer arcs. In the straight sections, *radiofrequency* (RF) cavities provide the electric fields necessary for particle acceleration. Superconducting dipole magnets in the arcs deflect the beams onto their circular paths. Additionally superconducting quadrupole magnet systems are used to focus and stabilize the beams, allowing protons of one fill to circulate for several hours. The two beams are crossed in four places, providing the four main experiments with collision events. ATLAS [59] and CMS [62] are multi-purpose detectors, designed for a broad range of physics topics. The LHCb detector [63] is specialised to detect and analyse processes involving b-quarks. Last, the ALICE experiment [64] analyses heavy ion collision data to investigate the behaviour of hadronic matter at high energies and densities.

2.1.2 Properties of collision events and beam parameters

The set of open physics questions (as described in Chapter 1.2) that can be accessed with the pp-collision data, is determined by the properties of the collision events themselves, as well as the beam parameters which influence the experimental performance. The most relevant beam parameters are introduced in the following.

Centre-of-mass energy The centre-of-mass energy, denoted as $\sqrt{s}$, is the amount of energy that is available in the collision. It directly quantifies the mass range of the experiment, i.e. a 1 TeV heavy Higgs can only be produced in an event with at least the same centre-of-mass energy. The production cross-sections of all physics processes are a function of the centre-of-mass energy. For a collision event, $\sqrt{s}$ is given by twice the energy of the colliding particles, so with the LHC set-up as described above the ATLAS data analysed here corresponds to $\sqrt{s} = 13\,\text{TeV}$. Reaching such high energies is unprecedented and made possible by colliding protons, instead of much lighter electrons and positrons. When accelerated, all particles suffer from energy losses due to *synchrotron-radiation*, the scale of which decreases with the fourth power of the particle mass in the case of circular accelerators (see e.g. [65]). These losses are much smaller for the heavier protons. But the downside of using protons is that they are composite particles. It is the constituents of the protons, the *partons* (i.e. quarks and gluons), which interact with each other in the collision event. Each parton carries only a fraction of the total momentum, and therefore the available centre-of-mass energy in the so-called *hard-scattering* event of interest is usually smaller than $\sqrt{s}$. This is explained in more detail in Chapter 2.4. A consequence is that the longitudinal momentum component of the partons involved in the collision is inaccessible, and therefore most quantities used in the analysis are reconstructed in the transverse plane.

The data taking years 2015-18, during which the LHC ran with $\sqrt{s} = 13\,\text{TeV}$ are referred to as the *(full) run II*. Previously, from 2010-2012, data was collected with lower energies of $\sqrt{s} = 7\,\text{TeV}$ to 8 TeV. This is referred to as *run I*.

Luminosity Aside from the centre-of-mass energy, the physics reach is also quantified by the *luminosity*. The instantaneous luminosity L relates the production rate of events of a certain process X per time unit $\frac{dN_X}{dt}$ to its production cross-section σ_X as follows:

$$\frac{dN_X}{dt} = \sigma_X \cdot L \tag{2.1}$$

Therefore it is clear that even if a process has a is very small production cross-section (as expected for e.g. heavy Higgs bosons), it could be observed with large enough luminosity. At the LHC, the proton beam consists of many *bunches* containing many protons each, and the instantaneous luminosity is given by the beam parameters as:

$$L = \frac{f_{\text{rev}} \cdot n_b \cdot N_p^2 \cdot \gamma}{4\pi \cdot \sigma^{*2}} \cdot F \tag{2.2}$$

Here, f_{rev} gives the revolution frequency of the protons in the LHC, n_b the number of bunches, N_p the number of protons in a bunch, γ the relativistic γ factor of the protons, σ^* the the transverse beam size at the interaction point and F a geometric reduction factor due to the crossing angle θ_c of the beams. The beam size σ^* can be expressed as $\sigma^* = \sqrt{\epsilon_n \cdot \beta^*}$, where ϵ_n is the normalised transverse beam emittance and β^* the beta function, measured at the point of collision. The reduction factor F depends on θ_c, σ^* as well as the bunch length, and at the LHC it is ≈ 0.9 [66]. For all above considerations, a Gaussian beam profile is assumed. The LHC is designed for peak instantaneous luminosities of $1 \times 10^{34}\,\text{cm}^{-2}\text{s}^{-1}$ [1] and a maximum of $2.1 \times 10^{34}\,\text{cm}^{-2}\text{s}^{-1}$ was reached in 2018 [67].

To evaluate how many events of a given process occurred during a period of time, for example during the full run II, Equation 2.1 is integrated over time, defining the total integrated luminosity, $\mathscr{L} = \int L\,dt$. Figure 2.2 shows the integrated luminosity over time during run II.

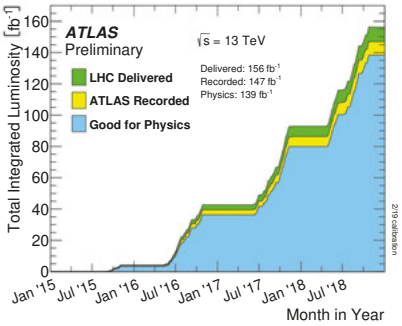

Figure 2.2: Total integrated luminosity over time during run II as deliverd by the LHC, recorded by ATLAS and "good for physics". From [67].

Not all of the delivered collision events can be recorded by ATLAS due to downtimes, and not all of the recorded data is suitable for analysis or "good for physics", e.g. due to not all required subsystems being fully functional at that moment. However the efficiencies are fairly high: in run II ATLAS recorded around 94% of the delivered luminosity and another 95% of that are "good for physics". In this thesis two iterations of the high mass Higgs search are presented. The first is based on the partial dataset taken in 2015-16 of 36.1 fb^{-1} and the second employs the full run II dataset of 139 fb^{-1} recorded in 2015-18.

Pile-up At the LHC, each proton bunch contains 10^{11} protons, and the spacing between them is only 25 ns. This leads to overlapping collision events happening in one single detector readout window. Such additional interactions are referred to as *pile-up*. Pile-up can either originate from the same bunch crossing - called *in-time pile-up* - or from the remnants of the previous or next bunch crossing - called *out-of-time pile-up*. In-time pile-up follows a Poisson-distribution with a mean μ, given by

$$\mu = \frac{L \cdot \sigma_{\text{inel.}}}{n_b \cdot f_{\text{rev}}} \tag{2.3}$$

where L is the instantaneous luminosity, n_b the number of bunches, f_{rev} the revolution frequency and $\sigma_{\text{inel.}}$ the total cross-section for inelastic scattering in the pp-collisions. This cross-section is known from measurements using so-called *minimum bias events* - events selected using a trigger as loose as experimentally possible, to not introduce any bias. For a centre-of-mass energy of $\sqrt{s}$ = 13 TeV such measurements were performed by for example ATLAS [68], TOTEM [69] and LHCb [70]. The ATLAS measurement of $\sigma_{\text{inel.}}(13\,\text{TeV}) = 78.1 \pm 2.9$ mb is in good agreement with theoretical predictions, as described in [68], and compatible with the other measurements within the respective uncertainty margins.

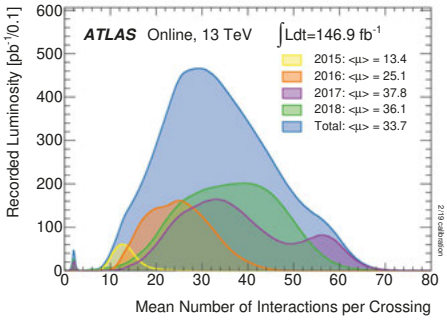

Figure 2.3: Mean number of interactions per bunch crossing μ for the different datataking years of run II. From [67].

Figure 2.3 shows the mean number of interactions per bunch crossing μ, following Equation 2.3, for the different data taking years of run II. The distributions are weighted with the respective integrated luminosity of each period. Pile-up is one of the major experimental challenges at the LHC, as it complicates particle reconstruction. As can be seen in Figure 2.3, the high luminosities during run II came at the cost of increased pile-up, especially in 2017 and 2018. This is of importance for the analysis of the full 2015-18 data set and addressed in Chapter 6.1.

2.2 The ATLAS detector

The ATLAS detector is one of the main experiments at the LHC. It is a general purpose detector designed with a broad physics analysis program in mind, intended to cover precision measurements of SM parameters as well as searches for Higgs particles and new physics processes. As such, it facilitates measuring the charged leptons, hadron jets and photons produced in the pp-collisions very precisely, but its design is particularly well geared to measure jet momenta and missing transverse energy with excellent resolution and to perform stand-alone muon measurements. The detector is cylindrical in design, forward-backward symmetric and covers almost the full solid angle around the interaction point, except near the beam pipe. It consists of multiple subsystems with different functions that are layered concentrically around the beam direction, as shown in Figure 2.4.

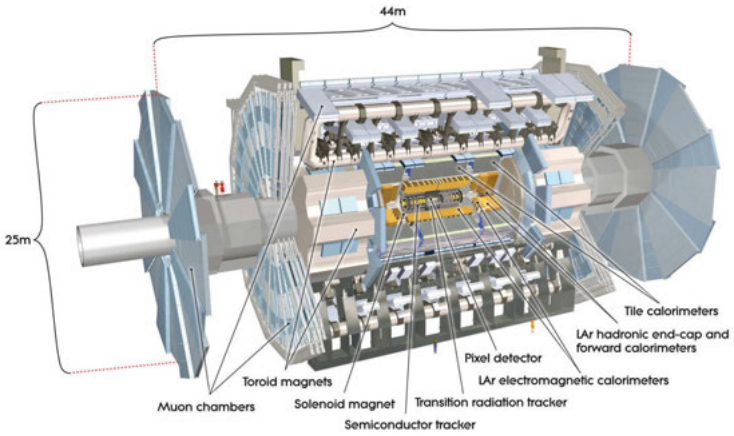

Figure 2.4: Schematic overview of the ATLAS detector. From [71].

Closest to the beam pipe, the *inner detector* (ID) serves to detect the tracks of charged particles. The inner detector's subcomponents are the *pixel detector*, *semiconductor tracker* and *transition radiation tracker*, all enclosed in the magnetic field of the *solenoid magnet*, as indicated in Figure 2.4. Next, a system of multiple *calorimeters* enables measurements of the energies of electrons, photons and hadrons with high precision. Last, the *muon spectrometer* (MS) is the outermost subsystem and - enclosed in the magnetic field of the *toroid magnets* - provides standalone measurements of muon tracks and momenta. Different particles can be distinguished as they interact differently with each detector component and therefore leave a characteristic signature. This forms the basis of the particle identification, which is discussed in more detail in Chapter 2.3.

Every subdetector contributes crucial information for the work presented in this thesis. The search for heavy Higgs bosons decaying as $H \to ZZ \to \ell\ell\nu\nu$- as presented in Chapters 5 and 6 - relies on an accurate reconstruction of electrons, muons and the missing transverse energy, quantifying the total transverse momentum of the neutrinos that cannot be detected. The reconstruction of electrons and muons requires the precise measurement of particle tracks, as provided by the ID and for muons also the MS. Charged particle tracks also play a role in the missing transverse energy reconstruction, but a key component in that is the measurement of particle energies as supplied by the calorimeters. In the following an overview of each main detector component is given, briefly outlining its setup and functionality. A complete review of the ATLAS detector design and technical specifications can be found in [59].

ATLAS coordinate system Before going into detail on the subdetectors, the coordinate system in which the respective coverages are commonly given needs to be clarified. At ATLAS (and in this thesis) a right-handed coordinate system is used, with its origin at the (nominal) interac-

tion point and the z-axis pointing along the beam direction. The positive z-direction is defined as pointing from ATLAS towards the LHCb detector, so counter-clockwise around the LHC ring. The x-axis points from the interaction point towards the center of the ring, and the y-axis upwards. The xy-plane is then the plane transverse to the beam direction. As the detector is cylindrical, it is convenient to use polar coordinates. The azimuthal angle Φ is the angle around the beam pipe, running from $-\pi$ to π and quantifying angular separation in the transverse plane. A value of $\Phi = 0$ corresponds to the positive x-axis direction. The angle with respect to the beam and therefore z-axis direction is given by the polar angle θ. It runs from 0 to π and a value of $\theta = 0$ corresponds to the positive z-axis direction. To describe the position of a relativistic particle often the lorentz-invariant *rapidity* y is used, defined as:

$$y = \frac{1}{2}\ln\left(\frac{E + p_z}{E - p_z}\right) \tag{2.4}$$

where E gives the particle's energy and p_z the z -component of its momentum. In the ultra-relativistic limit ($E >> m$), the rapidity is approximated by the *pseudo-rapidity* η, which depends on the polar angle as:

$$\eta = -\ln\tan\left(\frac{\theta}{2}\right) \tag{2.5}$$

The pseudo-rapidity η is most commonly used in ATLAS to describe the distance to the beam direction, with the regions of large η closest to the beam referred to as the *forward regions*. Along the z-direction the ATLAS detector is divided in different main sections: the cylindrically symmetrical *barrel* region with coverage $|\eta| < 1.4$ is sandwiched between two circular *end-caps*, which cover the range $1.5 < |\eta| < 5$. Most quantities used in the analysis are reconstructed in the transverse plane, and especially the *transverse momentum* p_{T} is commonly used in combination with the pseudo-rapidity to describe a particle's trajectory. The magnitude of the total momentum vector depends on these two quantities as $|\vec{p}| = p_{\mathrm{T}}\cosh\eta$. Distances between different particles' trajectories are then usually given by the angular separation $\Delta R = \sqrt{\Delta\Phi^2 + \Delta\eta^2}$.

2.2.1 Inner detector

ATLAS' main tracking detector is the ID [72], [73]. It allows to measure the momenta and trajectories of charged particles with high resolution, as well as to determine the (primary or secondary) vertex of their origin. To achieve this the ID is placed as close as possible to the interaction point, and it needs to maintain a low material density, so as to not alter a particle's trajectory due to multiple-scattering or even stop it fully. Since it is so close to the beams, it also needs to be able to withstand high doses of radiation.

These performance requirements dictate the ID's design, which consists of three subcomponents. Each of them is based on a different technique, but all follow the same basic principle of detection: a traversing charged particle ionizes the detector material and its track can be reconstructed from the measured charges. The ID is immersed in a 2 T solenoidal magnetic field, parallel to the beam direction. This is necessary for the determination of the momenta and charges of the particles. The resulting Lorentz-force deflects a charged particle onto a bent trajectory, the

curvature of which is proportional to its momentum and the direction of which depends on its charge.

Figure 2.5 gives an overview of the ID's subcomponents, indicating the extension of their radial coverage, R. The silicon *pixel detector* consists of four layers - including the *insertable b-layer* (IBL). It achieves the highest granularity, as it's closest to the interaction point and therefore crucial for vertex finding. Next, the *semiConductor tracker* (SCT) is based on silicon microstrips, distributed over four layers. Both the pixel detector and SCT cover the pseudorapidity range $|\eta| < 2.5$. The ID's outermost layers belong to the *transition radiation tracker* (TRT), which consists of gas-filled straw-tubes and extends to $|\eta| < 2.0$.

Insertable b-layer The IBL [75] is an additional layer of silicon pixels that was installed after the conclusion of the LHC's run I in between the previously inner-most pixel layer[1] and the beam pipe. This was necessary to maintain high tracking and vertex finding efficiencies, coping with the increased luminosity and the corresponding level of radiation damage during run II. As a consequence the IBL is only around SI3cm away from the beam line. It is made of 12 million pixels of size 50x250 μm^2, mounted on 14 staves that are placed at overlapping angles to provide hermetic coverage around the beam pipe. The hit resolution achieved is 8.5 µm in the transverse and 47 µm in the longitudinal direction.

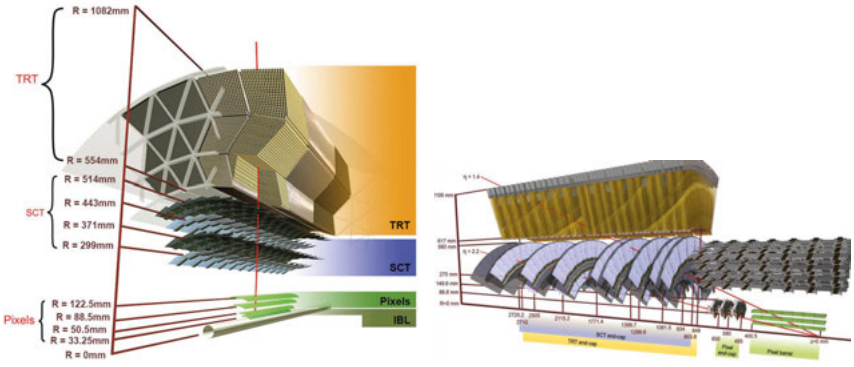

(a) Barrel (b) End-cap

Figure 2.5: Overview of the ATLAS inner detector components in (a) the barrel and (b) the endcap region. From [74] and [59].

Pixel detector The IBL is followed by three further layers of silicon pixel sensors in the barrel region [76]. In the endcaps, the pixel sensors are placed on three disks perpendicular to the beam direction. The whole system consists of 1744 modules, on which pixels of size 50x400 μm^2 and 250 µm thickness are arranged in a tile configuration. The modules are placed in such a way

[1] The inner-most layer of the pixel detector is called the *b-layer*.

that are no gaps, so that (ideally) each particle is expected to be recorded in each of the three layers. Here, hits can be resolved with an accuracy of 10 µm in the transverse and 115 µm in the longitudinal direction.

Semiconductor tracker The SCT is a strip detector consisting of 4088 modules mounted on four layers in the barrel and nine disks in each end-cap [77], [78]. Each module is composed of two planes of silicon detectors, glued back to back with an angle of 40 mrad, allowing reconstruction of a point in the xy-plane. The silicon detectors themselves consist of narrow micro-strips, with a distance between strips of 80 µm in the barrel, and between 55 µm to 95 µm in the end-caps. With the SCT a spatial resolution of 17 µm in the transverse and 580 µm in the longitudinal direction is achieved.

Transition radiation tracker The TRT consists of gas-filled straw tubes with a diameter of 4 mm and a transition radiation inducing medium between the tubes. A mixture of Xenon, CO_2 and oxygen gas is used in the straw tubes, and a 31 µm thick gold-plated tungsten wire runs through their centre, forming the anode. With the tube walls forming the cathode, a traversing particle ionizes the gas and due to the electric potential the resulting ions and electrons are separated. Measuring the drift time of the free charges, i.e. the time it takes before they are collected by the electrodes, allows to determine the position of the traversing particle. The result is a position measurement (relative to the anode wire) with an intrinsic resolution of 130 µm. In the barrel the straw tubes are 144 cm long and aligned parallel to the beam direction, measuring hits in the transverse plane. The tubes in the end-caps are 37 cm long and placed radially around the beam direction. When passing the medium in between the tubes, charged particles emit transition radiation. As the intensity of this radiation is dependent on the mass of the particle, with the help of the TRT heavy particles are distinguished from light particles - e.g. pions from electrons.

2.2.2 Calorimeter system

Calorimeters are used to measure the energy of a particle: they contain high-density material into which the particle induces a cascade of secondary particles, called a *shower*. All particles of the shower must be stopped within the calorimeter to be able to measure the total energy deposited by the incoming particle. Electrons and photons induce electromagnetic (EM) showers, while showers induced by hadrons such as pions, kaons etc. are referred to as hadronic showers. A differently defined length-scale is used to describe these two types of showers [79]: EM showers are characterized by the *radiation length* X_0. It is defined as the distance over which the electron or photon has reduced its energy by a factor e, due to its interaction with matter. Hadronic showers are described in units of the *interaction length* λ instead, which is the mean distance travelled by the hadron before undergoing an inelastic nuclear interaction. As more material is required to stop showers induced by hadrons, the ATLAS calorimeter system comprises a *electromagnetic* (ECAL) and a *hadronic calorimeter* (HCAL), with the ECAL placed first, as shown in Figure 2.6. After having passed the ID, electrons and photons shower and are stopped in the ECAL, whereas

the energy of hadrons is deposited and measured in the HCAL. Note that in general also neutral particles are stopped in the calorimeters, such as photons and neutral hadrons, but neutrinos are not detected, as they are subject only to the weak interaction. Muons on the other hand do not interact much with the calorimeter and pass on through to the muon spectrometer[2].

Both the ECAL and HCAL are sampling calorimeters: layers of absorbing material are alternated with layers of detecting material. The absorbing material, also called the passive material, is usually a dense material, with which incoming particles interact heavily, inducing the shower. The detecting material, also called called the active material, then serves to measure the energies of the particles produced in the shower. The full calorimeter system has a pseudorapidity acceptance of $|\eta| < 4.9$.

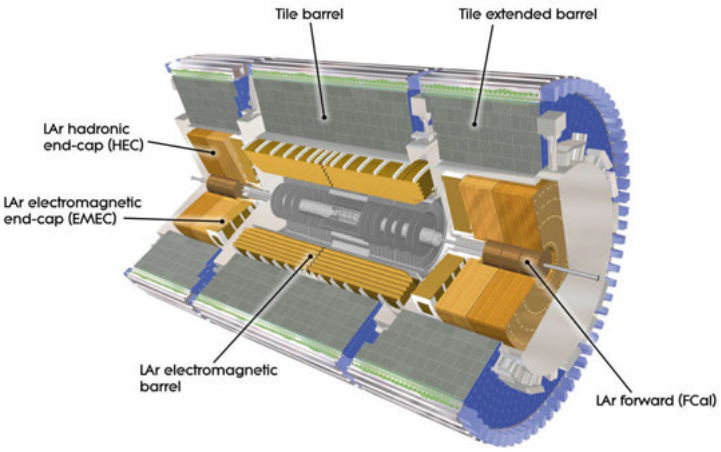

Figure 2.6: Schematic overview of the ATLAS calorimeter system. From [59].

The electromagnetic calorimeter As indicated in Figure 2.6 the ECAL [80] consists of a barrel part in the range $|\eta| < 1.475$ and two end-caps covering the range $1.375 < |\eta| < 3.2$. Each part uses liquid argon (LAr) as the active material and lead plates are used as the passive material. Liquid argon has the advantage of being radiation resistant and homogenous, ensuring a stable response over time. The lead absorber plates have an accordion shape, as this provides a uniform and symmetric coverage in Φ, without cracks. In the region $|\eta| < 1.8$, a *presampler* is installed in front of the ECAL. This is a thin, instrumented layer of argon, serving to measure the energy lost due to showers before reaching the calorimeter. The ECAL modules themselves consist of three layers with varying granularity in η, to obtain the best measurement. In total the ECAL has a

[2] Muons still deposit part of their energy in the calorimeter. This is referred to as the muon energy loss and needs to be modelled in the detector simulation, as discussed in Chapter 3.

depth of more than 22 X_0, but only around 1.5 λ, and therefore it is able to stop electrons and photons.

The hadronic calorimeter The HCAL consists of three main components: a *tile calorimeter* spanning the barrel region, the LAr hadronic endcap calorimeter (HEC) and the LAr forward calorimeter (FCal). The tile calorimeter [81] is equipped with scintillator tiles as active material and steel plates as absorbers. It covers the range $|\eta| < 1.7$. In the end caps, the two wheels of the HEC each use copper absorbers in combination with LAr and extend across $1.5 < |\eta| < 3.2$. Last, the FCal increases the pseudorapidity range to the very forward region $3.1 < |\eta| < 4.9$, also employing LAr as active medium. It it is built out of three layers, the first of which uses copper as active material, and the other two tungsten. The total depth of the HCAL is around 10 λ.

2.2.3 Muon spectrometer

Muons pass through the calorimeters without being stopped because they are minimally ionizing particles at relativistic energies. The MS [82] is therefore situated in the outermost layer of ATLAS, surrounding all other components. Charged particle tracks in the MS can be reliably identified as muons, since most other particles have either decayed or been stopped earlier in the detector [3]. Using a magnetic field, the MS provides both a high precision measurement of its momentum and trajectory as well as a faster readout used to reliably trigger the recording of data events containing a muon [4]. The MS is the largest part of ATLAS, consisting of over 4000 tracking chambers based on four different technologies, enclosed in the magnetic field of three superconducting air-core toroid magnet systems (one large one in the barrel, two smaller ones in the end-caps, with eight coils each). The toroidal magnetic field is inhomogeneous and the bending power[5] the muons experience is between 1.5 Tm to 5.5 Tm in the barrel ($|\eta| < 1.4$) and 1 Tm to 7 Tm in the end-caps ($1.6 < |\eta| < 2.7$). There is a transition region in between ($1.4 < |\eta| < 1.6$) with lower bending power. A stand-alone measurement of the muon track can be provided by the MS by registering the position of the muon in (at least) three different locations. In the muon reconstruction algorithm this MS track can also be combined with an inner detector track (cf. Chapter 2.3.2). Due to its large size, with more than 5 m of distance for the muon to travel from inner- to outermost edge, the MS measurement allows also to determine the momentum of highly energetic muons. The curvature of the trajectory of such muons is very small. The ID alone does not possess enough bending power or precision to measure the momentum above a certain p_T precisely. The MS is able to independently measure muon momenta with a resolution of better than 3% for muons with p_T in the $\mathcal{O}(10-100)$ GeV range and up to 10% for $p_T \approx 1$ TeV [83].

[3] There is a small probability for particles produced in the calorimeter showers to transverse into the MS and to be falsely detected as muons. This is referred to as *punch-through* and adversely affects both the resolution of the energy measurement and the efficiency of the muon reconstruction.

[4] See the next section for a general motivation of the necessity of dedicated triggers

[5] Bending power is defined as the integral $\int Bdl$, where B is the magnetic field component orthogonal to the direction of the muon, and dl the trajectory of an infinite momentum muon through the MS, i.e. a straight line through it.

Figure 2.7 gives an overview of the MS layout. Due to the eight coils of the toroid magnets, the MS system exhibits an eight-fold symmetry in Φ and is divided into 16 sectors in Φ: eight small ones around the toroid coils, and eight larger ones in between. The sectors overlap slightly to maintain hermetic coverage. A combination of precision and trigger chambers is installed in multiple layers, called *stations*.

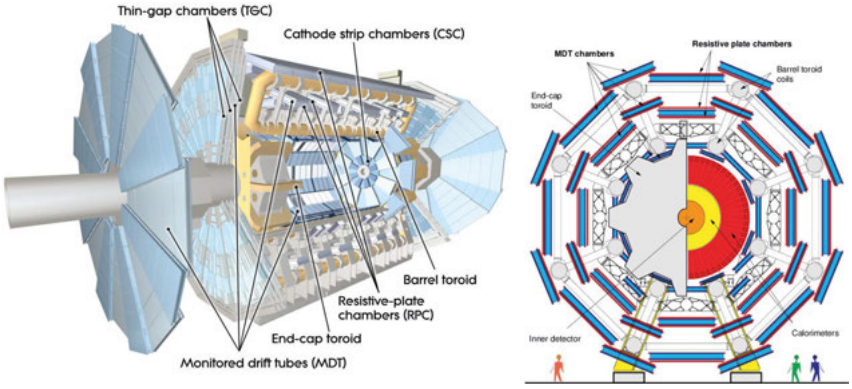

(a) (b)

Figure 2.7: Overview of the ATLAS muon spectrometer components in (a) a 3D cut-away view (b) a cross-section view in the barrel region, in the plane transverse to the beam direction. From [59] and [82].

Precision chambers High precision measurements of the muon tracks are provided by Monitored Drift Tube (MDT) chambers and Cathode Strip Chambers (CSC). Together they provide coverage up to $|\eta| < 2.7$. MDTs are drift chambers, built up from 30 mm wide aluminium tubes, filled with an argon and CO2 gas mixture. A tungsten anode wire runs through their center. The resolution of the drift time based position measurement in a single tube is around 80 µm in the transverse plane. A MDT chamber consists of three to eight layers of such drift tubes and this allows to achieve a combined resolution of 35 µm per chamber. In the barrel, MDT chambers are installed in three cylindrically layered stations, whereas in the end cap three stations of MDTs are mounted on three wheels, perpendicular to the beam axis. Due to its proximity to the interaction point for the inner radius ($2 < |\eta| < 2.7$) of the innermost wheel (called the small wheel) CSCs are used. The CSCs are capable of sustaining the high hit rates in this region due to their short drift time of 40 ns. They are trapezium-shaped multi-wire proportional chambers, consisting of a central anode wire with two cathode strips placed perpendicular to them. A CSC chamber provides a resolution of 40 µm in the bending plane, and of 5 mm in the transverse plane, where the segmentation is coarser.

Trigger chambers Information on the timing of the event and the trigger signal come from the trigger chambers, operating across the range $|\eta| < 2.4$. In the barrel region, three layers of

Resistive Plate Chambers (RPC) are used, whereas in the end-cap region four layers of Thin Gap Chambers (TGC) are employed. RPCs are composed of two resistive Bakelite plates, kept at a high voltage and with a 2 mm gas-filled gap in between them. The free charges produced when a traversing muon ionizes the gas are detected with two copper stripes, placed perpendicular to each other on the outside of the plates. The RPCs provide a rather coarse spatial resolution of 10 mm but a high time resolution of 1.5 ns. TGCs are multi-wire proportional chambers with a narrow gap between the cathode plates. They achieve a spatial resolution of 3 mm to 7 mm and similar timing resolution as the RPCs.

2.2.4 Trigger system

With the LHC's bunch spacing of 25 ns, 40 million pp-collisions happen per second. A single collision event corresponds to around 1.5 MB of data, coming from tens of thousands of read-out channels of the subdetectors. If all collision events were to be recorded, a data taking rate of petabytes per second would be needed. As this is not feasible, the *trigger system* makes the decision if an event should be processed, based on which particles are detected and with which (transverse) energy and momentum. The reasoning behind the trigger decision is the following: Most of the collision events at the LHC do not contain an interesting hard (i.e. high p_{T}) scattering event, such as the production of a Higgs resonance, but low p_{T} QCD interactions between the protons. Those events that are of interest for a physics analysis commonly have a prominent signature that can be used for a trigger, for example in the $\ell\ell\nu\nu$ heavy Higgs search the presence of at least one electron or muon with high p_{T}. The trigger and data acquisition system (TDAQ) is therefore a vital part of the ATLAS detector, as it is in charge of supplying all physics analysis with the kind of events they are looking for, while filtering the data down to a more manageable recording rate of 1 kHz.

A full description of the ATLAS TDAQ system in run II is given in [84], but briefly summarizing the trigger decision is taken in two stages: First by the hardware-based Level-1 (L1) trigger [85] and then by the software-based high level trigger (HLT) [86]. The L1 trigger is able to reduce the event rate to around 100 kHZ, where decisions to process an event further happen in as little as 2.5 µs. The L1 decision is based on the output of the calorimeter trigger towers and the MS trigger chambers, allowing to trigger on the presence of electrons, hadronic taus, photons, jets and $E_{\mathrm{T}}^{\mathrm{miss}}$ with the first, and of muons with the second. All information is combined by the central trigger processor, which takes the decision whether the event contains interesting activity and determining a corresponding region of interest. As time is crucial, only the regions-of-interest are passed to the HLT for further analysis. The HLT uses a streamlined version of the offline particle reconstruction algorithms to study the potential trigger signatures in more detail, exploiting the full granularity of the detectors and adding the tracking information from the ID.

To select the full range of interesting events, an analysis uses a list of different dedicated triggers, called a *trigger menu*. For the $\ell\ell\nu\nu$ search presented here, the presence of at least one electron or muon triggers the event. It is important that the trigger menu used is *unprescaled*: A trigger is prescaled if the rate of (expected) events matching its criteria is higher than the read-out rate of the detector, which results in only a predefined fraction of the events of interest being recorded.

To prevent the need for prescaling, some quality requirements need to be made on the lepton which fires the trigger, e.g. regarding its transverse momentum, identification or isolation. On the other hand, one needs to be careful that these requirements are not too stringent so that the impact on the signal acceptance is not too large. For this reason the lowest unprescaled triggers are used here. Due to the changing experiment conditions, the triggers and trigger menu can change over time.

2.3 Object identification and reconstruction

Since different types of particles interact differently with the various subdetectors, each kind of particle leaves a characteristic signature, as illustrated in Figure 2.8. Combining the information from the subdetectors therefore forms the basis of particle reconstruction and identification.

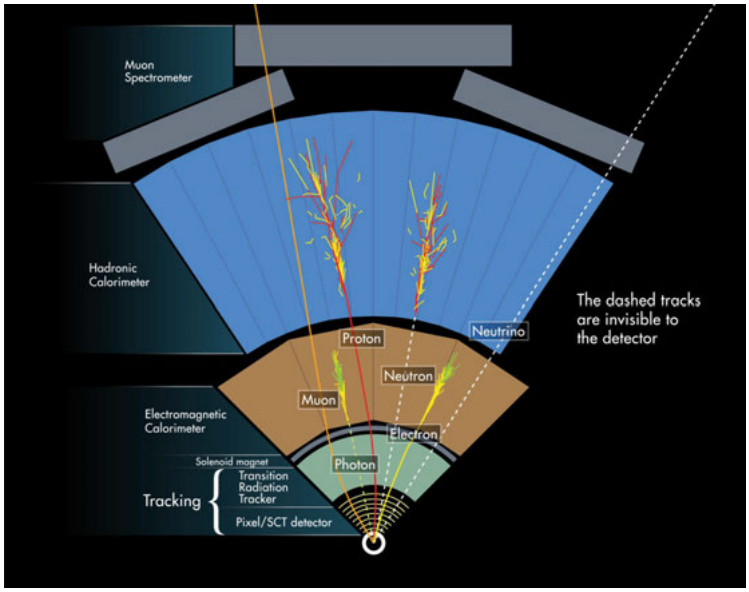

Figure 2.8: Illustration of the different detector signatures of different particles in ATLAS. From [87]

For the heavy Higgs search in the $\ell\ell\nu\nu$ final state, the lepton pair and the neutrinos need to be measured. The reconstruction of electrons and muons is therefore crucial. Neutrinos however cannot be directly detected with ATLAS, as they only interact weakly and easily pass through all detector material. But an indirect measurement of their transverse momentum is possible by reconstructing the *missing transverse energy*, $E_{\mathrm{T}}^{\mathrm{miss}}$. As the protons are only accelerated longitudi-

nally, the total transverse momentum in the collision is expected to be zero. An imbalance of the transverse momenta of all visible particles produced in the collision therefore implies the presence of particles escaping detection in the opposite direction. It is clear that the reconstructed $E_{\mathrm{T}}^{\mathrm{miss}}$ is only indicative of the total neutrino p_{T} if the visible part of collision products is well measured.

Aside from the lepton pair, the $\ell\ell\nu\nu$ final state can also contain additional quarks or gluons. These can arise as final state radiation, a process which becomes more probable at higher energies. When searching for a VBF heavy Higgs signature, two quarks are part of the leading order final state. Due to the nature of the strong interaction, no free quarks or gluons exist, and instead they *hadronize* immediately after being produced[6], creating a collimated beam of further hadrons. The detector therefore sees only this hadron beam, referred to as a *jet*. The reconstruction of jets is thus also important for the $\ell\ell\nu\nu$ analysis, as they enter in the $E_{\mathrm{T}}^{\mathrm{miss}}$ calculation and for the VBF analysis are key to selecting events that match the signal signature. In the following the specific algorithms used to reconstruct, calibrate and identify these most relevant physics objects are outlined. Each reconstruction algorithm is characterized by its efficiency (given a real particle, how likely is it to be reconstructed?) and its purity (how many times is another particle misidentified?). In view of the higher pile-up conditions during run II, the robustness of each reconstruction algorithm against pile-up is also an important property.

2.3.1 Electrons

Electrons are detected as a track in the ID and energy deposits in the ECAL, as indicated in Figure 2.9. Their reconstruction is therefore based on matching energy clusters in the calorimeter to nearby particle tracks in the ID. But since other particles, for example light hadrons, can lead to a similar signature, a likelihood discriminant is determined for each electron candidate. This helps to reduce the misidentification rate. Furthermore, electron candidates are required to be isolated from other objects, in order to suppress *non-prompt* electrons from heavy flavour decays. Comprehensive overviews of the electron reconstruction algorithms relied on for the work presented here are given in [89] and [90]. The following paragraphs outline each step only briefly.

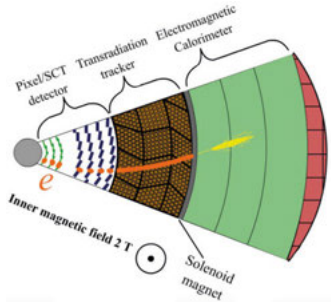

Figure 2.9: Illustration of an electron's signature in ATLAS. Adapted from [88].

Electron reconstruction The reconstruction of an electron starts with building an energy cluster in the calorimeter, which is then matched to an ID track to build the final electron candidate. Due to the coverage of the ID and the high granularity section of the ECAL, electrons are only reconstructed within $|\eta| < 2.47$. As the ATLAS software is in continuous development,

[6] With the exception of the top-quark, which decays before it hadronizes.

striving to improve especially in view of higher pile-up environments, the strategy with which the calorimeter cluster is built differs between the 2015-16 and full 2015-18 dataset analysis presented here: For the first dataset a *sliding window* approach [89] [91] is used, operating with a fixed window size for the clusters. For the second dataset the approach is to build topological clusters of a variable size, the so-called *super clusters* [90] [92]. The idea behind the supercluster approach is to more closely model the behaviour of the EM shower, and thereby improve the energy resolution of the reconstructed electron.

- In the sliding window clustering algorithm, the calorimeter is divided into elements of size $\Delta\eta \times \Delta\Phi = 0.025 \times 0.025$, referred to as *towers*. The energy deposit of a tower is calculated by summing the energies across the different calorimeter layers and used as input to the cluster finding algorithm. A cluster candidate is found by moving a window of 3×5 towers across the whole calorimeter and searching for regions where the total transverse energy E_{T} inside the window is at least 2.5 GeV. Duplicate, overlapping cluster candidates are removed in favour of the one with higher E_{T}. The efficiency of the cluster finding depends on the $|\eta|$ and E_{T} of the electron, reaching 99% for $E_{\mathrm{T}} > 15$ GeV. As the next step, the energy clusters are matched with an ID track as described below, building the electron candidate. After a succesful match to an ID track, the size of the calorimeter cluster is extended to 3×7 towers in the barrel region, and to 5×5 in the endcap, collecting more of the electron candidates energy.
- The supercluster approach starts with building topo-clusters in the calorimeter, by first identifying cells where the detected energy is above a certain noise threshold and then grouping neighbouring cells that satisfy this together. In the building of topo-clusters also hadronic calorimeter cells are included, however the electron reconstruction uses only the energy in the ECAL across most of the detector [7]. For further processing, only topo-clusters with an ECAL energy deposit of at least 400 MeV are considered, and this EM energy needs to be equal to at least half of the total energy of the topo-cluster. The latter criterion largely reduces the chance of selecting energy clusters from pile-up. Before building superclusters from the topo-clusters, the ID tracks are reconstructed and matched to the clusters, as described below. The topo-clusters are then scanned through in descending order of their E_{T}, and considered a possible seed to a supercluster if their E_{T} is larger than 1 GeV and they are matched to an ID track. Once such a seed cluster is found, adjacent satellite clusters are added to it, as they are likely deposits from a secondary EM shower coming from the same electron. Two criteria are used to identify a satellite cluster: The cluster must either be within a window of $\Delta\eta \times \Delta\Phi = 0.75 \times 0.125$ around the seed cluster's centre or within a window of $\Delta\eta \times \Delta\Phi = 0.125 \times 0.300$ if it shares the same best-matched ID track with the seed cluster. To build the electron candidate the superclusters are re-matched to the tracks, employing the same method as the initial matching of the topo-clusters.

In each case, tracks are reconstructed from hits in the ID layers, following the methods outlined in [93] and [94]. Each track candidate with $p_{\mathrm{T}} > 400$ MeV is fit with the ATLAS global χ^2 Track Fitter [95] - first under the pion hypothesis. If this fit fails, but the track candidate meets cer-

[7] The exception is the transition region $1.37 < |\eta| < 1.63$ for which also the readings in the presampler and the scintillator between the calorimeter cryostats are included.

tain requirements indicating it may belong to an electron which has lost part of its energy due to bremsstrahlung, the fit is redone under the electron hypothesis introducing also an energy-loss term. For electrons with $E_T > 10\,\text{GeV}$, as used in the analyses in this thesis, the efficiency of the track fitting step is greater than 98%. To further optimize the track reconstruction, the candidate track is refitted with a Gaussian sum filter (GSF) to account for the electron's non-linear energy loss via bremsstrahlung [96]. This step is only performed for tracks that are loosely matched to a calorimeter cluster based on their proximity in $\eta - \Phi$ space. To build a final electron candidate, the matching of ID track and calorimeter cluster is redone after the GSF fit, using tighter requirements on their $\eta - \Phi$ distance. Ambiguities in the track matching are resolved by selecting the track that is closest to the cluster when extrapolated to the calorimeter. A dedicated algorithm based on the recorded hits in different parts of the ID, the candidate's E/p ratio and p_T, as well as possible secondary vertices is used to distinguish electrons from photon conversions. For high p_T electrons as used here, the efficiency of the matching step is similar to that of the tracking step, reaching 98% or higher.

The main advantage of the superclustering approach is an improved resolution of the electron candidate's energy, even in a high pile-up environment. This is shown in Figure 2.10, where the resolution is quantified in terms of the effective interquartile range (IQE) [8] of the distribution of the ratio over measured and true energy. In Figure 2.10(a) the dependance of the IQE on the electron's true E_T (equal to its p_T) is shown for both methods, assuming zero pile-up. For highly energetic electrons, as mostly used in the high mass analysis, the improvement is small. However the superclustering is necessary to maintain good energy resolution despite the increased pile-up in the 2017-18 data, as shown in Figure 2.10(b).

[8] IQE = $(Q_3 - Q_1)/1.349$, with Q_1 the first and Q_3 the third quartile

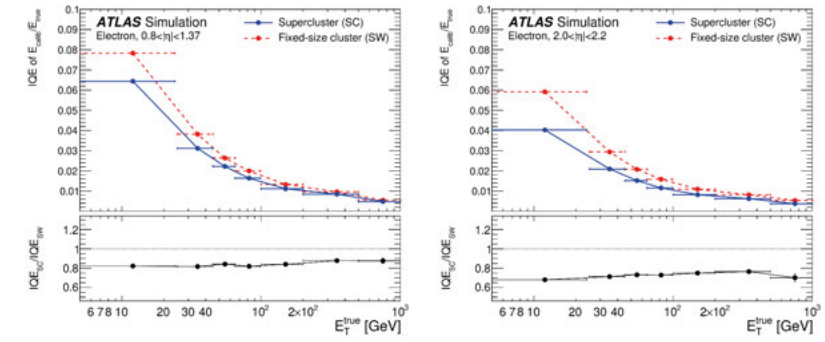

(a)

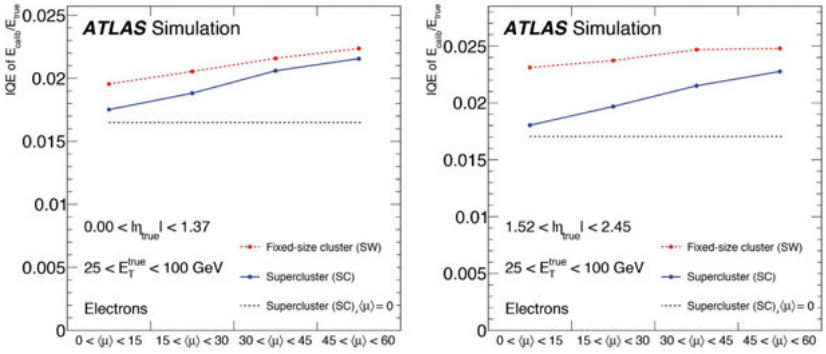

(b)

Figure 2.10: Comparison of electron energy resolution between the sliding window and supercluster approach. In (a) depending on the electron's true E_T assuming zero pile-up and in (b) depending on the average pile-up. For electrons in the barrel (left) or endcap (right) region. From [90].

Electron energy calibration The calibration of the electron candidate's energy based on the calorimeter clusters proceeds in three main steps. First, a multivariate algorithm taking into account the EM shower properties is applied to simulated and data events, optimizing the energy resolution. This algorithm is trained on simulation. Next, $Z \to e^+e^-$ events are used to adjust the absolute energy scale in data and to correct the resolution in simulation to match that in data. Last, independent samples are used to validate the calibration, i.e. low-energy electrons are studied in $J/\Psi \to ee$ events. The calibration procedure is detailed in [97].

Figure 2.11 shows the results of the electron energy calibration for the 2015-17 data. In the com-

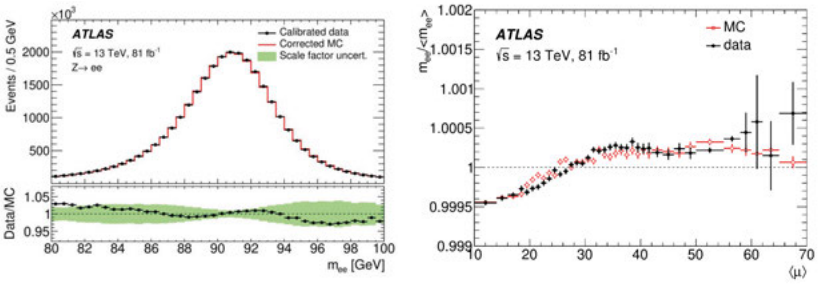

(a) (b)

Figure 2.11: Results of the electron energy calibration for the 2015-17 data. (a) A comparison of the dielectron invariant mass distribution in $Z \to e^+e^-$ events between data and MC simulation. (b) The relative variation of the peak position of the dielectron invariant mass distribution as a function of pile-up. From [90].

parison of the dielectron invariant mass distribution shown in (a), good agreement between data and simulation is observed (within the systematic uncertainties, indicated by the band in the ratio panel). Moreover, the relative position of the peak of this distribution only varies by less than 0.1% as a function of pile-up in both data and MC simulation.

Electron identification The final identification of electrons is based on a likelihood (LH) discriminant, improving the purity greatly. This LH discriminant takes into account variables that allow separating prompt electrons from contributions from hadron jets, converted photons or non-prompt electrons produced in heavy flavour decays. Such variables are for example the number of hits in the different layers of the ID, the distance in $\Delta\eta \times \Delta\Phi$ between calorimeter cluster and matched ID track, various quantifiers of the width of the EM shower induced, and the ratio of energy deposited in the HCAL with respect to the EM cluster energy. For each variable considered, a probability density function (p.d.f.) is determined for signal (i.e. true electrons) and background (i.e. non-prompt or fake electrons), either from data events employing the tag-and-probe method or from corrected simulation (cf. [90] and [89] respectively). The p.d.f.s are used to construct a likelihood discriminant, that quantifies whether an electron candidate is more likely to be signal or background (cf. Chapter 4.5 for more explanation on likelihoods). The identification of an electron candidate then corresponds to a requirement on the value of this discriminant (and in some cases on additional variables). To maintain stable efficiencies across the full kinematic range, the LH discriminant requirements are optimized in bins of η and E_{T}. Depending on how stringent (or *tight*) these requirements are, different *working points* (WPs) are defined. In general, the tighter the requirements, the higher the purity but the lower the efficiency of the WP (and vice versa).

In the high-mass $\ell\ell\nu\nu$ analysis presented here, signal electrons are required to satisfy the *medium* working point. As shown in Figure 2.12, the efficiency of this WP ranges from around 75% for elec-

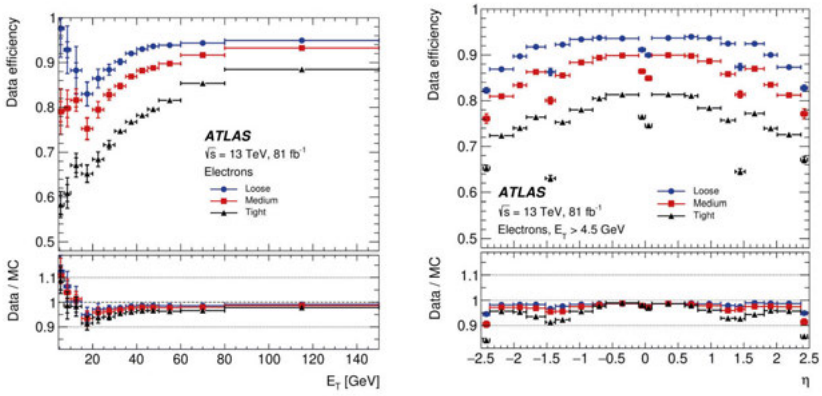

(a) (b)

Figure 2.12: Efficiency of the electron identification for the three different working points as a function of (a) E_{T} and (b) η. Based on the 2015-17 data and employing the superclustering approach. From [90].

trons with $p_{\mathrm{T}} > 20$ GeV (the threshold of $\ell\ell\nu\nu$ electron selection) to around 95% for p_{T} greater than 100 GeV, as measured on the 2015-17 data using the superclustering approach. The efficiency curves for the 2015-16 dataset with the sliding window approach are comparable. With the medium WP, only 0.05% of hadrons in the energy range $20 < E_{\mathrm{T}} < 80$ GeV are misidentified as electrons [98]. Moreover, in the $\ell\ell\nu\nu$ analyses electrons satisfying the *loose* WP are used to reject events with more than two leptons. As can be seen, the efficiency of this WP is higher, starting at 85% efficiency for 20 GeV electrons.

Electron isolation To further increase the purity of selecting prompt electrons over non-prompt electrons, electrons are required to be *isolated*, i.e. sufficiently far from other objects in the event. Whether the electron is isolated is probed by assessing how much activity is found near it, looking at its ID track and calorimeter cluster separately. Generally, this is done by summing the transverse energies of all ID tracks or calorimeter clusters found in a cone of a fixed radius ΔR around the electron candidate. Based on the efficiency of the isolation selection, different working points are defined. The electron isolation WP was further optimized after the analysis of the 2015-16 data, and therefore differs between the two analysis presented here. For the 2015-16 data analysis, *Loose* isolation is required, whereas for the full 2015-18 data analysis the isolation WP is called *FixedCutPFlowLoose*:

- The *Loose* working point is defined as providing 99% efficiency for both the calorimeter cluster and the ID track isolation, estimated by the variables $E^{\mathrm{iso}}_{\mathrm{T,\,cone}}$ and $p^{\mathrm{iso}}_{\mathrm{T,\,var}}$ respectively. The calorimeter-based isolation variable $E^{\mathrm{iso}}_{\mathrm{T,\,cone}}$ is calculated by summing up the transverse energies of topo-clusters within a radius of $\Delta R = 0.2$ around the electron's direction. The summation of all energies initially includes the energy of the electron itself, which is

subtracted in a next step assuming a fixed window size. As not all of the energy is always found within this window, a leakage correction is applied. Moreover, contributions from pile-up are corrected for by removing the median ambient energy density calculated from all energy deposits across the whole calorimeter. In contrast to using a fixed cone size, for the track isolation variable $p_{\mathrm{T,\,var}}^{\mathrm{iso}}$ a cone of variable radius is used. This variable cone accounts for the fact that the products of a boosted decay can be very close to each other and that the finer granularity of the ID allows much narrower cones than the calorimeter. The cone radius is determined as $\Delta R = \min(10\,\mathrm{GeV}/p_{\mathrm{T}}, R_{\mathrm{max}})$, where p_{T} is the transverse momentum of the electron track (in GeV) and R_{max} is set as 0.2 for the loose WP. In the summation of transverse track momenta within this cone only tracks with $p_{\mathrm{T}} > 1$ GeV and within $|\eta| < 2.5$ are considered. In addition, a requirement on the longitudinal impact parameter of the track is made to select tracks originating from the primary vertex and suppress pile-up contributions. A full overview of the definition of the loose isolation WP and its performance is given in [89].

- The *FixedCutPFlowLoose* WP presents an optimization of the standard loose working points that is more robust against pile-up. To achieve this, the calculation of the $p_{\mathrm{T,\,var}}^{\mathrm{iso}}$ and $E_{\mathrm{T,\,cone}}^{\mathrm{iso}}$ variables is modified. For the track isolation $p_{\mathrm{T,\,var}}^{\mathrm{iso}}$ a requirement on the the track to vertex association (TTVA) is implemented: Only tracks that are either part of the calculation of the primary vertex or pass the longitudinal impact parameter requirement but are not associated with any vertex are considered. The two variables are combined in a weighted sum, to build a single isolation selection variable. As the name indicates, the calorimeter cluster isolation $E_{\mathrm{T,\,cone}}^{\mathrm{iso}}$ is calculated using the *particle flow* (PFlow) algorithm. Relying on this algorithm provides an improved track to cluster association and estimate of the pile-up correction. More details on the PFlow algorithm are given in Chapter 2.3.3. The *FixedCutPFlowLoose* WP was optimized specifically for the $ZZ \to \ell\ell\ell\ell$ Higgs analyses, for which a high lepton selection efficiency is extremely important [99].

2.3.2 Muons

In the ideal case, a muon is detected as a track in the ID and another track in the MS, as indicated in Figure 2.13. Due to the respective magnetic fields, the muon track in the ID is bent in the Φ direction, and in the MS in the θ direction. When passing the calorimeters, muons lose a fraction of their energy due to interactions with the material. This energy loss is typically of the order of a few GeV (in the kinematic range of muons considered here) and needs to be modelled precisely to allow accurate reconstruction of the muon momentum. To reduce uncertainties on the muon momentum scale and resolution, the muon momenta are calibrated in a dedicated procedure. Reconstructed muons are selected with different efficiency according to different

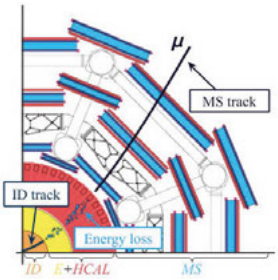

Figure 2.13: Illustration of a muon's signature in ATLAS. Detector cross-section image adapted from [82].

identification working points, imposing further quality requirements on the reconstruction. As explained for electrons above, the muons studied here are required to be isolated from other objects in the event. The following paragraphs give a brief overview of each step, while a full documentation of the muon reconstruction can be found in [100] based on the data recorded in 2015, and in [101] using the full 2015-18 data.

Muon reconstruction Muon reconstruction starts with the reconstruction of tracks in the MS. The track finding in the MS begins by forming MDT segments, i.e. a straight-line fit to the hits in each layer of an MDT chamber. The information on the muon candidate's position orthogonal to the bending plane is added by the RPC and TGC measurements. A fit of segments found in different layers of the MS then builds the muon candidate track, as described in detail in [100]. Muon candidate tracks in the ID are reconstructed indepedently and in the ideal case the ID and MS track are combined. ID tracks of muon candidates are reconstructed following the methods outlined in [93] and [94]. Figure 2.14 shows the expected relative transverse momentum resolution as a function of the truth transverse momentum of muons in the central region and small sectors of the MS (as an example), for the different cases of reconstructing muons from the ID or MS information only, or their combination. While the ID-only reconstruction performs best for

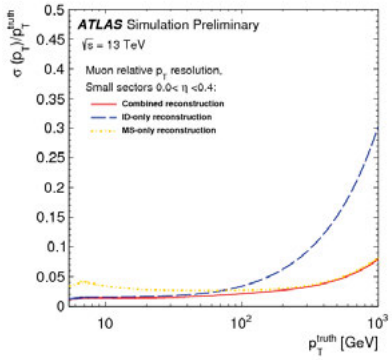

Figure 2.14: Expected relative transverse momentum resolution as a function of the truth transverse momentum for different cases of muon reconstruction. From [83].

low transverse momenta, the MS reconstruction provides a better resolution for high transverse momenta. The reason is, as mentioned earlier (cf. Chapter 2.2.3) the stronger bending power in the MS. The combined reconstruction thus ensures optimal resolution across a wide range of transverse momenta. However, it is not guaranteed that both tracks are detected for a given muon, due to e.g. gaps or dead material in the different subdetectors and their different ranges of coverage. If one of the tracks cannot be reconstructed, several other quantities can be used to reconstruct the muon, leading to four different muon types. Figure 2.15 illustrates the four different types, and which subdetector information they take into account:

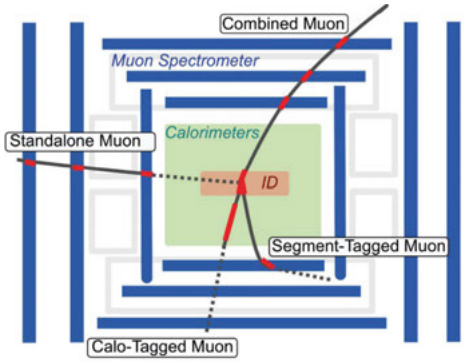

Figure 2.15: Illustration of the four different muon types defined in ATLAS. ME muons are denoted as *standalone muon* here. From [102].

- Combined (CB) muons are the result of a global refit of the ID and MS tracks. During the refit the MS track may be modified (i.e. by adding or removing hits), if it improves the fit quality. For most muons, the matching of the two tracks starts from the MS track, extrapolating it back to the ID. Combined muon reconstruction performs well in the range covered by both ID and MS, and is therefore widely relied on in analyses using muons of the "standard" kinematic range (i.e. not very low or high p_{T}), such as also the $H \to ZZ \to \ell\ell\nu\nu$ analyses presented here.
- Segment-tagged (ST) muons are built from the ID track only, if this track can be associated with at least one MS track segment. This allows to reconstruct muon trajectories that only register in one layer of MS chambers, for example due to passing through MS regions with reduced acceptance.
- Calorimeter-tagged (CT) muons are built from the ID track only, if it can be matched to an energy deposit in the calorimeter that is compatible with the signature of a minimum-ionizing particle as muons are in ATLAS. This type serves to recover muons passing through the MS region that is only partially instrumented ($|\eta| < 0.1$).
- Extrapolated (ME) muons are reconstructed from the MS track only, extrapolated and loosely matched to the interaction point. A well reconstructed MS track, with segments in at least two - or three in the forward region - layers is required. The track extrapolation has to take into account the muon energy loss in the calorimeters, to provide a measurement of the muon as it emerged from the interaction point. Using ME muons allows to recover muons that are outside the ID but within the MS coverage, i.e. within $2.5 < |\eta| < 2.7$.

For CB and ME muons, the muon energy loss in the calorimeters is modelled using a combination of the measured and the expected energy loss. The latter is based on an analytical parametrization that is derived from a detailed description of the detector geometry. With this approach, the mean energy loss can be determined with high precision, e.g. down to 30 MeV for a 50 GeV muon. Nonetheless, the description of the muon energy loss is one factor leading to discrepan-

cies between the measured and simulated momenta of muons. It is therefore necessary to apply a muon momentum calibration procedure, as described in the following.

Muon momentum calibration Although the ATLAS detector simulation (cf. Chapter 2.4) is based on detailed and realistic descriptions of the detector geometry, the alignment of detector components and the previously mentioned muon energy loss, discrepancies between the predictions obtained from MC simulation and the measurement in data remain. One reason for them is that it is technically not feasible to describe everything down to the smallest detail, as it would be too computationally expensive to generate a large number of events. Another cause for such disagreements is the fact that the MC simulation is typically produced before the data taking, so that specific detector inefficiencies are not yet known and therefore not modelled. Calibration procedures are applied to account for the (generally small) discrepancies between data and simulation. For muons, $Z \to \mu\mu$ and $J/\Psi \to \mu\mu$ events are used to derive correction factors for the simulated muon momenta, adjusting both the momentum *scale* and *resolution* in simulation - i.e. the shift and the width of the momentum spectrum - to reflect the behaviour in data. Only CB muons are used in the calibration procedure, and first the correction factors are determined independently for the ID and MS track. The momentum scale is affected by the average energy loss in the calorimeters characterized by the parameter s_0 (for MS muons only), as well as the scale of the magnetic field integral and global radial distortions in the detector, summarized in the parameter s_1. It is further assumed that the relative resolution of the muon transverse momentum, $\frac{\sigma(p_\mathrm{T})}{p_\mathrm{T}}$, can be parametrized as the quadratic sum (denoted by $\oplus$) of three terms:

$$\frac{\sigma(p_\mathrm{T})}{p_\mathrm{T}} = \frac{r_0}{p_\mathrm{T}} \oplus r_1 \oplus r_2 \cdot p_\mathrm{T} \tag{2.6}$$

Here, r_0 accounts for fluctuations of the energy loss (only for MS muons), r_1 summarizes the effects of multiple scattering and local radial distortions affecting the muon trajectory and r_2 describes the intrinsic resolution due to the spatial resolution of and any misalignment between the sub-detectors. Taking all the effects into account, the corrected transverse momentum in the ID or MS (denoted by Det) is parametrized as

$$p_\mathrm{T}^{\mathrm{Cor,\,Det}} = \frac{p_\mathrm{T}^{\mathrm{MC,\,Det}} + \sum_{n=0}^{1} s_n^{\mathrm{Det}}(\eta,\Phi)\left(p_\mathrm{T}^{\mathrm{MC,\,Det}}\right)^n}{1 + \sum_{m=0}^{2} r_m^{\mathrm{Det}}(\eta,\Phi)\left(p_\mathrm{T}^{\mathrm{MC,\,Det}}\right)^{m-1} G_m} \tag{2.7}$$

where $p_\mathrm{T}^{\mathrm{MC,\,Det}}$ refers to the uncorrected transverse momentum of the muon in MC simulation, the s_n and r_m are the scale and resolution parameters as described above and G_m denotes Gaussian distributions with a mean of zero and unit width. Values for the parameters s_n and r_m are extracted from data by fitting the invariant dimuon mass spectrum in $Z \to \mu\mu$ and $J/\Psi \to \mu\mu$ events, each giving access to different mass ranges. For this purpose, the detector is divided into 18 different regions of η reflecting the distribution of material and instrumentation as well as the magnetic field. In addition the MS is divided into two types of sectors in Φ- the *small* sectors encompass the magnetic coils, while the *large* sectors are between the coils. The correction parameters are therefore dependent on η and Φ, as denoted in Equation 2.7. A simultaneous,

binned maximum-likelihood fit (cf. Chapter 4.5) is performed using the dimuon invariant mass spectra in all regions. Specifically, binned templates of the distributions derived from MC are fit to the observed data. Several iterations of the fit are performed to achieve stable results, and the calibration parameters are first derived for ID muons. The best fit results from the ID calibration form the starting point for the MS calibration. To determine the correction for CB muons, the two are combined as

$$p_{\mathrm{T}}^{\mathrm{Cor,\,CB}} = f \cdot p_{\mathrm{T}}^{\mathrm{Cor,\,ID}} + (1-f) \cdot p_{\mathrm{T}}^{\mathrm{Cor,\,MS}} \tag{2.8}$$

where the weight f is extracted from the uncorrected simulated muon momenta. The systematic uncertainties associated with the calibration parameters are assessed by repeating the fit procedure with different conditions, for example using a different dimuon invariant mass range of the templates or a different parametrization of the background component. More details on the calibration fits and the estimation of systematic uncertainties can be found in [103].

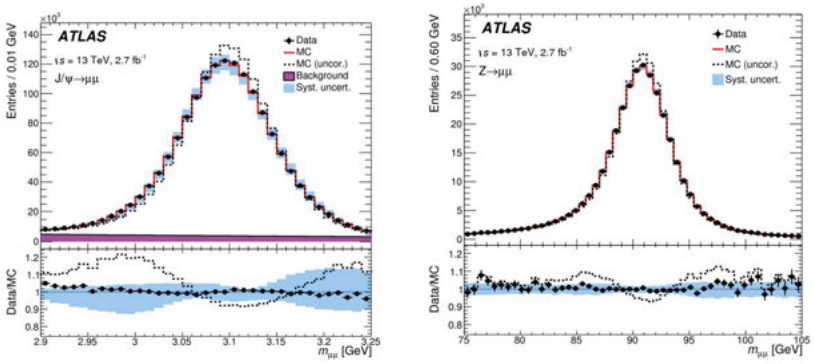

(a) (b)

Figure 2.16: Dimuon invariant mass distributions in data and corrected as well as uncorrected MC simulation in (a) $J/\Psi \to \mu\mu$ and (b) $Z \to \mu\mu$ events around the respective resonance mass. Using only CB muons and part of the 2015 data. From [100].

Figure 2.16 illustrates the results of the calibration, comparing the dimuon invariant mass distributions between data and uncorrected and corrected simulation. After the correction, the simulated distributions reproduce the data well, within the associated uncertainties. To study the performance of the calibration further, the dimuon invariant mass resonances shown in Figure 2.16 are fitted to derive estimates of the mass scale and resolution, which in turn provide an estimate of the momentum scale and resolution (cf. Chapter 3). For $Z \to \mu\mu$ events, the fit model consists of a Breit-Wigner function modelling the truth-level Z boson lineshape convolved with a resolution model, which is composed as the sum of a Crystal Ball and a Gaussian function. The peak position parameter of this Crystal Ball function serves as an estimate of the dimuon mass scale $m_{\mu\mu}$ and its width parameter is used to quantify the dimuon mass resolution $\sigma_{\mu\mu}$.

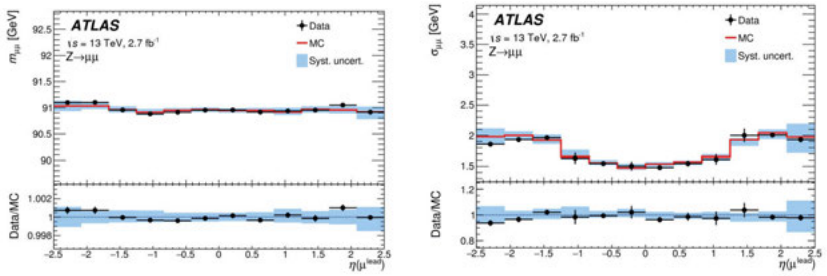

(a) (b)

Figure 2.17: Dimuon mass scale (a) and resolution (b) as a function of the pseudorapidity of the leading p_{T} muon, for data and corrected simulation in $Z \to \mu\mu$ events. Using only CB muons and part of the 2015 data. From [100].

The results of the scale and resolution measurement in $Z \to \mu\mu$ events are shown in Figure 2.17 as a function of the pseudo-rapidity of the leading p_{T} muon of the pair[9]. The corrected simulation is in good agreement with the data, highlighting that thanks to the muon momentum calibration a very accurate description of the muon momenta in simulation is achieved. From the dimuon mass resolution shown, it can be determined that the relative transverse momentum resolution of muons originating from Z boson decays is approximately 2.3% in the barrel region, and approximately 2.9% for muons in the endcaps.

A closer look at the dependence of the dimuon mass scale and resolution on the pseudo-rapidity, and how various detector effects affect it, is presented in Chapter 3, in which an alternative fit model for the dimuon invariant mass spectrum around the Z boson boson resonance is studied.

Muon identification Different observables are used to identify prompt (or signal) muons, distinguishing them from the background, e.g. muons originating from hadron decays. For example, for CB muons, the fit quality of the combined ID and MS refit of a muon track - characterized by the normalized χ^2- is expected to be poor, if the muon originates from a hadron that decayed during its passage through the detector. In such a case, it is likely that the muon travels in a slightly different direction from the hadron, leading to a kink in the full track. Another example of a discriminating variable is the q/p significance, defined as the absolute difference between the charge (q) over momentum (p) ratio of the the ID and MS track, normalised to the associated uncertainties. Additionally, the absolute difference between the transverse momentum as measured in the ID and the MS, normalised to the transverse momentum of the CB track, allows to assess whether the CB track is compatible with a single muon's trajectory.

[9] Only the $Z \to \mu\mu$ results are shown here, as this is the kinematic range relevant for the $H \to ZZ \to \ell\ell\nu\nu$ analyses presented in the following.

Aside from variables quantifying the CB fit quality, quality requirements are also made on the separate ID and MS tracks, such as on the number of hits used in each. A set of such selection criteria then defines a working point of the muon identification, providing a certain efficiency and purity. The $H \to ZZ \to \ell\ell\nu\nu$ analyses presented here, use only signal muons satisfying the *medium* identification criteria. This working point includes only CB muons in the range covered by both ID and MS ($|\eta| < 2.5$) and is optimized to provide minimal systematic uncertainties originating from the muon reconstruction and calibration. The full set of criteria defining this WP are listed in e.g. [100] and [101].

The reconstruction and identification efficiencies for muons (within $|\eta| < 2.5$) are measured with the tag-and-probe method, using $Z \to \mu\mu$ and $J/\Psi \to \mu\mu$ events in data and simulation. Here, the tag is always a *Medium* muon that fired the trigger, where different probes allow to measure the various efficiencies, e.g. ID tracks can be used to measure the reconstruction efficiency in the MS (and vice versa). Figure 2.18 shows the measured and expected muon efficiencies in different regions of phase space: in (a) the efficiencies of different working points as a function of p_{T} is shown as determined using $J/\Psi \to \mu\mu$ events, in (b) the same efficiencies are shown as a function of η for muons with a p_{T} of at least 10 GeV and as determined using $Z \to \mu\mu$ events, and finally (c) shows the resulting efficiencies across the full p_{T} range probed using both the $J/\Psi \to \mu\mu$ and $Z \to \mu\mu$ measurements, but only for medium muons. The ensemble of plots demonstrates that the medium WP provides stable efficiencies above 98% for muons with a transverse momentum of at least 20 GeV. The corresponding rate to misidentify hadrons as muons is below 0.2% (as determined using simulated $t\bar{t}$ events, cf. [101]). In the $H \to ZZ \to \ell\ell\nu\nu$ analyses only medium muons are used to reconstruct signal candidates, but muons satisfying the loose identification WP are used to veto events with additional leptons, as these provide even greater efficiency - especially at low p_{T}- albeit with lower purity.

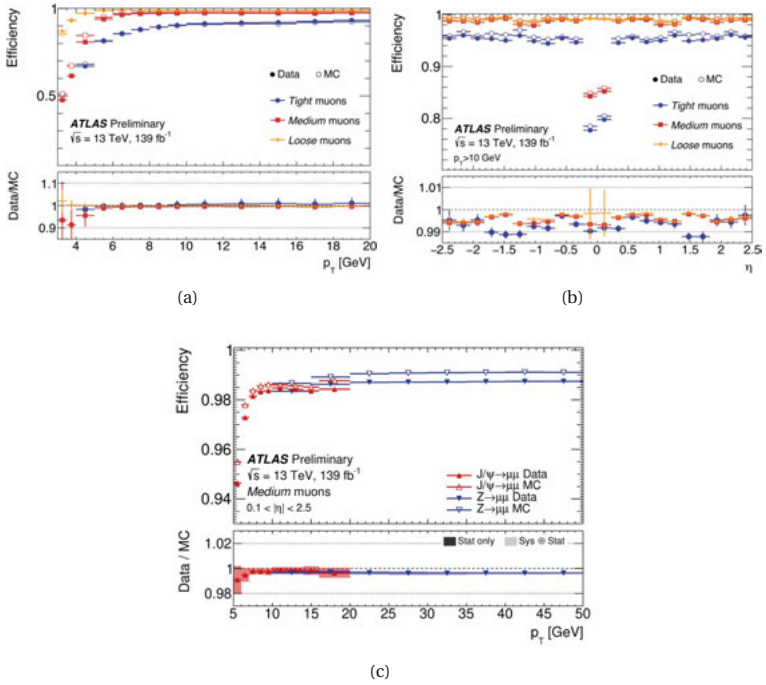

Figure 2.18: Muon efficiencies in different regions of phase space: (a) shows the efficiencies of different working points as a function of the muon transverse momentum p_{T}, measured using $J/\Psi \to \mu\mu$ events, and (b) shows those efficiencies as a function of η for muons with $p_{\mathrm{T}} > 10$ GeV and measured using $Z \to \mu\mu$ events. Finally, (c) shows the efficiency to reconstruct medium muons as a function of p_{T}, combining the $J/\Psi \to \mu\mu$ and $Z \to \mu\mu$ measurements. In each case the efficiencies in data and MC are shown seperately, and in the bottom panel the ratio of data over MC is shown including the statistical and systematic uncertainties. From [101].

Muon isolation For muons, isolation criteria similar to those for electrons already introduced above are applied in the $H \to ZZ \to \ell\ell\nu\nu$ analyses. This means that all considered muons must satisfy the *loose* working point in the analysis of the 2015-16 data, and the *FixedCutPFlowLoose* working point in the analysis of the full 2015-18 dataset.

- The loose WP is defined to deliver 99% efficiency and is based on a calorimeter-based and a track-based isolation variable. The calorimeter-based variable is defined in the same way as for electrons, as the sum of the (transverse) energies of all topo-clusters found in a cone of $\Delta R = 0.2$ around the muon direction. The track-based variable also follows the same definition as for electrons: it is the sum of the transverse momenta of all tracks within a cone of variable size, given by $\Delta R = \min(10\,\mathrm{GeV}/p_{\mathrm{T}}, R_{\mathrm{max}})$. For muons, the parameter R_{max}

is set to 0.3 and only tracks with a transverse momentum of at least 1 GeV are used. The ratio of each isolation variable over the transverse momentum of the muon forms the basis of the isolation selection criteria defining the working point. The performance of the loose isolation WP for muons is studied in detail in [100] using the 2015 data, and in [101] with the full 2015-18 dataset.

- The particle-flow based WP *FixedCutPFlowLoose* for muons is defined in exactly the same way as for electrons, as described in Chapter 2.3.1 and [99]. It is an optimization of the previously used standard isolation variables and employs the PFLOW algorithm, which makes it more robust against pile-up.

Efficiency measurements for both muon isolation working points can be found in [101], using the full 2015-18 dataset. While both working points provide similar efficiencies to select prompt muons (>97% for muons with a transverse momentum of at least 20 GeV), the *FixedCutPFlowLoose* working point provides slightly reduced rates of selecting non-prompt muons from heavy flavour decays).

2.3.3 Jets

Jets are reconstructed by combining the four-momenta of all particle signals found within a narrow cone of each other, in order to estimate the original quark or gluon momentum. Here, a sequential recombination algorithm called the *anti-*k_t algorithm [104] is employed for this purpose. The input four-momenta of the particle signals can either be obtained from topologically connected energy deposits in the calorimeter or a combination of calorimeter clusters and ID tracks. Jets reconstructed with the first approach, exclusively using the calorimeter readings, are referred to as EMTOPO jets in this thesis and they are used for the analysis of the 2015-16 dataset, presented in Chapter 5. The second approach relies on the *particle flow* (PFLOW) algorithm to combine the calorimeter with the tracking information, in order to improve the energy resolution of jets especially at low transverse momenta as well as their angular resolution and more efficiently reject pile-up contributions. PFLOW jets are used for the analysis of the full 2015-18 dataset, documented in Chapter 6. After building the jets from individual signals, each jet's energy needs to be calibrated to account for various detector effects. Moreover, contributions from pile-up jets are further suppressed by employing a dedicated discriminant, called the *jet vertex tagger* (JVT). Last, jets originating from b-quarks can be identified with the *b-tagging* algorithm, which exploits the long lifetime of hadrons containing b-quarks. Each of these steps is briefly outlined in the following.

Jet reconstruction The first step of the jet reconstruction is to prepare the inputs for the jet finding algorithm. This is done differently for EMTOPO and PFLOW jets:

- EMTOPO jets start from finding topo-clusters of calorimeter cell energies by merging the energy deposits of neighbouring cells if they are above a certain noise threshold. This topo-cluster finding algorithm is described in detail in [92] and it forms also the first step of super-cluster finding in the electron reconstruction as described above. Subsequently, the

topo-cluster energies are calibrated to the the electromagnetic (EM) scale, explaining how the name EMTOPO jets comes about. The calibrated topo-clusters are then passed to the anti-k_t algorithm for jet finding.

- PFLOW jet reconstruction utilizes both the ID tracks of charged hadrons and the calorimeter topo-clusters identified in the same way as for the EMTOPO jets. A full overview of the PFLOW algorithm employed for jet reconstruction at ATLAS is given in [105]. The central idea is to combine the measurements from the two subdetectors, by following a particle's *flow* through the detector and using the highest quality measurement of its signal. A charged particle is detected as a track in the ID with high precision, whereas neutral particles are only measured as energy deposits in the calorimeter. Therefore, to make optimal use of the measurements, for PFLOW jets the momentum measurement from a charged particle's ID track is used wherever the track resolution is better than that of the calorimeter measurement. In addition, the topo-clusters are used to include the signals from neutral hadrons. To avoid double counting signals, the energy clusters associated to the selected ID tracks must be removed from the calorimeter measurement: this is the key functionality of the PFLOW algorithm.

  The PFLOW procedure starts from the selected tracks. Only tracks within the range $|\eta| < 2.5$ and with $p_{\mathrm{T}} > 0.5$ GeV and fulfilling stringent quality requirements are taken into account. Tracks with a p_{T} greater than 40 GeV are excluded, as at such high energies the track is often not well isolated from other measurements (e.g. products of a boosted decay, or collimated FSR), which complicates the removal of its energy from the calorimeter measurement. Moreover, the tracks considered must not already be matched to a reconstructed electron or muon object. In the next step, each selected track is matched to a topo-cluster in the calorimeter, based on the compatibility of measured cluster energy and track momentum as well as their distance in ΔR. Once a track is matched to a cluster, it is determined how much energy a charged particle of the given momentum, as measured by the track, is expected to deposit in the calorimeter. This determination is made using expectation values from dedicated MC samples, based on the track momentum and the position of the topo-cluster. As hadrons rarely deposit all their energy in one single topo-cluster (especially at high energies), a dedicated criterion is employed to determine if the hadronic shower is split across several clusters. If this is the case, the additional clusters are merged with the original. The merging criterion is based on the difference between the expected and the measured energy deposit, normalised to the spread of the expected energy deposition. After correcting the topo-clusters for split showers, the energy deposits matched with selected ID tracks need to be removed from the calorimeter measurement. The subtraction is done cell-by-cell, unless the expected energy is larger than the measured cluster energy, then the entire cluster is removed. As a last step, potential remnant energies are removed if they are consistent with the expected fluctuation of the hadronic shower. The topo-clusters remaining after energy subtraction are then passed to the anti-k_t algorithm, together with all selected tracks that are associated with the primary vertex in the event.

The anti-k_t algorithm [104] is used to build the jets from the individual particle's signals as deter-

mined with either of the methods described above. To do so, it performs a pairwise clustering of objects, where an object can either be an individual signal or a pseudo-jet already built from multiple signals. An object i is combined with another object j if the distance d_{ij} between them is smaller than the distance d_{iB} between object i and the beam axis, where d_{ij} and d_{iB} are defined as:

$$d_{ij} = \min\left(k_{T,i}^{-2}, k_{T,j}^{-2}\right)\frac{\Delta R_{ij}^2}{R^2}$$
$$d_{iB} = k_{T,i}^{-2}, \tag{2.9}$$

Here $k_{T,i}$ refers to the transverse momentum of object i, ΔR_{ij}^2 is the angular separation between objects i and j and R is a constant resolution parameter. The resolution parameter R gives the size of the jet cone and for the work presented in this thesis it is set to 0.4. Once the distance of object i to the beam axis d_{iB} is larger than any d_{ij} it is considered a jet and removed from the list. The pairing procedure is iteratively repeated until there are no more objects left, but for the list of reconstructed jets.

PFLOW jets have several advantages over EMTOPO jets. They have an improved transverse momentum resolution, especially at lower p_{T}, because the ID momentum measurement is significantly more precise than the calorimeter energy measurement. For jets with a p_{T} around 30 GeV, the resolution of PFLOW jets is around 10% better, while at higher momenta, from 100 GeV on, both PFLOW and EMTOPO jets have a comparable resolution. Additionally, the angular resolution of PFLOW jets is much better, as the ID provides angular measurements of the jet constituents with higher precision. Lastly, and most importantly for the $H \to ZZ \to \ell\ell\nu\nu$ analyses presented here, PFLOW jet reconstruction is inherently more robust to pile-up. The reason is that selecting only tracks matched to the primary vertex excludes most contributions from charged particles originating from pile-up vertices.

Figure 2.19(a) illustrates the pile-up suppression benefit of PFLOW jets. The number of reconstructed fake jets arising from pile-up contributions is shown as a function of the pseudorapidity η for four different cases: EMTOPO ("EM+JES jets") and PFLOW jets ("Particle Flow jets") without and with a JVT cut. Simulated $Z \to \mu\mu$ events are used, and whether a jet is fake or real is determined by whether it can be traced back to a truth jet using a ΔR based cone matching. The simulation includes an overlay of pile-up that matches the 2016 data taking conditions, with an average number of interactions per bunch crossing of approximately 22. In each case, the jet energy calibration procedure (JES) is applied and the JVT cut serves to suppress pile-up contributions. Both are described below. It is evident that in the central region, $|\eta| < 2.5$, where the ID provides coverage, PFLOW jets are much less vulnerable to pile-up. Even when applying a looser JVT cut they perform much better than EMTOPO jets. This is achieved all the while maintaining, or even improving, the efficiency to reconstruct a true jet, as shown in Figure 2.19(b) as a function of the jet transverse momentum. Efficiently reconstructing jets and rejecting pile-up contributions is crucial for the $H \to ZZ \to \ell\ell\nu\nu$ analyses, as missing a jet or reconstructing a fake jet from pile-up both spoil the reconstruction of the missing transverse energy $E_{\mathrm{T}}^{\mathrm{miss}}$, as described in Chapter 2.3.5.

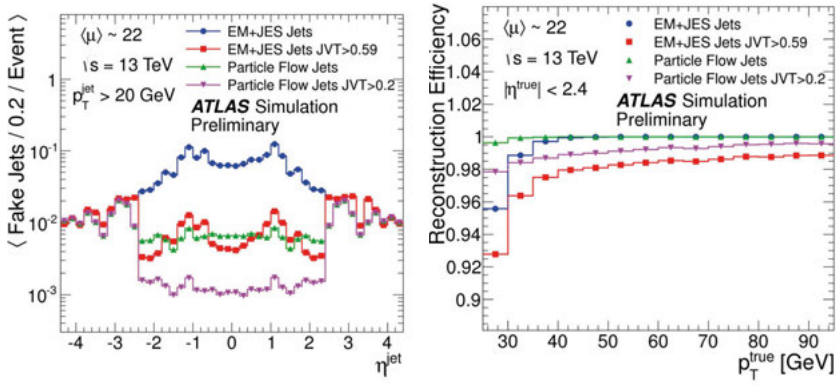

(a) (b)

Figure 2.19: Comparison of PFLOW and EMTOPO jets using simulated $Z \rightarrow \mu\mu$ samples with similar conditions as the 2016 data taking. In (a) the rate of reconstructing fake jets from pile-contributions is shown as a function of the jet's pseudorapidity η and (b) shows the reconstruction efficiency of true jets as a function of their transverse momentum p_T. From [106].

Jet energy calibration After building the jet, the measured jet energy needs to be calibrated to match the jet energy scale (JES) of truth jets reconstructed at particle-level. The measured JES does not necessarily correctly represent the particle level due to several detector effects such as particles missing from the jet reconstruction if they are outside of the selection acceptance or absorbed in dead material and not detected at all, leakage of particle signals between different subdetectors and the impact of pile-up. As shown in Figure 2.20 the JES calibration proceeds in six steps, each correcting the jet four-momentum. The first two steps are corrections that remove

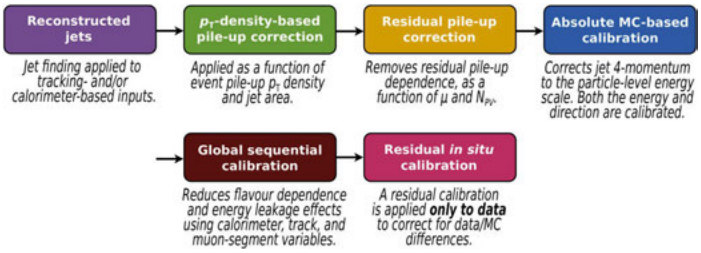

Figure 2.20: Overview of the different stages of the jet calibration procedure. From [107].

the additional energies deposited by particles originating from pile-up (both in-time and out-of-time pile-up). Next, the jet's four momentum is corrected to the particle level, adjusting its absolute energy scale and direction to match that of a truth jet. Additionally, a global sequential calibration is applied which improves the jet resolution by accounting for the different detector

responses for jets with different properties (e.g. its particle composition and energy distribution, which depend on whether the jet was initiated by a quark or gluon). Corrections based on several global variables are applied sequentially with the aim to remove the dependency of the jet response on these variables. While the previous two steps are simulation based, employing truth jets information from simulated di-jet events, the final *in situ* calibration corrects the data for remaining discrepancies between data and simulation. This is done by determining the jet response in data events that contain a well measured particle, for example a Z boson or photon recoiling against a jet. The ratio of the response in data and matching simulation is applied as a correction to data. A detailed description of each step of the jet calibration as applied to the ATLAS run II data is given in [107].

In each step of the calibration certain assumptions are made, which are associated with uncertainties. For example, the pile-up corrections are based on MC samples containing a specific modelling of the average number of interactions per bunch crossing, that may not exactly match that in a recorded data event. Additionally, the reconstruction uncertainties on all objects used in the in situ calibrations, such as photons, electrons and muons, need to be propagated. This leads to an uncertainty on the JES as well as the jet energy resolution (JER). Precise knowledge of both the JES and JER is crucial for the $E_{\mathrm{T}}^{\mathrm{miss}}$ reconstruction.

Figure 2.21(a) shows the total fractional uncertainty on the JES as a function of p_{T}, for jets in the central region ($|\eta| = 0$), comparing EMTOPO and PFLOW jets. In both cases, the JES is known with an uncertainty at the percent level (< 5%) across the considered range of transverse momentum. Similarly, the JER is well measured in the same range, as shown by Figure 2.21(b). Here, the improved resolution at low p_{T} when using the PFLOW jet reconstruction is evident.

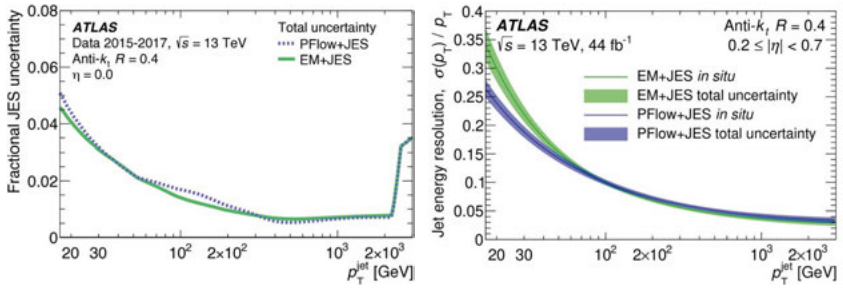

(a) JES uncertainty

(b) JER and its uncertainty

Figure 2.21: Results of the jet energy calibration with the 2015-17 data: in (a) the relative JES uncertainty and in (b) the relative JER with its uncertainty. Both are shown as a function of the jet transverse momentum and compared between EMTOPO and PFLOW jets. From [107].

Jet vertex tagger To further reduce the impact of pile-up on the jet reconstruction, a multivariate discriminate called the jet vertex tagger (JVT) [108] is used for jets in the central region, with $|\eta| < 2.4$. It is based on a two-dimensional likelihood, derived from simulated di-jet events.

The two variables it considers are:

- The jet-vertex-fraction (JVF), defined as the ratio of the scalar p_{T} sum of all tracks associated with the jet coming from the same primary vertex over the scalar p_{T} sum of all tracks associated with the jet. For the JVT, the denominator of the JVF is corrected for its dependence on the number of vertices in the event. The JVF variable ranges from 0 to 1, and for jets with little to no pile-up contribution it approaches 1.
- The ratio of scalar p_{T} sum of all tracks in the jet coming from the same primary vertex over the fully calibrated measured p_{T} of the jet (after pile-up corrections). Again, this variable yields larger values for jets with no pile-up contribution, where it quantifies the p_{T} fraction of the jet carried by charged particles.

Both variables are therefore suited to classify pile-up jets, and are combined for optimal discrimination power. In Figure 2.19 the beneficial effect of a JVT criterion is clearly visible. The performance of the JVT was studied in detail in [109], using run I data.

b-tagging Jets initiated by a b-quark (called b-jets) are identified using a dedicated *b-tagging* algorithm. The main criterion by which b-jets can be distinguished from jets initiated by lighter quarks (light-jets or c-jets) is the presence of a displaced secondary vertex, as illustrated in Figure 2.22. Due their long life-time hadrons containing b-quarks are able to travel for several millimeters through the detector, leading to at least one secondary vertex. The information of the secondary vertex (in particular its impact parameter d_0 and track properties) as well as on other jet properties such as its p_T, invariant mass and decay chain are exploited by the b-tagging algorithm. For the work presented in this thesis, a multivariate b-tagging algorithm called MV2 [111] is used. It is based on a gradient boosted decision tree. The output of the MV2 algorithm is a single discriminating variable, the distributions of which are shown in Figure 2.23 for simulated $t\bar{t}$ events. Depending on the desired efficiency to identify b-jets and to reject light- and c-jets, a specific cut on this discriminant is imposed, defining the working point. For the $H \to ZZ \to \ell\ell\nu\nu$ analyses presented here, the 85% WP is chosen - corresponding to an average efficiency of tagging the b-jet of 85% and an average rejection rate of other jets of around 30%.

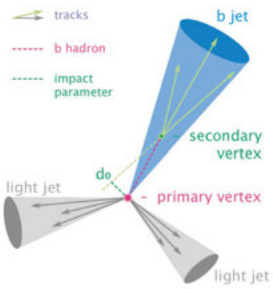

Figure 2.22: Illustration of a b-jet signature compared to light-jets. From [110].

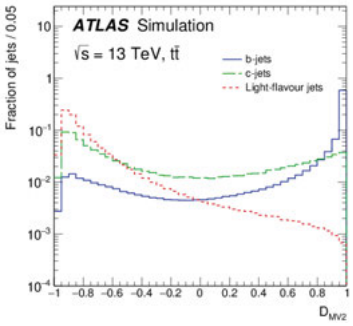

Figure 2.23: Distributions of the BDT based MV2 discriminant for different kinds of jets, in simulated $t\bar{t}$ events. From [111].

2.3.4 Overlap removal

With all the objects in a typical event reconstructed, one more step needs to be taken to treat overlapping objects. Overlapping objects cause problems in the event reconstruction for multiple reasons: The same physical object could be reconstructed as two separate detector objects, e.g. a jet could be correctly identified and reconstructed as a jet but the same track and energy clusters could also be misidentified as a fake electron. This leads to the overall energy of the

event being misreconstructed due to double counting. Furthermore, objects that are close to each other may disrupt each other's position and energy determination (e.g. in the case of overlapping hits or clusters that cannot be clearly associated with one object or the other), even if they are identified as two separate objects.

These problems are addressed by the overlap removal, a dedicated algorithm to remove one of the overlapping objects. The basis of the criterion to determine whether objects overlap is their geometric proximity quantified by the angular separation $\Delta R = \sqrt{\Delta\Phi^2 + \Delta\eta^2}$. The specific cut values and which object is to be removed for each case of overlap considered in the analyses presented here are listed in Table 2.1. In the case of an electron overlapping with a jet, the jet is removed from the event if their separation $\Delta R_{e,\text{jet}}$ is below 0.2. If $\Delta R_{e,\text{jet}}$ is larger than 0.2, but still below 0.4, and the jet in question passes the JVT requirements (classifying it as not originating from pile-up) the electron is removed instead. A muon is defined as overlapping with a jet if the separation $\Delta R_{\mu,\text{jet}}$ is below 0.4 and the decision whether the muon or the jet is removed depends on the number of tracks found in the jet: jets with no more than 2 tracks are removed, while in case of more than 2 tracks in the jet the muon is removed. Lastly, in rare cases an electron and a muon overlap. This is largely due to events in which the muon's FSR photon is misidentified as an electron and hence, the reconstructed muon and electron object would share the same track in the ID. The electron should then be discarded.

Overlapping objects	**Criterion**	**Action**
Electron and jet	$\Delta R_{e,\text{jet}} < 0.2$	Remove jet
	$0.2 < \Delta R_{e,\text{jet}} < 0.4$ and jet passes JVT	Remove electron
Muon and jet	$\Delta R_{\mu,\text{jet}} < 0.4$, if $N_{\text{Trk}}(\text{jet}) \leq 2$	Remove jet
	$\Delta R_{\mu,\text{jet}} < 0.4$, if $N_{\text{Trk}}(\text{jet}) > 2$	Remove muon
Electron and muon	Share same ID track	Remove electron

Table 2.1: Strategy to remove overlaps between reconstructed objects.

2.3.5 Missing transverse energy

For the $H \to ZZ \to \ell\ell\nu\nu$ analyses presented here, the reconstruction of the missing transverse energy $E_{\text{T}}^{\text{miss}}$ is crucial, as it is the way to measure - although indirectly - the total transverse momentum of the neutrino pair. As previously mentioned, neutrinos interact only weakly and therefore pass through the ATLAS detector undetected. Since the protons are accelerated in the longitudinal direction along the beam axis, it can be assumed that prior to the scattering reaction the transverse momenta of the interacting partons are in balance. Due to momentum conservation, the sum of the transverse momenta of all final state particles (after the scattering) should vanish, in the ideal case. The missing transverse energy $E_{\text{T}}^{\text{miss}}$ is then used to quantify the imbalance of momenta in the transverse plane, which indicates the presence of particles escaping detection. It is defined as the negative vectorial sum of the transverse momenta of all visible objects in the event, i.e. $\vec{E}_{\text{T}}^{\,\text{miss}} = -\sum_i \vec{p}_{\text{T}}^{\,\text{vis},i}$. In practice, all objects reconstructed and calibrated as described above serve as input to the $E_{\text{T}}^{\text{miss}}$ reconstruction - forming the so called *hard term*.

In general, the hard term consists of the signals of electrons, muons, photons, hadronically decaying τ-leptons and jets[10]. In addition to the hard term, a so called *soft term* is added as well, accounting for any signals registered in the detector that are associated with the primary scattering vertex in the event, but do not belong to any reconstructed and identified object. Each component of the $\vec{E}_{\mathrm{T}}^{\mathrm{miss}}$ is thus calculated as:

$$\begin{aligned} E_{x(y)}^{\mathrm{miss}} &= -\sum_{i \in \text{hard objects}} p_{x(y),i} - \sum_{j \in \text{soft signals}} p_{x(y),j} \\ &= E_{x(y)}^{\mathrm{miss},\mu} + E_{x(y)}^{\mathrm{miss},e} + E_{x(y)}^{\mathrm{miss},\gamma} + E_{x(y)}^{\mathrm{miss},\tau} + E_{x(y)}^{\mathrm{miss,jets}} + E_{x(y)}^{\mathrm{miss,soft}} \end{aligned} \tag{2.10}$$

Figure 2.24 illustrates the detector signatures of the different terms considered in the $E_{\mathrm{T}}^{\mathrm{miss}}$ reconstruction, highlighting the complexity of this variable. To avoid double counting, the ATLAS $E_{\mathrm{T}}^{\mathrm{miss}}$ reconstruction performs its own overlap removal, similar to that described above, and includes corrections for the muon energy loss in the calorimeters (cf. [112]). The soft term can be computed in different ways: either using only tracks in the ID or only energy deposits in the calorimeters, or from a combination of the two. In the $H \to ZZ \to \ell\ell\nu\nu$ analyses, the $E_{\mathrm{T}}^{\mathrm{miss}}$ reconstruction uses the *track-based soft term* (TST) definition [113]. It is built only from ID tracks associated to the primary scattering vertex, but uses calorimeter information on the hard objects to exclude overlapping tracks. This approach is relatively robust against pile-up contributions, but does not account for soft signals of neutral particles or outside of the ID acceptance. In general the $E_{\mathrm{T}}^{\mathrm{miss}}$ reconstruction is susceptible to pile-up and the resolution of all measured momenta. The $E_{\mathrm{T}}^{\mathrm{miss}}$ calculation is spoiled by counting momenta from unrelated objects produced by pile-up as well as by mismeasuring the momentum of a hard object. Therefore, the improvements offered by the PFLOW reconstruction algorithm for jets are also exploited for the $E_{\mathrm{T}}^{\mathrm{miss}}$ reconstruction: the analysis of the 2015+16 data, presented in Chapter 5, relies on EMTOPO jet and $E_{\mathrm{T}}^{\mathrm{miss}}$ reconstruction, whereas for the analysis of the full 2015-18 dataset, presented in Chapter 6, PFLOW based jets and $E_{\mathrm{T}}^{\mathrm{miss}}$ are used. A detailed study of the performance of EMTOPO $E_{\mathrm{T}}^{\mathrm{miss}}$ can be found in [114] and [112] describes and compares the PFLOW based $E_{\mathrm{T}}^{\mathrm{miss}}$. Using the PFLOW algorithm mainly affects the jet and soft term, but there is also a small effect on the electron and muon terms due to the overlap removal between jets and leptons. Specifically, there are a few different requirements used in the two different $E_{\mathrm{T}}^{\mathrm{miss}}$ reconstruction approaches:

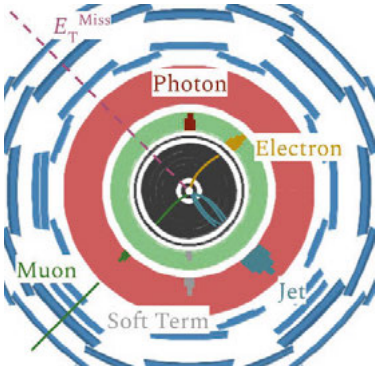

Figure 2.24: Illustration of the different signals forming the different terms of the $E_{\mathrm{T}}^{\mathrm{miss}}$ reconstruction.

- For the EMTOPO $E_{\mathrm{T}}^{\mathrm{miss}}$ reconstruction, jets with $p_{\mathrm{T}} > 60$ GeV and $|\eta| < 2.4$ are required to

[10] In the work presented here, photons and hadronic τ decays are not considered and not included in the reconstruction.

satisfy JVT > 0.59, in order to exclude pile-up contributions. Tracks enter the EMTOPO soft term, if their p_T is above 0.4 GeV and they can be matched to the primary vertex using the longitudinal and transverse impact parameters, d_0 and z_0. This is implemented by requiring d_0 significance < 2 and $|z_0 \sin\theta| < 3$ mm.

- In the PFLOW based E_T^{miss} reconstruction, the JVT requirement for jets is lowered to 0.5, due to the inherently better pile-up suppression using PFLOW jets. Moreover, in the PFLOW soft term only tracks with $p_T > 0.5$ GeV and with $|z_0 \sin\theta| < 2$ mm are considered, while the d_0 significance requirement is dropped.

As for the other objects described previously, also in the E_T^{miss} reconstruction different working points are defined, with different advantages. Here, the *tight* WP is used, meaning that forward jets with $|\eta| < 2.4$ and a transverse momentum below 30 GeV are excluded from the E_T^{miss} calculation. This removes contributions consisting mostly of pile-up, making this WP the most stable, but it negatively impacts the E_T^{miss} scale and resolution (especially at low p_T). The performance of the E_T^{miss} reconstruction is typically studied in events that do not contain invisible particles, where the truth E_T^{miss} is expected to be 0, such as $Z \to \mu\mu$ events. This allows to evaluate the size of all the detector effects leading to a measurement of *fake* E_T^{miss}, such as resolution effects, miscalibration, particles passing outside the detector acceptance and the impact of pile-up.

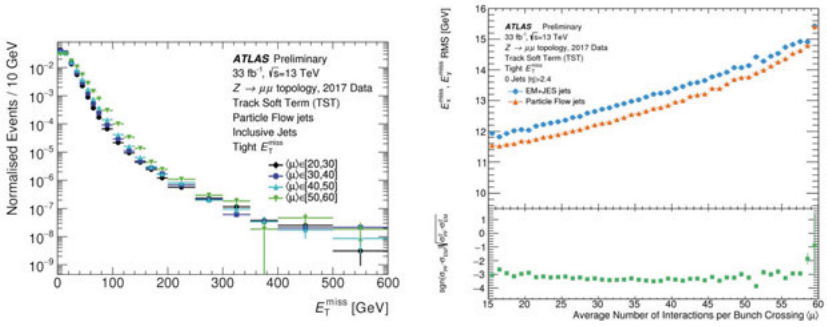

(a) (b)

Figure 2.25: Performance of the E_T^{miss} reconstruction: In (a) the PFLOW E_T^{miss} distribution in $Z \to \mu\mu$ events is shown in different regions of $< \mu >$, the average number of interactions per bunch crossing, and (b) shows the corresponding E_T^{miss} resolution as a function of $< \mu >$ for EMTOPO and PFLOW based E_T^{miss} reconstruction. Both using the 2017 dataset. From [115].

Figure 2.25(a) shows the missing transverse energy in $Z \to \mu\mu$ data events under different pile-up conditions, using the PFLOW E_T^{miss} reconstruction with the *tight* WP. The larger the pile-up, as quantified by the number of average interactions per bunch crossing, the broader the distribution and the worse the resolution. As the E_T^{miss} component distributions, E_x^{miss} and E_y^{miss}, are expected to be approximately Gaussian distributed with non-Gaussian tails, the root-mean-square (RMS) of each is used to quantify the E_T^{miss} resolution. The result is shown in Figure 2.25(b), com-

paring the PFLOW and EMTOPO $E_{\mathrm{T}}^{\mathrm{miss}}$ resolution as a function of pile-up. Although in both cases the degradation of the resolution with pile-up is nearly linear, the PFLOW algorithm provides an improved $E_{\mathrm{T}}^{\mathrm{miss}}$ resolution. A comparison of the EMTOPO and PFLOW $E_{\mathrm{T}}^{\mathrm{miss}}$ reconstruction in the high mass $H \to ZZ \to \ell\ell\nu\nu$ analysis is presented in Chapter 6.1.

2.4 Event simulation

Most analyses in ATLAS, including the search for a heavy Higgs decaying as $H \to ZZ \to \ell\ell\nu\nu$ presented here, use Monte Carlo (MC) event simulation to model the distributions of observables as predicted by theory. These predicted distributions are then compared to data, and any deviations between the two may indicate the existence of new physics processes. It stands to reason that the MC simulation therefore needs to describe the pp-collision event as well as the detector response in a great level of detail.

Event generation To model the complex phenomenology of pp-collisions, the *event generation* relies on numerical MC methods to produce simulated (truth) events, i.e. a description of the particles involved in the proton-proton interaction. Large numbers of such events are generated and weighted so that the resulting distributions of their properties, e.g. the transverse momentum of a lepton in a $H \to ZZ \to \ell\ell\nu\nu$ event, follows the (differential) cross-section predicted by theory in the corresponding region of phase space. As illustrated in Figure 2.26 for this purpose several stages of the pp-collision need to be described.

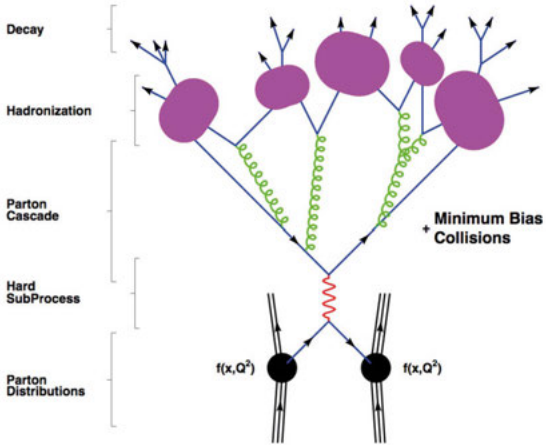

Figure 2.26: Illustration of the different components of a pp-collision event. Adapted from [116].

First, it is two partons (i.e. quarks or gluons) out of the incoming protons that participate in the

interaction, each of which carries only a fraction $x_i (i = 1,2)$ of the total proton momentum. The energy available in the interaction is therefore not the CM energy the protons are accelerated to, but the effective CM energy given as $\sqrt{\hat{s}} = x_1 x_2 \sqrt{s}$. While the exact values x_i in a specific event are not accessible, the probability density for a parton to carry a fractional momentum x at an energy scale Q^2 is given by the *parton distribution function* $f(x, Q^2)$. Quantum chronodynamics predicts the PDF dependence on the energy scale Q^2, and the behaviour as a function of x is determined from fits to deep inelastic scattering events measured by various experiments. Different methodologies and input datasets for the fit exist, leading to different PDF sets. For the work presented here, mainly PDF sets from the CTEQ [117] and NNPDF [118] groups are relied on (cf. Chapters 4.1 and 4.2 for details).

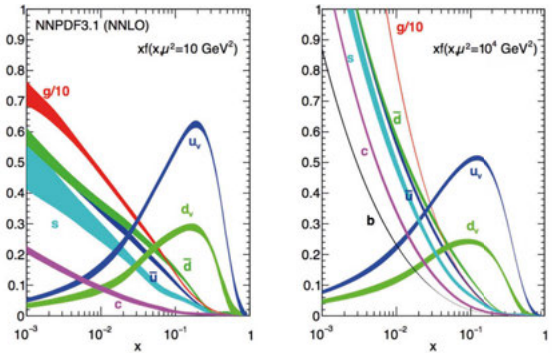

Figure 2.27: NNPDF3.1 NNLO PDFs as evaluated at an energy scale of $Q^2 = 10\,\text{GeV}^2$ (left) and $Q^2 = 10^4\,\text{GeV}^2$ (right). From [119].

Figure 2.27 shows the NNPDF 3.1 NNLO PDFs of different types of partons as a function of x, at two different energy scales. The PDFs of the valence quarks in the proton (2 up and 1 down quark) peak at fractional momenta around 0.2. The smaller fractions are dominated by sea gluons and quarks, especially at high energy scales. Moreover, the probability for a parton to carry a large fraction of the proton total momentum is small, but non-zero. Collecting more pp-collision data at the same CM energy can therefore give access to higher energy resonances, that simply are too rare to occur in a small dataset. Hence the "repetition" of $H \to ZZ \to \ell\ell\nu\nu$ analyses with a partial and a full dataset presented in this thesis.

The interaction of interest, such as the production and decay of a heavy Higgs boson, is referred to as the hard subprocess or *hard scattering*. It is characterized by a large energy transfer (i.e. hard) and thus distinguished from other low energy (i.e. soft) interactions such as the pile-up. Since they occur at high energies, the matrix elements and cross sections of hard scattering processes (involving only partons) are predicted by perturbative QCD - at a given order of calculation. Employing the PDFs $f_{a/A}(x_a, \mu_F^2)$ and $f_{b/B}(x_b, \mu_F^2)$ to find parton a, b in proton A, B at an energy scale of μ_F^2, the partonic cross-section $\hat{\sigma}_{ab\to X}$, and following the *factorisation theorem* [120], the full cross-section of the hadronic reaction $pp \to X$, denoted as $\sigma_{AB\to X}$, can be

expressed as:

$$\sigma_{AB\to X} = \sum_{a,b} \int dx_a dx_b f_{a/A}(x_a, \mu_F^2) f_{b/B}(x_b, \mu_F^2) \hat{\sigma}_{ab\to X}(x_a, x_b, \alpha_s(\mu_R^2)) \tag{2.11}$$

Here, the energy scale at which the PDFs are evaluated, μ_F^2, is the *factorisation scale*, representing the threshold between soft (i.e. non-perturbative) and hard (i.e. perturbative) QCD processes. Further, the partonic cross-section depends on the running coupling strength of the strong interaction α_s, which is a function of the *renormalisation scale* μ_R^2. The latter is commonly chosen near the (expected) momentum transfer Q^2 in the process of interest, so that $\alpha_s(\mu_R^2)$ estimates the effective strength of the strong interaction involved. However, neither the choice of μ_R^2, μ_F^2 or the PDF set are known with full certainty from first principles, and therefore all lead to a systematic uncertainty on the MC prediction, as further discussed in Chapters 5.3 and 6.3.

In the above descriptions only the primary particles involved in the hard scattering process are considered, but they are likely to emit further, secondary particles such as gluons as well. This can happen before or after the hard scattering and is thus referred to as *initial state radiation* (ISR) or *final state radiation* (FSR), respectively. Since gluons carry a colour-charge, an emitted gluon can emit further radiation, leading to a cascade of particles commonly named a *parton shower*. As the emitted particles are typically soft, the parton showering cannot be described by perturbative QCD. Instead, it is modelled using MC methods, which simulate the sequential emission of new particles in a specific, ordered pattern (e.g. by decreasing p_T). Such parton shower models also make assumptions on certain parameters (e.g. on the matching scale between hard interaction and parton shower), which lead to further uncertainties on the MC prediction.

After showering, once they reach the QCD scale, all quarks and gluons *hadronize*, meaning that they combine into colourless states and form hadrons. The hadrons subsequently decay into stable particles. This leads to the detection of *hadron jets*, as described in Chapter 2.3.3.

The final ingredient of a simulated pp-collision event is modelling the so-called *underlying event*. This refers to the interactions of all proton remnants that were not part of the hard scattering as well as the pile-up, which is estimated from minimum bias collisions as described in Chapter 2.1.2.

Detector simulation With the methods described above, a list of final state particles and their kinematic properties such as momentum and direction is obtained for each simulated event. In this thesis, the direct output of the event generation is referred to as the *truth level*, as it simulates the event as if measured with infinite precision. A dedicated detector simulation procedure must be applied to the truth level particles to model their interaction with the detector and the finite measurement precision. In ATLAS, this consists of three main steps [71]:

- First, the generated events are passed to the ATLAS simulation software, which uses GEANT 4 [121] to model the interaction of each particle with the detector material. Although the detector simulation provides an accurate description of the detector layout, due to limited (computing) resources it cannot model the geometry and materials in perfect detail. The detector simulation relies on a simplified description. This is one factor which necessitates

that dedicated calibration procedures are applied to all simulated objects, as described in the respective sections of Chapter 2.3.

- Next, the *digitization* takes place. During this stage the simulated particle interactions are translated into detector signals as they would be recorded in data events, for example also adding the detector noise. Moreover, the pile-up contribution is overlayed at this point.
- Last, the simulated signals (e.g. hits or energy deposits) are passed to the same reconstruction algorithms as used for data events, described in Chapter 2.3.

In this way a good modelling of the underlying physics process and the detector response is achieved, providing simulated events at *reconstruction level*. The detector simulation and object reconstruction also lead to uncertainties on the simulated distributions used in the analysis. As described before, for various reasons the simulation cannot match the data taking perfectly. Instead, correction factors, typically called *scale factors*, are applied at analysis level to match the simulation to the data. Each of these scale factors is associated with a systematic uncertainty. More details on the reconstruction related uncertainties considered here are given in Chapters 5.3 and 6.3.

3 Using the Z boson mass to determine the muon momentum scale

In particle physics experiments, such as ATLAS, the particles of interest are often short-lived and need to be reconstructed from their decay products, in order to shed light on the invisible intermediate stages of the reaction. Therefore it is crucial to measure the four-momenta of final state particles as precisely as possible. One example are muons, which are well reconstructed at ATLAS. Many analyses, for example cross-section measurements of (di)boson production processes, rely on accurate knowledge of the muon momenta. Due to commonly employed analysis strategies, this knowledge needs to be available for both the observed data and the corresponding MC simulation. Even though the detector geometry, material distributions and the muon interaction, are well modelled within the ATLAS simulation, small disagreements remain when data is compared to MC. Causes for this discrepancy include imperfect modelling of the energy loss the muons undergo when passing the calorimeter, imperfect knowledge of the magnetic field integral in the detector, or residual misalignments of detector components. In order to remedy these shortcomings the simulated muon momenta are calibrated with a correction factor derived from data. The standard ATLAS muon momentum calibration procedure is described in Chapter 2.3.2.

One process studied for the muon momentum calibration is the on-shell production of a Z boson and its subsequent decay into two muons, $Z \to \mu\mu$. It is a well understood process that occurs abundantly at the LHC and is easy to distinguish from other processes. Using the large sample provided by selecting $Z \to \mu\mu$ events, the invariant dimuon mass spectrum is fitted in both data and simulation and the calibration parameters are determined from the shape difference. It is important that the fit of the mass spectrum is of high quality with small systematic uncertainties. These systematic uncertainties are propagated into the calibrated muon momenta and therefore enter the eventual physics results of any analysis using reconstructed muons. This is an incentive to investigate the possibility of improving the dimuon mass fit model further, which is the aim of the studies described in this chapter. An alternative fit model for the $M_{\mu\mu}$ lineshape around the Z boson resonance to the one used in the standard ATLAS calibration procedure is proposed and its performance is studied on simulated $Z \to \mu\mu$ events. Its main advantage is that it includes a description of the truth Z boson lineshape, and therefore allows to obtain a best fit value of the Z boson boson mass m_Z - a parameter whose physical meaning is immediately clear - with high precision.

3.1 $Z \to \mu\mu$ event simulation and selection

3.1.1 Monte Carlo simulation

The studies presented in this chapter are based on a MC simulation of Drell-Yan $Z \to \mu\mu$ events at a center of mass energy of 13 TeV. The sample contains approximately 80 million simulated events. The production cross-section for this process corresponds to 1.901 nb. The hard-scattering events are generated with the POWHEGBOX generator [122], with an accuracy of NLO and employing the CT10 parton distribution functions [123]. To describe the process fully, possible additional initial- and final-state-radiation must be taken into account. Initial state radiation can arise from gluon radiation of the incoming quarks and therefore affect the momentum and angle of the Z boson produced. This QCD showering effect is modelled with the PYTHIA 8 software [124]. Furthermore, the outgoing muons have some probability to emit additional photons (as bremsstrahlung) and here this electroweak showering is modelled by the PHOTOS package [125]. As described in Chapter 2.4 the detector effects are modelled with the ATLAS simulation package, based on GEANT4 [71]. This software models the particle scattering in the detector material as well as the muon energy loss when traversing the detector. Additionally, the effect of having multiple interactions between the protons happening during a bunch crossing - the pile-up - is taken into account in this step. For the study presented here the detector simulation matches the run conditions of the 2017 data taking period.

3.1.2 Event selection

To distinguish the signal process $Z \to \mu\mu$ from background processes with similar signatures, for example $Z \to \tau\tau$ events, an event selection is necessary. The following selection is applied to the MC simulated events studied here.

Firstly, a pre-selection ensures that only events that can be reconstructed well and would actually be recorded are considered. A requirement on the transverse momentum of the reconstructed muon is made, where the precise p_{T} threshold depends on the number of muons in the event: for one muon in the event it is 20 GeV, while for two muons it is 5 GeV for both muons. Furthermore, only events where the lowest unprescaled single muon trigger fired are used for this study (cf. Appendix A). With this pre-selection already many events are filtered out, reducing the original 80 million to approximately 45 million events. Next, only muon pairs consistent with a Z boson decay are considered. At least one pair of reconstructed muons of opposite charge is required. Since only simulated events are studied here, it is possible to associate each reconstructed particle to a truth particle and access the information from which decay the truth particle originated. Hence, the selected reconstructed muons are required to be matched to truth muons which must be linked Z boson decay. Events with multiple Z boson boson decays and therefore muon pairs are allowed, but only constitute a small fraction of the sample. Further selections are applied to the reconstructed muons. All muon candidates considered must have a valid track in both the inner detector and muon spectrometer, and have a successful combined refit. The following requirements regarding the quality of the reconstructed muon tracks are made: The ID track has

to pass the respective quality cuts, while for the ME track a minimum number of three precision layers with at least three hits each is required. This criterion ensures that only muon candidates with a well-defined momentum measurement are selected. Since the measured momentum is derived from the curvature of the muon's trajectory within the magnetic field, it stands to reason that at least three stations are necessary in order to measure this curved trajectory accurately. Finally, it is required that the trigger is fired by one of the selected muons, determined by a so-called trigger match.

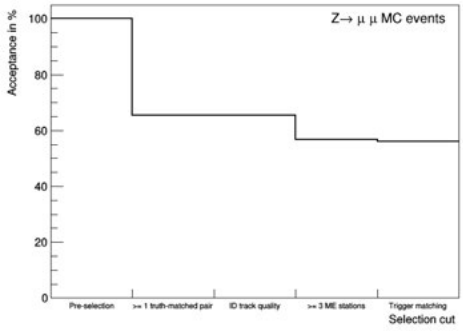

Figure 3.1: Relative acceptances of the event selection criteria.

Figure 3.1 shows the relative acceptance of each of these selection criteria. The total number of events after the pre-selection is used as the reference point of 100%. The overall acceptance of the event selection described here is approximately 55% .

3.2 Fitting the truth $M_{\mu\mu}$ line shape around the Z boson mass pole

There are two main goals behind the Z boson line shape fit model: First, it should describe the dimuon mass spectrum with very high precision. Second, it should correctly account for the underlying physics process. While the first objective can be achieved by using a CrystalBall function for example, such a model does not fulfil the latter criterion. Specifically, the mean of a CrystalBall fit model does not correspond to the pole mass of the Z boson. In contrast, the fit model proposed in this study makes use of the theoretical description of the Z line shape, so that the mass parameter M_Z is naturally included. Yet, this alone is not a sufficient description of the dimuon mass spectrum even at truth level, due to the muons undergoing final state radiation. Therefore, the fit model for the truth Z boson line shape consists of two components: the Z boson line shape itself, and a model for the FSR effects.

3.2.1 The Z boson line shape

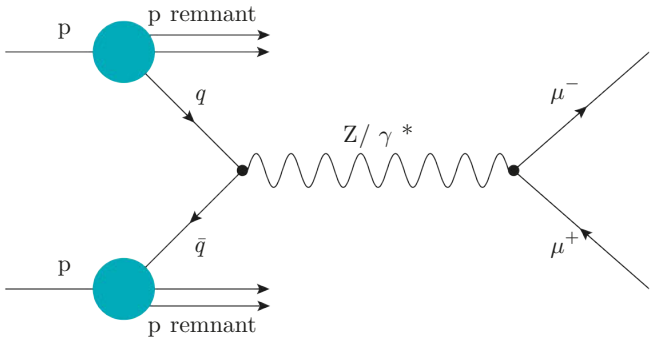

Figure 3.2: Feynman graph of the Drell-Yan production of a muon pair in a pp-collision (at leading order).

Figure 3.2 shows a Feynman graph illustrating the Drell-Yan process: a (virtual) quark anti-quark pair - arising from any form of internal interaction in the proton, as represented by the circle - annihilates into a photon or Z boson, which subsequently decays into a muon pair. Following the appropriate Feynman rules, the matrix element describing the hard scattering $q\overline{q} \to Z/\gamma^* \to \mu\mu$ can be determined. Noting that the process $pp \to \gamma^* \to \mu\mu$ is indistinguishable from $pp \to Z \to \mu\mu$, both amplitudes have to be taken into account, leading to an interference term in the cross section. Combining all normalisation constants a coefficient A for the pure photon term, a coefficient B for the interference term and a coefficient C for the Z resonance the calculation yields (following eg. [8]):

$$N(M_{\mu\mu}) \propto A \cdot \frac{1}{M_{\mu\mu}^2} + B \cdot \frac{M_{\mu\mu}^2 - M_Z^2}{\left(M_{\mu\mu}^2 - M_Z^2\right)^2 + M_{\mu\mu}^4 \Gamma_Z^2 / M_Z^2} + C \cdot \frac{M_{\mu\mu}^2}{\left(M_{\mu\mu}^2 - M_Z^2\right)^2 + M_{\mu\mu}^4 \Gamma_Z^2 / M_Z^2} \tag{3.1}$$

where M_Z is the pole mass and Γ_Z the width of the Z boson resonance. The center of mass energy of the hard scattering $q\overline{q} \to Z/\gamma^* \to \mu\mu$ is approximated by the invariant mass $M_{\mu\mu}$ of the two muons. The first term describes the contribution of the photon-exchange process, the third term describes a Z boson resonance with a Breit-Wigner distribution, and the second term models the interference between the two. In the Breit-Wigner term, the width of the Z boson resonance is dependent on the centre of mass energy, accounting for radiative corrections to the Z boson propagator through fermion loops [126] [127]. In [8] it has been shown that this function is indeed a suitable parametrization of the dimuon mass spectrum around the Z boson resonance, despite neglecting the form factors for the γ and Z boson.

A visualisation of this function and its three components in an interval around the Z mass is shown in Figure 3.3. Here, the PDG values [15] for the mass and width of the Z boson are used.

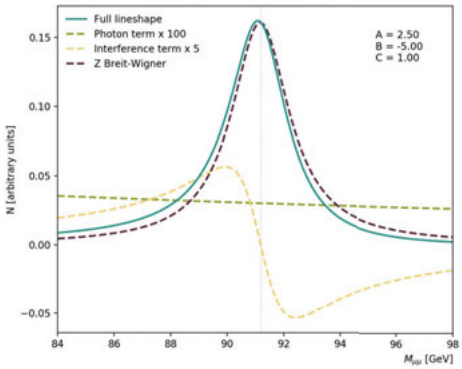

Figure 3.3: Visualization of the Z boson line shape fit model, as given by Equation 3.1. The mass and width of the Z boson are set to their PDG values [15] - the former of which is indicated by the dotted vertical line. For visibility, the photon and interference term are shown scaled up by a factor of 100 and 5, respectively.

The characteristic behaviour of each term can be seen: The largest contribution is the Z boson resonance which follows the shape of Breit-Wigner peaking at the Z boson rest mass. In contrast, the photon term contributes very little, as it decreases with the square root of the invariant mass. Finally, the interference term changes sign at the Z boson mass pole and therefore shifts the peak of the full line shape away from the pole mass.

As the studies in [8] were based on proton-proton collisions at $\sqrt{s}$ = 7 TeV, the first step is to test this fit model on simulated events with $\sqrt{s}$ = 13 TeV. This is done using truth muons, before they undergo FSR. The selection criteria described in Chapter 3.1.2 are applied to replicate the experimental conditions. Following [8], the coeffiecient C is set to 1. The width of the Z boson Γ_Z is also fixed - to its PDG value of 2.4952 GeV [15].

Figure 3.4 shows the resulting (binned) maximum likelihood fit and the corresponding best fit values of the parameters, as obtained using the RooFit [128] software. Indeed the function describes the truth $M_{\mu\mu}$ line shape well: The fit itself is of good quality, as evidenced by $\chi^2/\text{ndf} \approx 1$ and the flatness of the residuals[1]. As indicated in the figure, 407 775 selected dimuon events fall into the mass range considered and are thus included in the fit. A very accurate value of the Z boson boson mass parameter m_Z is obtained. Its best fit value of 91.1869(34) GeV is compatible with the measured value according to the PDG at (sub)-MeV level.

[1]The fit residuals are defined as the difference between data and fit function value.

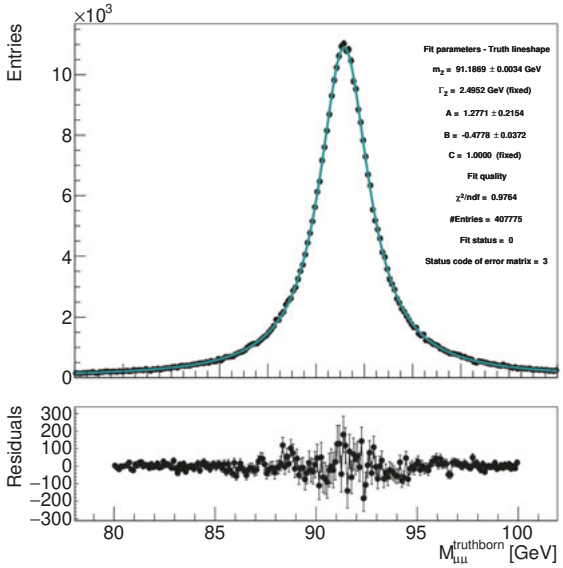

Figure 3.4: Fit of the dimuon mass spectrum at generator level using Equation. 3.1.

3.2.2 Effects of final state radiation

Final state muons have a certain probability of undergoing final state radiation (FSR). This means that the measured values of the muon momenta deviate from those that were involved in the hard scattering, even at truth level. Since the muon momenta decrease due the radiative loss, the peak region of the $M_{\mu\mu}$ distribution becomes depleted and the fitted value for m_Z is shifted to a lower value. This can be seen in Figure 3.5 which shows the result of fitting the truth line shape description of Equation 3.1 to the muon pairs after undergoing FSR. The fit quality is worsened significantly, as reflected by the pronounced structure is seen in the residuals. The best fit value $m_Z = 91.1464(38)$ GeV is now significantly lower than the input PDG value and the high precision seen before is lost. It is clear that a fit model using only Equation 3.1 is not sufficient in the realistic case and the effect of muons losing energy due to FSR has to be included.

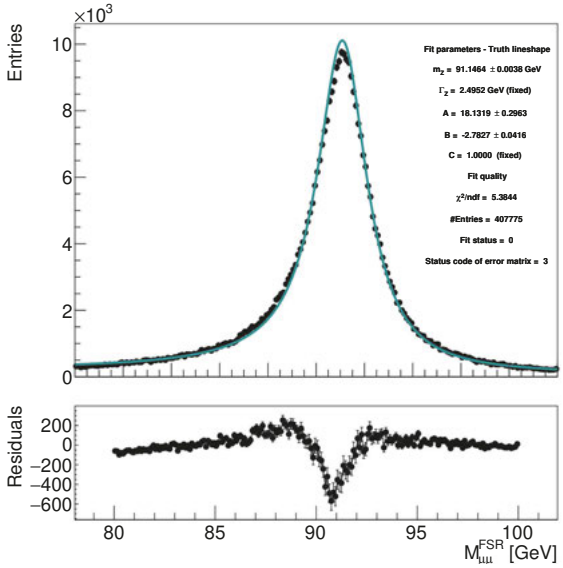

Figure 3.5: Fit of the dimuon mass spectrum after FSR at truth level using Equation 3.1.

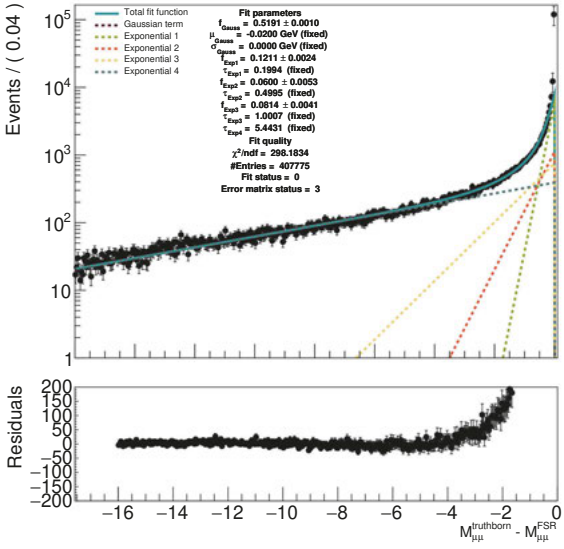

Figure 3.6: Fit of the FSR energy loss spectrum considering truth muons using the model given by Eqn. 3.2.

A model of the FSR loss function can be derived from truth MC simulation by considering the invariant mass difference between muon pairs at generator level and after undergoing FSR. The spectrum of $\Delta M \equiv M_{\mu\mu}^{\text{FSR}} - M_{\mu\mu}^{\text{truthborn}}$ is shown in Figure 3.6. It is fitted with a sum of a Gaussian, to describe the peak at 0, and four exponential decay functions [2] with distinct lifetimes that jointly describe the tail:

$$\begin{aligned} N(\Delta M) &= f_{\text{Gauss}} \cdot G(\Delta M, \mu, \sigma) \\ &+ f_1 \cdot G_0(\Delta M, 0, \sigma) * \exp(-\Delta M/\tau_1) \\ &+ f_2 \cdot G_0(\Delta M, 0, \sigma) * \exp(-\Delta M/\tau_2) \\ &+ f_3 \cdot G_0(\Delta M, 0, \sigma) * \exp(-\Delta M/\tau_3) \\ &+ (1 - f_{\text{Gauss}} - f_2 - f_3) \cdot G_0(\Delta M, 0, \sigma) * \exp(-\Delta M/\tau_4) \end{aligned} \tag{3.2}$$

where f_i are coefficients that run between 0 and 1. The parameters μ and σ represent the mean and width of the Gaussian G, while G_0 is a Gaussian of mean 0 and width σ, and finally the parameters τ_i describe the lifetimes of the exponentials. The resulting best fit values of the parameters are shown in Figure 3.6. It is important to note that it is not necessary for the model to give a good description of the peak at values near 0, since such a small decrease in mass is has negligible effect on the Z line shape. Since a large fraction of events is found in the region close to zero, the statistical power of this region is large, biasing the fit strongly towards correctly modelling this region at the expense of the quality of modelling the long tail, which is more relevant for the desired application.

To mitigate this bias, an artificial systematic uncertainty is assigned to each bin as a percentage of the squared bin content. For the two bins closest to $\Delta M = 0$, this uncertainty is chosen at 10%, while all other bins are assigned only 1% uncertainty. To further improve the fit quality, an iterative procedure is implemented: first the fit is performed with all parameters floating. The best fit values are used as the given (start) values for a second iteration, in which all parameters except the coefficients f_i are constrained. A third and last iteration is performed starting from the second iteration's best fit values. In this way, the negative tail can be modelled fairly accurately.

[2] A convolution of a narrow Gaussian with an exponential to either left or right is referred to as a decay function.

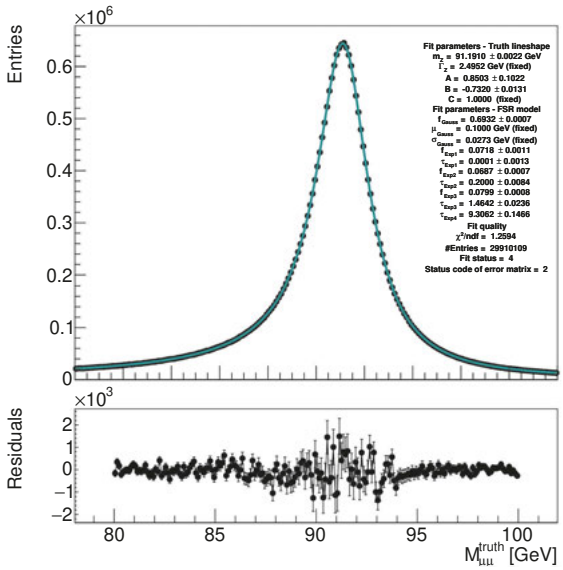

Figure 3.7: Fit of the dimuon mass spectrum after FSR at truth level, specifically including the FSR effect as modelled by Equation 3.2.

This model of the muon FSR can be convolved with Equation 3.1 in order to provide a more realistic fit function. For technical reasons, each term of Equation 3.2 is convolved separately with the line shape function. The best fit values for the FSR parameters previously derived cannot be transferred directly into the full model. First and foremost, because the FSR study was only performed a subset of events of the full sample. Moreover, the decay functions of the pure FSR model contain very narrow Gaussians and the full FSR fit function is artificially truncated at 0, which causes problems when convolved with the broader Z line shape. Therefore, it is natural that the width of the Gaussian from the FSR model needs to be larger when convolved and its mean is shifted away from 0. Lastly, the coefficients f_i of the different terms take different values since they are correlated with the free parameters A and B, which partially compensate the FSR effects on their own. Nevertheless the best fit parameter values determined in the separate FSR fit can be used as reasonable starting values. The coefficients as well as the lifetimes of the FSR model are left free in a fit of all events passing the (truth) selection. As can be seen in Figure 3.7, by specifically modelling and including the FSR effects, both the high fit quality as well as high precision of the fitted value for m_Z, are regained.

3.2.3 Optimizing fit parameters

It is possible to further improve the precision of the fitted Z mass by optimizing the coefficients A and B using an iteration of fits on truth events. First, the Z mass is fixed to its PDG value, while A and B are free parameters. Then, the coefficients A and B are fixed to the values found in the first step, while M_Z is left free. This procedure ensures a good fit quality, but it also introduces a bias on the result, as becomes clear when considering the fit shown in Figure 3.8. Here, the only free parameters are M_Z, A and B. Their correlation matrix is shown on the right hand side of the figure. While the correlation between the normalisation coefficient of the photon term (A) and M_Z is negligible, the coefficient B of the interference term is anti-correlated to M_Z. The reason is the interference terms' S-curve like shape, which shifts the position of the peak of the total distribution. Consequently, constraining the parameter B to an optimized value has a direct influence on the best fit value of M_Z, which must be reflected in a systematic uncertainty on M_Z. The uncertainty be estimated from the difference in M_Z obtained from a fit with the coefficients floating and a fit where they are fixed to their optimized values.

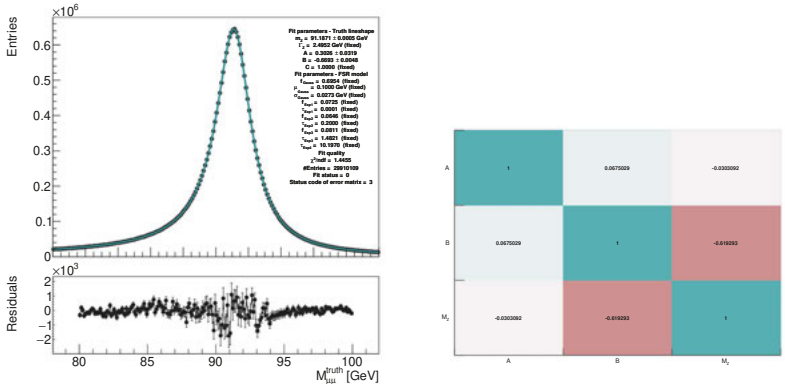

(a) (b)

Figure 3.8: Fit of the truth dimuon mass spectrum leaving only the parameters M_Z, A and B free in (a) and their correlation matrix in (b).

The full optimized fitting procedure of a given mass spectrum is then as follows: First, the fit is performed with free parameters A, B and M_Z. Next, the parameter M_Z is fixed to its PDG value. The best fit values for A and B resulting from this fit are used to constrain these coefficients in the last step. The difference in fitted M_Z between the first and last step is taken as an estimate of the systematic uncertainty. Figure 3.9 illustrates the second and third step of this procedure for all events passing the basic selection. Using the optimized coefficients, a best fit value of $M_Z = 91.1885 \pm 0.0013(\text{stat}) \pm 0.0025(\text{syst})\,\text{GeV}$ is obtained, which is fully compatible with the PDG value - establishing again that a very precise result for M_Z can be extracted using this technique.

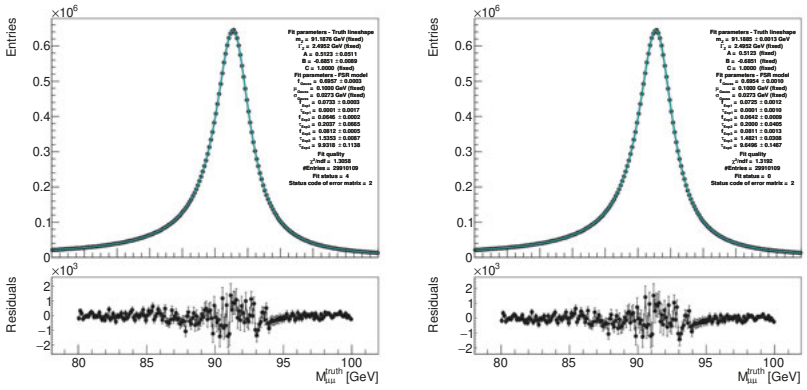

Figure 3.9: Second and third step of the fit optimization: In (a) the truth dimuon mass spectrum is fitted with the parameter M_Z constrained to its PDG value in order to find the optimized, fixed values for the coefficients A and B used for the fit in (b). The corresponding first step is shown in Figure 3.7.

3.2.4 Fitted line shape in different phase space regions

It is important that the performance of the fit is stable throughout all regions of phase space, so that it will give consistently reliable results for M_Z independently of any selection criteria applied to $Z \to \mu\mu$ events. It is not immediately obvious that this is the case: Recalling Equation 3.1 for the true line shape, there is a clear dependence on the invariant mass of the dimuon pair. At low masses, the contribution from the photon term is more significant, whereas the interference and Z term contribute most around the Z mass pole. Since the invariant mass of the dimuon pair translates to the momenta of the muons, one expects the coefficients A and B to depend on the average transverse momentum of the muon pair. For Z decays this can be defined as (cf. [100]):

$$p_{\mathrm{T}}^{*} = M_Z \sqrt{\frac{\sin\theta_1\theta_2}{2\cdot(1-\cos\alpha_{12})}} \tag{3.3}$$

where $\theta_{1/2}$ describe the polar angles of the two muons and α_{12} describes the opening angle between them. Furthermore, the likelihood of a muon to undergo FSR depends on its momentum. However, the model for the FSR spectrum is derived from a single fit of the full phase space. It is not clear a priori that this is sufficient.

To study the quality of the fit in all regions of phase space, 10 regions of p_{T}^{*} are defined in such a way that each of them contains a comparable number of events and the fit is performed separately in each of these regions. The results are presented in Figure 3.10, showing the difference

best-fit value for M_Z and its PDG value and the associated systematic uncertainty, as well as the optimized values of the coefficients A and B in each region. All are with respect to p_{T}^{*}. The deviations of M_Z from the PDG value are at the level of a few MeV.

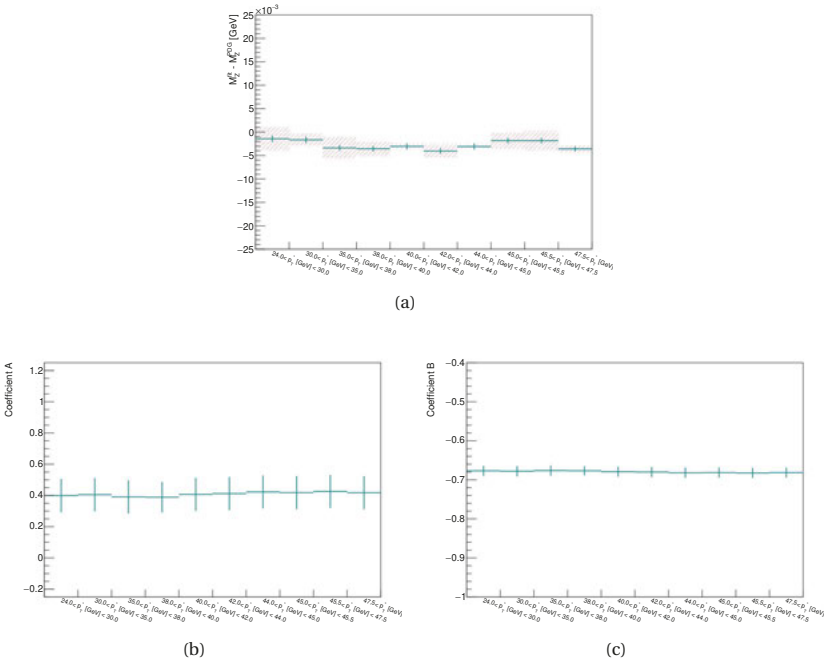

Figure 3.10: Fit results in different regions of the average momentum of the two muons, p_{T}^{*}: (a) shows the deviation of the fitted M_Z value from M_Z^{PDG}, where the error bars denote the statistical (fit) error and the dashed bars the systematic uncertainty. In (b) the best fit results for the coefficient A and in (c) for the coefficient B are shown.

Another possible dependence to be checked is on the the pseudo-rapidity of the leading p_{T} muon, $\eta(\mu_{\mathrm{lead}})$. For this purpose, the 18 regions of $\eta(\mu_{\mathrm{lead}})$ defined in the ATLAS muon momentum calibration as described in Chapter 2.3.2 and [103], are used:

$$\eta^{\mathrm{lim}} \in (-2.6, -2.3, -2.0, -1.7, -1.5, -1.25, -1.05, -0.8, -0.4, 0, 0.4, 0.8, 1.05, 1.25, 1.5, 1.7, 2.0, 2.3, 2.6) \quad (3.4)$$

Figure 3.11 shows fit results for the different parameters in each of these $\eta(\mu_{\mathrm{lead}})$ regions. Again, there appears to be no concern regarding the stability of the fit, nor a strong dependence of the coefficients on the phase space region.

Therefore, to simplify the method, it was decided to constrain the coefficients A and B to their optimized values from a fit of all events, rather than to optimize them in each phase space region

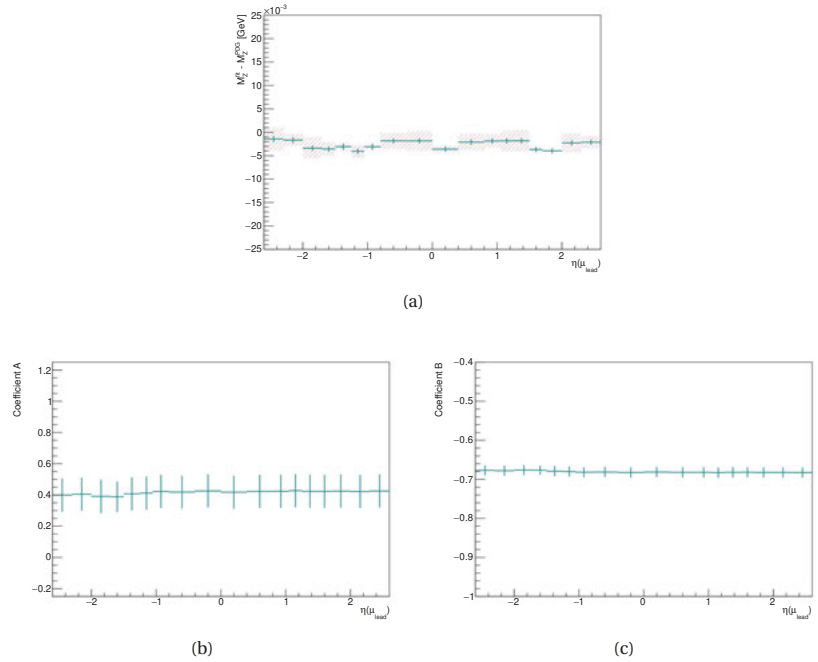

Figure 3.11: Fit results in different regions of the pseudo-rapidity of the leading p_{T} muon, $\eta(\mu_{\mathrm{lead}})$: (a) shows the deviation of the fitted M_Z value from M_Z^{PDG}, where the error bars denote the statistical (fit) error and the dashed bars the systematic uncertainty. In (b) the best fit results for the coefficient A and in (c) for the coefficient B are shown.

individually. Figure 3.12 summarizes the results, showing the good quality and stability of the fit is retained.

3.2.5 From mass to momentum

A fit of the dimuon mass spectrum can be used to correct the simulated muon momenta, by exploiting the fact that - to a good approximation - the relative mass and momentum resolution are proportional to each other, i.e.:

$$\frac{\sigma_{\mu\mu}}{M_{\mu\mu}} = \frac{1}{\sqrt{2}} \frac{\sigma_{p_\mu}}{p_\mu} \tag{3.5}$$

where $\sigma_{\mu\mu}$ gives the dimuon mass resolution, and σ_{p_μ} the muons individual momentum resolution. This relation holds for the case when both muons have similar momenta (which is true

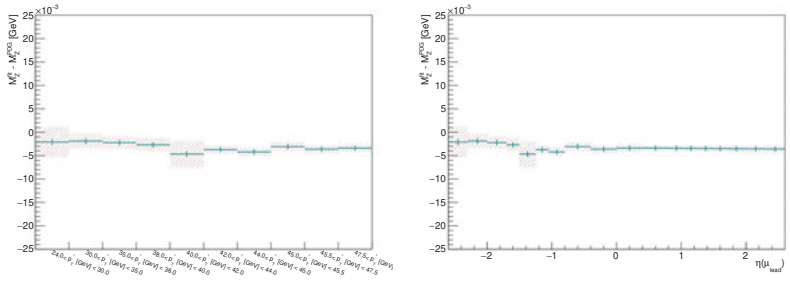

Figure 3.12: Deviations of the fitted M_Z value from M_Z^{PDG} in different regions of p_{T}^{*} (left) and $\eta(\mu_{\mathrm{lead}})$ (right), when constraining coefficients A and B to the same value throughout all regions. The error bars denote the statistical (fit) error, the dashed bars the systematic uncertainty.

for a Z decay at rest) and neglects any angular effects. For the given purpose it is a sufficient approximation [100].

To validate this relation, the absolute values of the true transverse momenta of both muons are smeared upwards by 1% of their magnitude, i.e. $p'_{\mathrm{T}} = p_{\mathrm{T}} + 0.01 \cdot p_{\mathrm{T}}$, while the angles are unchanged. The dimuon mass is recalculated using the smeared momenta. Figure 3.13 shows the resulting fit of the recalculated mass spectrum. The fitted value of M_Z becomes $M_Z = 92.1021 \pm 0.0008(\mathrm{stat})\,\mathrm{GeV}$ [3], far from the nominal value and thus illustrating that even such a small smearing of the momenta leads to a noticeable shift of the fitted M_Z value. It is clear from this study that an accurate fit of the Z line shape is sensitive to any systematic mismodelling of the muon momenta.

Moreover, it should be noted that the true dimuon mass spectra as studied so far are of course not a realistic case: The muon momenta can only be measured with a finite resolution and thus, when considering reconstructed muons there is always a level of smearing involved. To take that into account, the detector resolution function has to be modelled and included. This is described in the following.

3.3 Fitting the reconstructed $M_{\mu\mu}$ line shape around the Z boson mass pole

To fit the mass spectrum of reconstructed muon pairs, the detector resolution needs to be taken into account. A fit model for the resolution shapes is determined, constituting the final component of the full fit model for the reconstructed $M_{\mu\mu}$ line shape. The fit model can then be used to extract the dimuon mass scale and resolution, as is done as part of the muon momentum calibration procedure. For the studies presented here, the fit on reconstruction level is done for three

[3] No systematic uncertainty is given, since it does not make sense to specifically optimize the coefficients A and B for this case, as it is known the reconstructed mass peak position is incorrect due to the momentum smearing.

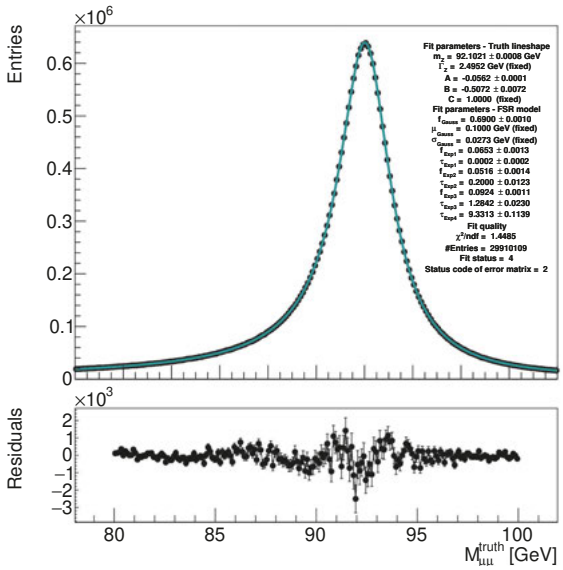

Figure 3.13: Fit of the dimuon mass spectrum at truth level, where a relative smearing of 1% has been applied to the p_{T} of the considered muons.

different types of muons, corresponding to different segments of the muon's detector signature. The inner detector track of the muon only is referred to as an *ID muon*, whereas the muon's track in the muon spectrometer extrapolated back to the primary vertex are called *ME muons*. Finally, the combined refit of the ID and ME tracks yield the *CB muons*. More details on the different types and how muons are reconstructed are given in Chapter 2.3.2.

3.3.1 Modelling the detector resolution

Using simulated events, the detector resolution can be extracted as the difference in reconstructed and truth mass. It is then fitted with a dedicated model. Since the mass resolution depends on the pseudo-rapidity of the reconstructed muons[4] this resolution fit is performed in the 18 η regions as defined in Equation 3.4. Due to the η dependence there is also no simple, straightforward model to use for the fit. In principle, the resolution is Gaussian within each infinitesimal η region, with an asymmetry to negative values for ME and (to a lesser extent) CB muons due to the Landau tail of the muon energy loss in the calorimeters. Thus, a sum of three Gaussians and an exponential decay function is chosen as the fit model. To reflect the possible asymmetries the

[4] Depending on its η the muon traverses different parts of the detector as well as different amounts of detector material

mean of one of the Gaussians is shifted away from zero by $\Delta\mu$. In order to reduce correlations between the free parameters, the width of all Gaussians are set as multiples of that of the first one, σ_1. All in all, the fit model for the detector resolution then reads:

$$\begin{aligned} \Delta M &= f_{\text{exp}} \cdot \exp(-\Delta M/\tau) * G_0\left(\Delta M, \mu, \sigma_1\right) \\ &+ f_1 \cdot G_1\left(\Delta M, \mu + \Delta\mu, \sigma_1\right) \\ &+ f_2 \cdot G_2\left(\Delta M, \mu, r_1\sigma_1\right) \\ &+ f_3 \cdot G_3\left(\Delta M, \mu, r_2\sigma_1\right) \end{aligned} \tag{3.6}$$

Figure 3.14 shows an example fit for CB muon pairs in a central η bin. The fit model of Equation 3.6 describes the mass resolution distribution sufficiently well.

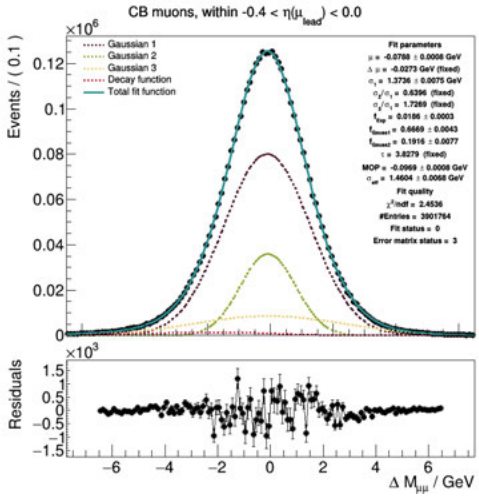

Figure 3.14: Example fit of the mass resolution using Equation 3.6, for CB muon pairs.

3.3.2 Full fit model for reconstructed muon pairs

The full fit model of the dimuon invariant mass lineshape around the Z boson mass when using reconstructed muon pairs is given by the convolution of the three separate components: the truth Z boson lineshape function as given by Equation 3.1, the FSR model defined by Equation 3.2 and the detector resolution as modelled using Equation 3.6. Due to the η dependence of the resolution, the fit of the reconstructed dimuon invariant mass distributions also needs to be performed in the 18 different η regions. An example fit for a central η slice is shown in Figure 3.15.

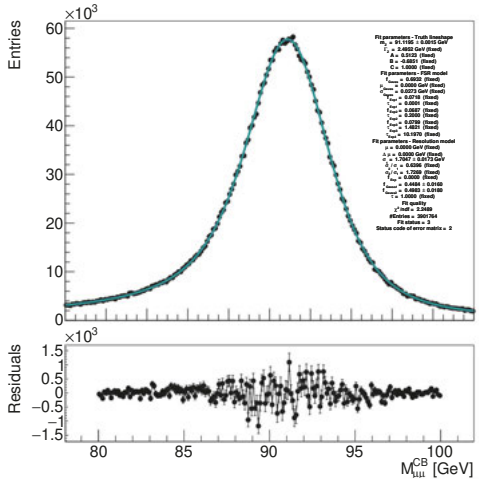

Figure 3.15: Example fit of the dimuon invariant mass spectrum using the full fit model, for CB muon pairs.

The proposed fit model evidently provides a good description of the reconstructed dimuon lineshape. A best fit value of $M_Z = 91.1277 \pm 0.0015(\text{stat}) \pm 0.0081(\text{syst})\,\text{GeV}$ is found, highlighting again the high precision and small uncertainties of this method. The remaining deviation between best fit value of m_Z and its PDG value of approximately 70 MeV is explained by inaccuracies in the detector description, such as in the muon energy loss modelling, as described earlier. Relative to the scale of the Z boson mass, these deviations are however very small - around or below the per-mille level, depending on the η region, showcasing how well the ATLAS simulation describes the interaction of muons with the detector.

3.3.3 Extracting the dimuon scale and resolution

As the final step of the studies, the dimuon scale and resolution are extracted using the proposed fit models. The dimuon scale and resolution allow to further study the performance of the detector simulation, as well as to validate the muon momentum calibration, as described in Chapter 2.3.2. Here, two different approaches are employed: First, the fit model of the detector resolution as given by Equation 3.6 is used directly to extract the scale and resolution from the distributions of the invariant mass resolution. Of course this is only possible using simulated events, where the truth muon momenta are known. A different approach is needed to extract the same quantities from data, which are required for the validation of the muon momentum calibration (recall Figure 2.17). The Z boson mass parameter m_Z of the full fit model proposed here is tested as a quantifier of the mass scale (which is proportional to the momentum scale, as given by Equation 3.5).

Using the detector resolution model Due to the shifted mean of the second Gaussian, the parameter which quantifies the peak position of the resolution function is the most probable value (MOP). The MOP is determined numerically by generating a data set of 1×10^7 points from the fit function and scanning this for its maximum value. This is the estimator for the dimuon mass scale. The resolution is given by the total effective width of the resolution model, which is determined from the individual widths of its components as:

$$\sigma_{\text{eff}} = \sqrt{f_{\text{exp}}\sigma_1^2 + f_1\sigma_1^2 + f_2(r_1\sigma_1)^2 + f_3(r_2\sigma_1)^2} \tag{3.7}$$

For each muon type, first a fit of all events in the full η range is performed in order to derive reasonable start values. To ensure comparability of the results in each bin all parameters apart from the mean μ, the width σ_1 and all fractions are set constant to their best fit values found in this way. The most probable value and effective width are then extracted in each region of η. Figure 3.16 shows the results for each muon type.

Different detector effects are apparent for the different muon types: While the shifts of the energy scale are small for ID muons, for ME muons they are significantly larger. The reason is the energy loss that the muons undergo when traversing the calorimeter (and other detector materials). In contrast, the material density in the ID is low. In both cases, larger (negative) scale shifts are observed for larger η, since a larger η means a longer path through the detector, and more interaction with the detector material. Moreover, the resolution of ID muons worsens with increasing η, as the ID's solenoid magnetic field is parallel to the beam line, and the Lorentz force only bends the momentum component perpendicular to the magnetic field. This component is small for muons with larger η, and hence the curvature of their tracks is small and harder to measure accurately. This effect is not seen for ME muons, as the magnetic field in the MS is perpendicular to the beam line. However, for ME muons, it is more difficult to reconstruct muons in the transition region of the magnetic field in the MS ($1.4 < |\eta| < 1.6$, cf. Chapter 2.2.3) where the field is more complex and less well modelled, resulting in larger scale shifts and worse resolution in this region. As the CB muons combine the ID and ME track information, the CB mass scale and resolution exhibit the features of both them, to a lesser degree.

Using the full fit model of the reconstructed $M_{\mu\mu}$ lineshape The extraction of the dimuon mass scale using the resolution model as described previously, is only possible for simulated events where the truth muon momentum is available. As part of the muon momentum calibration, the scale also needs to be extracted from data. Figure 3.17 shows that this is possible using the full fit model of the $M_{\mu\mu}$ lineshape, consisting of the description of the truth Z boson lineshape, the FSR loss function and the detector resolution model.

In the figure, the shifts of the mass scale are obtained by using the resolution model directly and as the deviation of the best fit value of m_Z from its PDG value, when fitting the $M_{\mu\mu}$ distribution. Using the m_Z from the full fit model reproduces the η dependence as derived with truth information. The proposed fit model could therefore be employed in the validation of the muon momentum calibration, allowing to compare the mass scale in data and MC simulation with high precision.

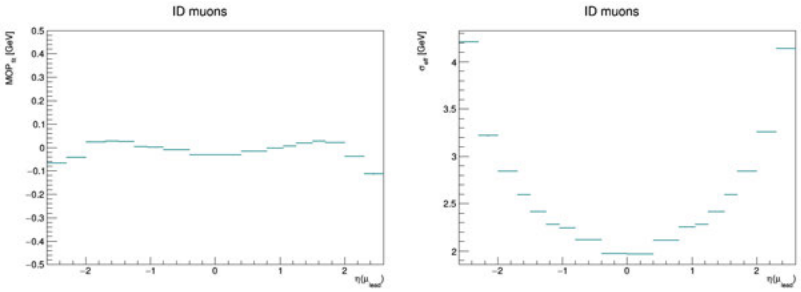

(a) ID muons

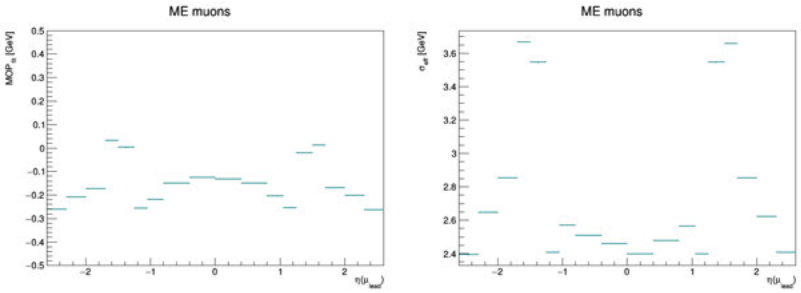

(b) ME muons

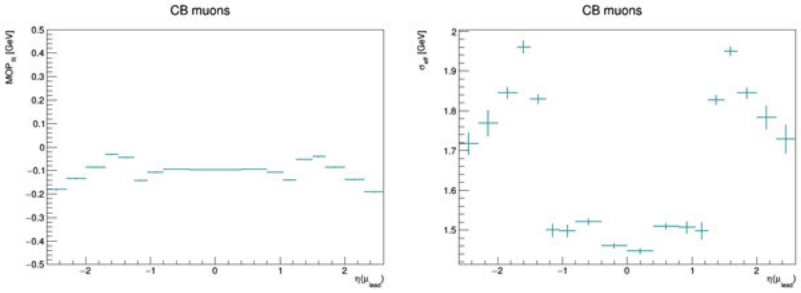

(c) CB muons

Figure 3.16: Dimuon mass scale (left) and resolution (right) in different regions of η, as extracted from simulated dimuon events using the resolution fit model given by Equation 3.6. For (a) ID, (b) ME and (c) CB muons.

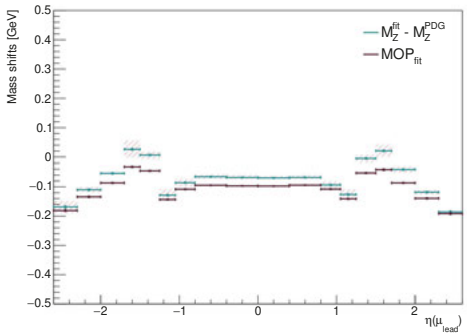

Figure 3.17: Comparison of the dimuon mass scale between extracting it from direct fits to the resolution function, $\mathrm{MOP}_{\mathrm{fit}}$, or using the full fit model of the dimuon lineshape as $M_Z^{\mathrm{fit}} - M_Z^{\mathrm{PDG}}$ in different regions of the pseudorapidtity η of the leading p_{T} muon.

4 High mass $ZZ \to \ell\ell\nu\nu$ search concepts

This chapter aims to introduce the basic analysis concepts and strategies, and to motivate *why* the two analyses presented in the following are designed the way they are. An overview of the signal modelling is given in Chapter 4.1 and the backgrounds and their modelling are described in Chapter 4.2. A dedicated methodology was developed to model the interference effects studied in the large-width heavy Higgs analysis. This is documented in Chapter 4.3. The general strategy of the search for heavy resonances in the $ZZ \to \ell\ell\nu\nu$ channel is explained in Chapter 4.4. Finally, Chapter 4.5 describes the concepts of statistical analysis that are employed for the interpretation of the search results.

4.1 Signal modelling

4.1.1 Narrow-width heavy Higgs signals

As motivated in Chapter 1.3, the search for a narrow-width heavy Higgs boson considers two different production modes: the *gluon-gluon fusion* (ggF) and *vector boson fusion* (VBF) processes. Both production modes are expected for a BSM Higgs boson, but with an unknown cross-section ratio. In the SM however, the ggF production mode outranges the VBF production mode by more than one order of magnitude [40]. Figure 4.1 illustrates the ggF and VBF signal signatures, showing the leading order Feyman graph of each production mode including the subsequent $H \to ZZ \to \ell\ell\nu\nu$ decay.

In the ggF case, the final state particles are two charged, light leptons of the same flavour but of opposite charge and two neutrinos. Here, light leptons refers only to electrons and muons. Since the neutrinos escape detection, they are reconstructed in terms of the missing transverse energy $E_{\mathrm{T}}^{\mathrm{miss}}$ in the event, as explained in Chapter 2.3.5. For high-mass Higgs bosons, which are produced at rest, the two decaying Z bosons recoil against each other, leading boosted lepton and neutrino pairs. Therefore, a considerable reconstructed $E_{\mathrm{T}}^{\mathrm{miss}}$ is expected as well as substantial transverse momenta p_{T} of the two leptons. In the VBF case, two jets arise already at leading order. As these jets are initiated by two quarks of the colliding protons, they are usually highly energetic and can be found in the forward regions of the detector. The signal signature searched for is thus the presence of a same flavour, opposite sign lepton pair with high p_{T}, along with sizeable missing transverse energy for the ggF analysis. In the VBF channels two energetic, well separated forward jets provide an additional signature.

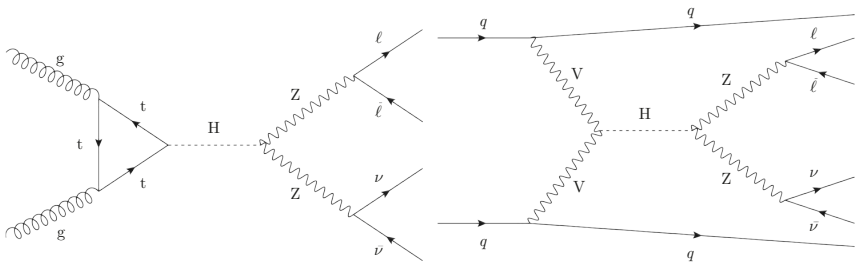

(a) ggF production (b) VBF production

Figure 4.1: Leading order Feynman graphs of the two signal signatures considered in the search for a narrow-width heavy Higgs: (a) the ggF and (b) the VBF production mode, including the $H \to ZZ \to \ell\ell\nu\nu$ decay.

Samples of simulated signal events are produced with the POWHEG-BOX v2 event generator [122] for both production modes in a mass range of m_H from 300 GeV to 2000 GeV. For masses below 1 TeV, samples are generated in steps of 100 GeV, and for masses above above in steps of 200 GeV. Figure 4.2 shows an example of the ZZ invariant mass spectrum for the m_H = 600 GeV signal at generator level. From the root mean square (RMS) of just 0.02 per-mille of the signal mass it can be clearly seen that the underlying model implements the negligible (or narrow) width approximation (NWA).

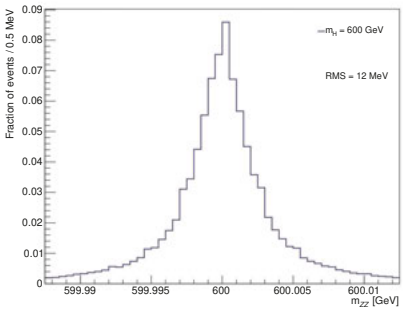

Figure 4.2: Generator level ZZ invariant mass spectrum of a heavy Higgs signal with mass m_H = 600 GeV in the NWA.

The accuracy of these samples in QCD effects is next-to-leading order (NLO), and the CT10 PDF set [123] was used. The event generator was interfaced to PYTHIA 8 [129] to model the parton showering as well as the Z boson decays.

4.1.2 Large-width heavy Higgs signals

For the large-width heavy Higgs analysis only the ggF production mode is considered. Events are generated for a heavy Higgs with a width of 15% of its mass, across the mass range of 400 GeV to 2000 GeV, in the same intervals as in the NWA case. Figure 4.3 shows the corresponding ZZ invariant mass spectra. The broadened resonance peak of the large width Higgs is clearly visible, compared to the NWA case. Here, the MADGRAPH5_aMC@NLO [130] event generator is used, also interfaced to PYTHIA 8. The NNPDF23 PDF set is employed and the accuracy in QCD effects is leading order.

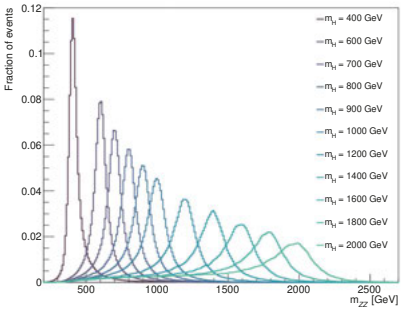

Figure 4.3: Generator-level ZZ invariant mass spectra for the signal samples with a heavy Higgs with 15% width.

To obtain large-width Higgs signals at any other width, or at other intermediate masses, an analytical reweighting technique is applied. The cross section as a function of the ZZ invariant mass m_{ZZ} for a heavy Higgs signal H with mass m_H and width Γ_H can be expressed as:

$$\sigma_H(m_{ZZ}) \approx \frac{1}{(m_{ZZ}^2 - m_H^2)^2 + m_H^2\Gamma_H^2} \cdot |A_H^P|^2 \cdot |A_H^D|^2 \tag{4.1}$$

where the first factor is the Higgs propagator term, and A_H^P and A_H^D denote the production and decay amplitudes. Assuming that those amplitudes are equal for a heavy Higgs boson H' with a different width or mass, the cross-section ratio can be written as:

$$\begin{aligned} W_{H'}(m_{ZZ}) &= \sigma_{H'}(m_{ZZ})/\sigma_H(m_{ZZ}) \\ &= \frac{(m_{ZZ}^2 - m_H^2)^2 + m_H^2\Gamma_H^2}{(m_{ZZ}^2 - m_{H'}^2)^2 + m_{H'}^2\Gamma_H^2} \end{aligned} \tag{4.2}$$

Equation 4.2 can be used to reweight an event of the generated H signal to any nearby H' signal, based on the invariant mass m_{ZZ} in the event. The above is purely based on theoretical considerations. For reconstructed events, the effect of the selection acceptance needs to be taken into account, too: The acceptance depends on the event kinematics and hence on the invariant mass of the event, but not (strongly) on the mass and width of the decaying Higgs boson. This can be seen in Figure 4.4, which compares the signal acceptances as a function of the invariant mass m_{ZZ} for different signal masses and widths at truth level. In Figure 4.4 the full kinematic event selection as described in Chapter 5.1 is applied.

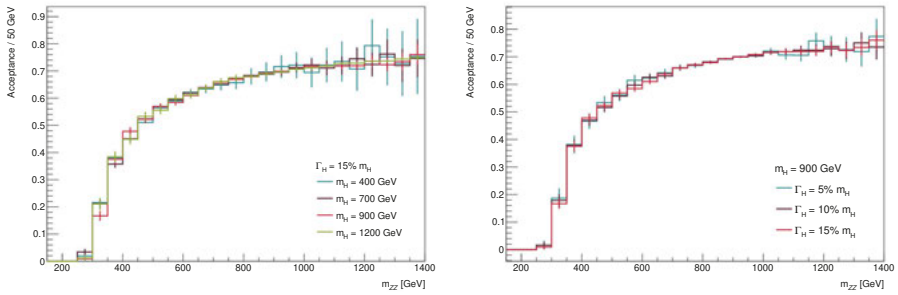

(a) Different signal masses

(b) Different signal widths

Figure 4.4: Selection acceptances as a function of the invariant mass m_{ZZ} for large width heavy Higgs signals of (a) different masses and (b) different widths.

The reweighting method is validated by reweighting a fully simulated signal to the properties of another sample that is also available from full simulation. The reweighting approach is considered valid if the reweighted shape and the original one agree. An example is shown in Figure 4.5: the transverse mass distribution of the m_H = 900 GeV, 5% width signal is derived from the m_H = 1.2 TeV, 15% width MC simulation using the reweighting technique. For comparison the original distribution from MC simulation is overlayed. Good agreement between the two is evident.

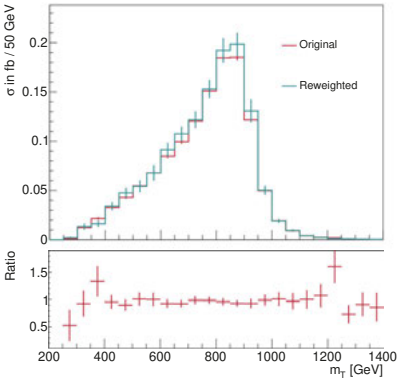

Figure 4.5: Comparison between original and reweighted m_T distribution when deriving the m_H = 900 GeV, 5% width signal from the m_H = 1.2 TeV, 15% width sample.

4.2 Backgrounds and their modelling

There are several background processes that result in the same final state signature as the signals. Measures need to be implemented to separate such background events from the signal events. This is done with a targeted event selection, introduced subsequently in Chapter 4.4. Here, an overview of the main background processes is given. Moreover, it is explained how exactly they

contribute to the signal signature and how they are modelled.

In general, for any analysis, there are two kinds of backgrounds: *Irreducible backgrounds* are processes which have the exact same final state as the signal. In contrast, *reducible backgrounds* refers to processes with different final state particles compared to the signal, but a very similar detector signature.

For the heavy Higgs search in the $\ell\ell\nu\nu$ final state, the major backgrounds can be classified into different types, depending on whether their final states feature *real* or *fake* leptons and have missing transverse energy or not. *Real leptons* refers to leptons originating from the hard scattering process. In contrast, objects which are mis-identified as leptons *and* leptons from subsequent decays - so called non-prompt leptons - are referred to as *fake leptons* in the following[1]. Similarly, real missing transverse energy is produced by the hard scattering while mis-identificiation and/or mis-reconstruction leads to fake missing transverse energy. The following four categories of $\ell\ell\nu\nu$ backgrounds arise:

- Processes with exactly two real leptons, as well as real missing transverse energy $E_{\mathrm{T}}^{\mathrm{miss}}$ due to neutrinos in the final state. The SM ZZ production with subsequent decay of the ZZ pair into the $\ell\ell\nu\nu$ final state fits into this category. These events are the dominant background contribution and form the only source of irreducible background.
- Processes with more than two real leptons and real $E_{\mathrm{T}}^{\mathrm{miss}}$, where (at least) one lepton is not identified and only exactly two are selected. The best example of this type are $WZ \rightarrow \ell\nu\ell^{+}\ell^{-}$ events, which constitute the second largest background.
- Processes with exactly two real leptons, but fake $E_{\mathrm{T}}^{\mathrm{miss}}$ which arises due to misreconstruction effects. The major contributor of such events is Z + jets production, where the Z boson boson decays into a pair of electrons or muons, and the fake $E_{\mathrm{T}}^{\mathrm{miss}}$ is related to mismeasurements of the jets.
- Processes with one real lepton and real $E_{\mathrm{T}}^{\mathrm{miss}}$, where the second lepton is a fake lepton. Examples of this topology are semileptonic $t\bar{t}$ events, with a misidentified lepton arising from the hadronic top decay. As the two leptons originate from two different particle decays, all $t\bar{t}$ processes are described as part of the *non-resonant dilepton background*.

[1] Although non-prompt leptons are of course actually leptons.

4.2.1 Non-resonant ZZ production

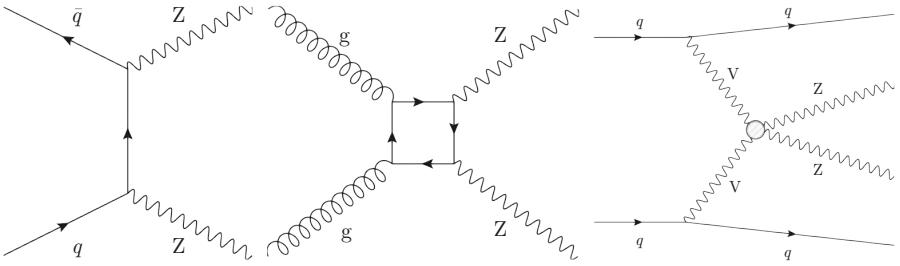

(a) $q\bar{q}ZZ$ production (b) $ggZZ$ production (c) $qqZZjj$ EW production

Figure 4.6: Leading order Feynman graphs of non-resonant ZZ production in pp-collisions via (a) the $q\bar{q}ZZ$, (b) the $ggZZ$ process and (c) vector-boson scattering contributing to the $qqZZjj$ EW process.

In the SM, there are several modes of non-resonant production of a Z boson pair in pp-collisions: the $q\bar{q}ZZ$, $ggZZ$ and $qqZZjj$ electroweak processes. Figure 4.6 shows the leading order Feynman graphs for each of them. The production via quark-antiquark scattering, $q\bar{q}ZZ$ (Fig. 4.6(a)), is by far the dominant contribution, since it is the only process that occurs at tree-level. In contrast, the gluon fusion production mode $ggZZ$ (Fig. 4.6(b)) is loop-induced and the electroweak (EW) contributions $qqZZjj$ EW (Fig. 4.6(c)) are at least of order $\mathcal{O}(\alpha_{\mathrm{EW}}^4)$. The exact composition of the total ZZ background varies, depending on the fiducial region considered. As the $qqZZjj$ EW process contains two jets in the final state at leading order, it is more relevant for the analysis of VBF than of ggF signatures. The reason is that the event selection of VBF signatures requires the presence of two jets.

Events in which the Z boson pair further decays as $ZZ \to \ell\ell\nu\nu$ result in exactly the same final state as the signal: two real leptons, with opposite charge but of the same flavour and with an invariant mass that is compatible with the Z boson mass, and two real neutrinos reconstructed as missing transverse energy $E_{\mathrm{T}}^{\mathrm{miss}}$. These kind of events constitute the leading background and therefore it is crucial to model them well in MC simulation.

For the analyses presented here, two sets of MC simulated samples are considered, produced with different event generators, as shown in Table 4.1[2]:

In the "POWHEG set" $q\bar{q} \to ZZ \to llvv$ events are generated using the POWHEG-BOX v2 generator [122], interfaced to PYTHIA 8 [129], which models the parton showering and Z boson decay. The matrix element is calculated up to next-to-leading order (NLO) for this process for final states with up to one jet. Additional jets in the final state originate from the parton showering model. To simulate $ggZZ$ events, the LO gg2VV generator [131] is employed. The $qq \to \ell\ell\nu\nu jj$ samples

[2] Both sets also include samples with $\ell\ell\ell\ell$ final states, generated with the same setup. However, their contribution to the fiducial region of the $\ell\ell\nu\nu$ analysis is minor.

"Powheg set"	Generator	Accuracy
$q\bar{q} \to ZZ \to llvv$	POWHEG-BOX v2 + PYTHIA 8	0, 1 jet @ NLO
$gg \to ZZ \to llvv$	gg2VV + PYTHIA 8	LO
$qq \to \ell\ell vvjj$	SHERPA 2.2.1	LO
"Sherpa set"	**Generator**	**Accuracy**
$q\bar{q} \to ZZ \to llvv$	SHERPA 2.2.2	0,1 jet @ NLO + 2,3 jets @ LO
$gg \to ZZ \to llvv$	SHERPA 2.2.2	LO
$qq \to \ell\ell vvjj$	SHERPA 2.2.2	LO

Table 4.1: Overview of MC simulated $ZZ \to \ell\ell vv$ background samples.

are generated using SHERPA 2.2.1 [132], also at LO. All samples of the "POWHEG set" use the CT10 PDF set [123].

For the "SHERPA set" all sub-processes of the $ZZ \to \ell\ell vv$ background are generated with SHERPA 2.2.2 [132]. With this choice, NLO accuracy for $q\bar{q}ZZ$ events with zero or one jet, and LO accuracy for $q\bar{q}ZZ$ events with two or three jets is achieved. The SHERPA $q\bar{q}ZZ$ samples therefore model also up to three jets with matrix element calculations. Here, the NNPDF3.0 NNLO PDF set [133] is used for all samples.

Several properties are shared by the samples in both sets: Both $ggZZ$ samples include the contribution from the Higgs boson at 125 GeV as well as the corresponding interference effects. Interference between processes is described in more detail in Chapter 4.3. Moreover, all $qq \to \ell\ell vvjj$ samples include electroweak contributions up to $\mathcal{O}(\alpha_{\mathrm{EW}}^6)$.

In both cases higher-order QCD corrections are applied to the $ggZZ$ samples, following recent NLO calculations in [134]. Corrections are also applied to the $q\bar{q}ZZ$ samples to incorporate higher-order EW effects. To match the accuracy of the POWHEG $q\bar{q}ZZ$ samples to that of SHERPA, a further set of higher-order QCD corrections is applied to the POWHEG $q\bar{q}ZZ$ samples only. The details of these corrections are explained in the corresponding analysis chapters, 5.2.1 and 6.2.1.

The "POWHEG set" of simulated $ZZ \to \ell\ell vv$ samples has also been used in the measurement of the SM $ZZ \to \ell\ell vv$ cross-section in pp-collisions with ATLAS [135]. With the higher-order corrections included, its cross-section prediction is found to be in agreement with the measured value. Further details on the event generation and comparisons to measured data for multi-boson processes (ZZ, WZ, VVV etc.) can also be found in [136].

A generator comparison of the most important samples is shown here, in the fiducial phase space of the $H \to ZZ \to \ell\ell vv$ analysis. The POWHEG $q\bar{q} \to ZZ \to llvv$ sample, with higher-order QCD corrections, is compared to the corresponding SHERPA sample. For the comparison between gg2VV and SHERPA $gg \to ZZ \to llvv$, the corresponding higher-order corrections are applied to both. Figure 4.7 shows the distributions of the reconstructed missing transverse engery, $E_{\mathrm{T}}^{\mathrm{miss}}$.

The $E_{\mathrm{T}}^{\mathrm{miss}}$ reconstruction is based on the PFLOW variables and the distributions are normalized to unit area.

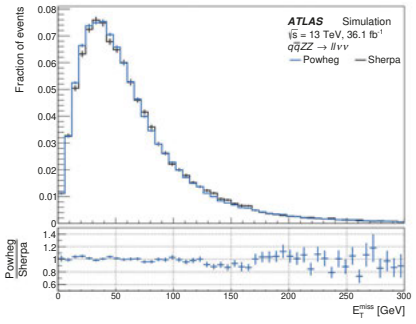

(a) $q\bar{q} \to ZZ \to llvv$

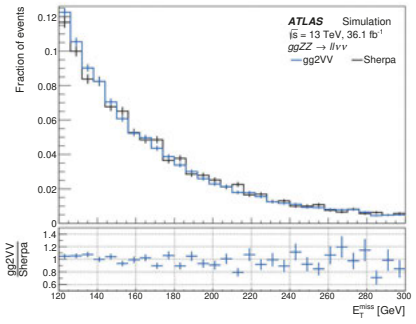

(b) $gg \to ZZ \to llvv$

Figure 4.7: Generator comparison of the reconstructed $E_{\mathrm{T}}^{\mathrm{miss}}$ distributions in simulated (a) $q\bar{q} \to ZZ \to llvv$ and (b) $gg \to ZZ \to llvv$ events.

Only a basic event selection is applied for the comparison: exactly one same-flavour, opposite sign lepton pair is required and its invariant mass is required to be within 15 GeV around the pole mass of the Z boson. For $gg \to ZZ \to llvv$ events, only the region with $E_{\mathrm{T}}^{\mathrm{miss}} > 120\,\mathrm{GeV}$ is selected, since the SHERPA samples of this process are produced with generator level-requirements on the p_{T} of the two neutrinos.

In the selected phase space, the shape of the $E_{\mathrm{T}}^{\mathrm{miss}}$ distributions agrees between the two generators considered. Table 4.2 lists the corresponding event yields for a luminosity of 36.1 fb^{-1} and their uncertainty from simulation statistics. For both processes, the yields match within a few %. Both sets of samples are therefore consistent and suited for the analysis.

$q\bar{q} \to ZZ \to llvv$

Generator	Yields
POWHEG	5338 ± 14
SHERPA	5253 ± 24

$gg \to ZZ \to llvv$

Generator	Yields
gg2VV	82.6 ± 0.6
SHERPA	75.4 ± 0.7

Table 4.2: Generator comparison of $ZZ \to \ell\ell\nu\nu$ event yields.

4.2.2 WZ production

The SM production of a WZ pair poses the second leading background to the searches presented in this thesis. It mostly consists of events with subsequent $WZ \to \ell\nu\ell^+\ell^-$ decay, where the lepton emerging from the W boson fails to be reconstructed, e.g. because it escapes outside the detector acceptance, while the leptons from the Z boson still pass the signal selection. Such $WZ \to \ell\nu\ell^+\ell^-$ events have the

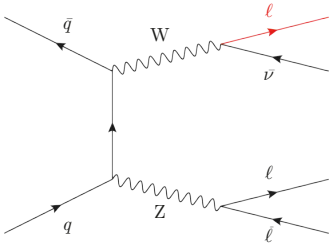

Figure 4.8: Leading order Feynman graph of $WZ \to \ell\nu\ell^+\ell^-$ background events. The lepton marked in red fails reconstruction.

same signature as the signal. Figure 4.8 illustrates the process with a leading order Feynman graph.

Events where the W boson decays hadronically ($WZ \to qq\ell^+\ell^-$) and higher-order electroweak diagrams, such as vector boson scattering ($WZ \to \ell\ell\ell\nu jj$), lead to final states with additional jets, and are therefore relevant to the VBF analysis.

"Powheg set"	**Generator**	**Accuracy**
$WZ \to \ell\nu\ell^+\ell^-$	POWHEG + PYTHIA 8	0,1 jet @ NLO
$WZ \to qq\ell^+\ell^-$	POWHEG + PYTHIA 8	NLO
$WZ \to \ell\ell\ell\nu jj$	SHERPA 2.2.1	LO
"Sherpa set"	**Generator**	**Accuracy**
$WZ \to \ell\nu\ell^+\ell^-$	SHERPA 2.2.2	0,1 jet @ NLO + 2,3 jets @ LO
$WZ \to qq\ell^+\ell^-$	SHERPA 2.2.2	NLO
$WZ \to \ell\ell\ell\nu jj$	SHERPA 2.2.2	LO

Table 4.3: Overview of MC simulated WZ background samples.

Table 4.3 gives on overview of the simulation samples used for the WZ background. The generator configurations are similar to those for the ZZ background simulation described earlier. POWHEG samples use the CT10 and SHERPA samples the NNPDF3.0 NNLO PDF set. The total WZ cross-section predicted by SHERPA agrees best with the value measured by ATLAS [136].

Again, a comparison is made of the two main samples in the relevant phase space. Special attention is paid to the shapes of the distributions analysed in the search signal region, since their normalisation is obtained from data as explained in Chapters 4.4, 5.2 and 6.2. Figure 4.9 shows the comparisons of the reconstructed transverse missing energy $E_{\mathrm{T}}^{\mathrm{miss}}$ and the transverse momentum of the lepton pair $p_{\mathrm{T}}^{\ell\ell}$. These two variables enter the calculation of the transverse mass observable m_{T}, as explained in Chapter 4.4.

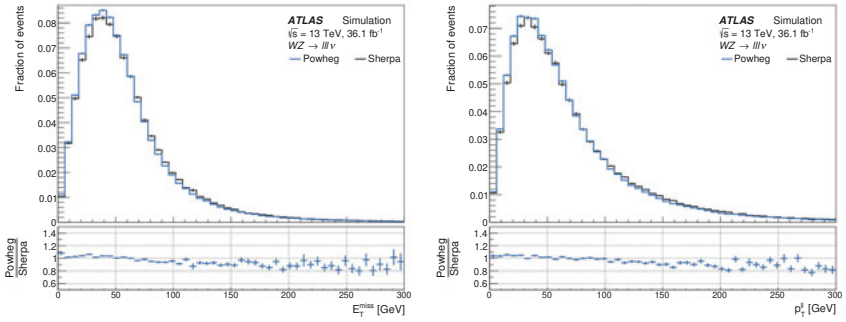

(a) $E_{\mathrm{T}}^{\mathrm{miss}}$ (b) $p_{\mathrm{T}}^{\ell\ell}$

Figure 4.9: Generator comparison for the $WZ \to \ell\nu\ell^+\ell^-$ background of (a) the $E_{\mathrm{T}}^{\mathrm{miss}}$ and (b) the $p_{\mathrm{T}}^{\ell\ell}$ distributions.

All distributions in Figure 4.9 are normalized to a unit area. In general, good agreement within statistical fluctuations is observed for $E_{\mathrm{T}}^{\mathrm{miss}}$ and $p_{\mathrm{T}}^{\ell\ell}$. However, for both a similar trend is apparent: for events with high energy final state objects, i.e. with $E_{\mathrm{T}}^{\mathrm{miss}}$ and $p_{\mathrm{T}}^{\ell\ell} >\approx 100\,\mathrm{GeV}$, the POWHEG samples predict rates that are around 10% lower than the SHERPA samples. This discrepancy may arise as a consequence of the formal higher order accuracy of the SHERPA simulation. However, the deviation is rather small - especially in view of the statistical uncertainties. Therefore the discrepancy should not significantly affect the search and both sets of samples are considered compatible.

4.2.3 Z + jets production

Another source of background is the production of one single Z boson in association with jets. If the Z boson decays into a pair of electrons or muons, and there is additional (fake) reconstructed missing transverse energy (e.g. due to mismeasured jet energies or some jet portions being outside of the detector acceptance), such a Z + jets event has the same detector signature as the signal. A leading order Feynman graph of the Z + jets process is displayed in Figure 4.10. The two quarks in the final state are marked in red. They are potentially identified as jets and are a source for fake missing transverse energy if mismeasured or partially missed.

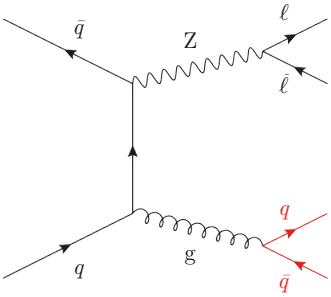

Figure 4.10: Leading order Feynman graph of Z + jets background events. Marked red are the two quarks resulting in jets and/or (fake) $E_{\mathrm{T}}^{\mathrm{miss}}$.

Z + jets events are higher order contributions to the Drell-Yan process - discussed already in Chapter 3 - but with additional initial or final state radiation. In addition, there are VBF and V-strahlung production modes of Z + jets events, which comprise two jets in the final state and

are denoted as EW $Z \to e^+e^- jj$ and EW $Z \to \mu^+\mu^- jj$ here. For the analyses presented here, the $Z \to \tau\tau$ decay is not considered as part of the Z + jets background, even though it may result in the signal signature, if both τ's decay leptonically. Such decays do not represent a resonance in the dilepton mass and are therefore considered to be part of the non-resonant dilepton background described in Chapter 4.2.4.

The Z + jets background is modelled with the SHERPA 2.2.1 event generator. Table 4.4 gives an overview of the samples and their accuracies.

Process	Generator	Accuracy
$Z \to e^+e^-$	SHERPA 2.2.1	0, 1, 2 jets @ NLO + 3, 4 jets @ LO
EW $Z \to e^+e^- jj$	SHERPA 2.2.1	0,1, 2 jets @ LO
$Z \to \mu^+\mu^-$	SHERPA 2.2.1	0, 1, 2 jets @ NLO + 3, 4 jets @ LO
EW $Z \to \mu^+\mu^- jj$	SHERPA 2.2.1	0,1, 2 jets @ LO

Table 4.4: Overview of MC simulated Z + jets background samples.

For the $Z \to e^+e^-$ and $Z \to \mu^+\mu^-$ samples an accuracy of NLO is achieved for up to two jets in the matrix element while events with up to four jets are calculated at LO. The EW $Z \to e^+e^- jj$ and EW $Z \to \mu^+\mu^- jj$ events are generated at LO, with up to two additional jets entering the matrix element calculation, i.e. in total up to four jets. All Z + jets samples use the NNPDF3.0 NNLO PDF set together with a dedicated tune of the parton shower model, specifically developed for the Z + jets process [6].

In general, the Z + jets process is very abundant in the pp-collisions at the LHC: its inclusive predicted cross-section (at NNLO) for a center-of-mass energy of 13 TeV is one order of magnitude larger than for example the production cross-section of ZZ events (cf. [135] and [137]). However, Z + jets events lead to the $\ell\ell\nu\nu$ signature only if they exhibit large missing transverse energy. Large $E_{\mathrm{T}}^{\mathrm{miss}}$ is rare, as the process itself does not contain any neutrinos causing real $E_{\mathrm{T}}^{\mathrm{miss}}$: in fact only 1 in 1000 simulated Z + jets events has $E_{\mathrm{T}}^{\mathrm{miss}} > 120$ GeV. Dedicated kinematic event selections, outlined in Chapter 4.4 and detailed in Chapters 5.1 and 6.1, reduce this fraction even further. It should also be noted that the fake $E_{\mathrm{T}}^{\mathrm{miss}}$ arising from imperfect detector and pile-up modelling is not easily describable in MC simulation. In this light, and considering the extreme computational expense to generate simulated Z + jets samples with sufficient statistics after all selections are applied, it was decided to use the observed data to correct the Z + jets background prediction, as described in detail in Chapters 5.2.3 and 6.2.3.

4.2.4 Non-resonant dilepton backgrounds

The *non-resonant dilepton background* consists of all processes which lead to the same signature as the signal, but where the lepton pair does not originate from the decay of a single resonance, such as the Z boson. Instead the lepton pair emerges from the decay of two unrelated particles.

This background is dominated by $t\bar{t}$ events, but also includes Wt, WW, $Z \to \tau\tau$ and single-top production processes. The corresponding relative fractions of the total non-resonant dilepton background are displayed in Figure 4.11, after a basic event selection, requiring a same-flavour, opposite sign lepton pair with an invariant mass within 15 GeV of the Z boson mass and $E_{\mathrm{T}}^{\mathrm{miss}} > 120$ GeV. Figure 4.12 illustrates the three leading processes - $t\bar{t}$, Wt and WW - with example leading order Feynman graphs. For each case, the dileptonic decay mode is shown, as this is the most obvious mode to contribute. But certainly also other decay modes, such as the semileptonic decay mode of $t\bar{t}$ happen to be selected, if one of the reconstructed leptons is non-prompt or fake.

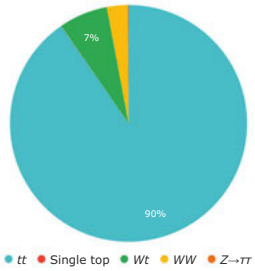

Figure 4.11: Composition of the non-resonant dilepton background with SFOS lepton pair and large $E_{\mathrm{T}}^{\mathrm{miss}}$. The combined contribution of $Z \to \tau\tau$ and single top events is less than 1%.

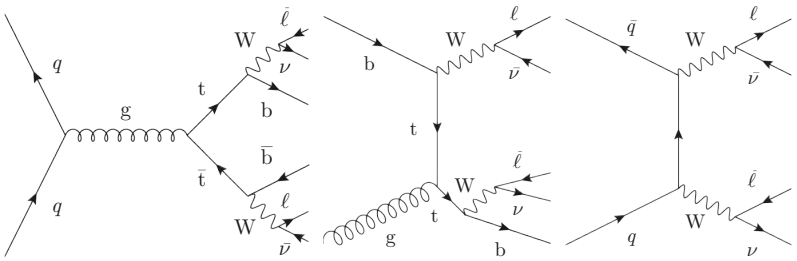

(a) $t\bar{t}$ production (b) Wt production (c) WW production

Figure 4.12: Example leading order Feynman graphs of the major contributors to the non-resonant dilepton background: (a) $t\bar{t}$ production, (b) Wt production and (c) WW production - all with dileptonic decay.

Different generator setups are used for the MC simulation of the non-resonant dilepton background processes and are detailed in Table 4.5.

Process	Generator	Accuracy
$t\bar{t}$	POWHEG + PYTHIA 6 or 8	NLO
Wt	POWHEG + PYTHIA 6 or 8	NLO
WW	POWHEG +PYTHIA 8	NLO
$Z \to \tau\tau$	SHERPA 2.2.1	0, 1, 2 jets @ NLO + 3, 4 jets @ LO
Single top	POWHEG + PYTHIA 6 or 8	NLO

Table 4.5: Overview of MC simulated non-resonant dilepton background samples.

All backgrounds involving top quarks are simulated using the POWHEG generator, interfaced to PYTHIA 6 for the 2015+16 data analysis and to PYTHIA 8 for the analysis of the 2015-2018 data. The PYTHIA 6 samples use the CT10 PDF set, while the PYTHIA 8 samples use the NNPDF3.0NLO PDF set. The single-top samples include both s- and t-channel contributions. A comparison of the top quark simulations to data is documented in [138] and the POWHEG samples are found to generally agree well with the data. The WW contribution is modelled with POWHEG +PYTHIA 8, using the CT10 PDF set. Finally, $Z \to \tau\tau$ (+jets) events are generated with the same SHERPA 2.2.1 setup as described in the previous section.

Although several of these processes are relatively abundant at the LHC, the non-resonant dilepton background plays only a minor role, as they can be well suppressed by simple analysis requirements. For example, the $t\bar{t}$ process features jets initiated by bottom quarks in its final state. With dedicated algorithms, those b-jets are identified (cf. Chapter 2.3.3) and vetoed in this analysis, reducing the $t\bar{t}$ contamination significantly. All the processes in the non-resonant dilepton background have in common that the lepton pair in the final state may be of different flavour. Therefore observed events with an $e\mu$ lepton pair are used to improve the MC prediction, as described in detail in Chapters 5.2.4 and 6.2.4.

4.2.5 Other backgrounds

Finally, a small background contribution originates from the associated production of a top-quark pair with a vector boson ($t\bar{t}V$) and triboson (VVV) events. These are summarised as *other backgrounds* in the following. All considered processes are rare, and lead to final states with more objects than the signal signature, hence they are strongly suppressed by a requirement of exactly two leptons. Table 4.6 summarizes the generators used for the simulation of the processes considered here.

Process	Generator	Accuracy
VVV processes		
$WWW \to 3\ell 3\nu$	SHERPA 2.2.1 or SHERPA 2.2.2	LO or NLO
$WWZ \to 4\ell 2\nu$ and $\to 2\ell 4\nu$	SHERPA 2.2.1 or SHERPA 2.2.2	LO or NLO
$WZZ \to 5\ell 1\nu$ and $\to 3\ell 3\nu$	SHERPA 2.2.1 or SHERPA 2.2.2	LO or NLO
$ZZZ \to 6\ell 0\nu$ and $\to 4\ell 2\nu$ and $\to 2\ell 4\nu$	SHERPA 2.2.1 or SHERPA 2.2.2	LO or NLO
$t\bar{t}V$ processes		
$t\bar{t}Z$	MADGRAPH5_aMC@NLO + PYTHIA 8	NLO
$t\bar{t}W$	MADGRAPH5_aMC@NLO + PYTHIA 8	NLO
$t\bar{t}WW$	MADGRAPH5_aMC@NLO + PYTHIA 8	NLO

Table 4.6: Overview of MC simulated other background samples.

All triboson samples are generated with SHERPA. The 2015+16 analysis uses version 2.2.1 in

combination with the CT10 PDF set for a prediction at LO, whereas the 2015-18 analysis prediction is at NLO using SHERPA version 2.2.2 with the NNPDF3.0 NLO PDF set. Only the production of on-shell vector bosons is included in these samples. For the $t\bar{t}V$ processes, the MADGRAPH5_aMC@NLO generator is used, together with the NNPDF3.0 NLO PDF set. Here the predictions are at NLO, and the $t\bar{t}Z$ process includes the Z boson decays to two electrons, muons, neutrinos or quarks.

4.3 Interference modelling

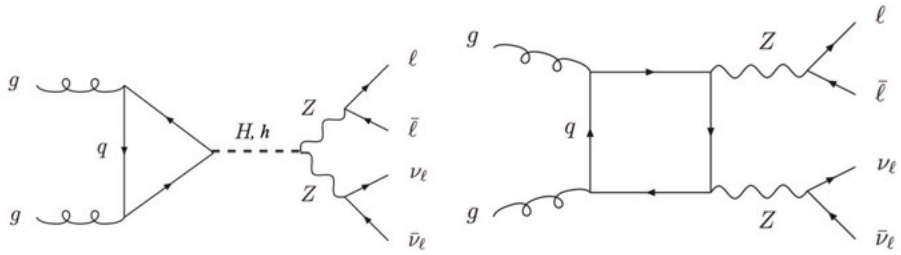

Figure 4.13: Feynman graphs for the three interfering processes: In (a) the ggF production of a heavy Higgs H or the 125 GeV Higgs h and (b) the $ggZZ$ background.

There are two processes which share the same initial and final state as the $gg \to H \to ZZ \to llvv$ signal process: First, the gluon-gluon fusion production of the light SM Higgs, h, at a mass of 125 GeV and its subsequent decay to a pair of Z bosons, which further decays into a charged lepton and neutrino pair. This corresponds to the second process illustrated by Figure 4.13(a). Second, the production of a ZZ pair from the gg continuum and its decay according to $gg \to ZZ \to llvv$, as shown in Figure 4.13(b). Since these processes are indistinguishable, they all contribute to the matrix element, leading to interference terms in the total cross section. Within a theoretical framework, it has been shown that the interferences can change the inclusive cross section by $\mathcal{O}(10\%)$ [139]. With a larger width of the high-mass Higgs one expects the interference effects to be more prominent. Hence, for large-width analyses as presented in this thesis, both the interference of the signal with the ZZ continuum background ($H-B$ interference) as well as with the light Higgs ($H-h$ interference) must be taken into account. Evidently, the $ggZZ$ background also interferes with the light Higgs contribution, but this term is already included in the MC samples used for this background. Therefore, it does not need to be modelled specifically. This section describes the methods employed in order to model the interference shapes and illustrates the impact on the search results.

4.3.1 Interference of ggF high mass Higgs signal and SM Higgs production

To model the $H-h$ interference, it is possible to derive an analytic reweighting function based on the transition amplitudes involved, similarly to the signal-to-signal reweighting technique described in Chapter 4.1.2.

In general, the total cross section of the signal considering only the the contributions from the light and heavy Higgs, and their interference, is described by the square of the contributing amplitudes A:

$$\begin{aligned}\sigma_{gg\to X\to ZZ} &= \frac{1}{2s}\cdot\int d\Omega |A_h(s,\Omega)+A_H(s,\Omega)|^2 \\ &= \frac{1}{2s}\cdot\int d\Omega |A_H(s,\Omega)|^2 + 2\,\mathrm{Re}\left(A_H(s,\Omega)A_h^*(s,\Omega)\right)+|A_h(s,\Omega)|^2 \end{aligned} \tag{4.3}$$

where the X is either the heavy H or light Higgs h, s denotes the center of mass energy squared in the event and Ω the solid angle [3]. For the sake of simplicity, the dependency on and integral over Ω is omitted from the notation in the following. Noting that for both processes the amplitude can be factorized, it can be written as the product of the production and decay amplitudes, A^P and A^D as well as the corresponding propagator for the Higgs:

$$A_{H,h} = A^P_{H,h}\cdot\frac{1}{s-s_{H,h}}\cdot A^D_{H,h} \tag{4.4}$$

Only $s_{H,h}$ is dependent on the mass and width of the Higgs under study, and for a SM-like heavy Higgs the production and decay amplitudes can be assumed to be the same as for the light Higgs (apart from an overall possible difference in coupling which is factorized out as μ in this analysis). Hence one can simplify the interference term:

$$\begin{aligned}\sigma_{h,H}(s) &\propto 2\cdot\mathrm{Re}\left(\frac{1}{s-s_H}\cdot\frac{1}{(s-s_h)^*}\right)\cdot|A^P_H|^2\cdot|A^D_H|^2 \\ &= 2\cdot\mathrm{Re}\left(\frac{1}{s-m_H^2+im_H\Gamma_H}\cdot\frac{1}{s-m_h^2-im_h\Gamma_h}\right)\cdot|A^P_H|^2\cdot|A^D_H|^2 \\ &= 2\cdot\frac{(s-m_H^2)\cdot(s-m_h^2)+m_H\Gamma_H m_h\Gamma_h}{\left[(s-m_H^2)^2+m_H^2\Gamma_H^2\right]\cdot\left[(s-m_h^2)^2+m_h^2\Gamma_h^2\right]}\cdot|A^P_H|^2\cdot|A^D_H|^2 \end{aligned} \tag{4.5}$$

, where the heavy Higgs boson has mass m_H and width Γ_H and the lighter Higgs is characterized by m_h and Γ_h. For the processes considered here, s is equal to the square of the truth invariant mass of the Z boson pair, m_{ZZ}. Furthermore, the cross section of the heavy Higgs signal can be expressed as:

$$\begin{aligned}\sigma_H(s) &\propto \frac{1}{|s-s_H|^2}\cdot|A^P_H|^2\cdot|A^D_H|^2 \\ &= \frac{1}{(s-m_H^2)^2+m_H^2\Gamma_H^2}\cdot|A^P_H|^2\cdot|A^D_H|^2 \end{aligned} \tag{4.6}$$

[3] The branching fraction of the decay $ZZ\to llvv$ does not play a role for the interference and need not be considered.

And hence, a reweighting function by which the the pure signal contribution can be transformed into the interference term can be derived from their ratios as:

$$\begin{aligned} W_{h,H}(s) &= \sigma_{h,H}(s)/\sigma_H(s) \\ &= 2 \cdot \frac{(s-m_H^2)\cdot(s-m_h^2) + m_H\Gamma_H m_h\Gamma_h}{(s-m_h^2)^2 + m_h^2\Gamma_h^2} \end{aligned} \tag{4.7}$$

This analytical function only contains known quantities and as it depends on $s = (m_{ZZ})^2$ can a priori be used to reweight the full invariant mass spectrum. Figure 4.14 shows example $H-h$ interference shapes as obtained from the reweighting. The procedure is as follows: first the heavy Higgs signal m_{ZZ} spectrum is determined from the Breit-Wigner-term in Equation 4.6. The resulting signal histogram in m_{ZZ} is normalised to unit area, and then reweighted to the corresponding interference histogram using Equation 4.7. These histograms are therefore independent of the (signal) normalisation cross-section, focussing rather on the shape of the interference. As expected, the interference has a turning point at the mass of the heavy Higgs boson - below it the interference is negative, above it is positive. The interference peaks are more sharply pronounced for smaller heavy Higgs masses (closer to the light Higgs mass) and smaller Higgs widths. This is in accordance with the expectation that the interference impact is more relevant for large widths.

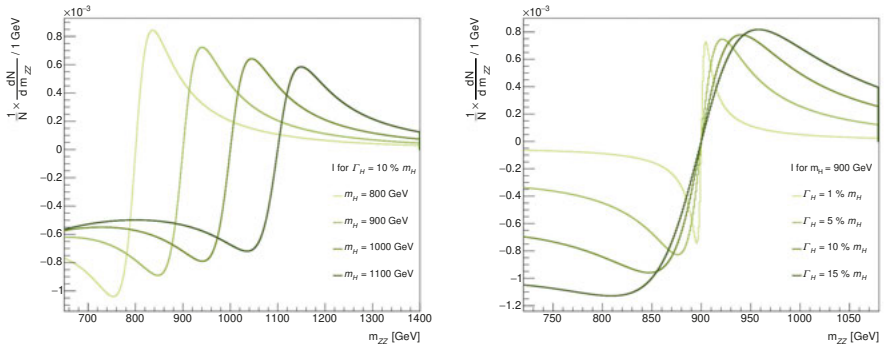

Figure 4.14: $H-h$ interference shapes in m_{ZZ} for (a) different masses and (b) different widths, as obtained by the reweighting procedure following Equations 4.6 and 4.7.

The above calculations are based on the truth-level ZZ invariant mass m_{ZZ}, but in the end the observable of the $\ell\ell\nu\nu$ analysis is the transverse mass m_{T} (cf. Chapter 4.4) at reconstruction level. As m_{T} is also an invariant mass (just missing the longitudinal information), the reweighting technique can also be used to obtain the m_{T} spectra of the $H-h$ interference. However, the observed cross sections include also an acceptance term (as a function of m_{ZZ}), due to the event selection. Comparing the expressions for the interference and signal term, Eqn. 4.5 and 4.6, it is obvious that they only differ in the propagator. Therefore, the acceptance term is assumed to

be the same between signal and interference (for the same mass and width) and it should cancel out in the ratio in Equation 4.7. Based on these assumptions, the m_{T} distributions of the $H-h$ interference are determined with this analytic reweighting technique - the results are shown in Chapter 4.3.3, after having also obtained the $H-B$ interference with the methodology described in the following.

4.3.2 Interference of ggF high mass Higgs signal and $ggZZ$ background

To model the interference between heavy Higgs signal and $ggZZ$ background, dedicated MC samples are fitted with an empirical function to obtain a description of the interference term for any signal mass and width on truth level.

Truth samples and event selection MC samples which include the $gg \to H \to ZZ \to llvv$ signal, the $gg \to ZZ \to llvv$ background and the interference term are produced with the gg2VV generator [131]. For the signal a SM-like Higgs boson is assumed, while for the background samples loop induced continuum ZZ production without any interference effects is modelled. The samples only contain truth level quantities. The corresponding predicted SM cross sections at LO for the signal and background only samples are given in Table 4.7.

Although it is not possible to simulate the interference term separately on its own since its exact structure is unknown, it can be derived from a sample containing the combination of signal, interference and background contributions (from here on referred to as SBI) and samples containing only the signal (S) and background (B) by histogram subtraction: $\mathrm{hist_I} = \mathrm{hist_{SBI}} - \mathrm{hist_S} - \mathrm{hist_B}$, where hist denotes a histogram of any observable of interest. An example showing the truth invariant mass distributions for all four cases is shown in Figure 4.15, where the signal and background are normalized to the SM prediction given in Table 4.7 and a luminosity of 36.1 fb^{-1}.

Signal	σ_{SM} at LO in fb
$m_H = 400$ GeV, $\Gamma_H = 5\%\ m_H$	38.50
$m_H = 700$ GeV, $\Gamma_H = 5\%\ m_H$	15.65
$m_H = 900$ GeV, $\Gamma_H = 5\%\ m_H$	6.95
$m_H = 1200$ GeV, $\Gamma_H = 5\%\ m_H$	2.26
$m_H = 1500$ GeV, $\Gamma_H = 5\%\ m_H$	0.83
$m_H = 400$ GeV, $\Gamma_H = 10\%\ m_H$	18.49
$m_H = 700$ GeV, $\Gamma_H = 10\%\ m_H$	7.53
$m_H = 900$ GeV, $\Gamma_H = 10\%\ m_H$	3.38
$m_H = 1200$ GeV, $\Gamma_H = 10\%\ m_H$	1.12
$m_H = 1500$ GeV, $\Gamma_H = 10\%\ m_H$	0.42
$m_H = 400$ GeV, $\Gamma_H = 15\%\ m_H$	11.89
$m_H = 700$ GeV, $\Gamma_H = 15\%\ m_H$	4.82
$m_H = 900$ GeV, $\Gamma_H = 15\%\ m_H$	2.19
$m_H = 1200$ GeV, $\Gamma_H = 15\%\ m_H$	0.74
$m_H = 1500$ GeV, $\Gamma_H = 15\%\ m_H$	0.28
Background	
$ggZZ$	31.72

Table 4.7: SM expectation values for the LW heavy Higgs signal cross sections at different mass and width points as well as the $ggZZ$ continuum background, at leading order.

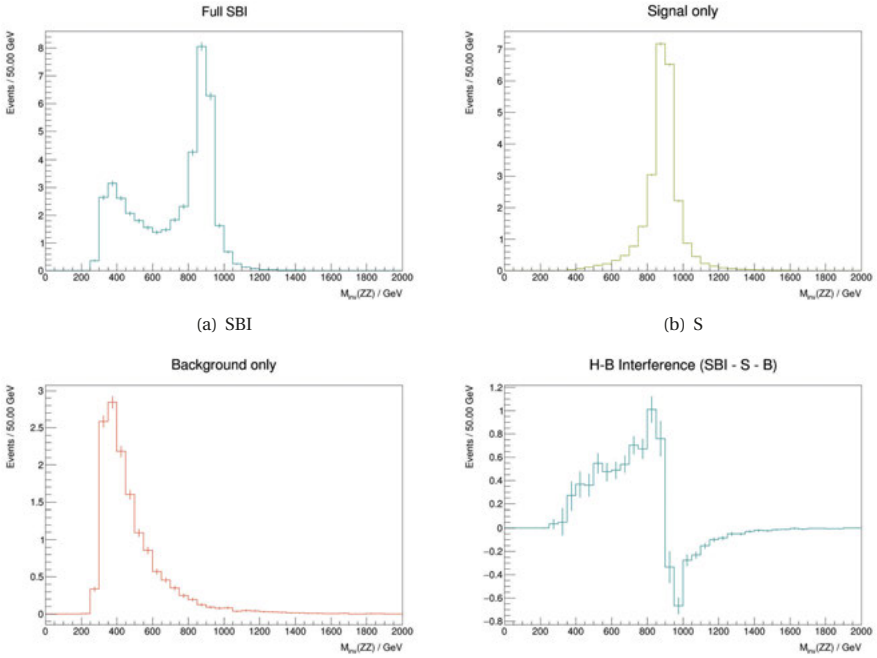

(a) SBI (b) S

(c) B (d) I = SBI - S - B

Figure 4.15: An example illustrating how the $H-B$ interference shape shown in (d) is obtained as SBI - S - B from (a), (b) and (c) respectively. The truth invariant mass m_{ZZ} distributions are shown for a heavy Higgs with $m_H = 900$ GeV and $\Gamma_H = 10\%$.

In order to assess the effect of taking the interference into account in a scenario that is as realistic as possible, the signal region selection definitions as given in Chapters 5.1 and 6.1, are applied on truth level. Only the b-jet veto is omitted as it is expected to have only a small impact on the signal and $ggZZ$ background process, which can only contain b-quarks as part of additional radiation. Additionally, truth jets that overlap with the selected leptons are removed. To ensure the correct pair of leptons is considered, each of them must originate from a Z boson decay. Moreover, the truth neutrinos are used to compute the missing transverse energy.

Fit function based modelling A parametrization of this interference in terms of the mass and width of the heavy Higgs is derived in the following, such that its shape can be obtained for any given signal hypothesis. Following the same argumentation as for the $H-h$ interference, the full cross section at leading order - now including also the $ggZZ$ background contribution - can

be written as

$$\begin{aligned}\sigma_{gg\to X\to ZZ} &= \frac{1}{2s}\cdot\int d\Omega |A_h(s,\Omega)+A_H(s,\Omega)+A_B(s,\Omega)|^2 \\ &= \frac{1}{2s}\cdot\int d\Omega \{|A_H(s,\Omega)|^2+|A_B(s,\Omega)|^2+|A_h(s,\Omega)|^2 \\ &+ 2\,\mathrm{Re}\left[A_H(s,\Omega)A_h^*(s,\Omega)\right]+2\,\mathrm{Re}\left[A_H(s,\Omega)A_B^*(s,\Omega)\right] \\ &+ 2\,\mathrm{Re}\left[A_h(s,\Omega)A_B^*(s,\Omega)\right]\}\end{aligned} \tag{4.8}$$

where the last term describes the interference between light Higgs and background, which is not considered further here. More importantly, the second to last term describes the $H-B$ interference. This term contains an integral which cannot be solved analytically, but it can be expressed as an empirical function and then fit to the MC simulation. The fit based method was developed for the search in the $\ell\ell\ell\ell$ channel, and is documented in detail in [140]. To briefly summarize, the integral in question is approximated by a complex valued polynomial and the full fit function for the interference shape is then given by:

$$\begin{aligned}\sigma_{HB}(m_{ZZ}) &= \mathscr{L}_{gg}\cdot\frac{1}{m_{ZZ}}\cdot Re[\frac{1}{s-s_H}\cdot(A+iB)] \\ &= \mathscr{L}_{gg}\cdot\frac{1}{m_{ZZ}}\cdot Re\left[\frac{1}{s-s_H}\cdot((a_0+a_1\cdot m_{ZZ}+...)+i\cdot(b_0+b_1\cdot m_{ZZ}+...))\right]\end{aligned} \tag{4.9}$$

where $\mathscr{L}_{gg}$ gives the gluon-gluon luminosity and a_i and b_j are the free fit parameters of the polynomial. Using the following definitions

$$\begin{aligned}s &= m_{ZZ}^2 \\ s_H &= M_H^2+i\Gamma_H M_H\end{aligned} \tag{4.10}$$

and calculating as follows

$$\begin{aligned}Re[\frac{1}{s-s_H}\cdot(A+iB)] &= Re[\frac{1}{m_{ZZ}^2-M_H^2-i\Gamma_H M_H}\cdot(A+iB)] \\ &= Re[\frac{m_{ZZ}^2-M_H^2-i\Gamma_H M_H}{(m_{ZZ}^2-M_H^2)^2+\Gamma_H^2M_H^2}\cdot(A+iB)] \\ &= Re[\frac{m_{ZZ}^2-M_H^2}{(m_{ZZ}^2-M_H^2)^2+\Gamma_H^2M_H^2}\cdot A+\frac{\Gamma_H M_H}{(m_{ZZ}^2-M_H^2)^2+\Gamma_H^2M_H^2}\cdot B \\ &+ i(\frac{m_{ZZ}^2-M_H^2}{(m_{ZZ}^2-M_H^2)^2+\Gamma_H^2M_H^2}\cdot B-\frac{\Gamma_H M_H}{(m_{ZZ}^2-M_H^2)^2+\Gamma_H^2M_H^2}\cdot A)] \\ &= \frac{m_{ZZ}^2-M_H^2}{(m_{ZZ}^2-M_H^2)^2+\Gamma_H^2M_H^2}\cdot A+\frac{\Gamma_H M_H}{(m_{ZZ}^2-M_H^2)^2+\Gamma_H^2M_H^2}\cdot B\end{aligned} \tag{4.11}$$

one arrives at this expression for the empirical fit function:

$$\sigma_{HB}(m_{ZZ}) = \mathscr{L}_{gg} \cdot \frac{1}{m_{ZZ}} \cdot \frac{m_{ZZ}^2 - M_H^2}{(m_{ZZ}^2 - M_H^2)^2 + \Gamma_H^2 M_H^2} \cdot A + \frac{\Gamma_H M_H}{(m_{ZZ}^2 - M_H^2)^2 + \Gamma_H^2 M_H^2} \cdot B \tag{4.12}$$

Here 4th order polynomials are used for A and B:

$$\begin{aligned} A &= a_0 + a_1 m_{ZZ} + a_2 m_{ZZ}^2 + a_3 m_{ZZ}^3 + a_4 m_{ZZ}^4 \\ B &= b_0 + b_1 m_{ZZ} + b_2 m_{ZZ}^2 + b_3 m_{ZZ}^3 + b_4 m_{ZZ}^4 \end{aligned} \tag{4.13}$$

The most important point is that the parameters of the polynomial do not depend on the mass or width of the signal hypothesis, hence they can be derived by a simultaneous fit to the truth interference curves at all available points (taken from the histogram subtraction as described above). The results of this fit are shown in Figure 4.16 for the various mass and width points. The corresponding best fit values of the parameters are listed in Table 4.8. Since there is no reason why the interference should be different for different flavour channels of the ZZ decay, both the $eevv$ and $\mu\mu vv$ events are fitted jointly, to enhance the available statistics.

Parameter	Value	Error
a_0	3.63×10^2	5.68×10^{-2}
a_1	-4.34	2.29×10^{-4}
a_2	1.72×10^{-2}	9.14×10^{-7}
a_3	-2.26×10^{-5}	3.54×10^{-9}
a_4	3.74×10^{-11}	1.22×10^{-11}
b_0	-3.33×10^2	2.84×10^{-1}
b_1	3.31	1.19×10^{-3}
b_2	-1.11×10^{-2}	4.81×10^{-6}
b_3	1.34×10^{-5}	1.82×10^{-8}
b_4	-2.50×10^{-9}	4.54×10^{-11}

Table 4.8: Best fit values for the parameters of the complex polynomial, as given by Equations 4.12 and 4.13.

Different methods to obtain the interference shape on reconstruction level are used in the 2015 +2016 and 2015-18 data analysis. For the first, the detector resolution effect as a function of the truth invariant mass m_{ZZ} is derived by comparing truth and reconstruction level signal samples. This so-called *c-factor* is then convolved with the truth interference shape from the fit. A simpler approach was used for the analysis of the full 2015-18 data: instead of deriving the resolution function explicitly, a histogram-based reweighting is employed, which contains the resolution function implicitly. First, the truth interference m_{ZZ} shape is derived for any given mass and width point using the fit function. Then, using the signal truth m_{ZZ} shape at this point, a m_{ZZ} weight histogram is derived from the ratio of interference over signal. To obtain the interference shape for any variable at truth and reconstruction level, the corresponding signal is reweighted using this histogram. A truth closure test on this method is shown in Figure 4.17: The truth m_{T}

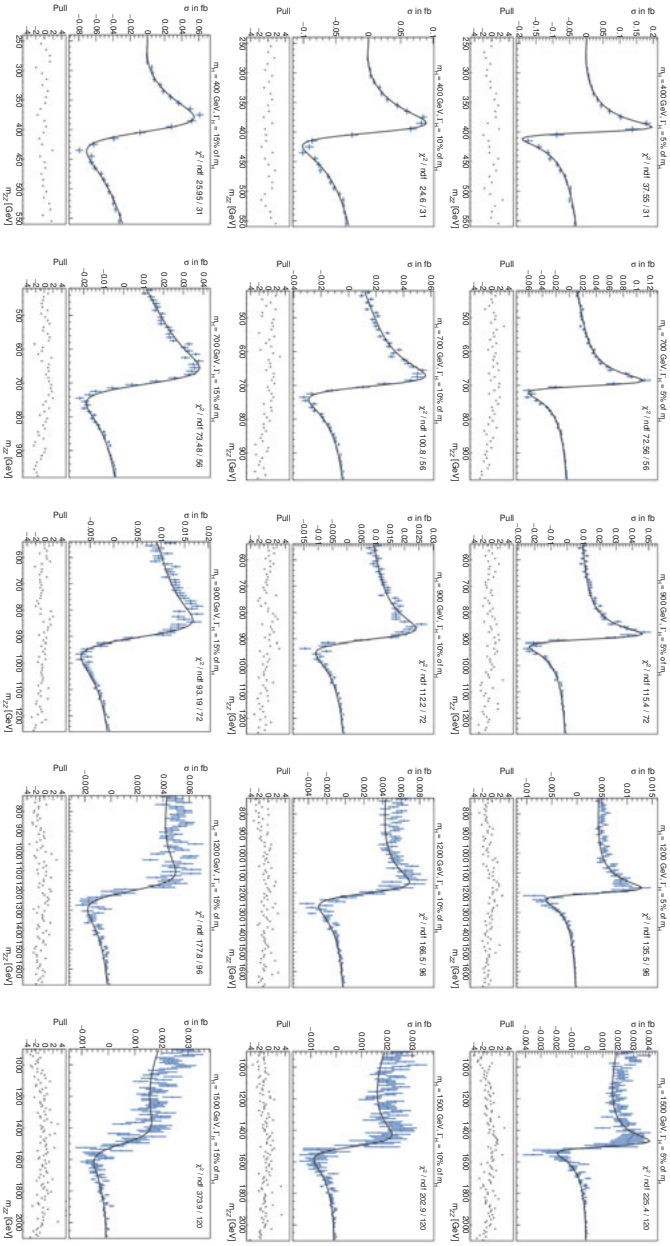

Figure 4.16: Fits of the truth $H - B$ interference shapes, using Equation 4.12. The truth signal region selection is applied.

interference shape determined directly from the sample via the histogram subtraction is compared to that obtained with the histogram based reweighting using the fit results for two different signals. Good agreement is found comparing the two, validating the method.

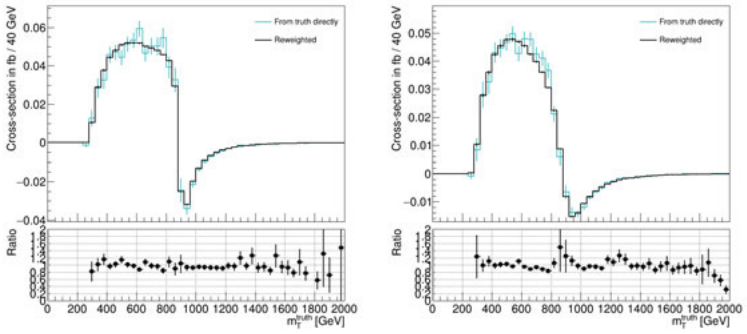

(a) 5% width (b) 15% width

Figure 4.17: Truth-level closure test for the histogram-based reweighting method to obtain the interference shape in m_T from the truth-level fit function to m_{ZZ}. The distributions shown correspond to a heavy Higgs signal of 900 GeV mass and a width of (a) 5% and (b) 15 %.

4.3.3 Combined effect of both interferences

Both the interference with the $ggZZ$ background and with the 125 GeV Higgs boson ggF process need to be considered to estimate the full effect on the high mass Higgs signal m_T distribution, as their distributions have a different sign: While the $H-h$ interference is negative below and positive above the signal mass, the $H-B$ interference shows the exact opposite behaviour[4]. Thus, the two interferences cancel each other at least partially. Figures 4.18 and 4.19 show a comparison of the signal, the two interference terms and the sum of signal and interferences at different mass and width points, respectively. To get a good estimate of the impact of the interference at the expected sensitivity of the search, all distributions are normalized to the expected upper limit on the cross-section when interference effects are not taken into account, and the full run II luminosity. Figure 4.18 shows that the effect of the interference is dependent on the mass: While for the two lower mass points the total yields are enhanced by the interference (S+I/S ratio is above 1), at higher masses the opposite is true (S+I/S becomes smaller than 1). However, across all mass points the same m_T dependence of the interference impact is observed: the low m_T side of the signal peak gets depleted, but the peak itself and the high m_T tail get enhanced. By taking into account the interference, the observed S+I distribution is shifted to higher m_T compared to the S only. This effect decreases with increasing mass. When looking at the same mass but with different width assumptions, as shown in Figure 4.19, it is apparent that the size of the interference

[4]This is in accordance with what e.g. [139] finds.

impact increases with increasing width, as expected.

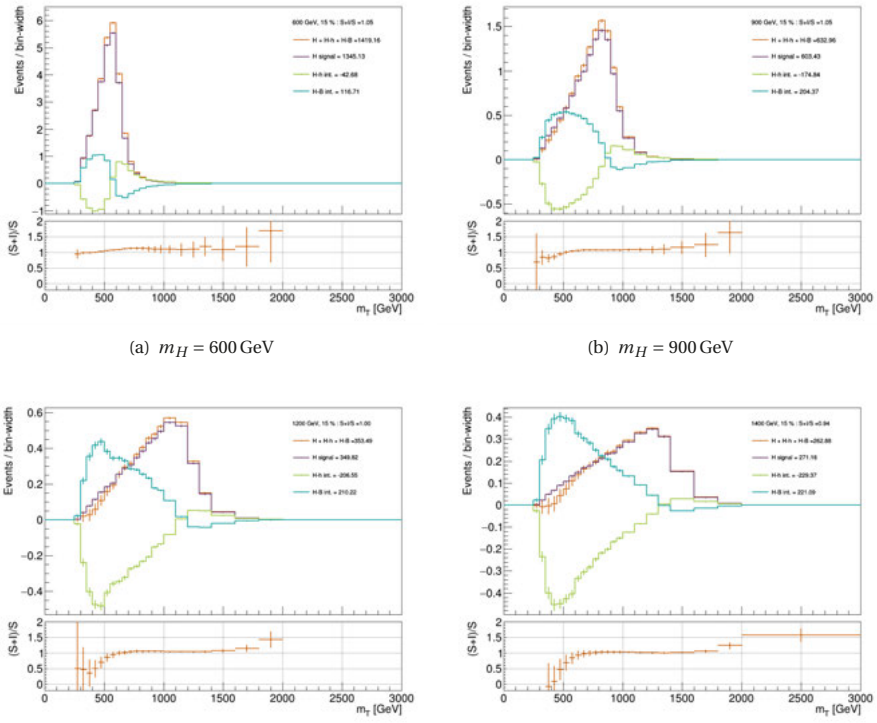

(a) $m_H = 600\,\text{GeV}$ (b) $m_H = 900\,\text{GeV}$

(c) $m_H = 1200\,\text{GeV}$ (d) $m_H = 1400\,\text{GeV}$

Figure 4.18: Reconstructed m_T shapes for signal and both interference terms for different signal masses each at a width of $\Gamma_H = 15\%$ of m_H, in the $\mu\mu\nu\nu$ channel. Normalized to the expected limit calculated without taking interference into account for the given signal and the full run II luminosity of 139 fb^{-1}.

Normalization and relative contribution To include the interference modelling in the limit setting, the overall normalisation needs to considered. Whereas in the previous plots all distributions were normalized to (approximately) the expected sensitivity at the mass point, the signal strength μ is a free parameter in the LWA fit setup. And while the signal cross section is scaled by μ, the interference term scales with $\sqrt{\mu}$. [5] Therefore, for small values of μ the interference has a larger impact in proportion to the signal than for larger values of μ. This effect needs to be taken into account when comparing the distributions, and is visualized in Figure 4.20: in (a), the

[5] Since $|\mu \cdot S + B|^2 = (\mu \cdot S)^2 + 2 \cdot \mu \cdot S \cdot B + B^2$

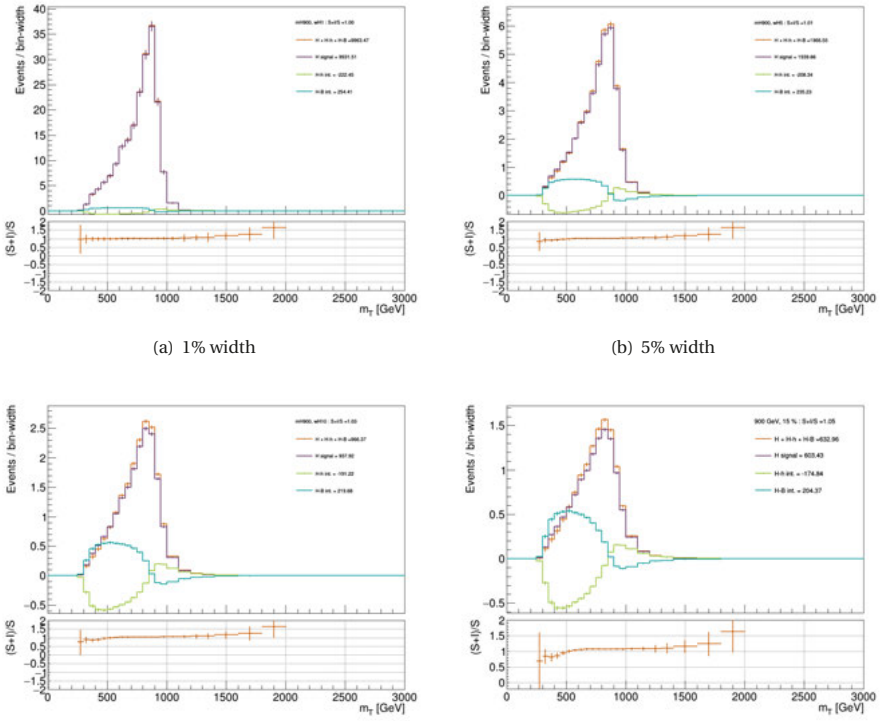

(a) 1% width

(b) 5% width

(c) 10% width

(d) 15% width

Figure 4.19: Reconstructed m_T shapes for signal and both interference terms for different widths each at a mass of $m_H = 900\,\text{GeV}$, in the $\mu\mu\nu\nu$ channel. Normalized to the expected limit calculated without taking interference into account for the given signal and the full run II luminosity of 139 fb^{-1}.

scaling is $\mu = 0.5$ and in (b) it is $\mu = 2$. Clearly, for $\mu = 0.5$ the relative impact of the interference is much more significant.

Therefore, separate templates for the interference and signal only distributions are used as inputs to the statistical interpretation, and the signal plus interference distribution is parametrised as $\text{S+I} = \mu \cdot \text{S} + \sqrt{\mu} \cdot \text{I}$. Both the shape and overall normalisation of S+I compared to S are then recalculated when μ changes.

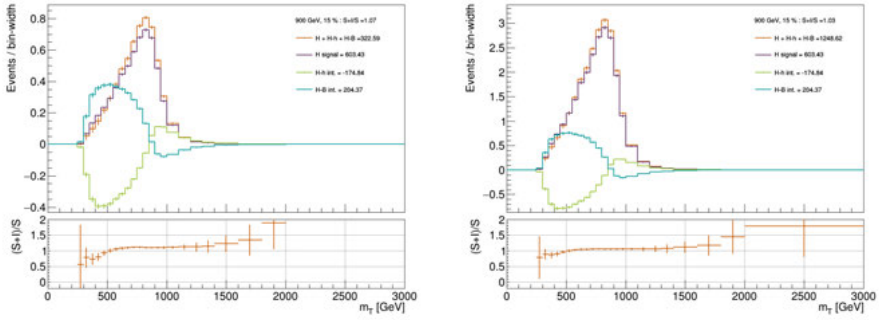

(a) $\mu = 0.5$ (b) $\mu = 2$

Figure 4.20: Reconstructed m_T shapes for signal and both interference terms for $m_H = 900$ GeV, $\Gamma_H = 15\%$ of m_H, in the $\mu\mu\nu\nu$ channel. Normalized to (a) half and (b) twice the expected limit calculated without taking interference into account for the given signal and the full run II luminosity of 139 fb^{-1}.

4.4 General search strategy

The general strategy of the presented searches is to compare the previously described MC simulation of signal and background to the observed data and to assess whether the data can be explained assuming the background only hypothesis, or the presence of a signal is detected. The comparison is made in a fiducial volume, i.e. a specific kinematical region, of the data, using only events that satisfy all criteria of the *event selection*. The event selection is based on the properties of the expected signal signature. To motivate why it is necessary, Table 4.9 shows the yields and associated MC statistical uncertainties for all backgrounds and for an example heavy Higgs signal with a mass of 1 TeV and a narrow width, when applying only a minimal selection: exactly one same flavour, opposite sign lepton pair with an invariant mass compatible with the Z boson is required. All yields in Table 4.9 are derived from the full run II MC simulation and scaled to a luminosity of 139 fb^{-1}. All example signals are normalized to the upper limit on the production cross section in each mode of the $\ell\ell\nu\nu$ search using the LHC's run I data [141], meaning that larger signal yields were already excluded previously to the work presented here. The chosen example mass corresponds to the upper bound of the search range using the run I data. It is ob-

Process	**Yields**		
ZZ	106669	±	75
WZ	142480	±	85
Z + jets	145891876	±	44136
Non-res. dilep.	337972	±	568
Others	2789	±	4
Total bkg	146481786	±	44140
ggF signal	55.9	±	0.1
VBF signal	74.0	±	0.2

Table 4.9: Expected background and example signal yields with minimal selection, for a luminosity of 139 fb^{-1}. The uncertainties are statistical only.

vious that with only the minimal selection the signals are dwarfed by the various backgrounds. In fact, the ratio of signal over total background events at this level is of the order of 10^{-7}. Moreover, the expected (maximum) signal yields are smaller than the statistical uncertainty on the total background by four orders of magnitude, and they are of approximately the same size as the uncertainty on e.g. the ZZ background. In this situation it would be impossible to determine whether any deviation between simulation and observed data is due to the presence of a signal or simply a fluctuation of the background. It is therefore clear that the fiducial volume of considered events must be reduced further, with dedicated selection criteria that suppress the backgrounds but ideally do not reject signal events. The following paragraph introduces the ideas behind the variables used for the event selection, while the specific selections are explained in the respective analysis chapters, Chapters 5.1 and 6.1.

Signal kinematics and event selection In the ideal, most probable case the heavy Higgs boson is produced approximately at rest, as the protons are colliding with symmetric momenta. The assumption of a stationary heavy Higgs determines the general signal kinematics of the subsequent decay into $ZZ \to \ell\ell\nu\nu$. Figure 4.21 shows a sketch of the expected signal kinematics in such an ideal event, where no additional radiation is present. Because the heavy Higgs is at rest when it decays, the two Z bosons recoil against each other. The azimuthal opening angle between the transverse momentum of the leptonically decaying Z boson and the missing transverse energy from the Z boson decay to neutrinos, $\Delta\phi(Z, E_T^{\text{miss}})$, is therefore expected to be large. Due to the recoil, both Z boson decays are also boosted, leading to their decay products being collimated. In the case of the $Z \to \nu\nu$ this means that the reconstructed missing transverse energy is expected to be significant, since as a vector quantity it takes into account both the magnitude of the neutrino momenta and the opening angle between them. Moreover, the angular separation $\Delta R_{\ell,\ell}$ between the two leptons is expected to be small for the same reason. Further dedicated criteria can be used to reject specific backgrounds: For example, in the case of a Z+jets background event, there is additional radiation present, but there are no neutrinos involved and therefore there is no real $E_{\text{T}}^{\text{miss}}$ produced. Thus, variables quantifying the quality of the $E_{\text{T}}^{\text{miss}}$ reconstruction, and how likely the $E_{\text{T}}^{\text{miss}}$ originates from invisible particles rather than detector effects, can be used to suppress this background further. One example of such a variable is the angular separation between $E_{\text{T}}^{\text{miss}}$ and any jet with a p_{T} of at least 100 GeV. If this separation is small, it is likely that the reconstructed $E_{\text{T}}^{\text{miss}}$ arises from a mismeasurement of the highly energetic jet. A requirement on this $\min\Delta\phi(\text{jet}_{p_{\text{T}}>100\,\text{GeV}}, E_{\text{T}}^{\text{miss}})$ being larger than a certain threshold is common to both analyses presented here. Variables quantifying the overall $E_{\text{T}}^{\text{miss}}$ reconstruction are also employed. As those are different between the two analyses they are described in detail in the respective Chapters 5.1

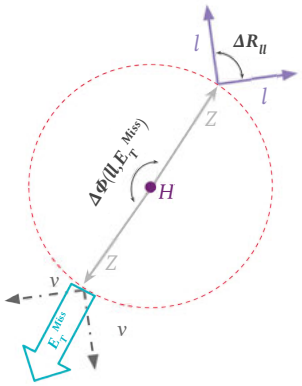

Figure 4.21: Sketch of the expected signal kinematics in the ideal, most likely case.

and 6.1. Last, as previously mentioned, any background involving at least one top quark will lead to the presence of b-tagged jets in the event. A veto on any such b-jet being present in the selected event is therefore applied.

To illustrate the above considerations, Figure 4.22 shows the distributions of the variables explained for the backgrounds and an example heavy Higgs signal with a mass of m_H = 600 GeV and narrow width. This signal mass is chosen as it roughly corresponds to the threshold to the region in which the $\ell\ell\nu\nu$ channel greatly benefits from its larger branching ratio and becomes more sensitive than the $\ell\ell\ell\ell$ analysis as discussed in Chapter 6.5. For signals of higher mass, the differences between the background and signal distribution are expected to be even more pronounced. In Figure 4.22, only the minimal event selection as used above for the yield comparison already is applied. All contributions in Figure 4.22 are described with the full run II MC simulation and scaled to a luminosity of 139 fb^{-1}. The signal shown Figure 4.22 has an arbitrary strength and only serves to provide good visibility.

To summarize, in contrast to the background, signal events exhibit larger missing transverse energy $E_{\mathrm{T}}^{\mathrm{miss}}$, a larger opening angle $\Delta\phi(Z, E_T^{\mathrm{miss}})$ between the Z bosons, a smaller angular separation between the two leptons $\Delta R_{\ell,\ell}$, but a larger angular separation between $E_{\mathrm{T}}^{\mathrm{miss}}$ and any highly energetic jet and no b-tagged jets. These observations form the basis of the event selection.

Event categorization After the event selection, events are divided into separate categories to increase the search sensitivity. The reason is that the purity of the signal - i.e. how much signal there is in contrast to the background - is not uniform throughout phase space and some categories may have significantly better local purity than the average. Analysing data in these categories rather than collectively, exploits this difference in signal purities in the statistical analysis and enhances the sensitivity. If that seems counter-intuitive at first, perhaps it can be better understood with a less abstract example: Suppose one is trying to put together a puzzle with 10 000 pieces that shows a picture of a beautiful sunset over the ocean and looking for a specific puzzle piece to continue the part showing the water. It will be significantly easier and faster to find this missing piece, if one has already sorted all pieces by colour and only needs to search through the blue ones, rather than the whole set. In the $H \to ZZ$ analyses presented here, two categories of events are defined, depending on with which production mode of the heavy Higgs boson the event is compatible: A VBF category is defined based on the presence of two highly energetic and well separated jets, while the ggF category contains all events that fail the VBF categorization. The details of the VBF region definition are given in Chapter 5.1.4.

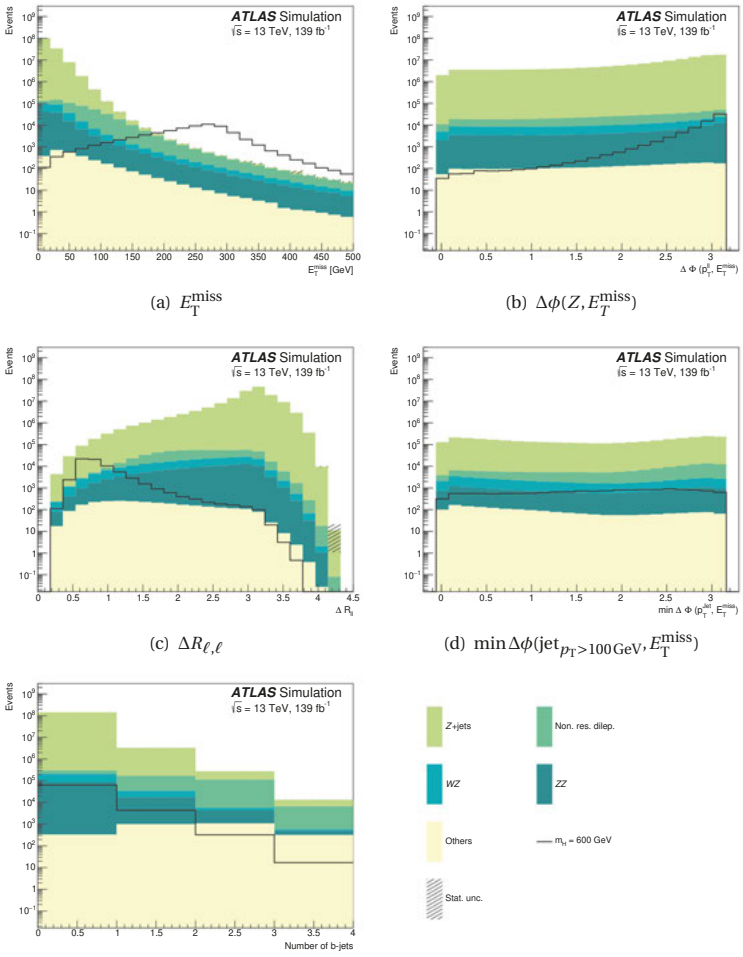

(a) $E_{\mathrm{T}}^{\mathrm{miss}}$ (b) $\Delta\phi(Z, E_T^{\mathrm{miss}})$

(c) $\Delta R_{\ell,\ell}$ (d) $\min\Delta\phi(\mathrm{jet}_{p_{\mathrm{T}}>100\,\mathrm{GeV}}, E_{\mathrm{T}}^{\mathrm{miss}})$

(e) $n_{\text{b-jets}}$

Figure 4.22: Distributions of the kinematic variables for backgrounds and an example heavy Higgs signal with a mass of 600 GeV and negligible width. Using the full run II MC simulation scaled to a luminosity of 139 fb^{-1}. The signal is normalised to an arbitrary cross-section best suited for visibility.

Transverse mass m_{T} as discriminating variable With the signal region defined by the event selection, a quantity to judge whether the observed data in this region agrees with the background only expectation needs to be chosen. In a simple counting experiment, this would be the total event yields of observed data and total expected background in the whole signal region. However, the search sensitivity can be further enhanced by using the full distribution of a discriminating variable. For a resonance search this is typically an invariant mass. The (non-resonant) backgrounds commonly follow an exponential invariant mass distribution, dropping off towards higher values, from which the peaking signal can easily be separated (especially at high masses). Due to the presence of neutrinos in the final state, the full invariant mass cannot be reconstructed in the $\ell\ell\nu\nu$ channel analyses. Instead the so-called *transverse mass* m_{T} is used, which is defined as follows:

$$m_{\mathrm{T}}^2 \equiv \left(\sqrt{m_Z^2 + |\vec{p}_{\mathrm{T}}^{\,\ell\ell}|^2} + \sqrt{m_Z^2 + |\vec{E}_{\mathrm{T}}^{\,\mathrm{miss}}|^2}\right)^2 - \left(\vec{p}_{\mathrm{T}}^{\,\ell\ell} + \vec{E}_{\mathrm{T}}^{\,\mathrm{miss}}\right)^2. \tag{4.14}$$

Here, m_Z describes the mass of the Z boson boson, $\vec{p}_{\mathrm{T}}^{\,\ell\ell}$ the transverse momentum vector of the lepton pair and $\vec{E}_{\mathrm{T}}^{\,\mathrm{miss}}$ the missing transverse energy vector (which is equal to the missing transverse energy momentum vector). In simple terms, this definition of m_{T} follows the energy-momentum relation but using only transverse quantities ($m_{\mathrm{T}}^2 = E_{\mathrm{T}}^2 - p_{\mathrm{T}}^2$) and it imposes a Z boson mass constraint on the lepton pair and the missing transverse energy. In particular this means the two Z boson bosons involved are expected to be on-shell, which is the case for the signal mass range considered (starting from 300 GeV in the $\ell\ell\nu\nu$ channel). As the longitudinal information is missing, the transverse mass gives a broader and less clearly pronounced resonance peak than the full invariant mass, even already at truth level. This is illustrated in Figure 4.23(a), which shows the transverse mass built from the truth matched leptons and truth $E_{\mathrm{T}}^{\mathrm{miss}}$ compared to the true invariant mass m_{ZZ} built from the truth Z bosons for an example large-width Higgs signal. A key characteristic of the transverse mass distribution is that it peaks below the true rest mass of the resonance, and then drops with a sharp edge. Another characteristic that is clearly visible here is the enforced constraint on on-shell Z bosons- the m_{T} distribution takes only values above $2\,m_Z$.

Using the transverse mass, the effect of the intrinsic signal width becomes less apparent. This is shown in Figure 4.23(b), which compares the reconstructed m_{T} distributions for all different width hypotheses considered for the example signal with a mass of 600 GeV.

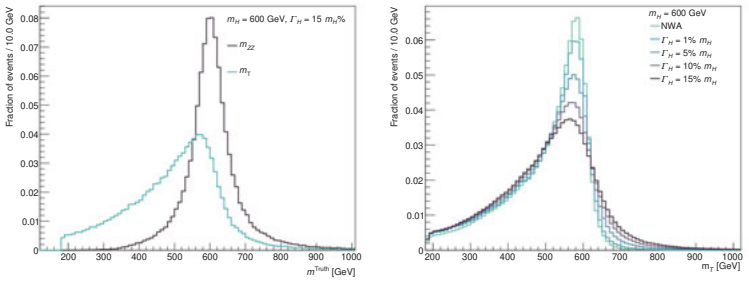

(a) (b)

Figure 4.23: Comparisons of the transverse mass distributions: In (a) m_{T} at truth level is compared to the true m_{ZZ} for a heavy Higgs signal with a mass of 600 GeV and a width of 15% of its mass. In (b) the reconstructed m_{T} is compared between different width hypotheses at the same mass.

The τ question Throughout this thesis, when talking about leptons, only electrons and muons are considered. Events are selected if they contain an ee or $\mu\mu$ pair and the general assumption is that this pair comes directly from a Z boson decay. However, a decay of the Z boson pair to a pair of τ leptons which then subsequently decays into two electrons or muons plus neutrinos leads to the same signature. In this case, several of the event selection criteria may not be fulfilled any longer. For example, the two lepton invariant mass is then not necessarily compatible with the Z boson rest mass. Also the transverse mass definition used, which imposes Z boson mass constraints on the m_{ll} and $E_{\mathrm{T}}^{\mathrm{miss}}$, is then no longer fully valid, as part of the $E_{\mathrm{T}}^{\mathrm{miss}}$ arises from the neutrinos of the τ lepton decays. Nevertheless, it turns out not to be necessary to implement any specific treatment for such dileptonic τ pair events, as their contribution is very small. While in general events involving a $Z \to \tau\tau$ decay constitute one third of the total signal events, only 6% of these decay into an electron or muon pair, due to the involved τ branching ratios. Hence, only around 2% of generated $\ell\ell\nu\nu$ signal events involve $Z \to \tau\tau$ decays. With the event selection applied this fraction is reduced even further: using the selection criteria from the full run II analysis and the example narrow-width heavy Higgs with a mass of 600 GeV, only around 0.02% of events in the signal region contain τ lepton decays. This level of contamination can safely be ignored [6].

Aside from this, signal events with τ leptons decaying hadronically are more common. In the context of the full run II search in the $\ell\ell\ell\ell$ channel, a study into incorporating the $2e2\tau$ and $2\mu2\tau$ channels into the analysis was performed at truth level [140]. Due to the τ decays several complications arise, such as the limited reconstruction efficiency of hadronic τ leptons and the more complicated invariant mass reconstruction due to the neutrinos involved. With realistic assumptions on these issues, the study found that the gain of including the τ channels was not significant enough to justify the effort.

[6] In fact the large-width heavy Higgs MC samples do not include any generated events involving τ leptons.

Background estimation It is crucial that all background processes are described correctly by the inputs to the statistical analysis of the data, because any deviation between background estimate and measured data due to mismodelling could be interpreted as the false presence of a signal. For this reason, wherever possible any relevant background MC simulation should be corrected (or at least cross-checked) with data. Such data-driven background estimates make use of control regions that are orthogonal to the signal region, i.e. regions in which (approximately) no signal is expected. Ideally a region is used that contains mostly events of the given background it serves to estimate, which is then referred to as a region with high *purity*. In the $\ell\ell\nu\nu$ analyses presented here, high purity control regions can be easily defined for the WZ and non-resonant dilepton backgrounds. The former is based on the presence of exactly three leptons, and the latter is based on the presence of an opposite flavour lepton pair. In contrast, the definition of a Z+jets control region is not as straightforward, with the analysis of the 2015 and 2016 data using an *ABCD* approach with four separate control regions. For the analysis of the full 2015-18 dataset a simpler approach using only one one-dimensional sideband region is chosen. Finally, the hardest background to define a control region for is the ZZ background, as its kinematics are very similar to the signal. In the 2015 and 2016 data analysis the ZZ contribution is fully estimated using MC simulation only, while in the 2015-18 data analysis the signal region data itself is used to correct the overall ZZ yield prediction. All these methods are described in detail in the respective analysis chapters, Chapters 5.2 and 6.2.

In summary, the general strategy is as follows:

- A signal region is defined by the kinematic event selection, and divided into the two orthogonal categories for ggF and VBF production.
- For each signal and background process a binned m_{T} template is built in each signal region category.
- Wherever possible, the background templates are corrected with data from an orthogonal control region.
- The m_{T} templates are compared to the observed signal region data, in a (binned) likelihood fit, to quantify whether there is an excess above the background only expectation.
- In the absence of such an excess, upper limits are set on the signal production.

In the following chapter, the statistical methods employed for the fit and interpretation are explained in more detail.

4.5 Statistical analysis concepts

The general principle of the search is to compare the observed data with the expectation. The expectation corresponds to a particular hypothesis or theory. Statistical methods are a tool to quantify the compatibility between data and this expectation. In the statistical interpretation of the heavy Higgs search, a hypothesis test is used to assess whether a heavy Higgs boson is

found. The basis of such a test is the formulation of a *likelihood*, which gives the probability of the observed data, under the assumption that the tested hypothesis is true. The likelihood for the hypothesis that a heavy Higgs boson indeed exists is dependent on the properties of the corresponding signal process such as its mass m_H and its production cross-section σ_H. Here, the statistical analysis is done for fixed values of m_H, scanning through a large range of possible masses, and effectively performing separate hypothesis tests at each point. The production cross-section (times the Higgs' branching ratio to a ZZ pair, as this is unknown) is the *parameter of interest* (POI) in the likelihood model. Maximizing the likelihood therefore yields the production cross-section value for which the observed data is most probable. Uncertainties on the expectation - both on the backgrounds and signal prediction - are incorporated in the likelihood in terms of *nuisance parameters*, and they have a negative impact on the sensitivity of the search. From the maximum likelihood, it can be inferred whether the observed data is compatible with the background only hypothesis, or an excess compatible with a heavy Higgs hypothesis is present. If no such excess is found, exclusion limits can be set on the cross-section σ_H.

The exclusion limit - at 95% confidence level (CL) - is the value of the POI for which the probability of observing the data under the signal hypothesis is equal to 5%. For all values of the POI larger than the exclusion limit this probability is smaller and therefore these values are excluded at the given CL. The exclusion limit is also called the upper limit for this reason. In the heavy Higgs search, an observed upper limit on σ_H of for example 10 fb for a mass of 1 TeV, means that the production of a 1 TeV Higgs boson with a larger cross-section than 10 fb is excluded by the data. But the same heavy Higgs boson with a smaller production cross-section of for example only 1 fb would still be compatible with the data. Thus the limit quantifies how much of the signal (in terms of σ_H) could exist, even when not clearly observing a resonance in the data.

There are situations in which the standard CL limit calculation yields a result that is unphysical, for example a negative upper limit value for a cross-section. This can happen if fewer events than expected from the background only hypothesis are observed. A negative signal yield then compensates such an observed deficit. As a consequence, all positive values of the signal cross-section are excluded by the 95% CL limit. But this is not a useful result, and does not correctly take into account the sensitivity of the search in so far as an underfluctuation of the background is indistinguishable from a negative signal in a region of low sensitivity, i.e. where the signal+background and background only distributions overlap. To avoid this issue, a modified CL approach called the CL_s limit is used for the results presented in here. In the CL_s limit calculation the CL limit is normalized with the *statistical power* of the test, which is the probability to accept the background only hypothesis if it is true. If the statistical power is small - meaning that the data is unlikely under the background only hypothesis - the CL_s limit is larger than the CL limit. In this way, an observed deficit in data is interpreted as a valid downward fluctuation and not as evidence against the signal. Each step of the statistical interpretation, leading to the eventual CL_s limit, is explained in the following.

4.5.1 Likelihood model

The first and main step of the statistical analysis is to build a probability model that predicts the observed event count in every bin measured for all hypotheses considered.

If the observed data is simply the total event yield n in the signal region and the corresponding expected yield according to a hypothesis α is given by μ_α, the likelihood (of the hypothesis α) is written as:

$$L(n|\mu_\alpha) = \text{Poisson}\left(n, \mu_\alpha\right) = \frac{\mu_\alpha^n}{n!} \exp\{-\mu_\alpha\} \tag{4.15}$$

The probability model of Equation 4.15 is known as a Poisson distribution. For a counting experiment that involves signal and background, the total yield μ_α can be written as the prediction of the total yield $\mu = s + b$, so that

$$L(n|s,b) = \text{Poisson}(n, s+b) \tag{4.16}$$

where s gives the expected signal and b the total expected background yield.

In particular, the signal yield itself is given by

$$s = \sigma_H \cdot \text{BR}(H \to ZZ \to \ell\ell\nu\nu) \cdot A_H \cdot \mathscr{L} \tag{4.17}$$

where σ_H gives the production cross-section for the heavy Higgs, $\text{BR}(H \to ZZ \to \ell\ell\nu\nu)$ its branching ratio to $ZZ \to \ell\ell\nu\nu$, A_H the signal acceptance into the defined signal region and $\mathscr{L}$ the integrated luminosity of the dataset. Only the production cross-section times branching ratio to ZZ is unknown - the branching ratio $\text{BR}(H \to ZZ \to \ell\ell\nu\nu)$ factorizes into $\text{BR}(H \to ZZ) \cdot \text{BR}(ZZ \to \ell\ell\nu\nu)$ and the acceptance A_H is determined from the signal MC simulation (as the fraction of generated events that pass into the signal region). This production cross-section is the parameter of interest of the search, and the signal yield can be rewritten as:

$$s = \underbrace{\sigma_H \cdot \text{BR}(H \to ZZ)}_{\text{POI}} \cdot \text{BR}(ZZ \to \ell\ell\nu\nu) \cdot A_H \cdot \mathscr{L} \tag{4.18}$$

If the background expectation b is exactly known, a maximum likelihood estimate based on Equations 4.16 and 4.18 allows for the determination of σ_H. The expected background yield of Equation 4.16 can be calculated as the sum over all background processes:

$$b = \sum_{k \epsilon \text{bkgs}} b_k \tag{4.19}$$

where in the analyses presented here expectation values b_k corrected by data from control regions are used for the WZ, Z+jets and non-resonant dilepton backgrounds. In the analysis of the full 2015-18 dataset, presented in Chapter 6, the total yield of the ZZ background is constrained by the signal region data itself. This is done by introducing another free parameter into

the likelihood, the ZZ normalisation factor μ_{ZZ}. It is used to scale both the $q\bar{q}ZZ$ and $ggZZ$ background, and thus the expected background yields are then given by:

$$b = \mu_{ZZ} \cdot (b_{q\bar{q}ZZ} + b_{ggZZ}) + \sum_{l \in \text{rest bkgs}} b_l \tag{4.20}$$

As mentioned earlier, the observable of the presented analyses is not simply the total number of events in the signal region, but an array of event counts measured in multiple bins of the transverse mass m_{T}, so that the information contained in the m_{T} distribution is effectively incorporated. Use of the m_{T} distribution boosts the sensitivity, as the m_{T} distribution of a high mass Higgs signal is well separated from that of the backgrounds. The likelihood of the full measurement is then simply the product of the likelihoods of each of the bins:

$$L(n|s,b)_{\text{binned}} = \prod_i^{n_{\text{bins}}} L(n_i|s_i,b_i) = \prod_i^{n_{\text{bins}}} \text{Poisson}(n_i, s_i + b_i) \tag{4.21}$$

Here, the signal and background yields per bin, the s_i and b_i, are given by the expressions 4.18 and 4.20 for each bin. While Equation 4.21 gives a general description of the likelihood model employed here, there are a few more particularities to take into account that are specific to the narrow- and large-width analyses. Moreover, uncertainties on the predictions s_i and b_i need to be included as well, as is explained in the following paragraphs.

Narrow-width heavy Higgs analysis In the narrow-width heavy Higgs analysis it is assumed that the heavy Higgs is produced in the ggF and the VBF mode. Both a ggF and VBF Higgs signal must therefore be modelled. However, the ratio of the two production modes is unknown for the heavy BSM Higgs production and the statistical model therefore makes no assumption on the value of this ratio. Instead, both signals are included in the likelihood, each with their own POI. The total signal yield (in a given bin) is then described by:

$$s = s_{\text{ggF}} + s_{\text{VBF}} = \left[\underbrace{\sigma_{\text{ggF}} \cdot \text{BR}(H \to ZZ)}_{\text{POI ggF}} \cdot A_{\text{ggF}} + \underbrace{\sigma_{\text{VBF}} \cdot \text{BR}(H \to ZZ)}_{\text{POI VBF}} \cdot A_{\text{VBF}} \right] \cdot \text{BR}(ZZ \to \ell\ell\nu\nu) \cdot \mathscr{L} \tag{4.22}$$

Both POIs are free parameters in the fit: While one of the POIs is studied - e.g. when extracting the upper limit on the ggF production the POI ggF is of interest - the other one is profiled, but it is constrained to take only positive values.

Large-width heavy Higgs analysis For the large-width heavy Higgs analysis only the ggF production mode is considered. However, here also the interference effects, as described in Chapter 4.3 need to be included. Instead of the interpretation directly in terms of $\sigma_H \cdot \text{BR}(H \to ZZ)$, the POI is expressed as the ratio of the observed over the expected yields: $\mu = \frac{\sigma_{\text{meas.}}}{\sigma_{\text{pred.}}}$.

As explained in Chapter 4.3.3, the magnitude of the interference term scales with $\sqrt{\mu}$ since only the sum of signal and interference can be observed. The signal yield (per bin) is therefore expressed as

$$s = \mu \cdot S(\sigma_{\text{pred.}}) + \sqrt{\mu} \cdot I(\sigma_{\text{pred.}}) \tag{4.23}$$

where S stands for the signal only and I for the interference only yield.

Systematic uncertainties The likelihood of Equation 4.21 is only valid if the expectation predicted by the hypothesis is known exactly. In reality every expectation has associated uncertainties. *Systematic uncertainties* arise from inaccuracies that are inherent to the hypothesis. They can be of experimental origin, i.e. related to the finite precision of the detector modelling such as for example the uncertainty on the muon momentum scale and resolution. Or they can be of theoretical origin, i.e. related to parameters in the model which are not known with full certainty, such as the choice of PDF. The details on which systematic uncertainties are included in the searches here are given in Chapter 5.3 and 6.3. All uncertainties affect the sensitivity of the search negatively. To account for this, systematic uncertainties enter the likelihood model as additional parameters - the so called nuisance parameters (NPs), of which the value is not known exactly. Information on known constraints on the NP values (e.g. "known with 20% uncertainty") is encoded in additional likelihood terms, named *auxiliary measurements*. For example, the likelihood term for the uncertainty on the muon momentum scale and resolution is determined in the muon momentum calibration procedure, as described in Chapter 2.3.2. Here, these likelihoods correspond to unit Gaussians, which constrain each nuisance parameter to its best estimate value with a width of $\pm 1\sigma$. These three values are also referred to as the *nominal* expectation and its *up* and *down* variation. Denoting the set of nuisance parameters as $\vec{\theta}$, with nominal values $\vec{\theta_0}$, the full likelihood model is then written as:

$$L(n|s,b,\vec{\theta})_{\text{binned}} = L(n|s,b)_{\text{binned}} \cdot L(\vec{\theta}|\vec{\theta_0}) = \prod_{i}^{n_{\text{bins}}} \text{Poisson}(n_i, s_i(\vec{\theta}) + b_i) \cdot \prod_{j}^{n_{\text{systematics}}} G(\theta_j|\theta_0, 1) \tag{4.24}$$

In the formalism of Equation 4.24 the magnitude of the effect of each uncertainty is encoded in $s_i(\vec{\theta})$ and the uncertainty on each θ encoded in the auxiliary measurement is always 1. Furthermore it is assumed that the auxiliary measurements describing the NP likelihoods are independent of each other and the main measurement. The ensemble of predictions $\vec{s}_i(\vec{\theta})$ may transform in a correlated and non-trivial way as a function of θ. These ensemble transformations are technically realized with the moment morphing technique [142].

There is also a statistical uncertainty on every predicted event yield due to the finite size of the generated MC samples. This MC statistical uncertainty is neglected in the analyses presented here, as it is much smaller than the statistical uncertainty on the observed data, and therefore has only minor impact.

4.5.2 CL_s limit setting

The likelihood model described above can now be used to infer information about the hypothesis from the data. Here, exclusion limits are set on the heavy Higgs' production cross-section,

characterizing how much signal at most can still be compatible with what is observed. But the first step is to decide whether the data is compatible with the background only expectation, or if there is a (signal induced) excess.

Test statistic and $p-$value To test a hypothesis, for example here to check if the background only hypothesis can be rejected in favour of an observed signal excess, a so-called *test statistic* is defined. The purpose of the test statistic is to monotonically order all possible observations by signal strength, ranking them from more background-like to more signal+background-like. According to the Neyman-Pearson lemma [143] such an ordering can be performed without loss of information by using the likelihood ratio

$$q_\alpha = -2\ln\left[\frac{L(\alpha)}{L(\hat{\alpha})}\right] \tag{4.25}$$

for the POI α and its maximum likelihood estimator (MLE) $\hat{\alpha}$. The likelihood ratio allows to evaluate how compatible the tested hypothesis (in the denominator) is with the alternative hypothesis (in the numerator). It summarizes the entire measurement in a single number q_α. The likelihood ratio in Equation 4.25 does not account for the presence of NPs. They can be accounted for by maximizing the likelihoods in both numerator and denominator, i.e.

$$q_\alpha = -2\ln\left[\frac{L(\alpha,\hat{\hat{\vec{\theta}}}(\alpha))}{L(\hat{\alpha},\hat{\vec{\theta}})}\right] \tag{4.26}$$

where $\hat{\hat{\vec{\theta}}}(\alpha)$ is the MLE of $\vec{\theta}$ for a given value of α and $\hat{\vec{\theta}}$ the MLE of $\vec{\theta}$ for $\hat{\alpha}$. In contrast to the definition in Equation 4.25 it cannot be proven that the test statistic following Equation 4.26 has maximal power. But in practice its power is close to maximal and it presents no practical issues other than increased computation time due to having to maximize the likelihoods with respect to the NPs.

If the distribution of q_α is known for a given hypothesis, the probability for the observed total yield (or higher) under the tested hypothesis can be calculated, by means of the the *p-value*

$$p_\alpha = \int_{q_\alpha^{\text{obs}}}^{\infty} f(q_\alpha|\alpha)\,dq_\alpha \tag{4.27}$$

where q_α^{obs} gives the observed value of the test statistic following Equation 4.26 and $f(q_\alpha|\alpha)$ is its probability distribution function (p.d.f.) under the hypothesis α. The $p-$value can be calculated for any hypothesis α. To confirm an excess the $p-$value of the background only hypothesis ($\alpha = 0$) needs to be sufficiently small. If no such excess is present and the background only hypothesis cannot be rejected, instead the limit value of α is derived: it is the value of α for which p_α (q_α^{obs}) is equal to 5% and it is determined by iteratively scanning through the range of possible values of α. To do so the p.d.f. $f(q_\alpha|\alpha)$ needs to be known. One way to determine $f(q_\alpha|\alpha)$ is to generate a large number of toy experiments for each hypothesis α. This makes the procedure very computationally expensive. Fortunately the calculation procedure can be substantially simplified by relying on Wilk's theorem [144]: given sufficient statistics the distribution $f(q_\alpha|\alpha)$ is

known asymptotically (as a log χ^2 distribution). The results presented in this thesis assume that Wilk's theorem holds and follow the asymptotic calculation[7].

CL_s exclusion limits In the limit setting the signal+background hypothesis is tested and the test statistic is specifically defined as one-sided, following:

$$q_\alpha = \begin{cases} -2\ln\left[\dfrac{L(\alpha,\hat{\hat{\theta}}(\alpha))}{L(\hat{\alpha},\hat{\hat{\theta}})}\right], & \text{if } 0 \le \hat{\alpha} \le \alpha \\ 0, & \text{if } \hat{\alpha} > \alpha \end{cases} \tag{4.28}$$

Setting q_α to 0 for values $> \hat{\alpha}$ ensures that all observations with a signal yield greater than that of the tested hypothesis are interpreted as maximally consistent with the hypotheses. The (observed) CL limit is calculated by using the asymptotic $f(q_\alpha|\alpha)$ with this definition of q_α to find the value of α for which the p-value equals 5%. However, as explained earlier, this approach can lead to the exclusion of regions of low sensitivity if a deficit is observed, which is undesirable. The solution used here is to follow the CL_s method [145] in which the definition of the p-value is modified as

$$p'_\alpha = \frac{p_\alpha}{1-p_0} \tag{4.29}$$

where p_0 is the $p-$value of the background only hypothesis. 1 - p_0 is the power of the test, and is small in regions of low sensitivity. The CL_s method leads to more conservative limits than the standard CL approach. With the modified $p-$value $p'_\alpha(q_\alpha^{\text{obs}})$ the observed limits are obtained. It is also useful to determine the expected results, characterizing the sensitivity of the search. This is done by injecting a specific hypothesis β (into the "data"), e.g. the background only hypothesis by setting α =0 and then calculating the result of the test for all other hypotheses (e.g. α = 0.1, ..., 1). The resulting ensemble of test outcomes (i.e. upper limit values) describes the expected sensitivity - an expected median limit with its uncertainty band in terms of standard deviation σ. For this calculation therefore the p.d.f. $f(q_\alpha|\beta)_{\alpha\neq\beta}$ needs to be known. In the asymptotic limit, $f(q_\alpha|\beta)_{\alpha\neq\beta}$ is described by a non-central χ^2 distribution with non-centrality parameter Λ_{NC}. This free parameter Λ_{NC} can be calculated using the so-called Asimov dataset as $\Lambda_{\text{NC}} = \sqrt{q_\alpha^{\text{Asimov}}}$ [146]. The Asimov dataset represents the median expected measurement with no fluctuations under the background only hypothesis. With Λ_{NC} known, $f(q_\alpha|\beta)_{\alpha\neq\beta}$ is fully defined and the expected limits can be calculated analytically. The full set of results of the search is therefore an observed and expected limit with uncertainty interval for each tested heavy Higgs mass m_H. In case the observed and median expected limit deviate from each other, the expected uncertainties can be used to quantify the disagreement: 68% of repeated measurements would have an upper limit outcome within the $\pm1\sigma$ range, while 95% of outcomes would be found within $\pm2\sigma$. Some deviations that fall within this range are expected even when the tested hypothesis is true, especially when covering a large range of possible signal masses.

[7] A cross-check comparing the asymptotic- to the toy-based limit was performed for a few signal mass points [9]. The two are compatible within a few %.

5 Analysis of the 2015 and 2016 data

This chapter describes the specifics of the analysis performed on a subset of the full data taken during the LHC's run II. The dataset considered corresponds to $\mathscr{L} = 36.1\ \text{fb}^{-1}$ and was recorded with the ATLAS detector in 2015 and 2016. An analysis in the $H \to ZZ \to \ell\ell\nu\nu$ channel was performed, following the basic principles explained in the previous chapter. Its results were combined with the results of the $H \to ZZ \to \ell\ell\ell\ell$ final state analysis and published in [5]. Here, only the $H \to ZZ \to \ell\ell\nu\nu$ analysis of the 2015+16 dataset is presented.

5.1 Event selection

5.1.1 Object selection

The first step of the analysis is to define and select the objects - the reconstructed particles. How exactly each object is reconstructed with the ATLAS detector is described in detail in Chapter 2.3. For the $\ell\ell\nu\nu$ analysis, the most important physics objects are charged, light leptons (electrons and muons), jets and the missing transverse energy $E_{\text{T}}^{\text{miss}}$.

	Selection criterion	
	Signal (veto) electrons	**Signal (veto) muons**
$\lvert\eta\rvert$ acceptance	$\lvert\eta\rvert < 2.47$	$\lvert\eta\rvert < 2.5$
Cosmic cuts	d_0 significance < 5	d_0 significance < 3
	$\lvert z_0 \cdot \sin(\theta)\rvert < 0.5\,\text{mm}$	$\lvert z_0 \cdot \sin(\theta)\rvert < 0.5\,\text{mm}$
Identification	Likelihood ID	Combined muons
	Medium (loose) working point	Medium (loose) working point
Isolation	Loose working point	Loose working point
p_{T} threshold	$p_{\text{T}} > 20(7)\,\text{GeV}$	$p_{\text{T}} > 20(7)\,\text{GeV}$

Table 5.1: Object selection criteria applied to electrons and muons.

Lepton selection Table 5.1 gives an overview of the selections applied to electrons and muons. First they are required to be within the $|\eta|$ region covered by the detector: for electrons this means $|\eta| < 2.47$ and for muons it is $|\eta| < 2.5$. Next, to reject leptons originating from cosmic backgrounds, requirements are made on the impact parameters with respect to the primary vertex of the leptons in the $x-y$- and z directions, defined as d_0 and z_0. In this analysis, only reconstructed muons of type *combined* are used, where the muon was reconstructed using a combined

refit of its ID and MS tracks (cf. Chapter 2.3.2). Electrons are reconstructed from a track in the ID as well as energy deposits in the calorimeter, using the sliding window approach described in Chapter 2.3.1.

There are two types of leptons considered in the analysis: signal leptons that come from the leptonic Z boson candidate, and veto leptons used only to exclude events with more than two leptons. The object selection criteria applied to the first are more stringent than those applied to the latter. When selecting the signal pair it is more important to ensure that the leptons are measured well and have a high purity. For the veto on additional leptons the selection criteria are loosened a bit, to maximize the efficiency of rejecting events with more than two leptons. Hence, for veto leptons a p_{T} threshold of only 7 GeV is imposed, while for signal leptons a p_{T} of at least 20 GeV is required. Veto leptons must fulfil the "Loose" working point of the identification algorithm, whereas for signal leptons the more stringent "Medium" working point is used. Last, both signal and veto leptons need to fulfil the "Loose" isolation criteria, to reduce backgrounds such as leptons from final state radiation or particles from heavy flavour quark decays and pile-up interactions.

	Selection criterion
$\|\eta\|$ acceptance	$\|\eta\| < 4.5$
p_{T} threshold	$p_{\mathrm{T}} > 20\,\mathrm{GeV}$
Identification	AntiKT4EMTopo jets
Pile-up removal	JVT < 0.59, if $p_{\mathrm{T}} > 60\,\mathrm{GeV}$, $\|\eta\| < 2.4$
B-tagging	MV2c10 at 85% efficiency

Table 5.2: Object selection criteria applied to jets.

Jet selection Jets are reconstructed using the anti$-k_t$ algorithm as described in Chapter 2.3.3 and required to be within $|\eta| < 4.5$ and have a transverse momentum of at least $p_{\mathrm{T}} > 20\,\mathrm{GeV}$. For the analysis of jets the EMTopo energies measured in the calorimeter are used. To suppress contributions from pile-up - that would spoil the $E_{\mathrm{T}}^{\mathrm{miss}}$ reconstruction - jets in the kinematic range $|\eta| < 2.4$ and $p_{\mathrm{T}} < 60\,\mathrm{GeV}$ are required to have a JVT discriminant of < 0.59, corresponding to an average efficiency of 92% and a pile-up fake rate of only 2%. Finally, jets originating from b-quarks are identified by applying the b-tag algorithm MV2c10 at a working point of 85% efficiency. The selection criteria applied to jets are summarized in Table 5.2.

$E_{\mathrm{T}}^{\mathrm{miss}}$ reconstruction The missing transverse energy, $E_{\mathrm{T}}^{\mathrm{miss}}$, is built from all the calibrated and selected physics objects in the event. Details on the reconstruction algorithms are discussed in Chapter 2.3.5. In this analysis, the soft term of $E_{\mathrm{T}}^{\mathrm{miss}}$ is based on tracks, and EMTopo jets are used. Overlaps are corrected for by e.g. removing the energies measured in calorimeter cells crossed by a muon.

To avoid double-counting of reconstructed objects, a dedicated overlap removal is performed. This procedure is detailed in Chapter 2.3.4.

5.1.2 Event preselection

As a first step, preselection cuts are applied to MC simulation and data events. These cuts are different from the main event selection in so far as their main purpose isn't to target a particular (signal) signature but they are more generic cuts to filter out events that are likely not well reconstructed.

Only data events from the *good runs list* are considered. This list includes only runs during which all (needed) sub-detectors were recording and are therefore *good* for physics analysis. Further data quality requirements ensure that SCT hits are associated to tracks, and that noise events (in the calorimeter) are rejected.

To select an event event for further analysis, a single lepton (electron or muon) should have triggered the event. For each data taking period, the lowest unprescaled triggers are chosen. An *or* combination of triggers with a low p_{T} threshold but somewhat strict identification or isolation criteria is used together with higher p_{T} threshold trigger but looser (or no) further criteria for both electrons and muons. The exact threshold depends on the data taking period, and a detailed table of the trigger menus is shown in Appendix A. Depending on the period, the lowest p_{T} for electrons is either 24 GeV or 26 GeV and triggered muons have at least a p_{T} of 20 GeV, 24 GeV or 26 GeV. The combination of these triggers reaches an efficiency of 99%.

All events are required to have a primary vertex with at least two associated tracks, indicating a hard scattering reaction. Additionally, a jet cleaning is applied: Using a dedicated set of criteria jets that are likely to not originate from the pp-collision but e.g. from cosmic backgrounds or noise in the detector are tagged as bad quality. If an event contains one or more bad quality jets it is discarded as the $E_{\mathrm{T}}^{\mathrm{miss}}$ reconstruction would be spoiled by such a jet.

5.1.3 Kinematic event selection

The next - and crucial - part of the analysis is a dedicated event selection based on kinematic variables, that serves to select the signal and to suppress backgrounds. Each selection criterion is motivated by the expected topology of signal events, that distinguishes it from the backgrounds. An overview of the selection criteria defining the inclusive signal region - meaning including both ggF- and VBF-like events - and the main background contributions they suppress is given in Table 5.3. More details on the physics behind each cut are explained in Chapter 4.4.

Selection criterion	Main backgrounds suppressed
SFOS pair with $p_{\mathrm{T}} > 30, 20\,\mathrm{GeV}$, Medium ID	-
Veto on 3rd lepton with $p_{\mathrm{T}} > 7\,\mathrm{GeV}$, Loose ID	WZ
$76 < m_{ll} < 106\,\mathrm{GeV}$	WW, top, $Z \to \tau\tau$
$E_{\mathrm{T}}^{\mathrm{miss}} > 120\,\mathrm{GeV}$	Z + jets
$\Delta R_{\ell,\ell} < 1.8$	Z + jets, WW, top, $Z \to \tau\tau$
$\Delta\phi(Z, E_T^{\mathrm{miss}}) > 2.7$	Z + jets, WW, top, $Z \to \tau\tau$
Fractional $p_{\mathrm{T}} < 0.2$	Z + jets
$\min \Delta\phi(\mathrm{jet}_{p_{\mathrm{T}}>100\,\mathrm{GeV}}, E_{\mathrm{T}}^{\mathrm{miss}}) > 0.4$	Z + jets
$E_{\mathrm{T}}^{\mathrm{miss}} / H_{\mathrm{T}} > 0.4$	Z + jets
b-jet veto (at 85% WP)	top

Table 5.3: Summary of kinematic event selection criteria as applied in the analysis of the 2015 and 2016 data to select both ggF and VBF production events.

Briefly summarizing, a typical signal event is expected to contain large missing transverse energy, $E_{\mathrm{T}}^{\mathrm{miss}}$, which is in balance with the leptonically decaying Z boson, and therefore with the same flavour, opposite sign (SFOS) lepton pair, and this topology motivates the following selections:

- Exactly one SFOS lepton pair is required and events with any additional leptons are rejected. Contributions from fully leptonic WZ decays resulting in (at least) three leptons are suppressed by this requirement.
- The invariant mass of the lepton pair is required to be compatible with the Z boson mass, rejecting backgrounds without a Z boson but also $Z \to \tau\tau$ events, where the reconstructed Z boson mass is below the pole mass due to the neutrinos involved in the τ decays.
- Large $E_{\mathrm{T}}^{\mathrm{miss}}$ is expected in the event, as the neutrinos are collimated. A cut on $E_{\mathrm{T}}^{\mathrm{miss}} > 120\,\mathrm{GeV}$ is used. This means that the $\ell\ell\nu\nu$ analysis is only sensitive to heavy Higgs bosons with masses above 300 GeV. The main background rejected by the cut on $E_{\mathrm{T}}^{\mathrm{miss}}$ is the Z + jets process, which is overwhelmingly large but usually does not contain significant amount of $E_{\mathrm{T}}^{\mathrm{miss}}$.
- Next, the angle between the leptons, $\Delta R_{\ell,\ell}$, is required to be smaller than 1.8 because in the heavy Higgs decay the $Z \to \ell\ell$ is boosted and recoils against the $Z \to \nu\nu$. For the same reason, the azimuthal angle between the $Z \to \ell\ell$ and $E_{\mathrm{T}}^{\mathrm{miss}}$, $\Delta\phi(Z, E_T^{\mathrm{miss}})$ is expected to be larger than 2.7. These cuts suppress background processes in which either the two leptons are not originating from a single decay such as WW, top or $Z \to \tau\tau$ events or where the $Z \to \ell\ell$ decay is not boosted such as Z + jets.
- There can be Z + jets events in which the Z boson recoils against a high-energetic jet that is not reconstructed (correctly). Such a topology would lead to a Z + jets event passing both

the kinematic cuts on ΔR and $\Delta\Phi$, as well as the large $E_{\mathrm{T}}^{\mathrm{miss}}$ requirement. Three further dedicated selection criteria serve to suppress this type of background: First, events are rejected if they contain a jet with a p_{T} of at least 100 GeV and the minimum azimuthal angle between such a jet and the $E_{\mathrm{T}}^{\mathrm{miss}}$ direction is less than 0.4 rad. Next, two selection cuts follow that are only applied to the 2015 and 2016 data: on the fractional p_{T} and the $E_{\mathrm{T}}^{\mathrm{miss}}/H_{\mathrm{T}}$ variables, as described in more detail in the following.

- Last, a veto on events which contain a b-tagged jet is implemented in order to eliminate contributions from processes involving top quarks, such as $t\bar{t}$ or $t\bar{t}V$ events.

The fractional p_{T} variable is defined as

$$\text{fractional}\, p_{\mathrm{T}} = \frac{|E_{\mathrm{T}}^{\mathrm{miss}}(+\text{jets}) - p_{\mathrm{T}}^{\ell\ell}|}{p_{\mathrm{T}}^{\ell\ell}} \tag{5.1}$$

where

$$E_{\mathrm{T}}^{\mathrm{miss}}(+\text{jets}) = \sqrt{\left(E_{\mathrm{x}}^{\mathrm{miss}} + \sum_{i}^{n_{\mathrm{jets}}} p_x^i\right)^2 + \left(E_{\mathrm{y}}^{\mathrm{miss}} + \sum_{i}^{n_{\mathrm{jets}}} p_y^i\right)^2} \tag{5.2}$$

, and $p_{\mathrm{T}}^{\ell\ell}$ denotes the transverse momentum of the lepton pair. It is the difference between the p_{T} of the lepton pair and the vectorial sum of $E_{\mathrm{T}}^{\mathrm{miss}}$ and all jet p_{T} in the event, normalised to $p_{\mathrm{T}}^{\ell\ell}$. In the absence of additional radiation in the event, the $p_{\mathrm{T}}^{\ell\ell}$ and $E_{\mathrm{T}}^{\mathrm{miss}}$ will be in balance, so that the fractional p_{T} will take a value ≈ 0. If additional radiation is present in the event, there are two possible cases, as the simplified examples in Figure 5.1 illustrate [1]: Figure 5.1(a) shows a signal-like event with real $E_{\mathrm{T}}^{\mathrm{miss}}$ and two additional jets. Assuming that every object is perfectly measured, the heavy Higgs recoils against the two jets, so that the sum of $E_{\mathrm{T}}^{\mathrm{miss}}$ and $p_{\mathrm{T}}^{\ell\ell}$ is in balance with the sum of the jet p_{T}. The fractional p_{T} of such an event takes a small value ≈ 0. uerde Figure 5.1(b) shows an event which has no real $E_{\mathrm{T}}^{\mathrm{miss}}$, but only a leptonic Z candidate recoiling against two jets. If one of those jets is not within the detector acceptance and the other jet is mismeasured, the reconstructed event contains fake $E_{\mathrm{T}}^{\mathrm{miss}}$ as well as an incorrect jet p_{T}. The $p_{\mathrm{T}}^{\ell\ell}$ is no longer in balance with the sum of $E_{\mathrm{T}}^{\mathrm{miss}}$ and the jet p_{T}, and therefore the fractional p_{T} for such an event is larger.

Thus, the fractional p_{T} variable indicates whether an event is in balance or not, and an unbalanced event is associated with fake $E_{\mathrm{T}}^{\mathrm{miss}}$. This can be observed in the distributions for signal and backgrounds before applying the fractional p_{T} cut, shown in Figure 5.2(a). Hence, events considered in this analysis are required to have a fractional $p_{\mathrm{T}} < 0.2$.

Much along the same line, the ratio of $E_{\mathrm{T}}^{\mathrm{miss}}$ over the visible scalar sum of transverse energy in the event, H_{T}, can also be used to quantify the quality of the $E_{\mathrm{T}}^{\mathrm{miss}}$ reconstruction. If the event is in balance and contains well reconstructed $E_{\mathrm{T}}^{\mathrm{miss}}$, this ratio should be ≈ 1, while if there are problems with the $E_{\mathrm{T}}^{\mathrm{miss}}$ reconstruction it will take a smaller value, near 0. Figure 5.2(b) shows the respective distributions confirming that for the signal the ratio is more likely to be near 1,

[1] It should be noted that these examples are simplified and only serve to visualize the meaning of the variable.

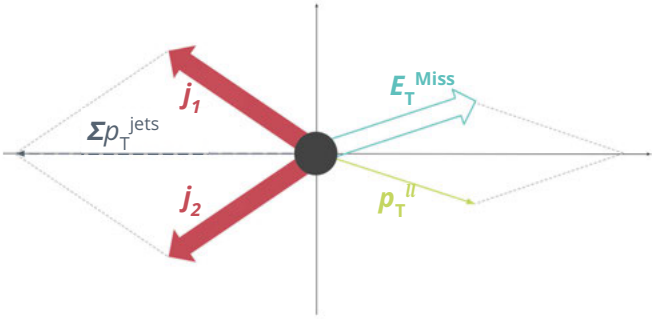

(a) Balanced event with real E_T^{miss}

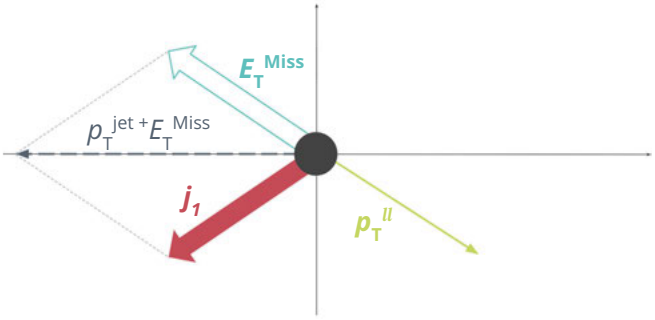

(b) Event where the p_T is not balanced due to fake E_T^{miss}

Figure 5.1: Simplified example events to illustrate the use of the frational p_T variable, defined as the ratio $\frac{|E_T^{miss}+\sum p_T^{jets}-p_T^{\ell\ell}|}{p_T^{\ell\ell}}$.

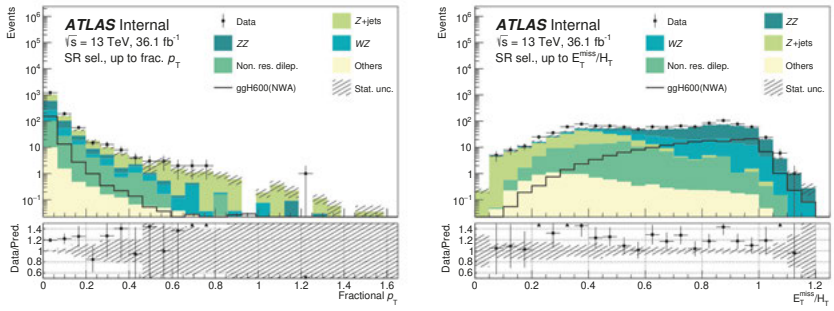

(a) Fractional p_{T} distributions

(b) $E_{\mathrm{T}}^{\mathrm{miss}}$ over H_{T} distributions

Figure 5.2: Distributions of (a) the fractional p_{T} and (b) the $E_{\mathrm{T}}^{\mathrm{miss}}$ over H_{T} cut variable, for the 2015 and 2016 data. In each case all event selection cuts prior to the shown variable are applied. Only the statistical uncertainty is shown.

while events with fake $E_{\mathrm{T}}^{\mathrm{miss}}$ such as from the Z+jets backgrounds are found at lower values. Hence, it is required for $E_{\mathrm{T}}^{\mathrm{miss}}$ over H_{T} to be above 0.4 .

To quantify the impact of the cuts, Table 5.4 shows an overview of the relative acceptances of each cut for an example signal and two important background processes - ZZ and Z+jets. The signal is a heavy Higgs boson produced in ggF with a narrow width and a mass of $m_H = 600\,\mathrm{GeV}$. The example ZZ sample describes only the $q\bar{q} \to ZZ \to llvv$ process, while for the Z+jets process all samples are included (cf. Chapter 4.2). The relative acceptance is calculated from the number of events passing the cut in question, divided by the number of events passing the previous one. The total acceptance of the kinematic selection is calculated with respect to the events passing the preselection, including the cut on m_{ll}.

It is evident that the kinematic event selection leads to a strong reduction of backgrounds while retaining a high signal efficiency. The backgrounds are already greatly suppressed by requiring large missing transverse energy. Whereas the Z+jets background has low acceptances for all cuts, the ZZ background is more difficult to reduce, as its kinematics are similar to the signal.

Criterion	**Rel. cut acceptance in %**		
	$ggH600$ signal	ZZ background	Z + jets background
$76 < m_{ll} < 106\,\text{GeV}$	100.00	100.00	100.00
$E_{\text{T}}^{\text{miss}} > 120\,\text{GeV}$	93.25	8.60	0.02
$\Delta R_{\ell,\ell} < 1.8$	98.89	74.61	17.33
$\Delta\phi(Z, E_T^{\text{miss}}) > 2.7$	84.75	80.50	50.78
Fractional $p_{\text{T}} < 0.2$	98.90	98.39	94.70
$\min\Delta\phi(\text{jet}_{p_{\text{T}}>100\,\text{GeV}}, E_{\text{T}}^{\text{miss}}) > 0.4$	97.80	98.51	34.21
$E_{\text{T}}^{\text{miss}}/H_{\text{T}} > 0.4$	96.87	97.82	42.41
B-jet veto	90.87	93.42	34.11
Total	66.54	4.58	7.11×10^{-5}

Table 5.4: Relative acceptances of selection cuts for a NWA Higgs signal with mass of 600 GeV produced in ggF, and the ZZ and Z + jets backgrounds. The total acceptance of the kinematic selection is calculated with respect to the events passing the preselection, including the cut on m_{ll}.

5.1.4 Event categorization

As described before in Chapter 4.4, the selected events are further divided into two categories to increase the sensitivity: A dedicated set of selection criteria is used to isolate events that enhance the VBF production mode of the heavy Higgs. All events in the signal region that do not fulfil the VBF criteria are sorted into the ggF category. The two categories are therefore orthogonal to each other.

Table 5.5 shows the definition of the VBF category. First, at least two jets in the event are required and the two jets with highest p_{T} should have a transverse momentum p_{T} > 30 GeV. As the two jets in the VBF production process are expected to be highly energetic and well separated, the following cuts on the properties of the two jets are made: their invariant mass m_{jj} is required to be larger than 550 GeV and their pseudo-rapidity difference, $|\Delta\eta_{jj}|$, should be larger than 4.4.

The cut values shown in Table 5.5 were obtained from an optimization procedure that took into account the signal significance while keeping a reasonable signal acceptance across the whole mass range.

Selection criterion	**> Value**
n_{jets}	> 1
$p_{\text{T, jet}}^{\text{leading}}$ $p_{\text{T, jet}}^{\text{subleading}}$	> 30 GeV
m_{jj}	> 550 GeV
$\lvert\Delta\eta_{jj}\rvert$	> 4.4

Table 5.5: Definition of the VBF category.

5.2 Background estimates

The event selection strategy described in the previous section aims to reduce the amount of events from background processes, but nonetheless some background contribution in the signal region remains. Figure 5.3 shows an overview of its relative composition.

Unsurprisingly, almost two thirds of the total background comes from continuum ZZ production, which is the only irreducible background to the search. In the 2015+16 data analysis presented in this chapter, the ZZ background is estimated from MC simulation only.

The second largest background contribution of around 30% consists of WZ events. While this process is actually more abundant than the ZZ production, its relevant final state contains at least three leptons and it can therefore be reduced very efficiently by the veto on an additional lepton. Moreover, it can be measured from data by using a control region with three leptons.

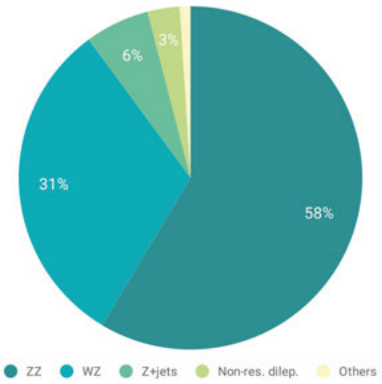

Figure 5.3: Background composition in the $H \to ZZ \to \ell\ell\nu\nu$ analysis signal region, in the analysis of the 2015 and 2016 data.

Although it contributes as little as 6% to the total background events, the Z + jets background can be problematic as it contains fake $E_{\mathrm{T}}^{\mathrm{miss}}$, which is difficult to model. So despite its small size, it is important to measure the Z + jets background from data. Here, this is done using an *ABCD* method with boolean variables.

Furthermore, a minor contribution comes from non-resonant dilepton processes, such as WW, Wt, $t\bar{t}$ or $Z \to \tau\tau$. Since in these processes the lepton pair does not originate from a single resonance decay, it can be estimated using data where the two leptons are of different flavour - the so-called $e\mu$ control region.

Last, *other processes* constitute as little as 2% of the total background, consisting mostly of $t\bar{t}V$, VVV and W + jets events.

The following chapters describe the various background estimation methods in detail.

5.2.1 ZZ modelling

As the Standard Model ZZ production exhibits similar event kinematics as the signal, it is not easily possible to define a control region for it without significant signal contamination. Moreover, in 2017, available measurements of its cross-section were affected by large experimental

uncertainties. Since the uncertainties on the theory prediction were smaller, the ZZ background is therefore taken directly from MC simulation in the analysis of the 2015+16 data presented here. In particular, the "POWHEG " set of ZZ samples described in Chapter 4.2.1 is used and state-of-the-art higher corrections order are added on top, as described in the following.

Higher order QCD corrections to $q\bar{q}ZZ$ Theory calculations [147] show that the inclusive cross section of the $q\bar{q}ZZ$ production at next-to-next-to-leading-order (NNLO) in QCD is significantly enhanced with respect to the calculation at NLO. These higher order QCD corrections are thus not negligible and need to be applied to the NLO $q\bar{q}ZZ$ MC samples used here. This is done by determining a corresponding *k-factor*, defined as the ratio of NNLO and NLO calculation. The k-factor is extracted using the calculated matrix element as a function of the invariant mass of the ZZ system, m_{ZZ}. Pre-selected events are used in the calculation, to avoid restricting the phase-space too much. Figure 5.4(a) shows the values of the derived k-factor versus the invariant ZZ mass, m_{ZZ}. In order to obtain the corrected $q\bar{q}ZZ$ distributions, each event is weighted with the k-factor corresponding to its m_{ZZ}. This results in a total increase of the $q\bar{q}ZZ$ yield in the signal region by around 10%.

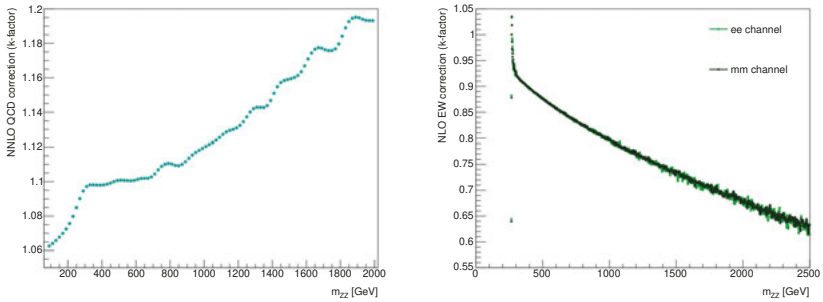

(a) NNLO QCD corrections (b) NLO EW corrections

Figure 5.4: k-factors applied to $q\bar{q}ZZ$ events: (a) accounting for NNLO QCD and (b) accounting for NLO EW corrections. Both as function of m_{ZZ} and as used in the 2015+16 data analysis.

Higher order EW corrections to $q\bar{q}ZZ$ Similarly, higher order corrections for electroweak effects are considered, to include electroweak $q\bar{q}ZZ$ processes at NLO. Several theory calculations e.g. [148] show that the effect of electroweak corrections is a reduction of the inclusive cross-section by several percent. Hence, the effect of EW corrections is opposite to that of QCD corrections and for a full, accurate description of the $q\bar{q}ZZ$ background both should be considered. Again, a k-factor is calculated as a function of m_{ZZ}. This k-factor is shown in Figure 5.4(b), separately for the $eev\nu$ and $\mu\mu\nu\nu$ channel, though the two are very similar.

Higher order QCD corrections to $ggZZ$

The $ggZZ$ samples of the "POWHEG " set used here are generated at leading order in QCD, although theory calculations of the $ggZZ$ cross-section under various assumptions at higher orders are available [134, 149, 150]. In accordance with what these calculations find, a constant k-factor of 1.7 ± 1.0 is applied to all generated $ggZZ$ events.

5.2.2 WZ estimate from 3ℓ control region

The WZ process is the second leading background in this analysis. As it mostly consists of $WZ \to \ell\nu\ell^+\ell^-$ events, it can be estimated from data events containing exactly three leptons in the final state. This 3ℓ control region is used to correct the normalisation of the WZ MC expectation in the signal region. The m_{T} distribution of the WZ background is taken from simulation directly.

Selection criterion	Main non-WZ contributions reduced
SFOS lepton pair with $p_{\mathrm{T}} > 30, 20\,\mathrm{GeV}$	-
Third lepton with $p_{\mathrm{T}} > 20\,\mathrm{GeV}$	-
$76 < m_{ll} < 106\,\mathrm{GeV}$	-
$m_{\mathrm{T}}(W) > 60\,\mathrm{GeV}$	Z + jets
b-jet veto (at 85% WP)	top

Table 5.6: Definition of the 3ℓ control region used to estimate the WZ background in the 2015 and 2016 data analysis.

An overview of the exact selection criteria defining the 3ℓ region is given in Table 5.6. First, a SFOS lepton pair is required with the same quality criteria as in the signal region. Second, exactly one additional electron or muon that fulfils the lepton reconstruction quality requirements and has have a transverse momentum greater than 20 GeV must be present in the event. To select events containing a Z boson decay, the SFOS lepton pair needs to have an invariant mass close to m_Z. Furthermore, events likely to contain a W boson are selected using the transverse mass $m_{\mathrm{T}}(W)$ of the third lepton and $E_{\mathrm{T}}^{\mathrm{miss}}$. It is defined as

$$m_{\mathrm{T}}(W) = \sqrt{2\, p_{\mathrm{T}}^{\ell_3}\, E_{\mathrm{T}}^{\mathrm{miss}} \cdot \left(1 - \phi(\ell_3, E_T^{\mathrm{miss}})\right)} \tag{5.3}$$

where $p_{\mathrm{T}}^{\ell_3}$ is the transverse momentum of the third lepton and $\phi(\ell_3, E_T^{\mathrm{miss}})$ the angle between the third lepton and $E_{\mathrm{T}}^{\mathrm{miss}}$ in the transverse plane . This definition of $m_{\mathrm{T}}(W)$ is commonly used in measurements of properties of the W boson, such as of its mass (eg. [151]). One of its key features is a peak below or around the pole mass of the W boson, that drops very sharply for higher values of $m_{\mathrm{T}}(W)$. For this reason, in order to select W boson events a cut on $m_{\mathrm{T}}(W)$ larger than 60 GeV is used here, suppressing contributions from other backgrounds and especially Z + jets in the 3ℓ

control region. Last, a veto on events with at least one b-tagged jet is implemented, removing contributions from processes involving top quarks. With this definition, the 3ℓ control region has a high purity: around 90% of events in it are from WZ processes.

Estimation of the WZ scale factor

To correct the overall WZ normalisation in the signal region, a scale factor, SF_{WZ}, is derived from the data and simulation in the control region.

The number of corrected WZ events in the signal region, $N_{\mathrm{SR}}(WZ)$, can be obtained from the number of WZ events in the signal region simulation , $N_{\mathrm{SR}}^{\mathrm{MC}}(WZ)$, and the number of WZ events in the 3ℓ region from both data and simulation, $N_{3\ell\,\mathrm{CR}}^{\mathrm{data}}(WZ)$ and $N_{3\ell\,\mathrm{CR}}^{\mathrm{MC}}(WZ)$, as:

$$N_{\mathrm{SR}}(WZ) = \mathrm{SF}_{WZ} \cdot N_{\mathrm{SR}}^{\mathrm{MC}}(WZ) = \frac{N_{3\ell\,\mathrm{CR}}^{\mathrm{data}}(WZ)}{N_{3\ell\,\mathrm{CR}}^{\mathrm{MC}}(WZ)} \cdot N_{\mathrm{SR}}^{\mathrm{MC}}(WZ) \tag{5.4}$$

where $N_{3\ell\,\mathrm{CR}}^{\mathrm{data}}(WZ)$ is calculated as the number of data events in the CR, after subtracting the MC contributions of all other contributing processes but WZ.

The scale factor calculation is done separately for ggF- and VBF-like events. The 3ℓ control region is split into the two categories by requiring the presence of at least two jets for the "VBF-like" category, and classifying all remaining events as "ggF-like". Due to the limited statistics, the full VBF categorization cannot be applied. The resulting scale factors including the statistical uncertainty arising from the finite size of the simulation samples are found to be:

$$\begin{aligned} \mathrm{SF}_{WZ}(\text{ggF-like}) &= 1.29 \pm 0.03 \\ \mathrm{SF}_{WZ}(\text{VBF-like}) &= 0.95 \pm 0.04 \end{aligned} \tag{5.5}$$

In the ggF-like category, the observed events exceed the expected by roughly 30%, while in the VBF-like category the simulation overestimates the number of events by roughly 5%. The source of such a deviation between expectation and data, could be due to a (specific) kind of mismodelling of the experimental conditions in the simulation, or (more likely) due to the theory calculation of the corresponding WZ cross section not being accurate, e.g. because of missing higher order corrections.

This also explains the difference between the two categories: For the ggF-like estimation POWHEG-BOX samples are used and in contrast to that the VBF-like estimation uses SHERPA samples, which are of a higher order. The reason for this choice is that SHERPA provides a better description of the kinematics of the jets.

Figure 5.5 shows the $E_{\mathrm{T}}^{\mathrm{miss}}$ distributions for MC simulation and data in the 3ℓ region, for both ggF- and VBF-like events. Here, the predicted WZ yields are already corrected with the data-driven scale-factors as given by Equation 5.6.

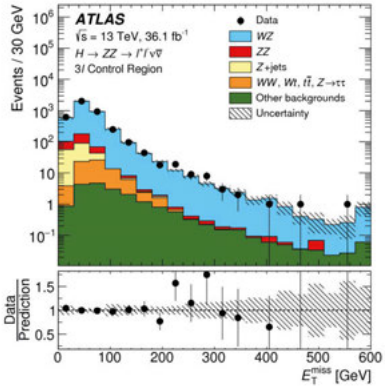

Figure 5.5: $E_{\mathrm{T}}^{\mathrm{miss}}$ distribution in the 3ℓ control region for the 2015 and 2016 data, after correcting the predicted WZ yields with the scale-factors. From [5].

Estimation of systematic uncertainties (on the scale factor)

Aside from the statistical uncertainty, also systematic uncertainties of the MC modelling affect the scale factor. But since the scale factor itself is calculated also from data events, to which no such systematic uncertainties apply, they cannot be directly assessed. Instead the so-called *transfer factor* can be used. Equation 5.4 can be rewritten in the following way

$$N_{\mathrm{SR}}(WZ) = \frac{N_{\mathrm{SR}}^{\mathrm{MC}}(WZ)}{N_{3\ell\,\mathrm{CR}}^{\mathrm{MC}}(WZ)} \cdot N_{3\ell\,\mathrm{CR}}^{\mathrm{data}}(WZ) = \mathrm{TF}_{WZ} \cdot N_{3\ell\,\mathrm{CR}}^{\mathrm{data}}(WZ) \tag{5.6}$$

and hence any relative systematic variation of the transfer factor TF_{WZ} corresponds to one of the scale factor SF_{WZ}, in the way it is propagated to the corrected WZ yield in the signal region. To determine the impact of systematics on the scale factor thus the transfer factor is calculated from the varied WZ MC event numbers for each systematics source, and then this varied transfer factor is compared to its nominal value to obtain the relative uncertainty on the scale factor.

An advantage of this method using the 3ℓ control region is that for many sources the impact in the two regions is similar, and therefore some contributions cancel. This means that the systematic uncertainty on the corrected WZ events in the signal region will be smaller than if the contribution was taken from MC simulation only.

Using the transfer factor, the WZ scale factors including the total systematic uncertainty (calculated from the square sum of all the separate uncertainties) are found to be:

$$\begin{aligned} \mathrm{SF}_{WZ}(\text{ggF-like}) &= 1.29 \pm 0.03(\text{stat.}) \pm 0.07(\text{syst.}) \\ \mathrm{SF}_{WZ}(\text{VBF-like}) &= 0.95 \pm 0.04(\text{stat.}) \pm 0.28(\text{syst.}) \end{aligned} \tag{5.7}$$

The total systematic uncertainty accounts for all experimental uncertainties related to the reconstruction of objects and events. In addition to this, another source of experimental uncertainty is specific to the 3ℓ method: it accounts for the fact that in the signal region only two leptons are selected, while in the control region three leptons pass all identification and selection criteria. Part of the WZ events contributing contain a mis-identified or mis-reconstructed lepton and the efficiency of such a mis-identifcation/reconstruction could be different in data and simulation. This relative third lepton inefficiency uncertainty is 1% or 4% in case the third lepton is an electron or muon. The impact of uncertainties arising from theory sources (such as the choice of PDF and QCD scale in the calculation) is found to be negligible in the ggF-like category, contributing only at the per-mille level. For the VBF-like categories, these uncertainties are significant with an impact of 29% .

5.2.3 Z + jets background estimation using the ABCD method

As explained above, the Z + jets background contribution in the signal region is small, but it contains no genuine $E_{\mathrm{T}}^{\mathrm{miss}}$ and this is not well described by the MC simulation. It is therefore crucial to estimate this background contribution from data. In the analysis of the 2015 and 2016 presented in this chapter, the *ABCD* method is used.

With this method three control regions, named *B*, *C* and *D*, are defined orthogonally to the signal region *A* by inverting two selection criteria that define region *A* at the same time. Given that events selected for the signal region *A* are required to pass both selection criteria, control regions *B* and *C* will then contain events that pass only one of them, and control region *D* those events that pass neither of the two criteria. An estimate for the number of Z + jets events in the signal region *A* - $N_A(Z+\text{jets})$- can then be obtained using the number of observed events in the three control regions after subtracting all non-Z + jets contributions using simulation - $N_B^{\text{data}}(Z+\text{jets})$, $N_C^{\text{data}}(Z+\text{jets})$ and $N_D^{\text{data}}(Z+\text{jets})$- as:

$$N_A(Z+\text{jets}) = N_C^{\text{data}}(Z+\text{jets}) \cdot \frac{N_B^{\text{data}}(Z+\text{jets})}{N_D^{\text{data}}(Z+\text{jets})} \tag{5.8}$$

Here, the assumption is that the transfer factor between the control regions *C* and *D* is the same as between the signal region *A* and control region *B*, meaning explicitly

$$\frac{N_C}{N_D} = \frac{N_A}{N_B} \tag{5.9}$$

for the background process in question. This is only valid if the two variables on which the selection criteria defining the regions are based are uncorrelated with each other.

Finding two suitable, uncorrelated selection variables proved a complicated issue for the Z + jets estimate. First, only events with $E_{\mathrm{T}}^{\mathrm{miss}} > 30\,\text{GeV}$ and $\frac{E_{\mathrm{T}}^{\mathrm{miss}}}{H_{\mathrm{T}}} > 0.1$ are considered. Due to the overall low statistics of the Z + jets contribution in the signal region, several selection variables are combined into one boolean. The two binary variables, v_1 and v_2, used to construct the *ABCD* regions

are defined as:

$$\upsilon_1 = E_{\mathrm{T}}^{\mathrm{miss}} > 120\,\mathrm{GeV}\,\textbf{and}\,\frac{E_{\mathrm{T}}^{\mathrm{miss}}}{H_{\mathrm{T}}} > 0.4 \tag{5.10}$$

and

$$\upsilon_2 = \text{fractional}\,p_{\mathrm{T}}\ < 0.2\,\textbf{and}\,\Delta\phi(Z, E_T^{\mathrm{miss}}) > 2.7\,\textbf{and}\,\Delta R_{\ell,\ell} < 1.8\,\textbf{and}\,n_{\text{b-jets}} = 0 \tag{5.11}$$

Using these boolean variables leads to increased statistics in the control regions, as events are allowed to fail any of the selection criteria included in υ_1 and υ_2, instead of just one.
The four resulting regions are illustrated in Figure 5.6: In the signal region A both υ_1 and υ_2 are true, in control region B only υ_2 is true, in control region C only υ_1 is true and in control region D neither υ_1 nor υ_2 are true.

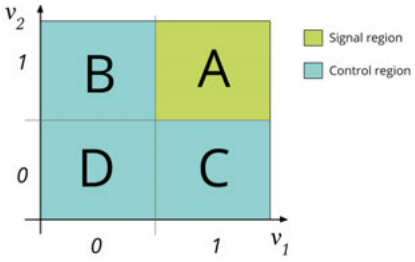

Figure 5.6: Scheme of *ABCD* regions used for the Z+jets estimate based on boolean variables υ_1 and υ_2, as defined in equations 5.10 and 5.11.

Figure 5.7 shows the missing transverse energy distributions in the three control regions. Here, the ZZ background is shown including the higher order corrections and the data-driven scale factor for the WZ background is applied. Several interesting features can be observed:

- Region B has a high Z+jets purity of around 96% . It contains events that fail either the $E_{\mathrm{T}}^{\mathrm{miss}}$ or $\frac{E_{\mathrm{T}}^{\mathrm{miss}}}{H_{\mathrm{T}}}$ selection. This also explains the truncated "peak" in the ZZ distribution: The normally smoothly falling ZZ $E_{\mathrm{T}}^{\mathrm{miss}}$ distribution is cut into at 120 GeV, as events with $E_{\mathrm{T}}^{\mathrm{miss}}$ greater than that only pass into this region if they fail the $\frac{E_{\mathrm{T}}^{\mathrm{miss}}}{H_{\mathrm{T}}}$ selection.
- Region C is not strongly dominated by Z+jets events, with a purity of only around 40%. Here it is required that both the $E_{\mathrm{T}}^{\mathrm{miss}}$ and $\frac{E_{\mathrm{T}}^{\mathrm{miss}}}{H_{\mathrm{T}}}$ selection are passed, and in general there are not many Z+jets events with large $E_{\mathrm{T}}^{\mathrm{miss}}$. Since at least one of the selection cuts represented in υ_2 must be failed, also events with b-tagged jets are allowed, leading to a large contribution of top events.
- Region D is the purest, containing around 98% Z+jets events.

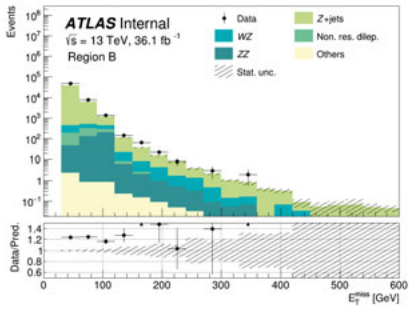

(a) Control region B

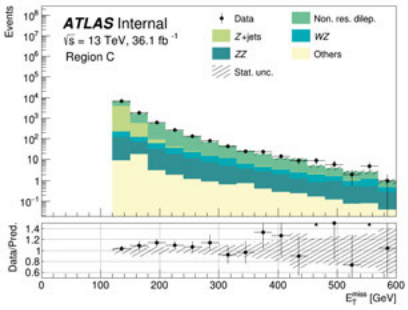

(b) Control region C

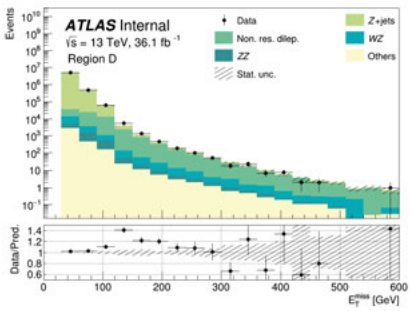

(c) Control region D

Figure 5.7: $E_{\mathrm{T}}^{\mathrm{miss}}$ distributions in the three control regions defined using the *ABCD* method with the boolean variables according to equations 5.10 and 5.11 as used to estimate the Z+jets background in the 36.1 fb^{-1} analysis. Higher order ZZ corrections are applied, and the WZ background is scaled with the data-driven scale factor described in section 5.2.2. Only the statistical uncertainty is shown.

Especially in the Z+jets dominated regions B and D , an excess of 20% or more of the data over the prediction can be observed in several bins, highlighting the importance of using a data-driven technique to estimate the Z+jets background. Accordingly, the ratio of events $\frac{N_B}{N_D}$ used to calculate the final Z+jets contribution to the signal region as according to Equation 5.8 takes different values for data and MC simulation.

Due to low statistics for VBF-like events, the full event selection plus VBF categorization cannot be applied when estimating the Z+jets contribution in this category. Instead, several of the cuts largely suppressing Z+jets events are relaxed or removed[2] and the inclusive estimate as described above (before any categorization cuts) is extrapolated to the VBF category using transfer

[2] e.g. the $\frac{E_T^{\mathrm{miss}}}{H_{\mathrm{T}}}$ requirement is lowered to 0.3 and the $\Delta\phi(Z, E_T^{\mathrm{miss}})$ cut not implemented

factors describing the efficiency of the categorisation cuts with MC simulation.

Several sources of systematic uncertainties on the Z + jets estimate using the *ABCD* approach are taken into account. First, it is observed that there is a noticeable difference between the ratios $\frac{N_A}{N_C}$ and $\frac{N_B}{N_D}$ in the MC simulation. This indicates a bias due to the usage of correlated variables to define the regions, and a non-closure of the method. A systematic uncertainty quantifying this bias is assessed by varying the additional cuts defining the control regions and comparing the overall ratios $\frac{N_A \cdot N_D}{N_B \cdot N_C}$ with the different cuts. Additionally the impact of the standard experimental uncertainties on these ratios is considered. The methodology related uncertainty made up of these two parts is then very large - up to 90% uncertainty on the final Z + jets estimate in the $eev\nu$ channel and 50% in the $\mu\mu\nu\nu$ channel of the ggF category.

On top of that, this method relies on subtraction of all non-Z + jets backgrounds from data, which are also affected by the standard experimental uncertainty sources. Taking this into account, an additional uncertainty of roughly 15% is added in each channel.

In total, the uncertainty on the Z + jets estimate is then larger than 90% in the $eev\nu$ and larger than 50% in the $\mu\mu\nu\nu$ channel for the ggF category. Due to the low statistics evolved, in the VBF category a conservative estimate of 100% uncertainty is assigned.

In order to model the shape of the m_{T} distribution in the signal region for Z + jets events, the *ABCD* method is not well suited, due to low statistics and large non-Z + jets background contributions especially in the high transverse mass m_{T} tails. Therefore, the shape is instead derived from MC simulation with a somewhat loosened signal region selection, to enhance the available statistics. This shape is normalised to the event yields as calculated using the *ABCD* method. Uncertainties on the shape are determined from the experimental sources, as well as taking into account the difference between MC based and data-driven shape.

5.2.4 Non-resonant dilepton backgrounds estimate from $e\mu$ control region

In a similar way as for the WZ background, a straightforward control region can be defined for estimating non-resonant dilepton backgrounds, such as WW, Wt, $t\bar{t}$ and $Z \to \tau\tau$ events. All of these processes can contain a lepton pair with different flavours, so $e\mu$ in the final state. The dedicated control region is therefore defined by requiring a lepton pair of different flavour, and applying the kinematic event selection as for the signal region otherwise. Table 5.7 lists those selection criteria. The purity of this control region is approximately 95% .

Selection criterion
$e^{\pm}\mu^{\mp}$ pair with $p_{\mathrm{T}} > 30, 20\,\mathrm{GeV}$, Medium ID
Veto on 3rd lepton with $p_{\mathrm{T}} > 7\,\mathrm{GeV}$, Loose ID
$76 < m_{e^{\pm}\mu^{\mp}} < 106\,\mathrm{GeV}$
$E_{\mathrm{T}}^{\mathrm{miss}} > 120\,\mathrm{GeV}$
$\Delta R_{e^{\pm},\mu^{\mp}} < 1.8$
$\Delta\phi(Z, E_T^{\mathrm{miss}}) > 2.7$
Fractional $p_{\mathrm{T}} < 0.2$
$\min \Delta\phi(\mathrm{jet}_{p_{\mathrm{T}}>100\,\mathrm{GeV}}, E_{\mathrm{T}}^{\mathrm{miss}}) > 0.4$
$E_{\mathrm{T}}^{\mathrm{miss}} / H_{\mathrm{T}} > 0.4$
b-jet veto (at 85% WP)

Table 5.7: Definition of the $e\mu$ control region used to estimate the non-resonant dilepton background in the 2015 and 2016 data analysis.

Figure 5.8 shows the expected and observed missing transverse energy distributions in the $e\mu$ control region, at preselection level. Overall good agreement between data and simulation is observed, with an excess at low $E_{\mathrm{T}}^{\mathrm{miss}}$. This originates from mismodelling of the Z + jets background at low $E_{\mathrm{T}}^{\mathrm{miss}}$, and does not contribute to the signal region.

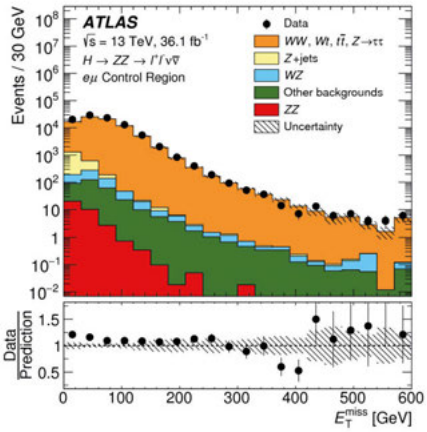

Figure 5.8: $E_{\mathrm{T}}^{\mathrm{miss}}$ distribution in the $e\mu$ control region for the 2015 and 2016 data. From [5].

As the relative probabilities for the non-resonant dilepton processes to decay into the different lepton flavour combinations $ee : \mu\mu : e\mu$ are $1:1:2$, the amount of same flavour events in the signal region - $N_{\mathrm{SR}_{ee}}$(Non-res. dilep.) and $N_{\mathrm{SR}_{\mu\mu}}$(Non-res. dilep.)- can be estimated using the amount

of data events in the $e\mu$ control region, $N^{\text{data}}_{e\mu\text{CR}}(\text{Non-res. dilep.})$, as follows:

$$N_{\text{SR}_{ee}}(\text{Non-res. dilep.}) = \frac{1}{2} \cdot \epsilon(p_{\text{T}}, \eta) \cdot N^{\text{data}}_{e\mu\text{CR}}(\text{Non-res. dilep.}) \tag{5.12}$$
$$N_{\text{SR}_{\mu\mu}}(\text{Non-res. dilep.}) = \frac{1}{2} \cdot \frac{1}{\epsilon(p_{\text{T}}, \eta)} \cdot N^{\text{data}}_{e\mu\text{CR}}(\text{Non-res. dilep.})$$

Here, $N^{\text{data}}_{e\mu\text{CR}}(\text{Non-res. dilep.})$ refers to the number of data events after subtracting all other background processes (using data-driven estimates where available, otherwise from MC simulation). The ϵ scale factor is necessary to take into account the different reconstruction efficiencies for electrons and muons, that depend on p_{T} and η. It is defined as

$$\epsilon^2(p_{\text{T}}, \eta) = \frac{N_{e_1(p_{\text{T}},\eta)e_2(p_{\text{T}},\eta)}}{N_{\mu_1(p_{\text{T}},\eta)\mu_2(p_{\text{T}},\eta)}} \tag{5.13}$$

where the numbers of $eevv$ and $\mu\mu vv$ events, $N_{e_1(p_{\text{T}},\eta)e_2(p_{\text{T}},\eta)}$ and $N_{\mu_1(p_{\text{T}},\eta)\mu_2(p_{\text{T}},\eta)}$, are binned in p_{T} and η of the two leptons and determined from data for the final background estimation. Four bins of η are used, as for each lepton the barrel and endcap region are considered separately. Each of these four η regions is then further divided into 6 bins in p_{T}. Across those regions, the ϵ-factor varies between 0.7 and 1.25.

With the binned $\epsilon(p_{\text{T}}, \eta)$ factor the event yields of the non-resonant dilepton background in the signal regions are derived separately for the ggF and VBF categories. A complication arises from the fact that the VBF category contains so few events, that the full VBF event categorization cannot be applied. Only the requirement of at least 2 jets in the event is made, the data passing this cut is used to extrapolate from control to signal region and then an additional transfer factor describing the efficiency of the m_{jj} and $|\Delta\eta_{jj}|$ cuts is applied. This transfer factor is based on MC simulation.

Aside from correcting the overall normalisation, also the shape of the transverse mass distribution is obtained from the control region data in the ggF category, using the ϵ factor described above.

Systematic uncertainties

To validate the method, and estimate associated uncertainties, it can be tested for closure using only MC simulation. Instead of the number of observed events the number of expected events is used in equations 5.13 and the efficiency factor $\epsilon(p_{\text{T}}, \eta)$ is derived using MC events as well. This estimate for the event yields in the signal region is compared to the event yields using MC simulation directly. While the two are compatible within statistical uncertainties, there is a small non-closure of the method. To cover this a systematic uncertainty of 5% is assigned. When comparing the MC derived $\epsilon(p_{\text{T}}, \eta)$ values to those derived using data, differences of a few percent are observed. These are propagated to the final estimation as a systematic uncertainty of the $\epsilon(p_{\text{T}}, \eta)$ factor.

In the ggF category the data driven m_{T} shape is used and the associated shape uncertainties are estimated by varying the $\epsilon(p_{\mathrm{T}}, \eta)$ factor by one standard deviation as well as from MC simulation. No shape information is used in the VBF category, but the use of a MC based transfer factor to describe the full fiducial region allows to asses the impact of experimental uncertainties as described for the WZ estimate in Chapter 5.2.2. On top of that, a systematic uncertainty is included that covers observed modelling issues of the VBF categorization variables m_{jj} and $|\Delta\eta_{jj}|$ for the non-resonant dilepton background processes.

5.2.5 Other backgrounds

Besides the main backgrounds described above, there are other background contributions from the W + jets, $t\bar{t}V$ and VVV processes, that contribute in total around 2% . The background contributions from the production of a top-quark pair in association with a vector boson - $t\bar{t}V$- and from triboson processes - VVV- are estimated based only on MC simulation. The W + jets background was found to be negligible.

5.3 Systematic uncertainties

Although the previous sections already described the details of a few systematic uncertainties specific to the background estimation methods, this chapter aims to give a full overview of all the systematic uncertainties involved in the analysis. Uncertainties arise from many different sources, but can in general be classified as either of *experimental* origin or as a *theory* uncertainty associated to a certain prediction. In particular, theory uncertainties are related to " unknowns" in the modelling such as the choice of PDF or QCD scale used for the MC generation. Experimental uncertainties arise from imprecisions of the reconstructed physical quantities. Systematic uncertainties associated a particular data-driven background estimate are also propagated, as well as the uncertainty on the luminosity.

Each uncertainty can have impact on both the overall normalisation or yield and shape of an observable. However, not every single one of them has a noticeable impact on the final results (i.e. small uncertainties on small backgrounds are not relevant). Table 5.8 gives an overview of which systematic uncertainties are considered for each process relevant for this analysis.

	Experimental sources			
Process	**Reconstruction**	**Data-driven**	**Luminosity**	**Theory**
Signal	✓	-	✓	✓
ZZ	✓	-	✓	✓
WZ	✓	✓	-	✓
Z + jets	✓	✓	-	-
Non-res. dilep.	-	✓	-	-
Others	✓	-	✓	-

Table 5.8: Overview of systematic uncertainty sources considered for each process.

For the signal, uncertainties affecting the signal yield prediction in simulation are assessed by estimating their impact on the signal acceptance (rather than normalised yield). For the backgrounds, SM cross-sections are used to normalise and the associated theory uncertainties are propagated. Uncertainties from experimental sources are considered for all processes, either by using MC simulation to evaluate the reconstruction uncertainties or by using data-driven methods. The luminosity uncertainty has to be propagated for all processes that are based on MC simulation. Due to their small size, no theory uncertainties are taken into account for the minor backgrounds.

More details on the respective uncertainty sources and the estimation of their impacts are described in the following two chapters: experimental uncertainties are described in 5.3.1 and theory ones in 5.3.2.

5.3.1 Experimental uncertainties

In general, experimental uncertainties are related to the reconstruction and measurement of a specific object in the event, or to overall measurement effects such as the pile-up modelling. When considering a specific object, systematic uncertainties apply to (the calibration of) its energy and/or momentum scale and resolution and the efficiencies of its reconstruction and identification. Basically, the uncertainty on one of these quantities, e.g. the resolution of a reconstructed object, gives a measure of how well we know it in simulation. While dedicated methods are in place to correct the scales, resolutions and efficiencies in simulation to match what is observed in data they have finite precision. For example, corrections to the reconstruction efficiencies of muons are calculated using data and simulated samples containing a given (finite) number of events. The resulting statistical uncertainty on the efficiency measurement is one component of the systematic uncertainty on the muon reconstruction efficiency and propagated to the analysis results.

Lepton uncertainties The uncertainties on reconstructed leptons are derived with data using the tag-and-probe method on samples enriched in $J/\Psi \to \ell\ell$ and $Z \to \ell\ell$ events. They are (typi-

cally) derived for different p_{T} and η regions. For electrons, uncertainties on the energy scale and resolution, as well as the efficiencies of reconstruction, identification, and isolation are considered [152]. For muons, the uncertainties due to the momentum scale and resolution corrections as described in Chapter 2.3.2 are used. In addition, uncertainties on the muon reconstruction and isolation efficiencies are assigned [100]. Moreover, for both electrons and muons uncertainties due to the modelling of the trigger efficiencies are taken into account [153].

Jet uncertainties Several sources of uncertainties on jets need to be taken into account. First, uncertainties on the jet energy scale and resolution are determined as described in [154] and [155]. They arise from the methodology of the *in-situ* calibrations as well as pile-up corrections that are employed. Uncertainties accounting for differences in the flavour composition and response are also evaluated. All in all, there would be 65 separate sources (and therefore nuisance parameters) related to the jet energy scale to consider, but this analysis makes use of the simplified correlations model in which they are grouped into only four separate nuisance parameters[3]. The uncertainties on the jet energy resolution are quantified by one single nuisance parameter. All of these uncertainties depend on the p_{T} of the jet in question.

On top of that, an uncertainty due to the efficiency of the JVT selection is included [108]. As described previously, this selection is used to decide whether a jet is likely to be originating from pile-up or not.

Last, since this analysis employs a veto on b-tagged jets, uncertainties on the flavour tagging of jets need to be included as well. They originate from the scale factors used to correct tagging efficiencies in MC simulation to match data and therefore affect separately the efficiency of tagging b-jets, c-jets or light-flavour-jets [156].

E_T^{miss} *uncertainties* The missing transverse energy, $E_{\mathrm{T}}^{\mathrm{miss}}$, is built from separate terms for each kind of selected object i.e. a jet term, an electron term, and a muon term. All tracks not associated to selected objects are taken into account by the soft term (cf. Chapter 2.3.5). Therefore, all uncertainties on selected objects as they are described above are propagated into the $E_{\mathrm{T}}^{\mathrm{miss}}$ directly, but a dedicated systematic uncertainty on the soft-term needs to be assigned in addition. This $E_{\mathrm{T}}^{\mathrm{miss}}$ uncertainty quantifies how well the scale and resolution of the soft term is described in MC simulation, and is derived using data and simulation samples enriched in $Z \rightarrow \mu\mu$ events. As these kind of events contain no genuine $E_{\mathrm{T}}^{\mathrm{miss}}$ any imbalance between the hard and soft term can be attributed to an uncertainty on the soft term measurement. For the uncertainty estimation, the soft term is split in a component longitudinal and one perpendicular to the hard term. The average value and variance of the longitudinal term, as well as the variance of the perpendicular term are compared between data and MC simulation in bins of p_{T} of the hard term. Taking the envelope of the differences then yields three separate uncertainties on the $E_{\mathrm{T}}^{\mathrm{miss}}$ scale and parallel and perpendicular resolution [114].

Pile-up uncertainty The uncertainty associated with the pile-up reweighting method employed

[3] Three general ones, and one specific one to account for a localized non-closure observed when using FastSimulation samples.

to match the pile-up profile of the simulation to that of data is estimated by varying the scale value μ used in the reweighting and comparing the scale-factors obtained with that to the nominal case [157].

Luminosity uncertainty For the 2015 and 2016 data, the luminosity uncertainty corresponds to 3.2% and was determined by combining the results of a special scan performed once per data-taking year and following the methodology described in [158].

Data-driven background estimation uncertainties For the data-driven estimations of the WZ, Z+jets and non-resonant dilepton backgrounds one nuisance parameter each is assigned to quantify the overall systematic uncertainty. Which sources are grouped into this nuisance parameter and how it is derived is detailed in the respective section of the previous chapter. It should be noted that by grouping uncertainties like this, any correlations of a single systematic source between different processes are lost (e.g. the muon momentum scale uncertainty between WZ and ZZ events will not be correlated). However, this should not pose a problem for this analysis as the overall impact of systematic uncertainties on these backgrounds is expected to be small compared to statistical uncertainties.

To give an insight into which of the experimental uncertainties described above are relevant for the analysis and in what context, Tables 5.9 and 5.10 list the top five leading as well as the total impact of all experimental uncertainty sources on the background yields for the $q\bar{q}ZZ$ and $ggZZ$ process and the signal acceptance of an example heavy NWA Higgs sample with a mass of 600 GeV, in the ggF and VBF category respectively. The luminosity uncertainty is not included in these tables.

In the ggF category, the total relative impact of experimental systematics is small at 2.7 to 3.75% for the ZZ background processes, and in the range of 3.6 to 3.9% for the example signal. The uncertainties on the electron identification or the muon reconstruction efficiency, the JVT efficiency and the jet energy scale feature among the leading uncertainties across all processes and channels. That the lepton-related uncertainties should play a leading role is intuitive as they are directly selected. The leading role of jet energy scale and JVT related uncertainties on the other hand, can be explained by the fact that both of them will be propagated into the $E_{\mathrm{T}}^{\mathrm{miss}}$. Aside from this the pile-up reweighting and the light flavour tagging uncertainties contribute.

(a) $q\bar{q}ZZ$ background

$eevv$ **channel**			$\mu\mu vv$ **channel**		
Uncertainty source	**Impact in %**		**Uncertainty source**	**Impact in %**	
Jet energy scale (NP 1)	-1.03	2.29	Jet energy scale (NP 1)	-1.86	2.22
Electron identification efficiency	-1.62	1.64	Muon reconstruction efficiency	-1.73	1.75
JVT efficiency	-1.42	1.44	JVT efficiency	-1.36	1.38
Electron energy scale	-0.68	1.08	Pile-up reweighting	-1.36	1.05
Light jet-tagging efficiency	-0.98	0.99	Light jet-tagging efficiency	-0.96	0.97
Total	**-2.90**	**3.75**	**Total**	**-3.46**	**3.66**

(b) $ggZZ$ background

$eevv$ **channel**			$\mu\mu vv$ **channel**		
Uncertainty source	**Impact in %**		**Uncertainty source**	**Impact in %**	
Electron identification efficiency	-1.73	1.75	Muon reconstruction efficiency	-1.79	1.81
Jet energy scale (NP 1)	-1.44	0.79	Pile-up reweighting	-1.49	0.59
JVT efficiency	-1.03	1.04	Jet energy scale (NP 1)	-0.90	1.16
Electron energy scale	-0.72	1.00	JVT efficiency	-1.01	1.02
Electron isolation efficiency	-0.81	0.82	Light jet-tagging efficiency	-0.72	0.73
Total	**-2.85**	**2.74**	**Total**	**-2.92**	**2.70**

(c) ggH signal at m_H = 600 GeV (NWA)

$eevv$ **channel**			$\mu\mu vv$ **channel**		
Uncertainty source	**Impact in %**		**Uncertainty source**	**Impact in %**	
Electron identification efficiency	-1.88	1.89	Muon reconstruction efficiency	-2.17	2.20
Jet energy scale (NP 1)	-1.72	1.70	Jet energy scale (NP 1)	-2.14	1.75
JVT efficiency	-1.60	1.63	JVT efficiency	-1.59	1.62
Electron isolation efficiency	-1.56	1.56	Light jet-tagging efficiency	-1.09	1.11
Light jet-tagging efficiency	-1.12	1.13	Pile-up reweighting	-1.10	0.70
Total	**-3.72**	**3.70**	**Total**	**-3.91**	**3.63**

Table 5.9: Leading experimental uncertainties on (a) the $q\bar{q}ZZ$ background yields, (b) the $ggZZ$ background yields in the signal region and (c) the signal acceptance for a heavy Higgs signal of mass 600 GeV and negligible width, for the ggF category. The last row lists the total impact of experimental certainties, including those not shown in this list.

(a) $q\bar{q}ZZ$ background

$eev\nu$ **channel**			$\mu\mu\nu\nu$ **channel**		
Uncertainty source	**Impact in %**		**Uncertainty source**	**Impact in %**	
Pile-up reweighting	-20.70	32.62	Jet energy scale (NP 1)	-24.84	16.25
Jet energy scale (NP 1)	-29.85	29.86	Jet energy scale (NP 3)	-19.22	17.63
Jet energy scale (NP 3)	-23.93	20.21	Jet energy scale (Non-closure NP)	-6.60	2.82
Jet energy scale (NP 2)	0.00	6.46	Pile-up reweighting	-4.46	4.46
Jet energy scale (Non-closure NP)	-5.79	6.46	Jet energy scale (NP 2)	-2.88	2.84
Total	**-44.09**	**49.54**	**Total**	**-32.61**	**24.81**

(b) $ggZZ$ background

$eev\nu$ **channel**			$\mu\mu\nu\nu$ **channel**		
Uncertainty source	**Impact in %**		**Uncertainty source**	**Impact in %**	
Jet energy scale (NP 1)	-15.36	6.75	Jet energy scale (NP 3)	-0.24	10.87
Jet energy scale (NP 3)	-11.53	5.05	Jet energy scale (NP 1)	-0.07	7.92
Pile-up reweighting	-7.28	11.03	Jet energy scale (NP 2)	-5.40	5.40
JVT efficiency	-3.20	0.21	Pile-up reweighting	-3.66	0.15
Jet energy scale (NP 2)	-2.62	2.62	Muon MS track resolution	-3.11	3.11
Total	**-21.11**	**14.42**	**Total**	**-8.66**	**15.55**

(c) VBF signal at m_H = 600 GeV (NWA)

$eev\nu$ **channel**			$\mu\mu\nu\nu$ **channel**		
Uncertainty source	**Impact in %**		**Uncertainty source**	**Impact in %**	
Jet energy scale (NP 1)	-3.45	2.95	Jet energy scale (NP 1)	-4.61	2.16
Jet energy scale (NP 3)	-2.81	2.11	Jet energy scale (NP 3)	-3.17	2.43
Electron identification efficiency	-1.82	1.84	Muon reconstruction efficiency	-2.16	2.19
Electron identification efficiency	-1.55	1.56	Pile-up reweighting	-1.56	1.09
Light jet-tagging efficiency	-0.80	0.80	Light jet-tagging efficiency	-0.73	0.74
Total	**-5.27**	**4.59**	**Total**	**-6.35**	**4.29**

Table 5.10: Leading experimental uncertainties on (a) the $q\bar{q}ZZ$ background yields, (b) the $ggZZ$ background yields in the signal region and (c) the signal acceptance for a heavy Higgs signal of mass 600 GeV and negligible width, for the VBF category. The last row lists the total impact of experimental certainties, including those not shown in this list.

In contrast, in the VBF category the relative impact of experimental uncertainties is much larger, especially for the ZZ backgrounds. Here the total impact on the $q\bar{q}ZZ$ yields is between 25 and 50%, and on the $ggZZ$ yields between 9 and 21%. This can be explained by the low statistics in this region - as there are only very few generated events passing the VBF selection, even a change of a single generated event more or fewer due to the systematic variation immediately leads to a sizeable relative change of the predicted yields. The obvious asymmetry between down- and up-variation for several of the uncertainties can also be explained by this. Nonetheless it is clear that in the VBF category jet-related uncertainties dominate the ZZ background. For the VBF signal the picture is a little bit different, and overall the experimental uncertainties are smaller - between 4 and 6% impact - as VBF signal jets are usually harder than background jets and therefore the resolution for VBF signal jets is expected to be better and less affected by uncertainties than in

the background case.

5.3.2 Theory uncertainties

In general, theory uncertainties arise from particular choices in the modelling, such as the specific PDF set and QCD scale used in the matrix element calculation, or the choice of parton showering model. Their impact can be significant, if the process in question is not well modelled. Hence, their impact should be assessed for the signals and largest backgrounds.

To estimate each of the theory uncertainties, a different choice is made and the predictions with several alternative choices are compared to the nominal case. Typically, the envelope around all the different variations is then used as the systematic.

The main processes in this analysis (narrow-width heavy Higgs signals, ZZ and WZ background) are all modelled using CT10 PDF sets in the nominal case, so the associated uncertainty is obtained by changing to MSTW2008nlo68cl or NNPDF3.0 PDFs. On top of that the CT10 PDF contains a set of eigenvector variations, which contributes to the overall PDF uncertainty as well.

For the QCD scale uncertainty estimation, the factorization and renormalisation scale are independently varied by a factor two away from their nominal values at $\mu_R = 1, \mu_F = 1$.

Last, the parton showering uncertainty is estimated by varying the shower parameters, such as the Multiple Parton Scatterings (MPI) or final state radiation (FSR) models. Here, it is evaluated comparing the nominal showering setup using PYTHIA 8 to HERWIG++ as alternative choice.

Signal theory uncertainties The impact of PDF, QCD and parton showering uncertainties on both the signal shapes and acceptances for the narrow-width heavy Higgs signals is evaluated. It was found that the impact of the shape uncertainty can be neglected. Typically the impact on the signal acceptances is small as well: The impact of the PDF uncertainty on narrow-width heavy Higgs acceptances ranges from 0.1 to 1.5% in the ggF category, and from 0.1 to 2.7% in the VBF category, depending on the mass point and flavour channel. For the QCD scale uncertainty, the impact is found between 0.1 and 0.8% in the ggF category, and between 0.1% and 5.3% in the VBF category. Finally, the parton showering uncertainty contributes between 0.2% and 9% in both categories. Since only signal region events are used to estimate these uncertainties, the fluctuation of theory uncertainties is larger in the VBF category where the signal acceptance is lower, and this estimation is based on small statistics. The theory uncertainties on large-width signals are assumed to be the same as for the corresponding narrow-width signal of the same mass.

ZZ background theory uncertainties The same theory uncertainties as for the signals are assessed for the dominant ZZ backgrounds. For the ZZ prediction, the envelope around different PDF and QCD scale variations is found to be (relatively) constant in m_{T}, and therefore no shape dependence needs to be considered. The impact of the QCD scale uncertainty on the total

$q\bar{q}ZZ$ and $ggZZ$ yields is around 10% for ggF events, and around 25% for VBF events. The PDF uncertainty on the other hand is smaller, changing the yields by between 3-4% in both categories. Finally, the parton shower uncertainty on the ZZ background is found to be negligible at an effect below 0.1% . For the $ggZZ$ process the large uncertainty on the flat k-factor is also included: a 60% uncertainty in the ggF category, while in the VBF category it is set to 100%.

No theory uncertainties are considered for the remaining backgrounds: For the WZ background the PDF and QCD scale uncertainties on the total yield were evaluated but found to be negligible in comparison with other uncertainties on the data-driven estimate, the Z + jets and non-resonant dilepton backgrounds are small and corrected using control region data anyway, and the other backgrounds are simply too small for their modelling uncertainties to be relevant.

5.4 Results and interpretation

5.4.1 Data in the signal regions

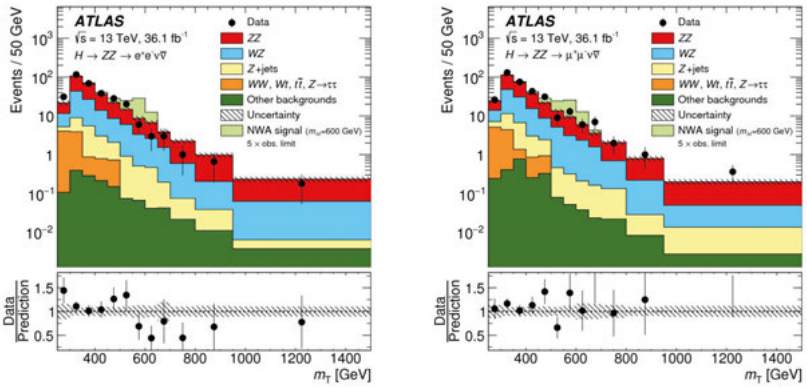

(a) $eev\nu$ channel

(b) $\mu\mu\nu\nu$ channel

Figure 5.9: Expected and observed transverse mass, m_{T}, distributions for the 2015 and 2016 data (a) in the $eev\nu$ channel and (b) in the $\mu\mu\nu\nu$ channel. Events from both ggF and VBF categories are included. The last bin includes the overflow. Data-driven estimates for WZ, Z + jets and non-resonant dilepton backgrounds are shown. As an example, the narrow-width heavy Higgs signal at a mass of $m_H = 600\,\mathrm{GeV}$ is drawn on top of the expected backgrounds, normalized to 5 times its upper cross-section limit. From [5].

Figure 5.9 shows the expected and observed distributions of the transverse mass observable, m_{T}, for the 2015 and 2016 data. Events from the ggF and VBF categories are shown. The full kinematic event selection described in Chapter 5.1 is applied, and data-driven estimates are shown for WZ, Z + jets and non-resonant dilepton backgrounds, following the methods detailed in Chapter 5.2.

For illustration purposes, also an example signal is drawn on top of the expected backgrounds: the narrow-width heavy Higgs signal at a mass of 600 GeV. It is normalized to 5 times the upper limit on its production cross-section.

The corresponding event yields are listed in Table 5.11. Here, events in the ggF and VBF category are shown separately. As there are only a few events in the VBF category, the m_{T} shape information is not used in the interpretation of this category, only a simple counting experiment will be performed.

While in all categories the amount of observed events slightly exceeds the (nominal) expectation, no significant and clearly localized excess in both flavour channels is seen in the m_{T} distributions. Hence, exclusion limits for the production of a heavy Higgs boson are derived.

(a)

Process	**Yields in the ggF region**	
	$eev\nu$ channel	$\mu\mu\nu\nu$ channel
ZZ	177.2 ± 28.0	179.7 ± 28.3
WZ	92.8 ± 4.3	99.5 ± 3.2
Z + jets	16.6 ± 11.4	19.3 ± 17.2
Non-resonant dilepton	9.2 ± 1.4	10.7 ± 0.9
Other	1.1 ± 0.1	1 ± 0.1
Total Bkg.	297.0 ± 24.2	310.2 ± 27.4
Data	320	352

(b)

Process	**Yields in the VBF region**	
	$eev\nu$ channel	$\mu\mu\nu\nu$ channel
ZZ	1.01 ± 0.68	1.08 ± 0.58
WZ	0.63 ± 0.19	0.66 ± 0.19
Z + jets	0.33 ± 0.33	0.43 ± 0.43
Non-resonant dilepton	0.16 ± 0.15	0.23 ± 0.21
Other	0.02 ± 0	0.01 ± 0.01
Total Bkg.	2.15 ± 0.65	2.41 ± 0.66
Data	4	5

Table 5.11: Observed and expected yields and their systematic uncertainties in the (a) ggF and (b) VBF signal regions, for the 2015 and 2016 data. Data-driven estimates for WZ, Z + jets and non-resonant dilepton backgrounds are shown.

5.4.2 Cross-section limits on narrow-width heavy Higgs

Exclusion limits on the production cross-section times branching fraction to ZZ pair, $\sigma \cdot \mathrm{BR}(H \to ZZ)$, of a narrow-width heavy Higgs are determined using the CL_s procedure, as explained in Chapter 4.5. Both production categories (ggF and VBF) and flavour channels ($eevv$ and $\mu\mu vv$) are included in a simultaneous fit to the total four regions. As the ratio between ggF and VBF production is unknown for a BSM Higgs, the cross-section for each mode is fitted separately, while the other is left free. The resulting observed and expected limits as a function of signal mass, m_H, are shown in Figure 5.10. Across the whole mass range considered, from 300 GeV to 1.2 TeV, no statistically significant excess is seen in data over the expectation and the expected and observed limits are compatible within two standard deviations. The observed upper limits on $\sigma \cdot \mathrm{BR}(H \to ZZ)$ range from approximately 15 fb to 1080 fb in the ggF production mode, and from 22 fb to 1830 fb in the VBF production category.

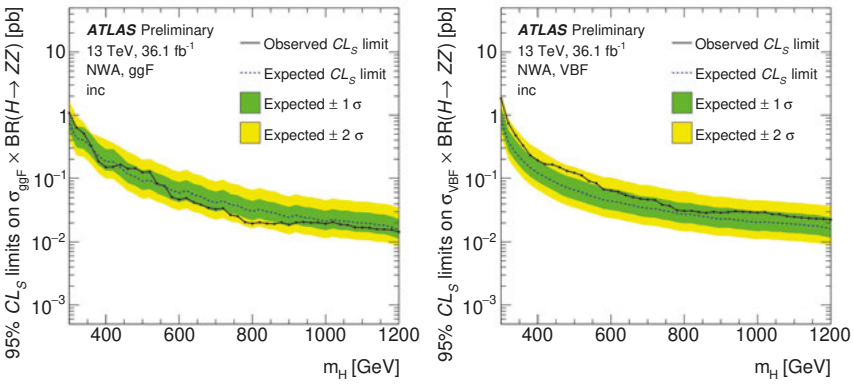

(a) ggF production

(b) VBF production

Figure 5.10: Expected and observed upper limits on the production cross-section times branching fraction to ZZ pair, $\sigma \cdot \mathrm{BR}(H \to ZZ)$, of a narrow-width heavy Higgs in (a) ggF and (b) VBF production mode. For the 2015 and 2016 data.

The sensitivity of the search depends on the exact signal hypothesis: For both ggF and VBF signals, the limits decrease with increasing mass. One reason is that high mass signals are more easily separated from the backgrounds, the bulk of which is found at low m_{T} values. Additionally, the signal acceptance for masses at the low end of the search range is impacted by the harsh $E_{\mathrm{T}}^{\mathrm{miss}}$ cut. Hence the sensitivity to higher mass signals is better. When comparing the ggF versus VBF limits, it is clear that the sensitivity to VBF signals is worse. This is because the VBF category has very few events and is evaluated only as a counting experiment.

Overall the impact of systematic uncertainties on the exclusion limits is small - typically below 1% and at most a few percent. However, this impact depends on the production mode and

signal mass in question. In the ggF category, uncertainties originating from the Z+jets and non-resonant dilepton estimation are leading at low m_H, but become less relevant for higher m_H. For example, the Z+jets uncertainty impacts the ggF limit by roughly 3.2% at 300 GeV, but only 1.8% at 1 TeV. Uncertainties on the ZZ modelling have larger impacts in the higher mass range, ranging from 2 % to 13 %. In the VBF category, also jet-related uncertainties become important. For example, the jet energy scale uncertainty impacts the VBF limit by at most 6%. In both categories, lepton uncertainties typically contribute 0.1 % to 1 % in total, while uncertainties on the missing transverse energy impact the result by as little as 0.02 % to 0.04 %. A more detailed look at the systematic uncertainties and their impacts is taken in the analysis of the full run II dataset, in Chapter 6.4.2.

5.4.3 Cross-section limits on large-width heavy Higgs

For the interpretation as cross-section limits on a large-width heavy Higgs only ggF category events are used, as only ggF production signals are modelled. The interference of this ggF signal with the SM Higgs at 125 GeV mass ($H-h$) and the $ggZZ$ background ($H-B$) is modelled following the methodology detailed in Chapter 4.3. Furthermore, in the large-width analysis (LWA) the search range is restricted to 400 GeV to 1000 GeV. Due to the large signal width the search is not really sensitive below 400 GeV: with a large signal width the peak of very low mass signals is broad, with a significant fraction of events not passing the $E_{\mathrm{T}}^{\mathrm{miss}}$ requirement. The signal acceptance of LWA signals is diminished in comparison to NWA signals due to such "cut-off" effects.

Figure 5.11 shows the upper limits on the LWA production cross-section for four different width assumptions: 1% , 5% , 10% and 15% of the heavy Higgs mass. While the observed and expected limits with uncertainty band include the interference modelling, for comparison also the median expected limit without including interference effects is shown. Also here no clear signal excess over the prediction is seen in data.

Several effects can be observed when comparing the limits between different signal widths:

- First, with increasing width the cross-section limits become larger. This is explained by the signal peak becoming broader, therefore less clearly separated from the backgrounds.
- Next, the observed limits also become smoother with increasing with. This is expected as well, since with a broader signal peak more background events are found below the signal and therefore the result becomes less affected by statistical fluctuations.
- Last, the larger the width the clearer is the impact of including the interference. This is also as expected from theory considerations. However, on the whole, the impact of the interference is minor - much smaller than the uncertainty on the limits. Across the mass range considered here the interference actually enhances the sensitivity, leading to better expected limits. A more detailed look at the interference effects and their impacts on the limits is given for the full run II analysis, in Chapter 6.4.4.

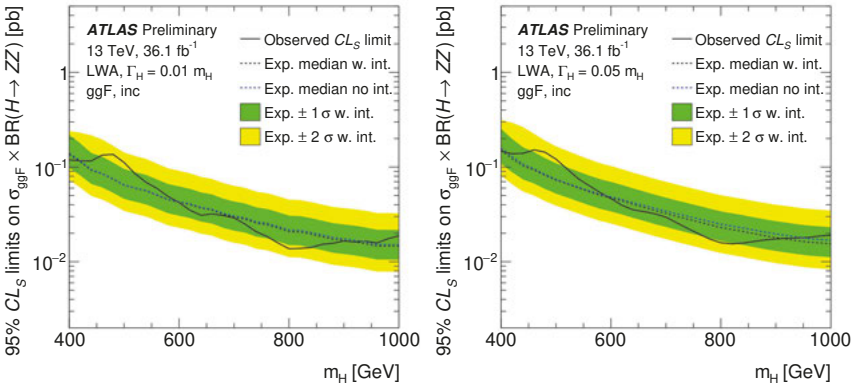

(a) 1% width

(b) 5% width

(c) 10% width

(d) 15% width

Figure 5.11: Expected and observed upper limits on the production cross-section times branching fraction to ZZ pair, $\sigma \cdot \mathrm{BR}(H \to ZZ)$, of a heavy Higgs with a width of (a) 1%, (b) 5%, (c) 10% and (d) 15% of its mass. The observed and expected limits with uncertainty bands include the interference modelling, as described in Chapter 4.3, and for comparison the median expected limit without including interference is also shown. For the 2015 and 2016 data.

6 Analysis of the full run II dataset

This chapter discusses the search for a high mass resonance in the $ZZ \to \ell\ell\nu\nu$ channel using the full run II ATLAS dataset of 139 fb^{-1} collected from 2015 to 2018, as well as the combination of its results with the same search in the $ZZ \to \ell\ell\ell\ell$ channel. The combined results were published in [6].

Compared to the 2015 and 2016 data, the 2015 to 2018 data offers a factor four increase in integrated luminosity. This benefits especially the sensitivity to very high invariant masses (> 1 TeV), as such events are generally rare. The increased data statistics also allow to make further improvements to the analysis, the main ones being:

- The range of the search can be extended to include masses up to 2 TeV.
- The normalisation of the dominant and irreducible ZZ background can be derived directly from the data in the signal region, using a free normalisation factor in the final fit.
- Also in the VBF category the m_{T} shape information can be exploited.

Additionally, other optimizations and changes to the analysis were put in place, such as:

- The event selection has been (partly) re-optimized, now using jets and $E_{\mathrm{T}}^{\mathrm{miss}}$ reconstructed using the PFLOW algorithm.
- Due to the short-comings of the $ABCD$ method previously used to estimate the Z+jets contribution, this background is now estimated using the one-dimensional sideband method.

Aside from this, the analysis follows the same principles and general strategy as the 2015 and 2016 data analysis. Details of the 2015-2018 analysis are discussed in the following, focussing mostly on the changes and updates. At the end of the chapter, also the $ZZ \to \ell\ell\ell\ell$ analysis is briefly discussed, before presenting the combined results.

6.1 Event selection

6.1.1 Object selection

The object selection for the full run II analysis mostly follows the one described in Chapter 5.1.1, with a few changes, as listed in Table 6.1 and discussed below.

First, a new lepton isolation working point is used, based on PFLOW reconstructed quantities. Especially for the analysis in the $ZZ \to \ell\ell\ell\ell$ channel this was found to increase efficiency, so it is

also applied to electrons and muons in the $ZZ \to \ell\ell\nu\nu$ analysis. Details of the isolation working points are given in Chapters 2.3.1 and 2.3.2.

Second, the p_{T} threshold for jets considered in the analysis was raised to 30 GeV, in order to harmonize and be consistent with the VBF and $ZZ \to \ell\ell\ell\ell$ selections.

A major update is to use PFLOW algorithm based jets and missing transverse energy $E_{\mathrm{T}}^{\mathrm{miss}}$, which is motivated and studied in more detail in the following.

With the change to PFLOW jets also a tighter requirement on the Jet Vertex Tagger property, used to reject pile-up jets, was found necessary, due to the different definition of the $E_{\mathrm{T}}^{\mathrm{miss}}$ soft-term when using PFLOW. With the tighter cut, pile-up jets are rejected just as well as in the EMTOPO case, but the efficiency for keeping very high p_{T} jets is higher [112].

Selection criterion	Value in 2015-16 data analysis	Value in 2015-18 data analysis
Lepton isolation	Loose working point	FixedCutPFlowLoose working point
Jet p_{T} threshold	$p_{\mathrm{T}} > 20$ GeV	$p_{\mathrm{T}} > 30$ GeV
Jet identification	AntiKT4EMTopo	AntiKT4PFlow
Jet pile-up removal	JVT < 0.59, if $p_{\mathrm{T}} > 60$ GeV, $\lvert\eta\rvert < 2.4$	JVT < 0.5, if $p_{\mathrm{T}} > 60$ GeV, $\lvert\eta\rvert < 2.4$
$E_{\mathrm{T}}^{\mathrm{miss}}$ reconstruction	EMTOPO	PFLOW

Table 6.1: Changes to object selection criteria in the analysis of the 2015-2018 dataset, compared to the 2015 and 2016 data analysis.

Study of PFLow reconstructed $E_{\mathrm{T}}^{\mathrm{miss}}$ performance

As discussed in more detail in Chapters 2.3.3 and 2.3.5, the idea behind particle-flow based jet and $E_{\mathrm{T}}^{\mathrm{miss}}$ reconstruction is to combine measurements from different subdetectors in an optimal way, to improve the energy, momentum and angular resolutions. A key benefit of this algorithm is that it naturally suppresses contributions from pile-up interactions. This is the main motivator to study the performance of PFLOW $E_{\mathrm{T}}^{\mathrm{miss}}$ for the full run II analysis: especially in the 2017 data the average pile-up was much higher than previously, with a peak around $\langle\mu\rangle = 60$.

Since the study had to be done at a very early stage of the full run II analysis, only simulated samples matching the running conditions of the 2015+16 and 2017 data were available. Systematic uncertainties on the $E_{\mathrm{T}}^{\mathrm{miss}}$ reconstruction are not studied at this stage since according to [112] they are comparable between the two algorithms.

A general overview comparison is made in Figure 6.1: the $E_{\mathrm{T}}^{\mathrm{miss}}$ distributions at the pre-selection level of all backgrounds, an example signal with a mass of 600 GeV and data are compared side-by-side. Just by eye, it can already be seen that there are no major differences between the reconstruction algorithms and for both of them the overall data to MC agreement is good.

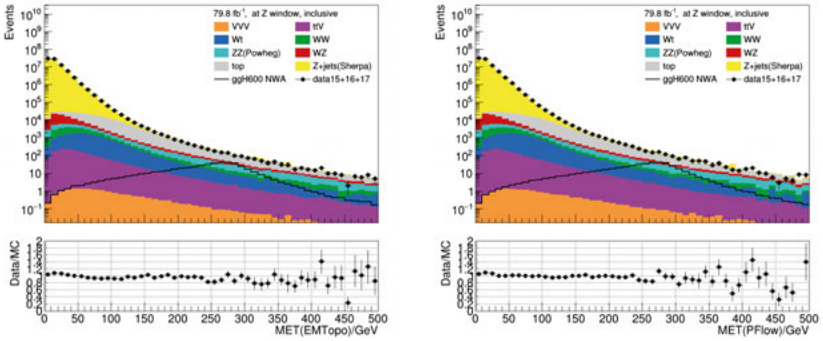

(a) EMTOPO (b) PFLOW

Figure 6.1: Distributions of the missing transverse energy, $E_{\mathrm{T}}^{\mathrm{miss}}$, reconstructed with (a) EMTOPO jets and (b) PFLOW jets. Shown for the 2015-2017 data and matching simulation, corresponding to 79.8 fb^{-1}.

To study the performance of the PFLOW based $E_{\mathrm{T}}^{\mathrm{miss}}$ reconstruction further, direct comparisons are made using only MC simulation matching Legend the 2017 data taking conditions which have the highest average pile-up out of the whole run II. If the PFLOW based reconstruction offers a benefit in terms of pile-up suppression, this is where the effect would be most noticeable.

Figure 6.2 compares the EMTOPO and PFLOW $E_{\mathrm{T}}^{\mathrm{miss}}$ distributions directly for the main backgrounds ZZ, WZ and Z+jets as well as an example heavy, narrow-width signal with a mass of 600 GeV, produced in the ggF mode at the pre-selection level. The distributions are normalized to unit area, to be able to compare the shapes. In the lower panel the ratio of the EMTOPO distribution divided by the PFLOW one is shown. Overall, and especially for processes with real $E_{\mathrm{T}}^{\mathrm{miss}}$ such as the signal, ZZ and WZ backgrounds, the two $E_{\mathrm{T}}^{\mathrm{miss}}$ reconstruction algorithms perform very similarly.

As another check the overall yields in the signal region are compared between using EMTOPO and PFLOW $E_{\mathrm{T}}^{\mathrm{miss}}$ variables, following the definition of the 2015 and 2016 data analysis given in Table 5.3. Any improvement in the energy and angular resolution or reconstruction quality of the missing transverse energy $E_{\mathrm{T}}^{\mathrm{miss}}$ would have an effect here, since the signal region definition is based on variables such as $\Delta\phi(Z, E_T^{\mathrm{miss}})$ or $\frac{E_{\mathrm{T}}^{\mathrm{miss}}}{H_{\mathrm{T}}}$.

Yields in the signal region			
Process	EMTopo	PFlow	**Rel. difference**
ZZ	421.25 ± 4.00	412.59 ± 3.93	-2%
WZ	169.10 ± 1.87	172.86 ± 1.87	$+2\%$
Z + jets	61.82 ± 7.72	55.00 ± 7.20	-11%
ggH600 NWA	132.14 ± 0.57	129.94 ± 0.55	-2%

Table 6.2: Comparison of yields in the signal region when using EMTopo or PFlow based $E_{\mathrm{T}}^{\mathrm{miss}}$ reconstruction, for the main backgrounds and an example signal with a mass of 600 GeV. The signal is normalized to its SM cross-section expectation. From simulation matching the 2017 data, corresponding to 44.31 fb^{-1}.

While for the processes with real $E_{\mathrm{T}}^{\mathrm{miss}}$ the difference between EMTopo and PFlow yields is minor - only around 2% in each case - it is larger for the Z + jets process which does not contain real $E_{\mathrm{T}}^{\mathrm{miss}}$. Simply by changing to PFlow $E_{\mathrm{T}}^{\mathrm{miss}}$ the contribution of this process can be reduced by around 11% . However, it needs to be noted that the Z + jets contribution suffers from large relative statistical uncertainties and the observed reduction when using PFlow lies in fact within the statistical uncertainty on the EMTopo yield. It is therefore not completely clear that this is a real advantage of the PFlow algorithm, or just a lucky statistical fluctuation[1]. Nevertheless it is clear from the comparisons that the PFlow based $E_{\mathrm{T}}^{\mathrm{miss}}$ reconstruction does not perform worse than the previously used EMTopo algorithm. In both cases, the ratio of signal over total background (considering only the three main backgrounds included in this study) is found to be around 0.2, when the signal is normalized to its SM cross-section prediction.

[1] Here only the flavour inclusive yields are shown, but when comparing $eevv$ and $\mu\mu vv$ channel separately this reduction is visible in both channels, posing a small hint that maybe it is not simply due to fluctuations.

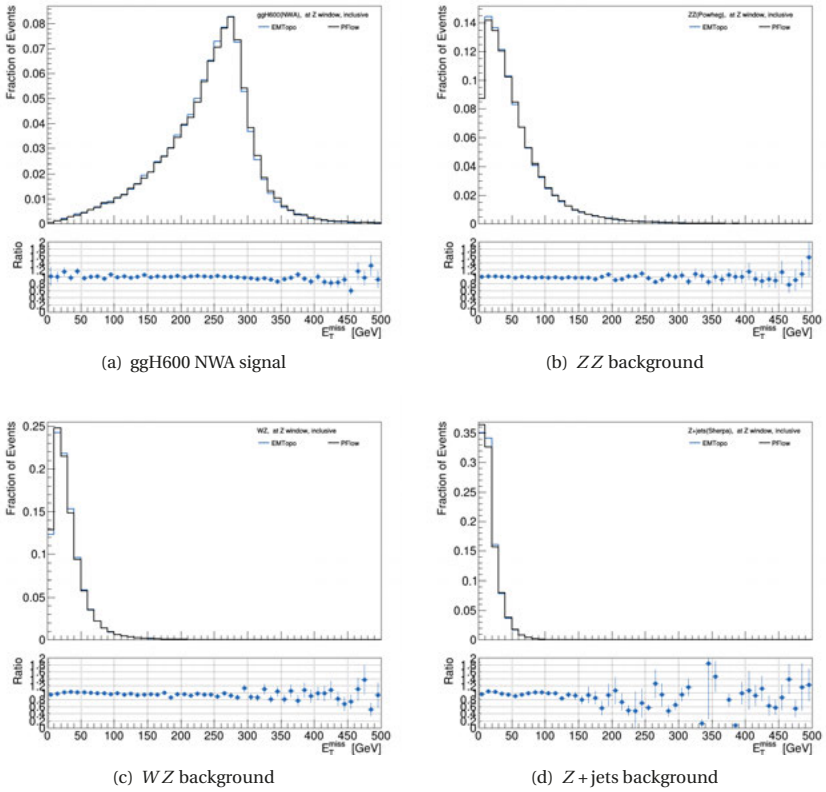

(a) ggH600 NWA signal

(b) ZZ background

(c) WZ background

(d) Z + jets background

Figure 6.2: Direct comparisons of the $E_{\mathrm{T}}^{\mathrm{miss}}$ distributions using the EMTOPO and PFLOW algorithm for an example signal and the main background processes.

A likely explanation why none of the apparent benefits of the PFLOW are seen in the scope of this analysis, is that specifically the high p_{T} regime is considered here. In this regime, the impact of the mostly low p_{T} pile-up interactions should be smaller. In fact, using the PFLOW algorithm to reconstruct $E_{\mathrm{T}}^{\mathrm{miss}}$ only changes the calculation of the soft term, which is mostly based on low p_{T} particles. To illustrate this point, Figure 6.3 shows direct comparisons of the reconstructed EMTOPO and PFLOW $E_{\mathrm{T}}^{\mathrm{miss}}$ distributions to its truth distribution, for the example signal at $m_H = 600\,\mathrm{GeV}$. Indeed, in both cases the reconstructed shape agrees fairly well with the truth shape.

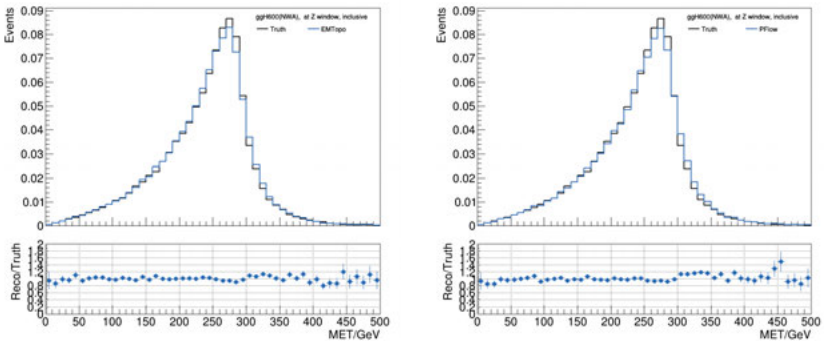

(a) EMTOPO (b) PFLOW

Figure 6.3: Direct comparisons of the reconstructed and truth $E_{\mathrm{T}}^{\mathrm{miss}}$ for the ggF, NWA Higgs signal at a mass of 600 GeV, at pre-selection level. Using the (a) EMTOPO and (b) PFLOW algorithm.

All in all, the PFLOW based $E_{\mathrm{T}}^{\mathrm{miss}}$ was found equally suited for this analysis as the previously used EMTOPO $E_{\mathrm{T}}^{\mathrm{miss}}$. The PFLOW based reconstruction may offer a slightly improved suppression of fake $E_{\mathrm{T}}^{\mathrm{miss}}$ backgrounds, such as Z + jets. At the time this study was completed, it was already clear that the main focus of further development in the field of $E_{\mathrm{T}}^{\mathrm{miss}}$ reconstruction would be the PFLOW algorithm. Therefore, the change to PFLOW $E_{\mathrm{T}}^{\mathrm{miss}}$ was mainly as a matter of *future-proofing*.

6.1.2 Event pre-selection

The pre-selection of events is the same as in the 2015 and 2016 data analysis, as explained in Chapter 5.1.2. But of course, new trigger menus are added for the data-taking years 2017 and 2018. The details are given in Appendix A. For both years, the p_{T} threshold for the single lepton trigger is 26 GeV.

For the full run II analysis, a study of the signal efficiencies of the trigger selection was performed [9], as concerns were raised that especially for very high mass signals the efficiency of single-muon triggers may not be sufficient. Indeed it was found that the trigger efficiencies in the muon channel lie around 96%, which is a bit lower than in the electron channel, where they are close to 100% for masses below 1.6 TeV and around 97% at the highest mass point of 2 TeV. Nonetheless, as the inefficiency is only a few % at most, the strategy to use the lowest unprescaled single lepton triggers was judged to be adequate.

6.1.3 Optimization of the kinematic event selection

Table 6.3 summarizes the event selection used for the full run II analysis. Comparing to the 2015 and 2016 data analysis, a few selection criteria were re-optimized:

- The requirement on the fractional p_{T} variable had only little benefit, and it is therefore dropped from the event selection.
- Previously, the $E_{\mathrm{T}}^{\mathrm{miss}}/H_{\mathrm{T}}$ ratio was used as an indicator of the $E_{\mathrm{T}}^{\mathrm{miss}}$ reconstruction quality. For the full run II analysis, a more elaborate quantifier is available: the object-based $E_{\mathrm{T}}^{\mathrm{miss}}$-significance [159]. A cut on $E_{\mathrm{T}}^{\mathrm{miss}}$-significance > 10.0 replaces the $E_{\mathrm{T}}^{\mathrm{miss}}/H_{\mathrm{T}}$ requirement. The cut value was optimized in a dedicated study, described in the following.
- It was found that the requirement on $\Delta\phi(Z, E_T^{\mathrm{miss}})$ could be lowered to 2.5, as also documented in the following.

Selection criterion	Main backgrounds suppressed
SFOS pair with $p_{\mathrm{T}} > 30, 20\,\mathrm{GeV}$, Medium ID	-
Veto on 3rd lepton with $p_{\mathrm{T}} > 7\,\mathrm{GeV}$, Loose ID	WZ
$76 < m_{ll} < 106\,\mathrm{GeV}$	WW, top, $Z \to \tau\tau$
$E_{\mathrm{T}}^{\mathrm{miss}} > 120\,\mathrm{GeV}$	Z + jets
$\Delta R_{\ell,\ell} < 1.8$	Z + jets, WW, top, $Z \to \tau\tau$
$\Delta\phi(Z, E_T^{\mathrm{miss}}) > 2.5$	Z + jets, WW, top, $Z \to \tau\tau$
$\min \Delta\phi(\mathrm{jet}_{p_{\mathrm{T}}>100\,\mathrm{GeV}}, E_{\mathrm{T}}^{\mathrm{miss}}) > 0.4$	Z + jets
$E_{\mathrm{T}}^{\mathrm{miss}}$-significance > 10.0	Z + jets
b-jet veto (at 85% WP)	top

Table 6.3: Summary of kinematic event selection criteria as applied in 2015-18 data analysis to select both ggF and VBF production events.

The distributions of all kinematic variables used as selection criteria are shown in Appendix B. Table 6.4 shows the relative acceptances of each selection cut, as well as the total relative acceptance with respect to the pre-selection level, for an example signal and the ZZ and Z + jets backgrounds. Each contribution is taken directly from MC simulation, no additional corrections are applied. In particular, the SHERPA ZZ samples are used here.

Compared to the 2015 and 2016 data analysis, the total acceptance of the example signal is increased by a few percent, while the ZZ background acceptance is decreased, mostly due to a significantly decreased acceptance of the $E_{\mathrm{T}}^{\mathrm{miss}}$ cut for this background. This could be an effect of using PFLOW based $E_{\mathrm{T}}^{\mathrm{miss}}$ reconstruction or due to the switch in generators (the 2015+16 data analysis used the POWHEG ZZ samples). On the other hand, the Z + jets background acceptance is similar to before, but since this is a small contribution compared to the dominant ZZ background the new signal region definition presents an improvement to the analysis.

Criterion	Rel. cut acceptance in %		
	$ggH600$ signal	ZZ background	Z + jets background
$76 < m_{ll} < 106\,\text{GeV}$	100.00	100.00	100.00
$E_{\text{T}}^{\text{miss}} > 120\,\text{GeV}$	93.29	2.95	0.02
$\Delta R_{\ell,\ell} < 1.8$	98.89	75.54	18.94
$\Delta\phi(Z, E_T^{\text{miss}}) > 2.5$	92.18	85.54	65.51
$\min\Delta\phi(\text{jet}_{p_{\text{T}}>100\,\text{GeV}}, E_{\text{T}}^{\text{miss}}) > 0.4$	97.87	96.22	39.57
$E_{\text{T}}^{\text{miss}}$significance > 10	91.04	86.61	13.12
B-jet veto	94.44	96.40	51.02
Total	71.56	1.53	7.20×10^{-5}

Table 6.4: Relative acceptances of the event selection criteria for an example NWA heavy Higgs signal with mass of 600 GeV produced in ggF, the ZZ and Z + jets background. The total acceptance of the kinematic selection is calculated with respect to the events passing the preselection, including the cut on m_{ll}.

Introducing $E_{\text{T}}^{\text{miss}}$ significance as a selection variable

While the Z + jets background contribution is already significantly reduced by the base event selection as given in Table 6.5, some contribution of Z + jets events with high, fake $E_{\text{T}}^{\text{miss}}$ remains. To suppress such events, the 2015-16 data analysis used two dedicated selection variables: the ratio $E_{\text{T}}^{\text{miss}}/H_{\text{T}}$ and the fractional p_{T} difference (cf. Chapter 5.1). For the full run II analysis, possible improvements by replacing these variables with the better performing object-based $E_{\text{T}}^{\text{miss}}$-significance was studied. Again, this study is based on the first part of the full dataset only, corresponding to the 2015-2017 data.

Base event selection
SFOS lepton pair, compatible with m_{ll}
$E_{\text{T}}^{\text{miss}} > 120\,\text{GeV}$
$\Delta R_{\ell,\ell} < 1.8$
$\min\Delta\phi(\text{jet}_{p_{\text{T}}>100\,\text{GeV}}, E_{\text{T}}^{\text{miss}}) > 0.4$
b-jet veto (at 85% WP)

Table 6.5: Selection criteria defining the *base selection*.

A detailed derivation of the $E_{\text{T}}^{\text{miss}}$-significance calculation can be found in [159], but the concepts are briefly described here: The idea behind the object-based $E_{\text{T}}^{\text{miss}}$-significance is to take into account the individual resolution of each object considered in the $E_{\text{T}}^{\text{miss}}$ reconstruction, to build a quantifier of how likely it is that the reconstructed $E_{\text{T}}^{\text{miss}}$ only originates from resolution effects or mismeasurements of the visible particles in the event. The higher the $E_{\text{T}}^{\text{miss}}$-significance value of an event is, the more likely it is that the observed $E_{\text{T}}^{\text{miss}}$ originates indeed from invisible particles, like neutrinos.

In particular, the (squared) $E_{\text{T}}^{\text{miss}}$ significance - $\mathscr{S}^2(E_{\text{T}}^{\text{miss}})$- is a log-likelihood ratio based test of the hypothesis that there are actually no invisible particles in the event, and therefore no real $E_{\text{T}}^{\text{miss}}$. This ratio is determined by maximizing the likelihood function, $\mathscr{L}\left(E_{\text{T}}^{\text{miss}} \,|\, p_{\text{T}}^{\text{inv}}\right)$ that the observed value of $E_{\text{T}}^{\text{miss}}$ is measured, given the total transverse momentum of invisible particles

- $p_{\mathrm{T}}^{\mathrm{inv}}$- under the conditions that $p_{\mathrm{T}}^{\mathrm{inv}} \neq 0$ and $p_{\mathrm{T}}^{\mathrm{inv}} = 0$. Meaning that:

$$\mathscr{S}^2(E_{\mathrm{T}}^{\mathrm{miss}}) = 2\ln\left(\frac{\max_{p_{\mathrm{T}}^{\mathrm{inv}}\neq 0}\mathscr{L}\left(E_{\mathrm{T}}^{\mathrm{miss}} \mid p_{\mathrm{T}}^{\mathrm{inv}}\right)}{\max_{p_{\mathrm{T}}^{\mathrm{inv}}=0}\mathscr{L}\left(E_{\mathrm{T}}^{\mathrm{miss}} \mid p_{\mathrm{T}}^{\mathrm{inv}}\right)}\right) \tag{6.1}$$

The likelihood function, $\mathscr{L}\left(E_{\mathrm{T}}^{\mathrm{miss}} \mid p_{\mathrm{T}}^{\mathrm{inv}}\right)$, can be derived from the probability density functions of all reconstructed objects, which quantifies how likely it is to measure the observed transverse moment p_{T} of the object, given its true value.

Assuming that these probability density functions are Gaussian, that all p_{T} measurements are independent of each other and that momentum is conserved in the transverse plane (meaning that the sum of all true, visible p_{T} equals $-p_{\mathrm{T}}^{\mathrm{inv}}$), it is found that $\mathscr{L}\left(E_{\mathrm{T}}^{\mathrm{miss}} \mid p_{\mathrm{T}}^{\mathrm{inv}}\right)$ depends on the difference between observed $E_{\mathrm{T}}^{\mathrm{miss}}$ and true invisible transverse momentum $p_{\mathrm{T}}^{\mathrm{inv}}$, as well the sum of Gaussian covariance matrices for all objects. The latter propagate the respective resolutions of each measurement. Here, all visible particles in the hard term need to be included, as well as a covariance matrix for the measurement of the soft term.

Given that σ_L^2 and σ_T^2 describe the total resolutions of both hard and soft term, in the longitudinal and transverse direction to $E_{\mathrm{T}}^{\mathrm{miss}}$ itself, the $E_{\mathrm{T}}^{\mathrm{miss}}$ significance takes the following form:

$$\mathscr{S}^2(E_{\mathrm{T}}^{\mathrm{miss}}) = \frac{|E_{\mathrm{T}}^{\mathrm{miss}}|^2}{\sigma_L^2(1-\rho_{LT}^2)} \tag{6.2}$$

with ρ_{LT}^2 describing the correlation between longitudinal and transverse measurement.

From this definition it becomes clear that indeed events with real $E_{\mathrm{T}}^{\mathrm{miss}}$ are characterized by large $E_{\mathrm{T}}^{\mathrm{miss}}$-significance : the denominator contains the resolution terms, so for a fixed value of $E_{\mathrm{T}}^{\mathrm{miss}}$ the $E_{\mathrm{T}}^{\mathrm{miss}}$ significance will be smaller the larger the resolutions, indicating that the measurement is more uncertain. Specifically, this also means that contributions from jets induced by pile-up decrease the $E_{\mathrm{T}}^{\mathrm{miss}}$ significance value.

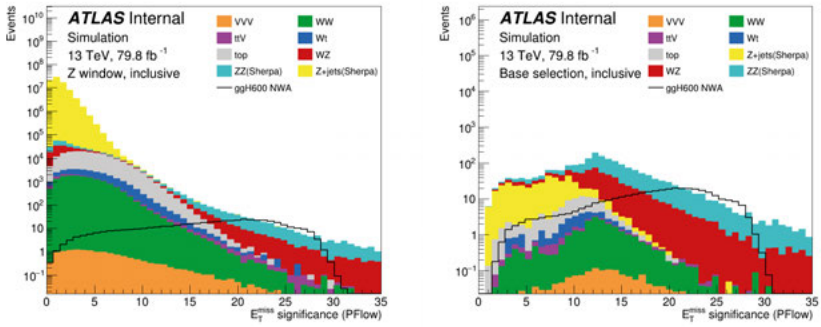

(a) At pre-selection level

(b) With base selection, as in table 6.5

Figure 6.4: Object-based $E_{\mathrm{T}}^{\mathrm{miss}}$ significance distributions for backgrounds and example signal at (a) pre-selection level and (b) with the base event selection. From MC simulation matching the 2015-17 data with an integrated luminosity of 79.8 fb^{-1}.

Figure 6.4 shows the $E_{\mathrm{T}}^{\mathrm{miss}}$-significance distributions for all events passing the pre-selection stage as well as those events passing the base event selection given in Table 6.5. Indeed, processes involving fake $E_{\mathrm{T}}^{\mathrm{miss}}$, such as Z + jets, tend to exhibit low values of the $E_{\mathrm{T}}^{\mathrm{miss}}$-significance < 10, while for processes with true $E_{\mathrm{T}}^{\mathrm{miss}}$ like the example signal or the ZZ background it takes larger values > 10. Using a cut on the $E_{\mathrm{T}}^{\mathrm{miss}}$-significance around 10 can therefore help in further suppressing fake $E_{\mathrm{T}}^{\mathrm{miss}}$ contributions, even after the base selection is already applied.

One concern when combining data from the runs in 2015-16, 2017 and 2018 is the different pile-up conditions between them, quantified by the average number of interactions per bunch crossing $\langle\mu\rangle$. It needs to be studied whether the $E_{\mathrm{T}}^{\mathrm{miss}}$ significance is efficient and well modelled also in high pile-up conditions. This is addressed by Figure 6.5 showing the distributions at the base selection level for events with low, medium or high pile-up. Due to the different running conditions, the region with $\langle\mu\rangle < 30$ is mostly populated by simulated events corresponding to data taking periods 2015-16, while the region with $\langle\mu\rangle > 50$ consists mostly of simulated events corresponding to data taking conditions in 2017. In all three regions the separation power between signal with real $E_{\mathrm{T}}^{\mathrm{miss}}$ and the Z + jets background with fake $E_{\mathrm{T}}^{\mathrm{miss}}$ is retained. The $E_{\mathrm{T}}^{\mathrm{miss}}$-significance is therefore suited as a selection variable for the full run II dataset.

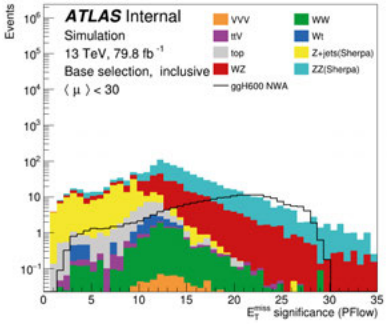

(a) Low pile-up, $\langle\mu\rangle < 30$

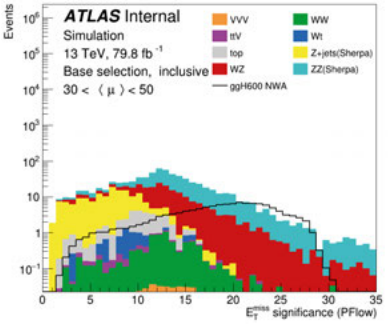

(b) Medium pile-up, $30 < \langle\mu\rangle < 50$

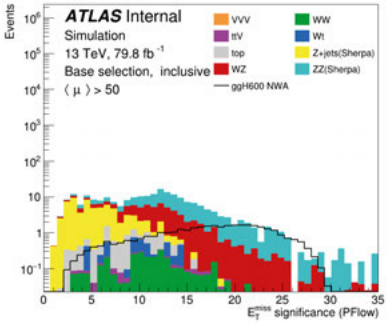

(c) High pile-up, $\langle\mu\rangle > 50$

Figure 6.5: Object-based $E_{\mathrm{T}}^{\mathrm{miss}}$ significance distributions after applying the base event selection in low, medium and high pile-up conditions, as defined by the $\langle\mu\rangle$ thresholds. From MC simulation matching the 2015-17 data with an integrated luminosity of 79.8 fb^{-1}.

An optimization scan is performed for the $E_{\mathrm{T}}^{\mathrm{miss}}$-significance with the ggH 600 GeV narrow-width heavy Higgs signal. Only events passing the base selection are considered, and cut values in the range from 5 to 15 are scanned through in steps of 0.2. At each point the bin-wise Asimov significance

$$Z_{\mathrm{Asimov}}^{\text{bin-wise}} = \sqrt{\sum_{\text{bin}} 2 \cdot ((S_{\text{bin}} + B_{\text{bin}}) \ln(1 + S_{\text{bin}}/B_{\text{bin}}) - S_{\text{bin}})} \tag{6.3}$$

is calculated as a figure of merit from the resulting m_{T} distributions, taking into account the different shapes between background and signal processes. The individual Asimov significances

for each m_T bin are summed in quadrature for this quantity.

To ensure the validity of the significance calculation, the m_T histograms are binned in a way that all bins with a non-zero signal contribution have at least 5 background events. An example m_T shapes plot with this binning is shown in Figure 6.6(a). Here the signal is normalized to the upper limit on its cross-section from the 2015 and 2016 data analysis.

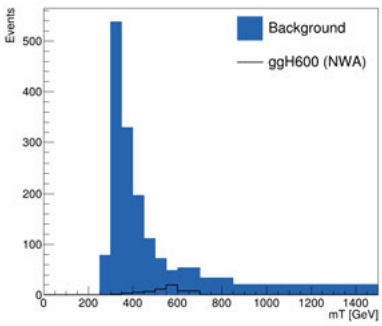

(a) Example m_T distributions

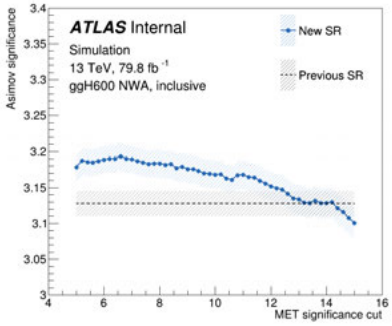

(b) Bin-wise significance scan

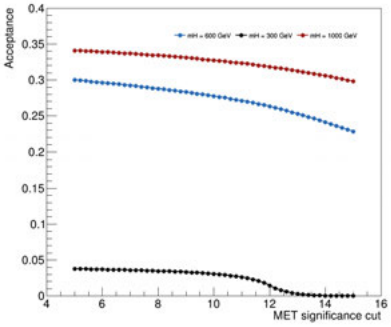

(c) Signal acceptances

Figure 6.6: (a) Example m_T distributions for background and example signal after applying the event selection including a cut on E_T^{miss} significance > 10, (b) bin-wise Asimov significance for different cut values of the E_T^{miss} significance and (c) corresponding values of the signal acceptance for different signal masses.

Figure 6.6(b) shows the resulting bin-wise significance for each probed cut value of the E_T^{miss} significance, compared to the significance obtained with the previous selection. The uncertainty band only takes statistical uncertainties into account. For any cut value of the E_T^{miss} significance lower than ≈ 12 a small improvement of the significance is evident. However, the dependency of

the significance on the cut value is fairly stable and slightly decreasing (only by about 2% for the full range scanned, and less than 0.9% in the range between 5 and 12), likely due to the loss of statistics with decreasing signal acceptance for higher cut values.

Fig. 6.6(c) therefore shows the signal acceptances over the scanned range. Since the search presented here covers a large mass range, two more signals are added - with m_H = 300 and 1000 GeV - in order to see the effect at different points in the search range. While the acceptance of the two higher mass signals is only slowly decreasing with tighter cuts (in accordance with the slowly decreasing significance), for the lowest mass point considered at 300 GeV there is a steeper decrease of acceptance for values above 11 that reaches 0 acceptance around a cut value of 13. To retain good acceptance for lower mass signals, a lower cut value is therefore better. However from these studies a choice of exact cut value is not obvious.

Therefore, the studies are extended using a more realistic figure of merit: The expected cross-section limit at 95% confidence, including rough estimates on the relative uncertainties for each background contribution. These uncertainties are estimated based on the results from the 2015 and 2016 data analysis and assigned as follows:

- 10% on the ZZ backgrounds
- 10% on the WZ background
- 50% on the Z + jets background
- 20% on background processes estimated from the $e\mu$ control region [2]

Now only the range between 5 and 11 is scanned, in steps of 1.

[2] In the following labelled as *other backgrounds*

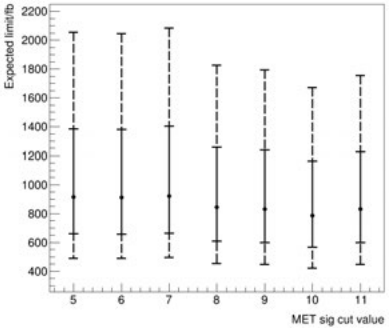

(a) m_H = 300 GeV

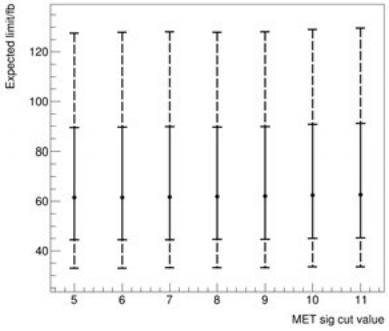

(b) m_H = 600 GeV

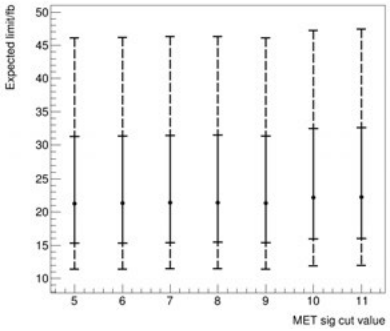

(c) m_H = 1 TeV

Figure 6.7: Expected limits for the three test mass points at different cut values of the $E_{\mathrm{T}}^{\mathrm{miss}}$ significance, when using estimated systematic uncertainties on each background contribution. The error bars indicate the 1σ (solid) and 2σ (dashed) uncertainties on the median expected limit.

The results of the limit setting are shown in Figure 6.7. For the two higher mass points of 600 GeV and 1 TeV the limits show only slight variation for different cut values. For this mass range, the Z + jets contribution is not important, as Z + jets processes typically exhibit a low transverse mass, m_{T}. At the 300 GeV mass point, the expected median limits however show a clearer optimum for the $E_{\mathrm{T}}^{\mathrm{miss}}$ significance cut at the value of 10, with the differences between each cut value here being in the order of several %. Taking all of this into account, a cut value of 10 is chosen for the $E_{\mathrm{T}}^{\mathrm{miss}}$ significance.

Re-optimizing the $\Delta\phi(Z, E_T^{\text{miss}})$ cut

Additionally, a short investigation into the $\Delta\phi(Z, E_T^{\text{miss}})$ cut was performed. As explained previously, this cut suppresses Z+jets events, since a large $\Delta\phi(Z, E_T^{\text{miss}})$ indicates that the $Z \to \ell\ell$ decay and $E_{\text{T}}^{\text{miss}}$ are in balance. This is expected for the signal process, where the heavy Higgs is produced and decays at rest, but less likely for Z+jets events where fake $E_{\text{T}}^{\text{miss}}$ arises. With the optimized usage of the cut on $E_{\text{T}}^{\text{miss}}$ significance, which was shown to be very effective at suppressing Z+jets already, the question arose how much discrimination power the cut on $\Delta\phi(Z, E_T^{\text{miss}})$ adds and whether it may be loosened to increase signal statistics.

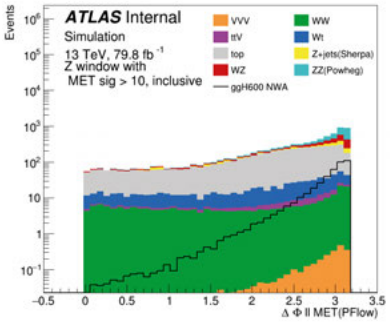

(a) $\Delta\phi(Z, E_T^{\text{miss}})$ with pre-selection, and $E_{\text{T}}^{\text{miss}}$-significance > 10

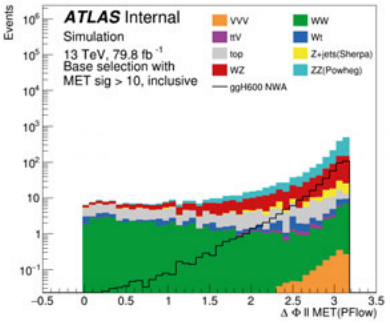

(b) $\Delta\phi(Z, E_T^{\text{miss}})$ with full selection, excluding $\Delta\phi(Z, E_T^{\text{miss}})$ cut

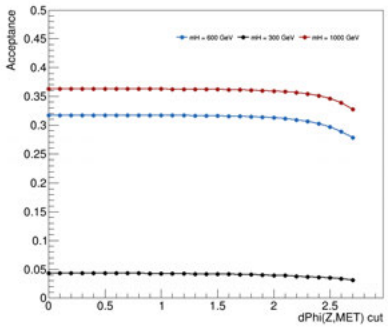

(c) Signal acceptances

Figure 6.8: Distributions of the $\Delta\phi(Z, E_T^{\text{miss}})$ when applying (a) only the pre-selection and a cut on $E_{\text{T}}^{\text{miss}}$ significance > 10 and (b) the full signal region selection without any cut on $\Delta\phi(Z, E_T^{\text{miss}})$ itself, as well as (c) signal acceptances for three example signals versus cut value of $\Delta\phi(Z, E_T^{\text{miss}})$.

Figures 6.8(a) and 6.8(b) show the $\Delta\phi(Z, E_T^{\text{miss}})$ distributions when applying only the pre-selection and a cut on $E_{\text{T}}^{\text{miss}}$ significance > 10, as well as when applying the full signal region selection, excluding the cut on $\Delta\phi(Z, E_T^{\text{miss}})$ itself. It is clear that a cut on high values of $\Delta\phi(Z, E_T^{\text{miss}})$ can improve background suppression, however it may indeed be beneficial to lower the previously used value of 2.7. This is confirmed by Figure 6.8(c), showing the signal acceptance versus $\Delta\phi(Z, E_T^{\text{miss}})$ cut value: a steep decrease is observed beyond $\Delta\phi(Z, E_T^{\text{miss}}) = 2.5$.

A comparison of the expected median limits between keeping the cut as it is and lowering it to 2.5 is shown in Table 6.6. The same setup as in the $E_{\text{T}}^{\text{miss}}$-significance optimization is used. Lowering the cut indeed improves the limits and thus, the cut value of $\Delta\phi(Z, E_T^{\text{miss}}) > 2.5$ is chosen.

	Median expected limit in fb		
$\Delta\phi(Z, E_T^{\text{miss}}) >$	$m_H = 300\,\text{GeV}$	$m_H = 600\,\text{GeV}$	$m_H = 1\,\text{TeV}$
2.5	542.57	40.94	13.57
2.7	606.14	42.07	13.87

Table 6.6: Median expected limits for the three test mass points at different cut values of $\Delta\phi(Z, E_T^{\text{miss}})$, when using estimated systematic uncertainties on each background contribution.

6.1.4 Event categorization

The strategy to classify events according to their (likely) production mode into a ggF and VBF category is the same as employed in the 2015 and 2016 data analysis. In fact, the optimization scans to define the VBF region, based on the di-jet properties m_{jj} and $|\Delta\eta_{jj}|$, were re-done, but came to the same conclusion [9]. The VBF selection criteria are summarized in Table 5.5.

Binning of the m_{T} distributions

New in the full run II VBF analysis is that the full m_{T} distribution is exploited, and not only the total event yield. Previously this was only done in the ggF category, but is now also possible for VBF events due to the increase in data statistics and an optimization of the m_{T} binning in the category. The m_{T} binning in the ggF category was also reoptimized.

Two criteria were considered in the binning optimization: First, bins with zero expected (backgrounds) events are avoided, as they might cause problems in the statistical interpretation. Especially for the VBF category this means that the binning has to be very coarse - only a total of four bins are used in the range from 100 GeV to 1700 GeV. In the ggF category on the other hand, there are enough expected background events especially at low m_{T} that up to m_{T} values of 1 TeV bins of width 50 GeV can be used. Beyond that the binning needs to be coarser. Second, the expected sensitivity or expected exclusion limit for a given m_{T} binning needs to be considered. The limit is affected by the m_{T} binning choice because the coarser the binning is, the less precise the shape information becomes. Coarser binning can have a significant impact on the limit especially on

the very high mass signals, as illustrated in Figure 6.9. As an example, the expected m_T distributions for the backgrounds and the 2 TeV signal are shown in the ggF category, with different binning: in (a) with bins of width 50 GeV across the whole range and in (b) with the optimized binning, using coarser bins at higher m_T. Here the signal shown is purely for illustration purposes and normalized to an arbitrary cross-section. The first choice is not chosen because there are several empty bins. This is not the case for the optimized binning, but the loss of sensitivity is clearly reflected in the $S/\sqrt{(S+B)}$ ratio.

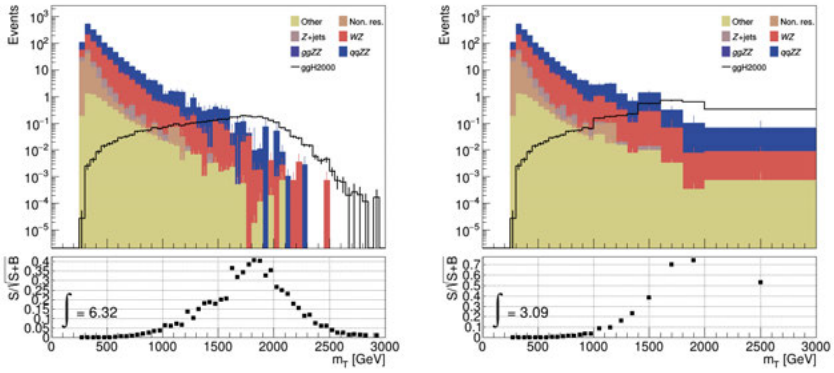

(a) 50 GeV bins across the whole range

(b) Optimized binning, with coarser bins > 1 TeV

Figure 6.9: Examples of m_T binning in the ggF category: (a) shows the m_T distributions for all backgrounds and the highest mass signal at 2 TeV with a fine binning of 50 GeV bins across the whole range, and (b) shows the same distributions but with the optimized binning, that exhibits no bins with zero expected backgrounds.

The final, optimal binning choices are shown in Figure 6.10 for both categories. Signals of three different masses are shown in addition to the optimized background, normalized to arbitrary cross-sections. In both categories, the final bin also includes all events beyond the upper boundary. This is especially important in the VBF category, where the range ends at 1.7 TeV. All VBF signals with masses above 1.7 TeV have a significant fraction of entries in the last bin, making the VBF measurement effectively a counting experiment for high signal masses.

6.1.5 Signal acceptances

It is important to study the signal acceptance as a function of the mass to ensure that not too many events are rejected by the kinematic cuts. Figure 6.11 shows the signal acceptances for ggF signals in the ggF category and VBF signals in the VBF category. The acceptance is defined as the number of weighted events in the respective signal region divided by the total sum of event weights in the MC sample. The event weights include generator level weights, as well as exper-

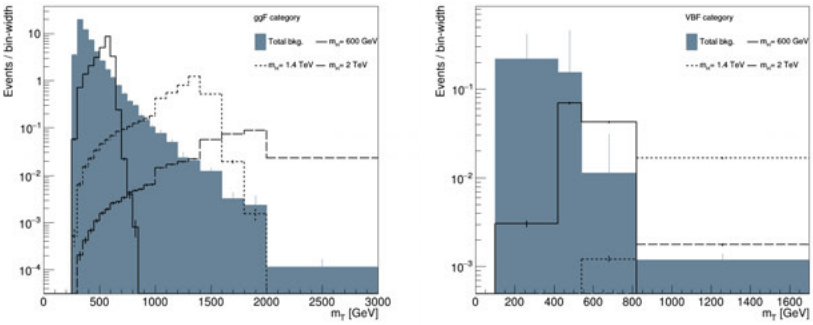

(a) ggF category (b) VBF category

Figure 6.10: Optimized m_{T} binning in the (a) ggF and (b) VBF category. Shown for the total expected background, as well as three example signals of different mass. The signals are normalized to arbitrary cross-sections. In both cases the final m_{T} bin includes all events beyond the boundary.

imental weights correcting efficiencies in MC simulation to match those in data, and need to be taken into account as their distributions may not be uniform across the phase space. Signal acceptances are calculated separately for the two flavour channels defined in this analysis. The total acceptance of signal events is then the sum of partial $eevv$ and $\mu\mu vv$ acceptances.

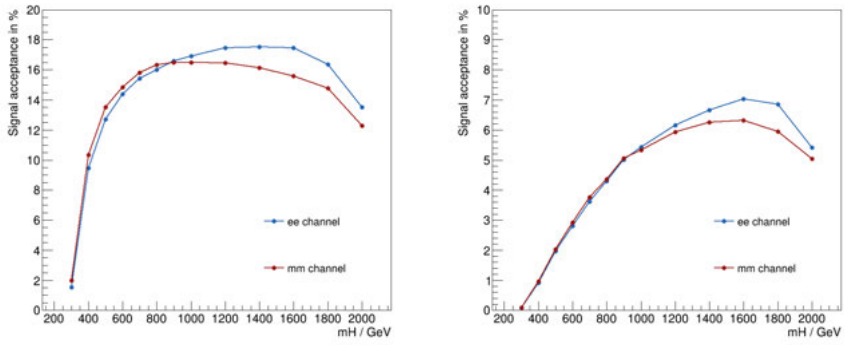

(a) ggF signals (b) VBF signals

Figure 6.11: Signal acceptances for NWA heavy Higgs signals at different mass points, produced in the (a) ggF and (b) VBF production mode.

The acceptance of ggF signals in the ggF category is higher than that of VBF signals in the VBF

category, with the former reaching maximal values between 16 and 18% for the two flavour channels, and the latter only between 6 and 8% . This is explained by the stringent requirements made on the jet transverse momenta and di-jet properties defining the VBF category, that reject about 50% of the VBF signal events.

In both categories, the acceptance is lowest for the lowest mass point of 300 GeV due to the high $E_{\mathrm{T}}^{\mathrm{miss}}$ cut. It then rises fairly steeply with increasing mass (as the signals get further away from being cut off on the lower bound by the $E_{\mathrm{T}}^{\mathrm{miss}}$ cut) reaching maximal values for signals above 1 TeV. In the muon channel above 800 GeV the acceptance starts to drop with respect to the electron channel due to the fact that (radiative) high p_{T} muons are more difficult to reconstruct than electrons.

At masses above 1.5 TeV the acceptance drops for both channels. This is (likely) caused by the fact that the lepton pairs produced from such high mass Higgs decays are strongly boosted, resulting in the two leptons being so close to each other that the lepton isolation criteria are no longer fulfilled.

6.2 Background estimates

Due to the updated selection the background composition as shown in Figure 6.12 is slightly changed in comparison to the 2015 and 2016 data analysis (cf. Chapter 5.2). Still, almost two thirds of the background are due to ZZ events and nearly another third originates from WZ processes. More noticeable is the change in the Z+jets and non-resonant dilepton background relative contributions: Z+jets now contributes as little as 4% (previously 6%), which is likely due to the usage of the more efficient $E_{\mathrm{T}}^{\mathrm{miss}}$-significance variable. On the other hand, the non-resonant dilepton contribution increased to 5% (from 3%).

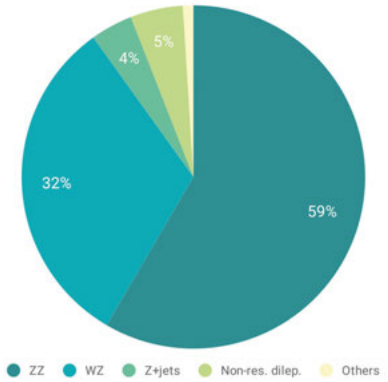

Figure 6.12: Background composition in the signal region.

Most of the background estimation methods follow the same principle as in the 2015 and 2016 data analysis, but there are two major updates:

- The overall ZZ normalisation is derived from the data in the signal region, using a floating normalisation factor in the fit.
- The Z+jets background is estimated from a one-dimensional sideband, defined by the $E_{\mathrm{T}}^{\mathrm{miss}}$- significance variable.

The remaining background estimates follow the same strategy as before, with minor updates:

- The WZ normalisation is estimated from data using the 3ℓ control region.
- The non-resonant dilepton background yield is estimated from data using the $e\mu$ control region.
- The minor *other* backgrounds (consisting of $t\bar{t}V$, VVV and W+jets) are estimated from simulation. Their total contribution is smaller than 0.5% .

6.2.1 ZZ modelling

Constraining the ZZ normalisation with signal region data It is possible to constrain the total yield of the ZZ background using the observed data in the signal region. This is done by introducing a normalisation factor - μ_{ZZ}- into the likelihood, that scales both the $q\bar{q}ZZ$ and $ggZZ$ process. In the final fit this parameter is allowed to float. The main advantage is that the analysis now depends less on the predictions for the total ZZ background normalisation

from theory. In the $\ell\ell\nu\nu$ analysis one common μ_{ZZ} factor is used for both the ggF and VBF category.

With this approach, systematic uncertainties on the total ZZ yields should no longer play a role, as the prediction is derived from the data. However, since both $q\bar{q}ZZ$ and $ggZZ$ are scaled with the same normalisation factor, even though they are different processes with different kinematics, the relative uncertainties on the $q\bar{q}ZZ$ and $ggZZ$ acceptance need to be taken into account. Chapter 6.3.3 describes how the relative uncertainties are determined. On top of that, m_{T} shape uncertainties on the ZZ processes still need to be included, presented in Chapter 6.3.2.

To check that the sensitivity is not impacted, likelihood scans and expected limits with a free μ_{ZZ} were compared to the case of fixing the ZZ background to its MC prediction [140]. Early estimates for systematic uncertainties of both experimental and theory origin were included. Indeed, the results in both cases were found to be very similar: leaving the normalisation free worsened the expected limits by less than 1% .

While the ZZ normalisation is now derived from data, the corresponding shapes of the m_{T} distributions are fully based on MC simulation. In the 2015-2018 data analysis an improvement in accuracy of the m_{T} shape prediction was made by using SHERPA 2.2.2 samples for the ZZ process (cf. Chapter 4.2 for details and a comparison of generators).

Higher order EW corrections to $q\bar{q}ZZ$ Corrections to achieve NLO accuracy in EW effects are applied to the $q\bar{q}ZZ$ simulation, using a k-factor derived from theory calculations following [160]. The effect of the EW correction is shown in Figure 6.13. Here, the EW corrections are applied as event weights (based on the truth $E_{\mathrm{T}}^{\mathrm{miss}}$) at the pre-selection level and o nly $q\bar{q} \rightarrow ZZ \rightarrow llvv$ events are considered. As described in [160] the EW corrections can be applied either in addition to the QCD effects, or as a multiplication. It is not clear which of the two is the correct option. Therefore, the central k-factor here corresponds to the average of both options, and an uncertainty is assigned from the difference between the two approaches. This uncertainty is indicated by the shaded area in Figure 6.13. Indeed the EW corrections are sizeable, leading to an overall decrease of the $q\bar{q}ZZ$ yield by about 10% and they are particularly large for high m_{T} where the uncorrected $q\bar{q}ZZ$ events are scaled down by as much as 30% .

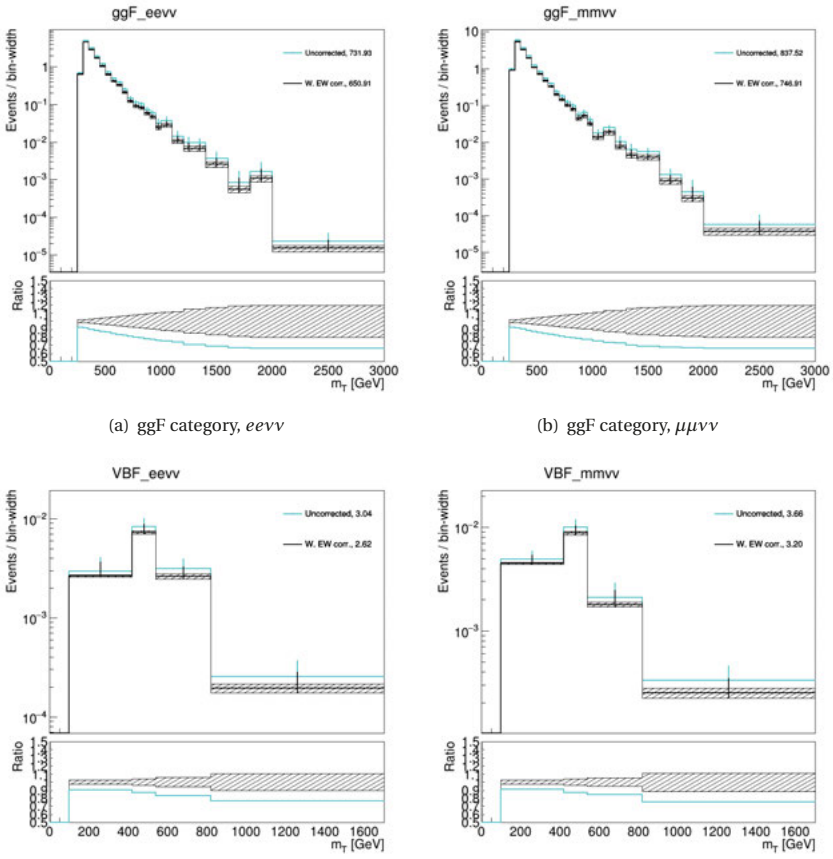

(a) ggF category, $eevv$

(b) ggF category, $\mu\mu vv$

(c) VBF category, $eevv$

(d) VBF category, $\mu\mu vv$

Figure 6.13: Effect of applying the k-factor for EW corrections to the $q\bar{q}ZZ$ contribution, and its associated uncertainties.

Higher order QCD corrections to $ggZZ$ The $ggZZ$ simulation with SHERPA provides LO accuracy in QCD effects and therefore the flat k-factor of 1.7 is applied again, as described in Chapter 5.2.1.

$qqZZjj$ EW contribution In contrast to the previous analysis, the contribution from the EW production of a ZZ pair with two additional jets via vector boson scattering, $qqZZjj$ EW, is now included as a separate background template. The corresponding sample is generated with

SHERPA 2.2.1. However, this background is small: it contributes less than 1% to the total background in the ggF category, and around 10% in the VBF category. For this reason, and because the VBF region has very low statistical power, the $qqZZjj$ EW contribution is not scaled with the floating normalisation factor μ_{ZZ}.

6.2.2 WZ estimate from 3ℓ control region

As explained previously, $WZ \to \ell\nu\ell^+\ell^-$ events with one non-reconstructed lepton constitute the second largest background and can be estimated from a 3ℓ control region. More details on this approach are given in Chapter 5.2.2, the focus here is on the updated results.

Table 6.7 lists the selection criteria defining the 3ℓ control region. To improve the purity of the control region further (up to 92%), a cut on the $E_{\mathrm{T}}^{\mathrm{miss}}$-significance variable is introduced. A VBF-like category is defined from all events with at least two jets, and the remainder of events is treated as ggF-like.

Figure 6.14 shows the $E_{\mathrm{T}}^{\mathrm{miss}}$ distributions in the 3ℓ control region for the two categories, for data and MC simulation. Here, only the statistical uncertainty is shown, and no further corrections are applied to the simulation.

Selection criterion
SFOS lepton pair with $p_{\mathrm{T}} > 30, 20\,\mathrm{GeV}$
Third lepton with $p_{\mathrm{T}} > 20\,\mathrm{GeV}$
$76 < m_{ll} < 106\,\mathrm{GeV}$
$m_{\mathrm{T}}(W) > 60\,\mathrm{GeV}$
$E_{\mathrm{T}}^{\mathrm{miss}}$-significance > 3
b-jet veto (at 85% WP)

Table 6.7: Definition of the 3ℓ control region used to estimate the WZ background.

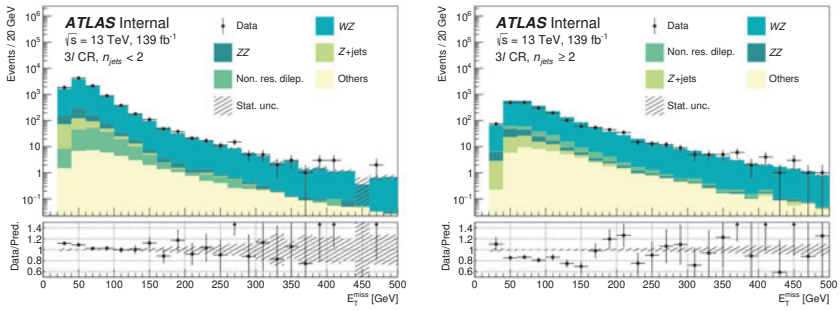

(a) ggF-like events

(b) VBF-like events

Figure 6.14: $E_{\mathrm{T}}^{\mathrm{miss}}$ distributions in the 3ℓ control region, for (a) ggF-like and (b) VBF-like events. Only the statistical uncertainty is shown, and all contributions are directly from MC simulation, without additional corrections. The last bin includes all events beyond the boundary shown.

For the full run II analysis the WZ process is generated with SHERPA, instead of the previously used POWHEG. While both samples technically have an accuracy of NLO in QCD effects, the SHERPA samples include some higher order corrections, such as multi-jet matrix elements. For this reason, the WZ cross-sections predicted by SHERPA agree more closely with the measured values [136]. As the data from the 3ℓ region is used to correct the WZ yield in this analysis anyway, it does not matter that these corrections were not included previously, but the change of generator choice has an impact on the observed scale-factors. For the full run II analysis, with the SHERPA samples, the scale-factors are:

$$\begin{aligned} \mathrm{SF}_{WZ}(\text{ggF-like}) &= 1.074 \pm 0.009(\text{stat.}) \pm 0.052(\text{syst.}) \\ \mathrm{SF}_{WZ}(\text{VBF-like}) &= 0.85 \pm 0.05(\text{stat.}) \pm 0.27(\text{syst.}) \end{aligned} \tag{6.4}$$

Especially the ggF-like value is now very close to 1, with a very small statistical uncertainty. The systematic uncertainties are estimated from the transfer-factor in the same way as described in Chapter 5.2.2. For the final result they are propagated separately for each source, instead of grouped into one total uncertainty as previously done. This separate treatment allows to keep track of correlations between uncertainties from the same source between different processes.

6.2.3 Z + jets background estimation from a 1D sideband

For the analysis of the full run II data set, the Z + jets background contribution is estimated from data using a *one-dimensional sideband method*. This simpler method replaces the previously used *ABCD* approach.

The sideband control region is defined by inverting the $E_{\mathrm{T}}^{\mathrm{miss}}$-significance requirement, since this variable exhibits good separation power between Z + jets and processes with genuine missing transverse energy. To increase the purity even further, the $E_{\mathrm{T}}^{\mathrm{miss}}$-significance requirement is not only inverted but also lowered to 9. The control region and sideband region are therefore disjoint, as illustrated in the schematic shown in Figure 6.15. Furthermore, to enhance the statistics in the sideband, the requirement on $\min\Delta\phi(\mathrm{jet}_{p_{\mathrm{T}}>100\,\mathrm{GeV}}, E_{\mathrm{T}}^{\mathrm{miss}})$ is dropped. All other selection criteria are unchanged, as summarized in Table 6.8.

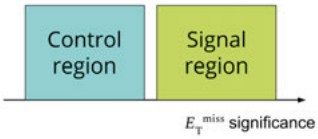

Figure 6.15: Schematic of the definition of the Z + jets one-dimensional sideband region.

Selection criterion
SFOS lepton pair with $p_{\mathrm{T}} > 30, 20\,\mathrm{GeV}$
$76 < m_{ll} < 106\,\mathrm{GeV}$
$E_{\mathrm{T}}^{\mathrm{miss}} > 120\,\mathrm{GeV}$
$\Delta\phi(Z, E_T^{\mathrm{miss}}) > 2.5$
$E_{\mathrm{T}}^{\mathrm{miss}}$-significance < 9
b-jet veto (at 85% WP)

Table 6.8: Definition of the sideband control region used to estimate the Z + jets background for the 139 fb^{-1} analysis.

The Z + jets contribution in the signal region, $N_{\mathrm{SR}}(Z + \text{jets})$, is then estimated as

$$N_{\mathrm{SR}}(Z + \text{jets}) = N_{\mathrm{CR}}^{\mathrm{data}}(Z + \text{jets}) \cdot \frac{N_{\mathrm{SR}}^{\mathrm{MC}}(Z + \text{jets})}{N_{\mathrm{CR}}^{\mathrm{MC}}(Z + \text{jets})} \tag{6.5}$$

with $N_{\mathrm{CR}}^{\mathrm{data}}(Z+\mathrm{jets})$ and $N_{\mathrm{CR}}^{\mathrm{MC}}(Z+\mathrm{jets})$ describing the number of $Z+$jets events in the sideband for data and MC respecitively and $N_{\mathrm{CR}}^{\mathrm{MC}}(Z+\mathrm{jets})$ the number of MC simulated $Z+$jets events in the signal region. To obtain $N_{\mathrm{CR}}^{\mathrm{data}}(Z+\mathrm{jets})$ non-$Z+$jets contributions are subtracted from the data in the sideband.

The estimate of the $Z+$jets contribution is done separately for the ggF and VBF category. Figure 6.16 shows the missing transverse energy distributions in the two sideband categories: in both regions, the pure MC prediction does not describe the observed data distribution well, emphasising again the need for a data-driven method to model the $Z+$jets background.

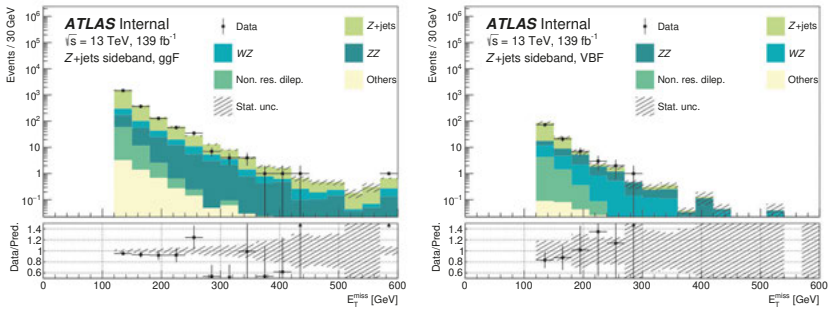

Figure 6.16: $E_{\mathrm{T}}^{\mathrm{miss}}$ distributions in the one-dimensional sideband control region, for ggF-like and VBF-like events. Only the statistical uncertainty is shown, and all contributions are directly from MC simulation, without additional corrections. The last bin includes all events beyond the boundary shown.

The main advantage of this method compared to the *ABCD* approach is that there are no complications arising due to defining regions based on correlated variables. However, a disadvantage is that it fully relies on MC simulation to estimate the ratio of $Z+$jets events between signal and control regions, which may not be well modelled. This is the leading source of systematic uncertainty for the sideband method.

In particular, the impact of systematic uncertainties is determined by comparing this ratio for the nominal case and each variation. In the ggF category, the experimental uncertainties have the largest impact, with a total uncertainty of 30 to 40% , depending on the flavour channel. Jet and $E_{\mathrm{T}}^{\mathrm{miss}}$ related uncertainties are the leading contributors here, in accordance with the fact that only $Z+$jets events with fake $E_{\mathrm{T}}^{\mathrm{miss}}$ due to mismeasurements enter the signal region. Theory uncertainties, due to choice of QCD scale, PDF, parton showering model and generator are also considered and have an impact of roughly 15% in the ggF region. Additionally a methodology uncertainty is assigned by varying the cuts defining the sideband, resulting in a 3% additional uncertainty, compared to a 15% statistical uncertainty.

In contrast, in the low-statistics VBF region, the statistical uncertainty is around 60%. Here the methodology uncertainty is large: varying the $E_{\mathrm{T}}^{\mathrm{miss}}$- significance requirement impacts the ratio by 20% and varying the VBF defining m_{jj} and $|\Delta\eta_{jj}|$ criteria even has an effect of another 70%. Theory uncertainties are of the order of 40% and largely driven by the QCD scale uncer-

tainty.

In total, a systematic uncertainty of around 30% is assigned to the estimate in the ggF category and of around 80% in the VBF category. While these uncertainties are large, they are still smaller than the uncertainties on a purely MC-based estimate, which are close to 100%.

Comparing the results of the data-driven approach with the pure MC prediction, the following ratios are measured:

$$N_{\mathrm{SR}}^{\text{data-driven}}(Z+\text{jets})/N_{\mathrm{SR}}^{\mathrm{MC}}(Z+\text{jets})(\text{ggF}) = 0.91 \pm 0.11(\text{stat.}) \pm 0.41(\text{syst.}) \tag{6.6}$$
$$N_{\mathrm{SR}}^{\text{data-driven}}(Z+\text{jets})/N_{\mathrm{SR}}^{\mathrm{MC}}(Z+\text{jets})(\text{VBF}) = 0.82 \pm 0.50(\text{stat.}) \pm 0.65(\text{syst.})$$

, i.e. in both categories the data-driven yield is smaller than the MC expectation.

Besides correcting the total Z + jets yield using the data in the sideband, also the transverse mass distribution in the signal region is derived from the sideband. A bin-by-bin transfer function is used to translate the m_{T} shape from the sideband to the m_{T} shape in the signal region. The resulting distributions are compared to the MC prediction in Figure 6.17. To show only the pure shape effect, the distributions are normalized to unit area. In most bins, the two yields agree within the statistical errors shown.

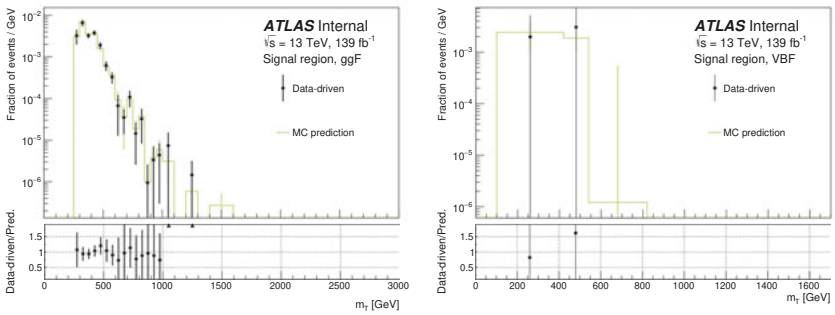

(a) ggF category (b) ggF category

Figure 6.17: m_{T} distributions in the signal region as derived from MC simulation or from the sideband data, for (a) ggF-like and (b) VBF-like events. Only the statistical uncertainty is shown. Bin contents are divided by the respective bin width.

6.2.4 Non-resonant dilepton backgrounds estimate from $e\mu$ control region

The non-resonant dilepton background yield is estimated from data using the $e\mu$ control region, following the same method as already described in Chapter 5.2.4. The $e\mu$ control region is defined with the exact same kinematic selection as the signal region (see Table 6.3), but requiring an opposite flavour lepton pair instead. The corrected yield estimate is then derived separately for

the ggF and VBF category. However, as already previously encountered, when applying the full VBF categorization no data events remain. Therefore, the VBF region is defined only from events containing at least 2 jets and an MC based transfer factor is used to extrapolate the effect of the m_{jj} and $|\Delta\eta_{jj}|$ requirements. Figure 6.18 shows the missing transverse energy distributions in the two categories of the $e\mu$ control region.

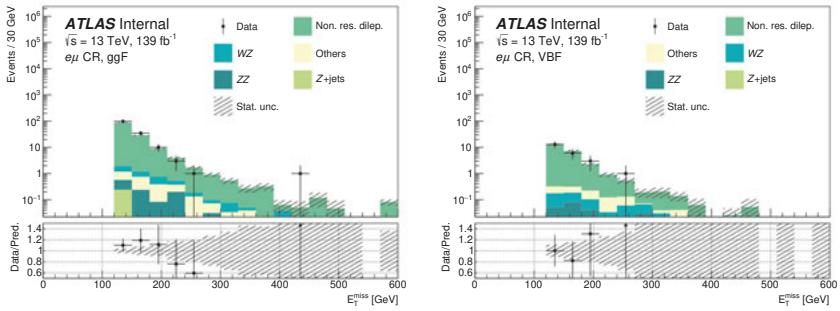

(a) ggF category (b) VBF category

Figure 6.18: $E_{\mathrm{T}}^{\mathrm{miss}}$ distributions in the $e\mu$ control region, for (a) ggF-like and (b) VBF-like events. Only the statistical uncertainty is shown and all contributions are obtained from MC simulation, without additional corrections. The last bin includes all overflow events.

Comparing the final data-driven estimates with the MC prediction, the following ratios are measured:

$$N_{\mathrm{SR}}^{\text{data-driven}}(\text{Non-res. dilep.})/N_{\mathrm{SR}}^{MC}(\text{Non-res. dilep.})(\text{ggF}) = 1.03 \pm 0.09(\text{stat.}) \pm 0.02(\text{syst.}) \quad (6.7)$$
$$N_{\mathrm{SR}}^{\text{data-driven}}(\text{Non-res. dilep.})/N_{\mathrm{SR}}^{MC}(\text{Non-res. dilep.})(\text{VBF}) = 0.92 \pm 0.21(\text{stat.}) \pm 0.62(\text{syst.})$$

Here, the systematic uncertainty in the ggF category includes the methodology related uncertainties, due to the statistical error on the $\epsilon(p_{\mathrm{T}},\eta)$ factor and the choice of its binning as well as the non-closure on MC, as described previously. For the VBF category, the transfer factor modelling the acceptance of the m_{jj} and $|\Delta\eta_{jj}|$ requirements is based on MC simulation, so all uncertainties from experimental sources on this transfer factor have to be included. This leads to a much larger uncertainty of around 60%.

6.3 Systematic uncertainties

An overview of the systematic uncertainties for each process is given in Table 6.9. As previously explained, each systematic uncertainty has an impact on both the total yield and m_{T} shape of the process, but not all impacts are always relevant for the final results. Which impacts can be neglected for which processes will be clarified in the following.

	Experimental sources			
Process	**Reconstruction**	**Data-driven**	**Luminosity**	**Theory**
Signal	✓	-	✓	✓
ZZ	✓	✓	-	✓
WZ	✓	✓	-	✓
Z + jets	✓	✓	-	✓
Non-res. dilep.	✓	✓	-	-
Others	✓	-	✓	-

Table 6.9: Overview of systematic uncertainty sources considered for each process.

In general, uncertainties of experimental origin - related to the event reconstruction or to a particular data-driven estimation method - are included for all processes, while theory uncertainties on minor backgrounds are neglected. For signal and other backgrounds, the luminosity uncertainty is propagated as they are the only processes fully relying on MC simulation.

Compared to the 2015 and 2016 data analysis, the ZZ background systematics are different because the normalisation is now derived from data. There is now also a data-driven uncertainty component on the total ZZ yield, and relative $q\bar{q}ZZ$ to $ggZZ$ acceptance uncertainties need to be included as explained in Chapter 6.3.3.

The uncertainties on the WZ background are propagated source by source as separate nuisance parameters, allowing to retain correlations between the experimental systematics for different processes. For the less relevant Z + jets and non-resonant dilepton backgrounds only one total systematic and one statistical uncertainty each are assigned.

6.3.1 Experimental uncertainties

The different groups of experimental uncertainties, their origins and their typical sizes were already described in Chapter 5.3.1. In principle, all of this is unchanged and also valid for the analysis of the full run II dataset. However, the ATLAS reconstruction software is an ever evolving project, and especially in view of high precision analyses becoming possible, significant efforts were taken to reduce uncertainties. This can be achieved by using improved algorithms, such as for example the use of a dynamical cell clustering algorithm for the reconstruction of electrons, as described in Chapter 2.3.1. But a reduction of systematic uncertainties is also natural in some cases due to the increased dataset size - as the statistical uncertainty of e.g. calibration samples used is also part of the eventual reconstruction systematic. In other cases the systematics were re-evaluated and increased a bit instead. For example, while the uncertainties on the muon reconstruction efficiency could be further decreased with the full run II dataset, the uncertainty on the muon momentum scale calibration actually increased. Instead of going into more detail on all the changes in general, the most important experimental uncertainties on the signal and ZZ background are discussed in the following.

Before doing so it should however also be noted that not only the sizes of uncertainties change with further development of the reconstruction software, but also more detailed experimental sources were considered. The full run II analysis presented here considered a total of 95 separate nuisance parameters for the reconstruction uncertainties: 40 related to the electron and 14 to the muon reconstruction and efficiency, 35 covering the jet and flavour tagging associated uncertainties, 3 for the $E_{\mathrm{T}}^{\mathrm{miss}}$ reconstruction uncertainties and 1 quantifying the uncertainty of the pile-up reweighting. Most of them however have small impact, and in the final fit (normalisation) systematics are excluded if their relative impact is below 0.1%. This new scheme, where more uncertainties are decorrelated, is more suited for a combination of the results with other channels.

Table 6.10 shows the leading five and total experimental uncertainties on the $q\bar{q}ZZ$ and $ggZZ$ background and an example signal at m_H =600 GeV with a narrow width and with a large width of $\Gamma_H = 0.15\ m_H$ in the ggF category. For both signals and ZZ backgrounds the total experimental uncertainty ranges between 2% to 4% and uncertainties related to the jet reconstruction, lepton efficiencies and the pile-up reweighting play leading roles. Specifically for the two signals under different width assumptions the impacts of experimental uncertainties are nearly identical.

The uncertainty due to the jet flavour composition is dominant for all processes, its origin is as follows: For the calibration dedicated MC samples are used assuming a given fraction of jets initiated by quarks compared to jets initiated by gluons. This fraction may not match the actual fraction of jet types as in the analysis' phase space, and therefore leads to the flavour composition uncertainty. Previously, in the analysis of the 2015 and 2016 dataset, this uncertainty was not considered.

(a) $q\bar{q}ZZ$ background

eevv **channel**			*μμvv* **channel**		
Uncertainty source	**Impact in %**		**Uncertainty source**	**Impact in %**	
Jet Flavour Composition	1.30	-1.45	Jet Flavour Composition	1.15	-1.59
Jet energy resolution (NP 1)	-1.06	1.06	Muon reconstruction efficiency	-0.52	0.92
Pile-up reweighting	1.04	-0.79	Jet energy scale (Pile-up NP 1)	0.59	-0.88
Electron energy scale	-0.91	0.80	Jet energy scale (Pile-up NP 4)	0.65	-0.85
Jet energy scale (Pile-up NP 4)	0.88	-0.72	Jet energy scale	0.68	-0.85
Total	**3.12**	**3.28**	**Total**	**2.62**	**3.22**

(b) $ggZZ$ background

eevv **channel**			*μμvv* **channel**		
Uncertainty source	**Impact in %**		**Uncertainty source**	**Impact in %**	
Jet Flavour Composition	1.91	-1.96	Jet Flavour Composition	1.77	-1.83
Jet energy scale (Pile-up NP 4)	1.11	-1.10	Jet energy resolution (NP 1)	-1.44	1.44
Pile-up reweighting	1.01	-0.48	Jet energy scale	1.01	-1.08
Jet energy scale	1.01	-0.99	Jet energy scale (Pile-up NP 1)	0.83	-1.06
Jet energy scale (Pile-up NP 1)	0.84	-0.96	Jet energy scale (Pile-up NP 4)	1.01	-0.89
Total	**3.76**	**3.90**	**Total**	**3.79**	**3.99**

(c) ggH signal at m_H = 600 GeV (NWA)

eevv **channel**			*μμvv* **channel**		
Uncertainty source	**Impact in %**		**Uncertainty source**	**Impact in %**	
Jet Flavour Composition	1.22	-1.37	Jet Flavour Composition	1.26	-1.31
Electron identification efficiency (NP 8)	-0.34	0.98	Muon reconstruction efficiency	-0.58	1.24
Jet energy scale	0.66	-0.80	Jet energy scale	0.72	-0.77
Jet energy scale (Pile-up NP 1)	0.57	-0.79	Jet energy scale (Pile-up NP 1)	0.57	-0.73
Pile-up reweighting	0.78	-0.17	Muon isolation efficiency	-0.08	0.72
Total	**3.12**	**3.56**	**Total**	**3.12**	**3.50**

(d) ggH signal at m_H = 600 GeV, Γ_H =15%m_H

eevv **channel**			*μμvv* **channel**		
Uncertainty source	**Impact in %**		**Uncertainty source**	**Impact in %**	
Jet Flavour Composition	1.42	-1.50	Jet Flavour Composition	1.39	-1.48
Electron identification efficiency (NP 8)	-0.31	1.05	Muon reconstruction efficiency	-0.56	1.30
Jet energy scale	0.83	-0.87	Jet energy scale	0.79	-0.85
Pile-up reweighting	0.83	-0.16	Jet energy scale (Pile-up NP 1)	0.63	-0.78
Jet energy scale (Pile-up NP 4)	0.75	-0.79	Muon isolation efficiency	-0.04	0.77
Total	**3.52**	**3.96**	**Total**	**3.52**	**3.92**

Table 6.10: Leading experimental uncertainties on (a) the $q\bar{q}ZZ$ background yields, (b) the $ggZZ$ background yields in the signal region and the signal acceptance for a heavy Higgs signal of mass 600 GeV with (c) negligible and (d) 15% width, for the ggF category. The last row lists the total impact of experimental certainties, including those not shown in this list.

(a) $q\bar{q}ZZ$ background

$eev\nu$ **channel**			$\mu\mu\nu\nu$ **channel**		
Uncertainty source	**Impact in %**		**Uncertainty source**	**Impact in %**	
Jet energy resolution (NP 1)	-26.03	26.03	Jet Flavour Composition	-9.32	16.99
Jet Flavour Composition	-3.78	13.29	Jet energy scale	-10.51	13.01
Jet energy resolution	-10.35	10.35	Jet energy resolution (NP 1)	-11.77	11.77
Jet energy resolution (NP 2)	-9.51	9.51	Jet energy resolution (NP 2)	-9.87	9.87
Jet energy resolution (NP 6)	-9.24	9.24	Jet Flavour Response	1.92	-9.26
Total	**35.62**	**38.43**	**Total**	**29.49**	**34.74**

(b) $ggZZ$ background

$eev\nu$ **channel**			$\mu\mu\nu\nu$ **channel**		
Uncertainty source	**Impact in %**		**Uncertainty source**	**Impact in %**	
Jet Flavour Composition	-8.43	9.68	Jet Flavour Composition	-12.47	17.95
Jet energy scale	-5.69	9.07	Jet energy scale (Pile-up NP 1)	-4.50	12.13
Jet Flavour Response	5.82	-3.49	Jet energy scale	-5.49	11.82
Jet energy scale (Pile-up NP 1)	-5.20	4.15	Jet energy resolution (NP 3)	-9.99	9.99
Jet energy scale (Pile-up NP 4)	-4.66	4.51	Jet energy resolution (NP 1)	-9.31	9.31
Total	**16.13**	**18.30**	**Total**	**24.10**	**32.56**

(c) VBF signal at m_H = 600 GeV (NWA)

$eev\nu$ **channel**			$\mu\mu\nu\nu$ **channel**		
Uncertainty source	**Impact in %**		**Uncertainty source**	**Impact in %**	
Jet Flavour Composition	-2.21	2.04	Jet Flavour Composition	-2.64	2.04
Jet energy scale	-1.69	1.74	Jet energy scale	-1.92	1.85
Jet energy scale (Pile-up NP 1)	-0.88	1.12	Jet energy scale (Pile-up NP 4)	-1.51	1.29
Electron identification efficiency (NP 8)	-0.32	1.09	Muon reconstruction efficiency	-0.55	1.32
Jet energy scale (Pile-up NP 4)	-0.90	1.04	Jet energy scale (Pile-up NP 1)	-1.01	0.49
Total	**4.31**	**4.61**	**Total**	**4.79**	**4.61**

Table 6.11: Leading experimental uncertainties on (a) the $q\bar{q}ZZ$ background yields, (b) the $ggZZ$ background yields in the signal region and (c) the signal acceptance for a hevay Higgs signal of mass 600 GeV and negligible width, for the VBF category. The last row lists the total impact of experimental certainties, including those not shown in this list.

Table 6.11 shows the same shortlist for the ZZ backgrounds and a VBF example signal at m_H =600 GeV in the VBF category. The uncertainties are larger here, between 15% and 40% for the backgrounds and around 5% for the signal, and more asymmetric, due to the low event counts in the VBF signal region. Jet related uncertainties are again dominant.

While the above discussion concerns only the normalisation impact of each uncertainty source, of course also each of them comes with a variation of the m_T shape. A dedicated filtering algorithm was implemented to decide which experimental shape uncertainties need to be considered: The variation histogram is checked bin by bin against the nominal shape and only if in at least one bin the systematic variation is larger than the statistical uncertainty in the bin the systematic is kept. No shape uncertainties of experimental origin pass this criterion.

The luminosity uncertainty for the full run II dataset corresponds to 1.7% [161] and was not in-

cluded in the rankings presented above.

6.3.2 Theory uncertainties

As explained before, the theory uncertainty takes into account the uncertainties due to choices of PDF sets, QCD scales and parton shower models. Here, most samples use the NNPDF or CT10 PDF set for the nominal case, and the related uncertainties are evaluated from the envelope of the variations due to internal PDF error sets and comparing to different choices, following the guidelines given in [162]. The internal PDF error sets account for experimental and methodology related uncertainties in the derivation of the PDF from data. The QCD scale uncertainty is estimated by varying the renormalisation and factorisation scales by a factor of two or half, in different combinations, and taking the envelope.

For the parton showering systematic (referred to as PS in the following), the parameters of the respective showering algorithm are varied. This means variations of the resummation scale (QSF), the CKKW matching scale and the PS recoil scheme, for the SHERPA generated samples, and variations of the tune, multi-parton- and FSR model for the samples showered with PYTHIA 8. Due to low statistics in the samples a single parton shower systematic is built from the separate terms in each case, to be more robust against fluctuations.

Signal theory systematics

For the narrow-width, heavy Higgs signal processes, the impact of the PDF, QCD and PS uncertainties on the acceptance and shape are studied. Truth signal samples from the search in $H \to ZZ \to \ell\ell\ell\ell$ are used, where one of the lepton pairs is treated as a neutrino pair. The full event selection as defined for the $\ell\ell\nu\nu$ analysis presented here is applied at truth level, except for the requirement on $E_{\mathrm{T}}^{\mathrm{miss}}$ significance and the b-jet veto (which have no immediate truth equivalent, and are also expected to have only a minor impact for signals).

Figure 6.19 shows the impact of the theory uncertainties on the signal acceptances for ggF and VBF signals in their respective category. Typically the impact is small. The PDF systematics range from around 0.5% to 1% in both categories. While the QCD and PS uncertainty contribute less than 1% in the ggF category, especially the QCD uncertainty is larger for the VBF category, reaching up to around 4%. The VBF uncertainties show more fluctuations due to the lower statistics.

In addition to the uncertainties on the signals in their respective production category, the cross-category uncertainties were also checked - so for ggF signals in the VBF category and vice-versa. They are very similar, with the exception that the PS uncertainty on ggF signals in the VBF category is larger, with up to 12% impact. This is due to the fact that the ggF signals samples are generated at NLO, with only up to one jet in the matrix element.

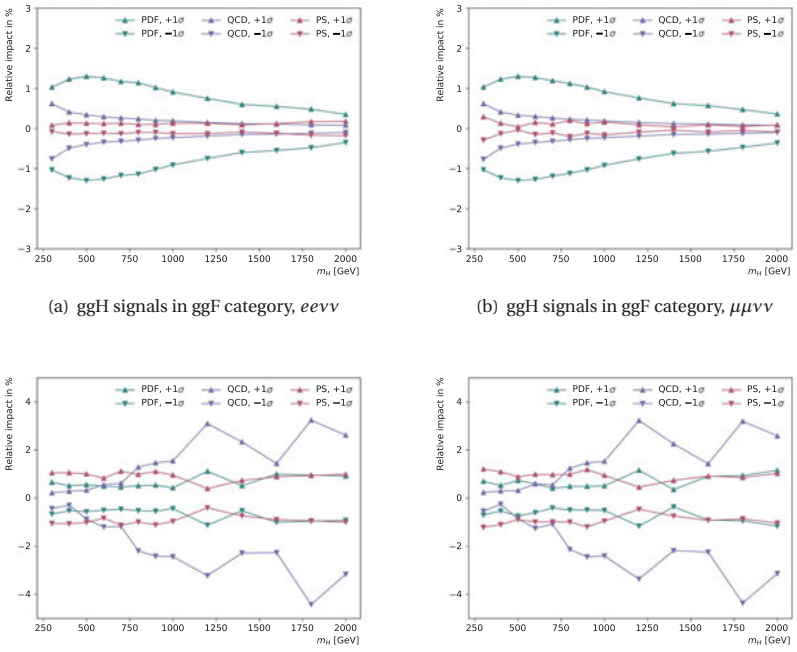

(a) ggH signals in ggF category, $eevv$

(b) ggH signals in ggF category, $\mu\mu vv$

(c) VBF signals in VBF category, $eevv$

(d) VBF signals in VBF category, $\mu\mu vv$

Figure 6.19: Relative impact of theory uncertainties on the ggF signals in the ggF category in (a) the $eevv$ and (b) the $\mu\mu vv$ channel and on the VBF signals in the VBF category in (c) the $eevv$ and (d) the $\mu\mu vv$ channel.

The impact of the associated m_{T} shape uncertainties on the expected limits was found negligible for all mass points.

For the large-width, heavy Higgs signal processes it is assumed that systematic effects are the same for different widths of the signal (provided the same mass). Hence, the values given above are also applied to the corresponding LWA signals for each mass point and any given width.

ZZ background theory uncertainties

For the dominant ZZ background, the PDF, QCD and PS uncertainties are evaluated. Figures 6.20 and 6.21 show the corresponding systematic variations as a function of the transverse mass m_{T} on the $q\bar{q}ZZ$ and on $ggZZ$ processes, in the ggF and VBF category respectively. The relative impacts on the total yield of each process are given in Table 6.12. For all uncertainties the impact

on the m_{T} shape is largest in the high m_{T} regions, with up to 10% to 20% impact. While the PDF uncertainty is only around 2% in both categories, the PS uncertainty is larger in the VBF category, up to around 16%. For the QCD uncertainty there is a large discrepancy between the $q\bar{q}ZZ$ and $ggZZ$ process - on $q\bar{q}ZZ$ the impact is 5% and 16% in the ggF and VBF category, it is above 40% on the $q\bar{q}ZZ$. This is because the $ggZZ$ samples are only generated at leading order in QCD. Here, especially the PS uncertainty estimation and the distributions in the VBF category suffer from statistical fluctuations due to small sample sizes.

	Relative impact in %					
	ggF			VBF		
Process	**PDF**	**QCD**	**PS**	**PDF**	**QCD**	**PS**
$q\bar{q}ZZ$	1.7	5.3	3.8	1.7	16	16.3
$ggZZ$	1.8	40.7	3.8	2.0	45.2	11.2

Table 6.12: Relative impact of the theory uncertainties on the $q\bar{q}ZZ$ and $ggZZ$ yields in the signal region.

In addition to the theory uncertainties described above, for the $q\bar{q}ZZ$ process a source of uncertainty are also the EW corrections. How this is evaluated was described in section 6.2.1 and the uncertainty as a function of m_{T} was shown in Figure 6.13. To summarize, the impact on the total $q\bar{q}ZZ$ yield is an uncertainty of 3% to 4%, and the shape impact is large for high m_{T}, reaching up to 20%.

Aside from the main ZZ processes, $q\bar{q}ZZ$ and $ggZZ$, the PDF and QCD uncertainties are also evaluated for the much smaller $qqZZjj$ EW process. Here, the impact of the QCD uncertainty on the total yield is around 2-3% and of the QCD uncertainty it is 5% in the ggF and 10% in the VBF category. The impact on the m_{T} shapes is similar as seen before, with variations up to 10% for the high m_{T} range.

WZ background theory uncertainties

For the WZ background the PDF and QCD uncertainties are evaluated as well. Their impact on the yield is considered as a source of uncertainty on the WZ scalefactor from the 3ℓ control region. Both contribute only between 0.5% and 2% in the ggF category, but are larger in the VBF category where the PDF uncertainty impact is around 4% and the QCD uncertainty roughly 10%. The associated m_{T} shape uncertainties are found negligible (effect below 1% on the expected limits).

6.3.3 Calculation of relative $q\bar{q}ZZ$-$ggZZ$ acceptance uncertainties

Since the total ZZ yield will be constrained from data no direct uncertainties on the total ZZ yields need to be considered. However, both $q\bar{q}ZZ$ and $ggZZ$ are scaled with one common normalisation factor μ_{ZZ}, even though they cover different regions of phase space and therefore

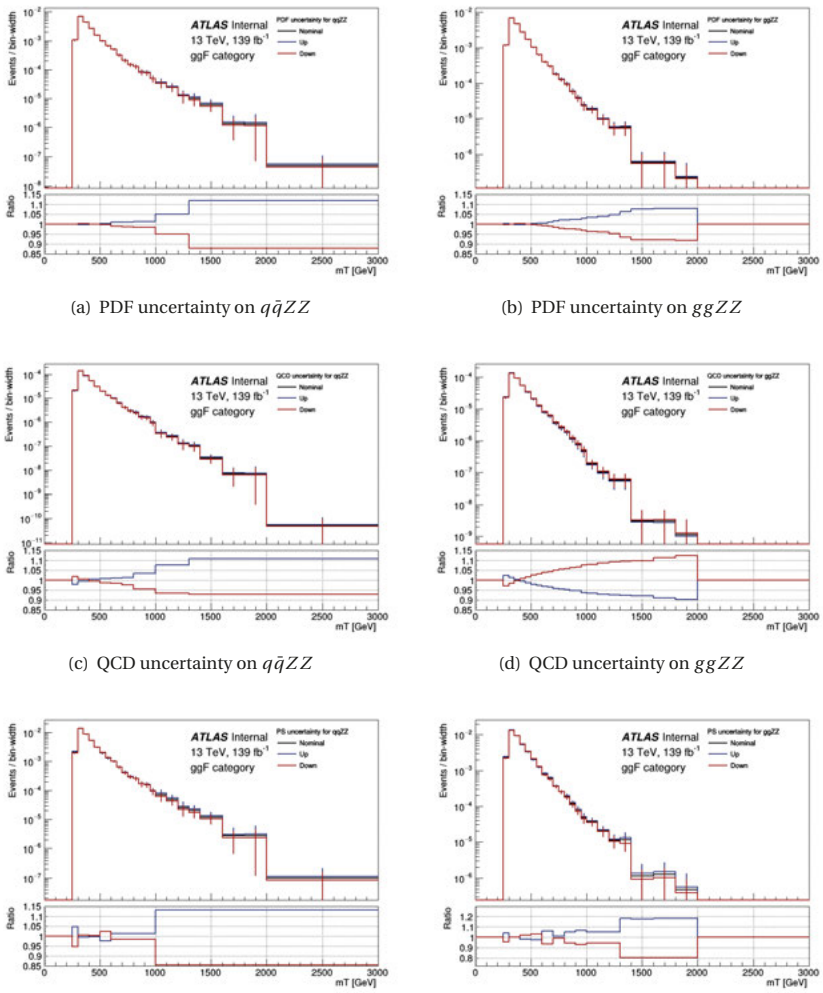

(a) PDF uncertainty on $q\bar{q}ZZ$

(b) PDF uncertainty on $ggZZ$

(c) QCD uncertainty on $q\bar{q}ZZ$

(d) QCD uncertainty on $ggZZ$

(e) PS uncertainty on $q\bar{q}ZZ$

(f) PS uncertainty on $ggZZ$

Figure 6.20: Theory uncertainties on the ZZ background n the ggF category: due to PDF choice on (a) the $q\bar{q}ZZ$ and (b) the $ggZZ$, due to QCD scale on (c) the $q\bar{q}ZZ$ and (d) the $ggZZ$ and due to the parton-showering on (e) the $q\bar{q}ZZ$ and (f) the $ggZZ$.

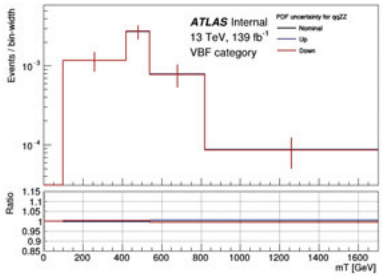

(a) PDF uncertainty on $q\bar{q}ZZ$

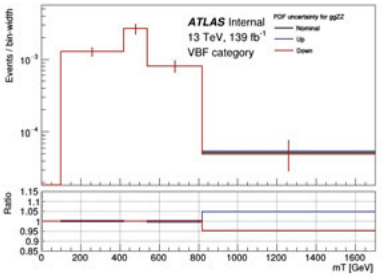

(b) PDF uncertainty on $ggZZ$

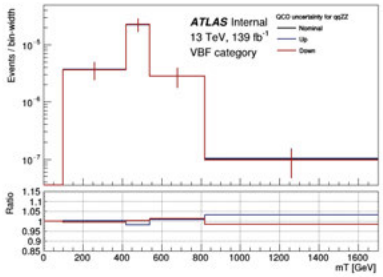

(c) QCD uncertainty on $q\bar{q}ZZ$

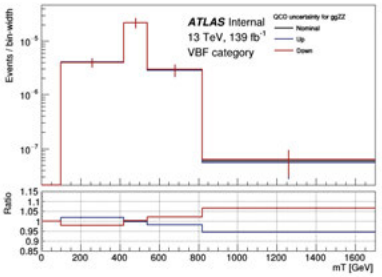

(d) QCD uncertainty on $ggZZ$

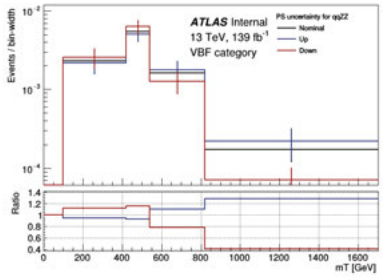

(e) PS uncertainty on $q\bar{q}ZZ$

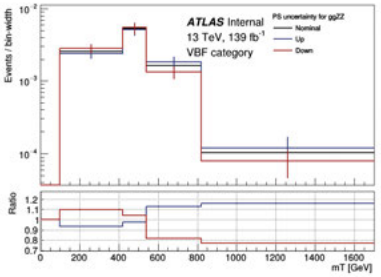

(f) PS uncertainty on $ggZZ$

Figure 6.21: Theory uncertainties on the ZZ background in the VBF category: due to PDF choice on (a) the $q\bar{q}ZZ$ and (b) the $ggZZ$, due to QCD scale on (c) the $q\bar{q}ZZ$ and (d) the $ggZZ$ and due to the parton-showering on (e) the $q\bar{q}ZZ$ and (f) the $ggZZ$.

uncertainties have different impact on them. Specifically, the total yield of ZZ events in the signal region $N_{\mathrm{SR}}(ZZ)$ is expressed as

$$N_{\mathrm{SR}}(ZZ) = \mu_{ZZ} \cdot \mathscr{L} \cdot A_{q\bar{q}ZZ} \cdot \sigma_{ZZ} + \mu_{ZZ} \cdot \mathscr{L} \cdot A_{ggZZ} \cdot \sigma_{ZZ} \tag{6.8}$$

where $\mathscr{L}$ is the integrated luminosity of the dataset, σ_{ZZ} the total production cross-section of the ZZ background and $A_{q\bar{q}ZZ}$ and A_{ggZZ} the acceptance of $q\bar{q}ZZ$ and $ggZZ$ events, respectively.

Including the $A_{q\bar{q}ZZ}$ term in the μ_{ZZ}, this can be written as:

$$N_{\mathrm{SR}}(ZZ) = \mu_{ZZ} \cdot \mathscr{L} \cdot \sigma_{ZZ} \cdot \left(1 + \frac{A_{ggZZ}}{A_{q\bar{q}ZZ}}\right) \tag{6.9}$$

Now the $\frac{A_{ggZZ}}{A_{q\bar{q}ZZ}}$ gives the relative acceptance between $q\bar{q}ZZ$ and $ggZZ$ events, and its uncertainty $\sigma(\frac{A_{ggZZ}}{A_{q\bar{q}ZZ}})$ can be derived from the uncertainties on the absolute acceptances, $\sigma_{A_{q\bar{q}ZZ}}$ and $\sigma_{A_{ggZZ}}$ in the following way. For any function $f(x,y)$ of two variables x and y, with uncertainties σ_x and σ_y, the uncertainty on f is calculated following the laws of error propagation as

$$\sigma_f^2 = \sigma_x^2 \left(\frac{\partial f}{\partial x}\right)^2 + \sigma_y^2 \left(\frac{\partial f}{\partial y}\right)^2 + 2\sigma_x \sigma_y \rho_{xy} \left(\frac{\partial f}{\partial x}\right)\left(\frac{\partial f}{\partial y}\right) \tag{6.10}$$

where ρ_{xy} gives the correlation factor between x and y. For $f = \frac{A_{ggZZ}}{A_{q\bar{q}ZZ}}$ and taking the relative uncertainty $\frac{\sigma_f}{f}$, one obtains

$$\left(\frac{\sigma(\frac{A_{ggZZ}}{A_{q\bar{q}ZZ}})}{\frac{A_{ggZZ}}{A_{q\bar{q}ZZ}}}\right)^2 = \left(\frac{\sigma_{A_{ggZZ}}}{A_{ggZZ}}\right)^2 + \left(\frac{\sigma_{A_{q\bar{q}ZZ}}}{A_{q\bar{q}ZZ}}\right)^2 - 2\left(\frac{\sigma_{A_{ggZZ}}}{A_{ggZZ}}\right)\left(\frac{\sigma_{A_{q\bar{q}ZZ}}}{A_{q\bar{q}ZZ}}\right)\rho_{A_{ggZZ},A_{q\bar{q}ZZ}} \tag{6.11}$$

If A_{ggZZ} and $A_{q\bar{q}ZZ}$ are fully correlated, the correlation factor $\rho_{A_{ggZZ},A_{q\bar{q}ZZ}}$ is 1, and thus the uncertainty becomes:

$$\left(\frac{\sigma(\frac{A_{ggZZ}}{A_{q\bar{q}ZZ}})}{\frac{A_{ggZZ}}{A_{q\bar{q}ZZ}}}\right)_{\mathrm{corr}} = \left|\left(\frac{\sigma_{A_{ggZZ}}}{A_{ggZZ}}\right) - \left(\frac{\sigma_{A_{q\bar{q}ZZ}}}{A_{q\bar{q}ZZ}}\right)\right| \tag{6.12}$$

It is assumed in this analysis that all experimental uncertainties are fully correlated between $q\bar{q}ZZ$ and $ggZZ$, hence the relative uncertainty in this case is built as the difference between the absolute $q\bar{q}ZZ$ and $ggZZ$ uncertainties.

In contrast, all theory uncertainties are assumed to be fully uncorrelated between the two processes, and then the relative uncertainty corresponds to the square sum of the individual uncertainties:

$$\left(\frac{\sigma(\frac{A_{ggZZ}}{A_{q\bar{q}ZZ}})}{\frac{A_{ggZZ}}{A_{q\bar{q}ZZ}}}\right)_{\mathrm{uncorr}} = \sqrt{\left(\left(\frac{\sigma_{A_{ggZZ}}}{A_{ggZZ}}\right)^2 + \left(\frac{\sigma_{A_{q\bar{q}ZZ}}}{A_{q\bar{q}ZZ}}\right)^2\right)} \tag{6.13}$$

All uncertainties on the $q\bar{q}ZZ$ and $ggZZ$ are converted into relative acceptance uncertainties following this scheme, and in the process they are also symmetrized (the symmetric uncertainty is built from the larger of the up and down variation). Table 6.12 shows the resulting leading and total relative uncertainties in both analysis categories.

In both categories, the total uncertainty on the relative $q\bar{q}ZZ$- $ggZZ$ acceptance is large and varies between 40% and 60%. Theory uncertainties are dominant. The QCD scale uncertainty is particularly large due to the the previously explained discrepancy of accuracy between $q\bar{q}ZZ$ and $ggZZ$ samples. In the VBF category, also jet and $E_{\mathrm{T}}^{\mathrm{miss}}$ uncertainties are relevant.

(a) ggF category

$eev\nu$ **channel**			$\mu\mu\nu\nu$ **channel**		
Uncertainty source	**Impact in %**		**Uncertainty source**	**Impact in %**	
ZZ Scale QCD	-41.04	41.04	ZZ Scale QCD	-41.04	41.04
ZZ Scale Shower	-5.38	5.38	ZZ Scale Shower	-5.38	5.38
$q\bar{q}ZZ$ EW corr.	-3.23	3.23	$q\bar{q}ZZ$ EW corr.	-3.12	3.12
ZZ Scale PDF	-2.48	2.48	ZZ Scale PDF	-2.48	2.48
Jet Flavour Composition	-0.61	0.61	Jet energy resolution (NP 1)	-0.86	0.86
Total	**41.61**	**41.61**	**Total**	**41.62**	**41.62**

(b) VBF category

$eev\nu$ **channel**			$\mu\mu\nu\nu$ **channel**		
Uncertainty source	**Impact in %**		**Uncertainty source**	**Impact in %**	
ZZ Scale QCD	-47.95	47.95	ZZ Scale QCD	-47.95	47.95
Jet energy resolution (NP 1)	-23.18	23.18	ZZ Scale Shower	-19.79	19.79
ZZ Scale Shower	-19.79	19.79	Jet energy resolution (NP 2)	-6.64	6.64
Jet energy resolution (NP 2)	-8.70	8.70	Jet Flavour Response	-6.42	6.42
Jet energy resolution (NP 5)	-8.29	8.29	$E_{\mathrm{T}}^{\mathrm{miss}}$ resolution	-6.25	6.25
Total	**61.26**	**61.26**	**Total**	**55.81**	**55.81**

Table 6.13: Leading relative and total uncertainties on the $q\bar{q}ZZ$ to $ggZZ$ acceptance, considering experimental and theory sources. In (a) the ggF category and (b) the VBF category. The last row lists the total impact of all uncertainties, including those not shown in this list.

6.4 $ZZ \to \ell\ell\nu\nu$ results and interpretation

6.4.1 Data in the signal regions

A simultaneous fit to the observed data in all signal regions is performed, following the methodology described in Chapter 4.5. Here, a background only fit is done - all signal parameters of interest are fixed to 0, while the ZZ normalisation factor μ_{ZZ} and all nuisance parameters are left free. Figure 6.22 shows the expected and observed transverse mass distributions after the fit.

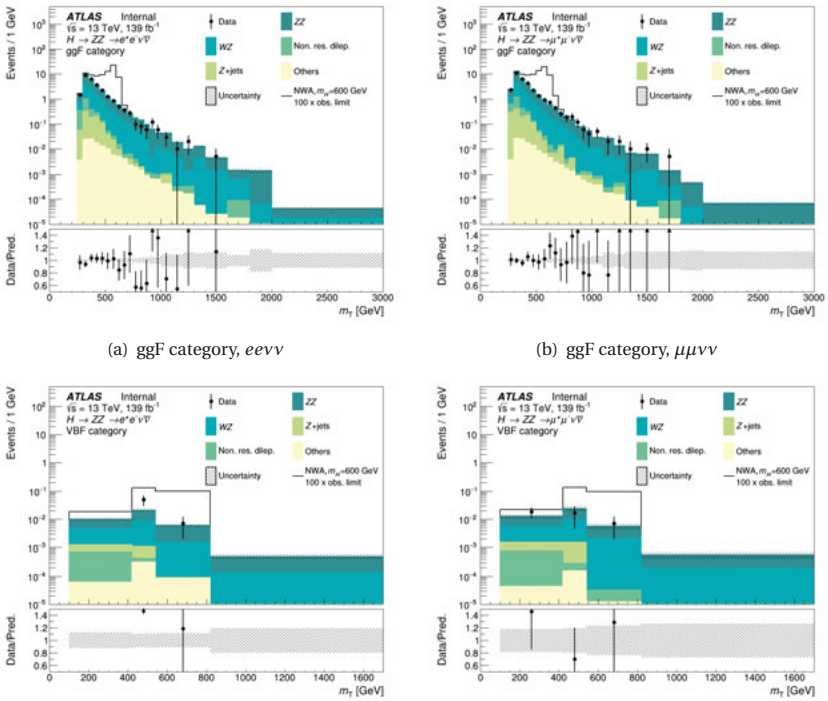

(a) ggF category, $eevv$

(b) ggF category, $\mu\mu\nu\nu$

(c) VBF category, $eevv$

(d) VBF category, $\mu\mu\nu\nu$

Figure 6.22: Post-fit expected and observed transverse mass distributions for the full run II data in (a) the ggF category, $eevv$ channel, (b) the ggF category, $\mu\mu\nu\nu$ channel, (d) the VBF category, $eevv$ channel and (d) the VBF category, $\mu\mu\nu\nu$ channel. The last bin includes all events beyond the boundary.

Data-driven yield estimates, following the control region methods described in Chapter 6.2, are used for the WZ, non-resonant dilepton and Z+jets backgrounds. The normalisation of the main ZZ background is constrained from the observed data in the signal region with the free

parameter μ_{ZZ}. Its best fit value is

$$\mu_{ZZ} = 1.06 \pm 0.06 \tag{6.14}$$

so the post-fit ZZ yield is 6% larger than expected from the MC prediction. Table 6.14 presents the corresponding yields and their uncertainties. All experimental and theory systematic sources as detailed in the previous chapter are included and correlations taken into account. For this analysis, the statistical uncertainty arising from the finite sizes of the MC samples used was found to be much smaller than the observed data statistical uncertainty and is therefore neglected. The data-driven background uncertainties include a component accounting for the statistical uncertainty in the control regions. The total uncertainty on the ZZ background includes the propagated error of the best fit μ_{ZZ}, reflecting the data statistical uncertainty.

While in all regions the observed data exceeds the prediction, the observed and predicted total event yields are compatible with each other within one standard deviation. The maximum local deviation is found at 980 GeV and its local significance is 0.85σ. Thus no significant excess is found, and in the following exclusion limits on the production cross-section of a heavy resonance are set.

(a)

Process	**Yields in the ggF region**	
	$ee\nu\nu$ channel	$\mu\mu\nu\nu$ channel
ZZ	814.7 ± 48.0	928.9 ± 54.4
WZ	412.4 ± 13.9	454.7 ± 12.3
Z + jets	42.5 ± 12.9	59.9 ± 22.2
Non-resonant dilepton	65.9 ± 5.7	76.6 ± 6.6
Other	5.9 ± 0.4	5.9 ± 0.4
Total Bkg.	1341.3 ± 52.0	1525.9 ± 60.4
Data	1323	1542

(b)

Process	**Yields in the VBF region**	
	$ee\nu\nu$ channel	$\mu\mu\nu\nu$ channel
ZZ	4.73 ± 0.51	5.30 ± 0.45
WZ	2.49 ± 0.51	3.02 ± 1.46
Z + jets	0.25 ± 0.21	0.38 ± 0.32
Non-resonant dilepton	0.22 ± 0.16	0.26 ± 0.18
Other	0.09 ± 0.02	0.04 ± 0.01
Total Bkg.	7.78 ± 0.77	9.00 ± 1.57
Data	8	10

Table 6.14: Post-fit observed and expected yields and their uncertainties in the (a) ggF and (b) VBF signal regions, for the full run II data.

6.4.2 Impact of systematics uncertainties

The impact of systematic uncertainties on the result, as well as any potential issues with them, is evaluated by means of a *systematics ranking*. For such a ranking, first a fully unconditional fit is performed with all parameters of interest and all nuisance parameters free. Then, each nuisance parameter is individually set to its -1σ and $+1\sigma$ variation and the fit is repeated. The result of the conditional fit is compared to that of the unconditional fit, and the difference in the best fit value of the parameter of interest gives the post-fit impact of the nuisance parameter in question. Normalizing this difference to the best fit value of the parameter of interest in the unconditional fit yields the relative impact of each nuisance parameter on the result. All nuisance parameters are then ordered by their relative impact, and in the following only the leading 15 are shown. In the fit model, each nuisance parameter is constrained by a Gaussian centred at 0 (the nominal value) and with width 1 (corresponding to 1σ variation) - hence its initial value before the fit is

0 ± 1. If a nuisance parameter's best fit central value is $\neq 0$, it is *pulled*. If its post-fit error is smaller than 1, it is *constrained*. Such pulls and constraints occur due to correlations or overestimation of systematic uncertainties, and can indicate problems with the fit model.

In the following, ranking plots for fitting to Asimov and observed data are discussed, as the first gives a better estimate of the actual impact of each uncertainty on the upper cross-section limit, while the latter is needed to understand what happens in the fit to observed data.

On Asimov data

For the ranking plots shown in this section, signal-injected Asimov datasets are used. They describe the nominal background prediction with the respective signal scaled to its expected upper limit added on top, using data-driven background estimates from the control regions but the pure MC prediction for the ZZ process with $\mu_{ZZ} = 1$. In this way, the systematics impact on the upper cross-section limit for the given signal can be best estimated. All four analysis regions are included in the fit, but only one kind of signal is injected at a time: for the ranking on the ggF parameter of interest only ggF signal is injected, and the VBF signal is set to 0 (and vice versa). Four example mass points out of the full mass range of the narrow-width heavy Higgs signals are tested. Figure 6.23 shows the resulting systematics ranking for the ggF and Figure 6.24 for the VBF parameter of interest.

The overall impact of each systematic uncertainty is small, reaching maxima of around 15% in both cases. No unexpected pulls or constraints are observed, except for a small constraint on the nuisance parameter representing the systematic uncertainty of the Z+jets estimation. This is explained by the fact that at $\approx 45\%$ in the ggF and $\approx 80\%$ in the VBF category this uncertainty is very large. A similar constraint is observed on the shape uncertainty from the $q\bar{q}ZZ$ EW corrections, which is the largest shape uncertainty included, particularly in the high m_{T} tails.

Different systematic uncertainty sources are relevant at different masses: For example, at the lowest considered mass point of $m_H = 300\,\mathrm{GeV}$ uncertainties on the Z+jets and non-resonant dilepton background estimates are more relevant than at higher masses, since the bulk of events of these processes are at low m_{T} values, overlapping with the low mass signals. Overall, and especially for the higher mass points > 1 TeV, the shape uncertainties related to the theory modelling of the $q\bar{q}ZZ$ background are dominant. In the VBF category also experimental uncertainties on the jet reconstruction feature among the leading systematics.

Nuisance parameter ranking on observed data

Figure 6.25 shows the nuisance parameter ranking when fitting to the observed data instead. Here only the $m_H = 600\,\mathrm{GeV}$ signal example is shown.

While overall the ranking is similar to what is observed on Asimov data the relative impact of each nuisance parameter becomes larger. The reason is that the fitted signal strength on observed data is very small, in the order of $\mathcal{O}(10^{-4})$, but the absolute change from setting a systematic to

its variation stays of similar size, as it mostly depends on the background uncertainties. In the Asimov case, the injected signal strength corresponds to an upper limit, but the central value of the signal strength on data can be much smaller.

In the data ranking, similar constraints are observed as were already seen in the Asimov fits. Additionally, a few nuisance parameters are pulled, such as the uncertainties on the $q\bar{q}ZZ$ EW corrections and ZZ QCD uncertainties. This is likely due to correlations between those nuisance parameters and the other free fit parameters, as visualized in Figure 6.26. The correlation matrix is derived from a slightly different fit set-up: to allow checking also the correlation between the ggF and VBF signals both signal strengths are free parameters in the fit. For better readability, only nuisance parameters with at least one correlation above 0.1 are shown. Negative correlations between the ggF and VBF signal strength parameters of interest are observed. Nuisance parameters relating to the ZZ normalisation, such as the ZZ QCD scale modelling uncertainty, are (negatively) correlated to the free μ_{ZZ}. Moreover, the μ_{ZZ} factor is negatively correlated to largest uncertainties on the other backgrounds. This is as expected.

To better understand why certain uncertainties are dominant or pulled, their (pre-fit) impact on the total background prediction is compared to the observed data. This is illustrated in Figure 6.27 for the leading systematic uncertainty from the example ranking: the $q\bar{q}ZZ$ EW correction uncertainty in the ggF, and the ZZ QCD uncertainty in the VBF category. While for the first the impact on the total background yields is small, it leads to large variations up to 20% in the high m_{T} tails where also the discrepancy between prediction and observed data is largest. For the leading VBF uncertainty, the impact on the total background yields is more sizeable. However, it should be noted that in each case the discrepancy between data and prediction is much larger than any of the systematic variations of the prediction. This highlights that the analysis is not very sensitive to systematic uncertainties.

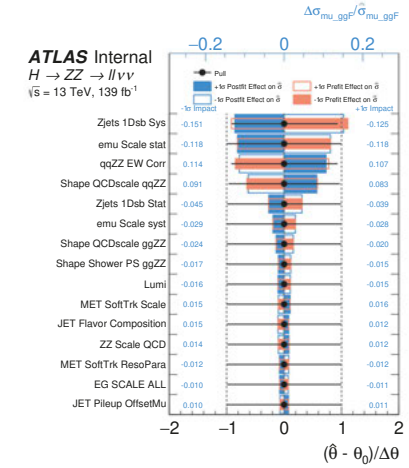

(a) $m_H = 300\,\text{GeV}$

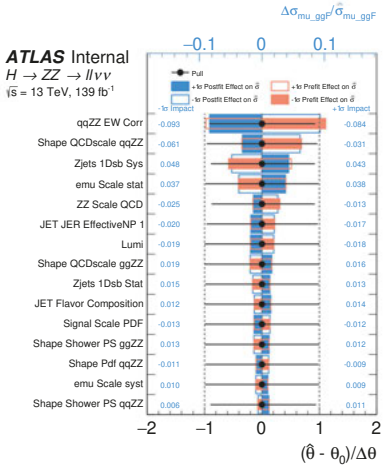

(b) $m_H = 600\,\text{GeV}$

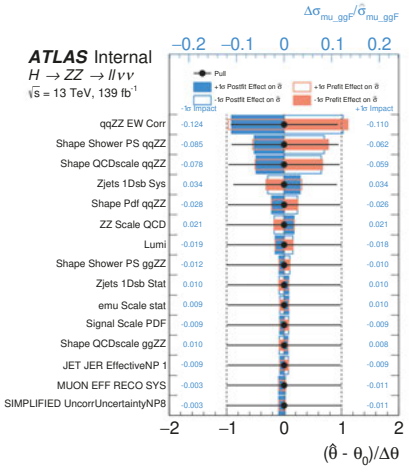

(c) $m_H = 1\,\text{TeV}$

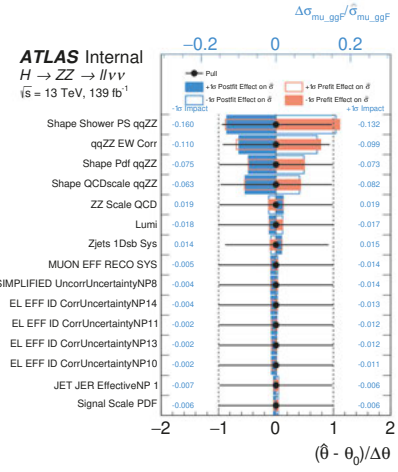

(d) $m_H = 1.4\,\text{TeV}$

Figure 6.23: Nuisance parameter ranking derived from fits to signal injected Asimov data, where the signal is normalised to its expected upper cross-section limit. For narrow width heavy Higgs signals produced in the ggF mode and with masses of (a) $m_H = 300\,\text{GeV}$, (b) $m_H = 600\,\text{GeV}$, (c) $m_H = 1\,\text{TeV}$ and (d) $m_H = 1.4\,\text{TeV}$.

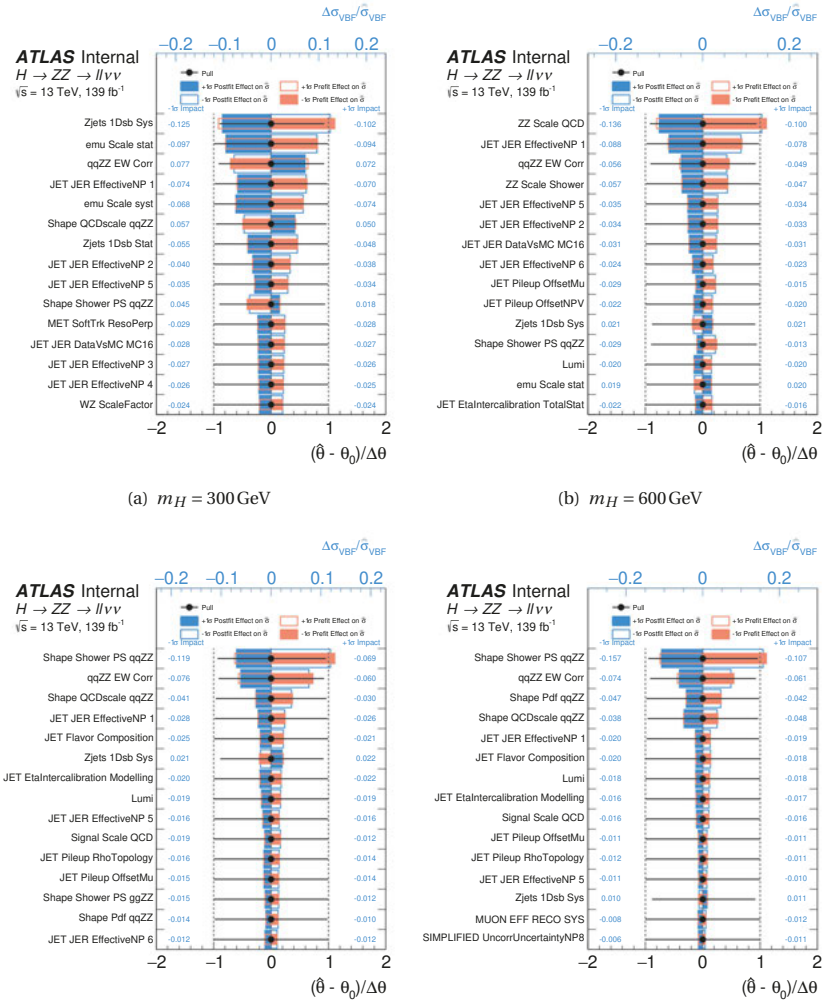

(a) $m_H = 300\,\text{GeV}$ (b) $m_H = 600\,\text{GeV}$

(c) $m_H = 1\,\text{TeV}$ (d) $m_H = 1.4\,\text{TeV}$

Figure 6.24: Nuisance parameter ranking derived from fits to signal injected Asimov data, where the signal is normalised to its expected upper cross-section limit. For narrow width heavy Higgs signals produced in the ggF mode and with masses of (a) $m_H = 300\,\text{GeV}$, (b) $m_H = 600\,\text{GeV}$, (c) $m_H = 1\,\text{TeV}$ and (d) $m_H = 1.4\,\text{TeV}$.

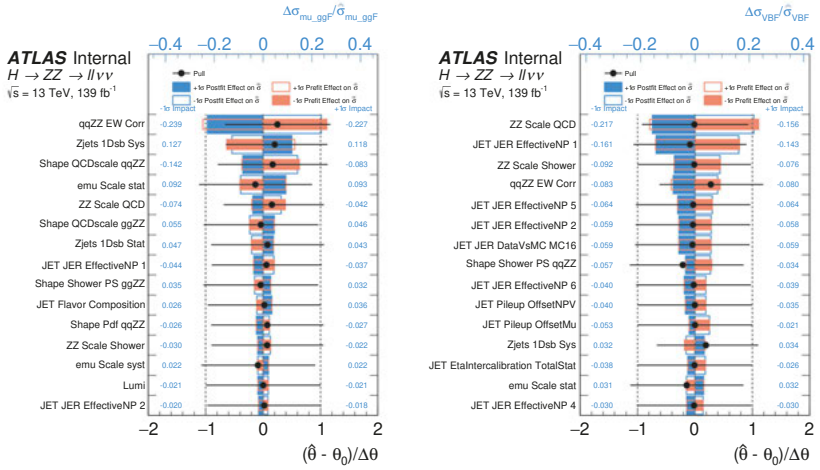

(a) ggF signal (b) VBF signal

Figure 6.25: Nuisance parameter ranking derived from fitting the signal + background model to the observed data, for a narrow-width, heavy Higgs signal with $m_H = 600\,\text{GeV}$ in (a) the ggF and (b) the VBF production mode.

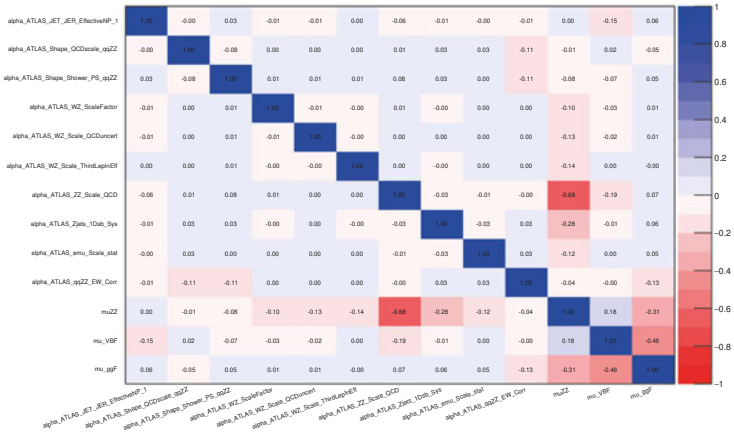

Figure 6.26: Correlation matrix derived from fitting the signal + background model to the observed data, for a narrow-width, heavy Higgs signal with $m_H = 600\,\text{GeV}$.

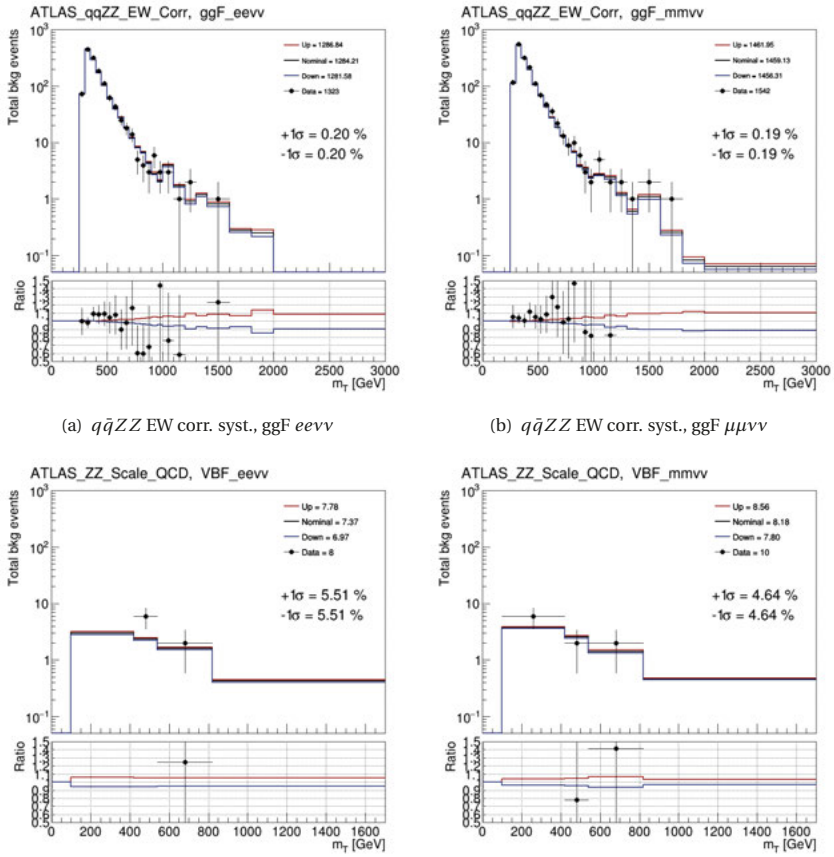

(a) $q\bar{q}ZZ$ EW corr. syst., ggF $ee\nu\nu$

(b) $q\bar{q}ZZ$ EW corr. syst., ggF $\mu\mu\nu\nu$

(c) ZZ QCD syst., VBF $ee\nu\nu$

(d) ZZ QCD syst., VBF $\mu\mu\nu\nu$

Figure 6.27: Comparison of the pre-fit variation of the total background expectation with observed data, for the leading systematic in each category: The $q\bar{q}ZZ$ EW correction systematic uncertainty in the ggF (a) $ee\nu\nu$ and (b) $\mu\mu\nu\nu$ channel and the ZZ QCD systematic uncertainty in the VBF (c) $ee\nu\nu$ and (d) $\mu\mu\nu\nu$ channel.

6.4.3 Cross-section limits on narrow-width heavy Higgs production

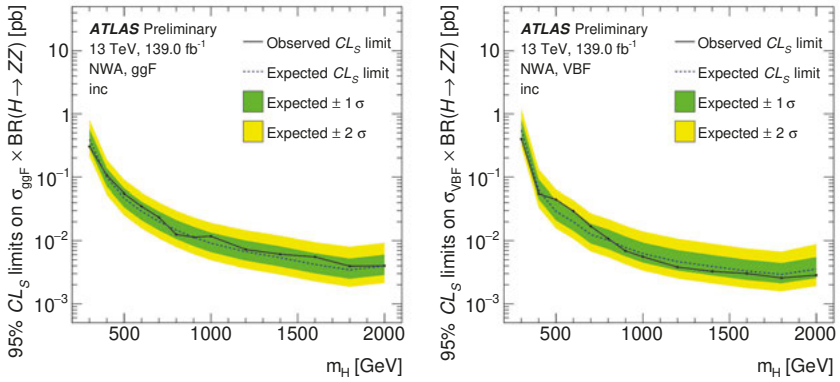

(a) ggF production (b) VBF production

Figure 6.28: Expected and observed upper limits on the production cross-section times branching fraction to ZZ pair of a narrow-width heavy Higgs in (a) ggF and (b) VBF production mode, using the full run II data.

Since no excess is seen in the m_{T} distributions, upper limits on the production cross-section of a heavy Higgs in the narrow-width approximation are derived, following the methods described earlier in Chapters 4.5 and 5.4. Here, there are three parameters of interest in the fit - the ggF and VBF signal strength as well as the ZZ background normalisation factor μ_{ZZ}. Although μ_{ZZ} is found to be greater than one when fitting to observed data, the expected limits are based on the assumption that it is equal to one. Figure 6.28 shows the resulting cross-section limits as a function of signal mass, for a signal produced in the ggF or VBF mode. Only the limits at masses where MC samples exist are shown and the connecting lines are simply for visualization. As input to the final combination with the $\ell\ell\ell\ell$ channel's results, further intermediate mass points are added. This is described later, in Chapter 6.5.2.

Across the whole mass range the expected and observed limits are compatible within two standard deviations. No clear evidence for a new resonance is found.

The observed upper limits on $\sigma \cdot \mathrm{BR}(H \to ZZ)$ range from approximately 4 fb to 300 fb in the ggF production mode and from 3 fb to 400 fb for the VBF signals. As expected, this is a significant improvement over the results of the analysis of the 2015 and 2016 data.

To make a more direct comparison of the two analyses presented in this thesis, Figure 6.29 shows the observed and median expected limit for the full run II data compared to the limits obtained by scaling the 2015 and 2016 results to match the luminosity of 139 fb^{-1}. This comparison quantifies the improvement in the new analysis. While the improvement is substantial for masses

above 1 TeV in the ggF channel, the improvements in the VBF analysis are even larger. Likely the major factor is that the simple counting experiment done for VBF on the 2015 and 2016 data, was replaced by also using the shape of the VBF category m_{T} distributions in the limit setting. Since all regions are always considered in the simultaneous fit this change also improves the ggF results. It can also explain why the improvement increases with increasing mass, since very high mass signals exhibit better shape separation with respect to the background.

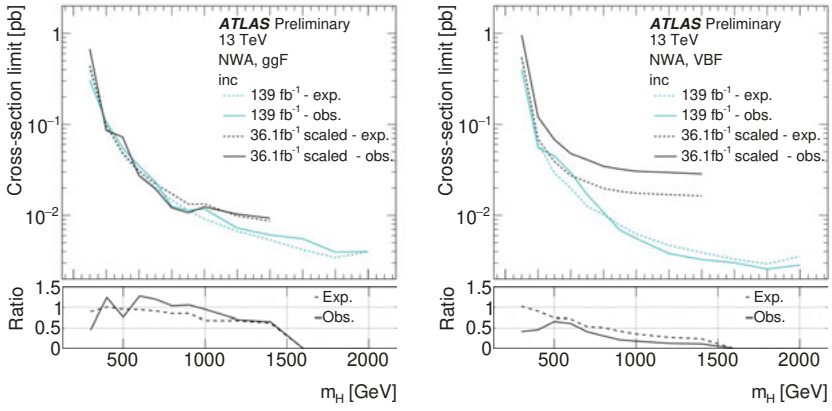

(a) ggF production

(b) VBF production

Figure 6.29: Comparison of expected median and observed upper limits between the two analyses presented in this thesis.

6.4.4 Cross-section limits on large-width heavy Higgs production

For the large-width heavy Higgs interpretation only events in the ggF category are used in the fit, and only mass points above 400 GeV are considered. While the signal inputs for the case of Γ_H =15% m_H width are derived directly from simulation samples, the other signal widths are obtained from those samples using the signal-to-signal analytic reweighting described in Chapter 4.1. The signal systematic uncertainties propagated to the limit are assumed to be the same for all widths.

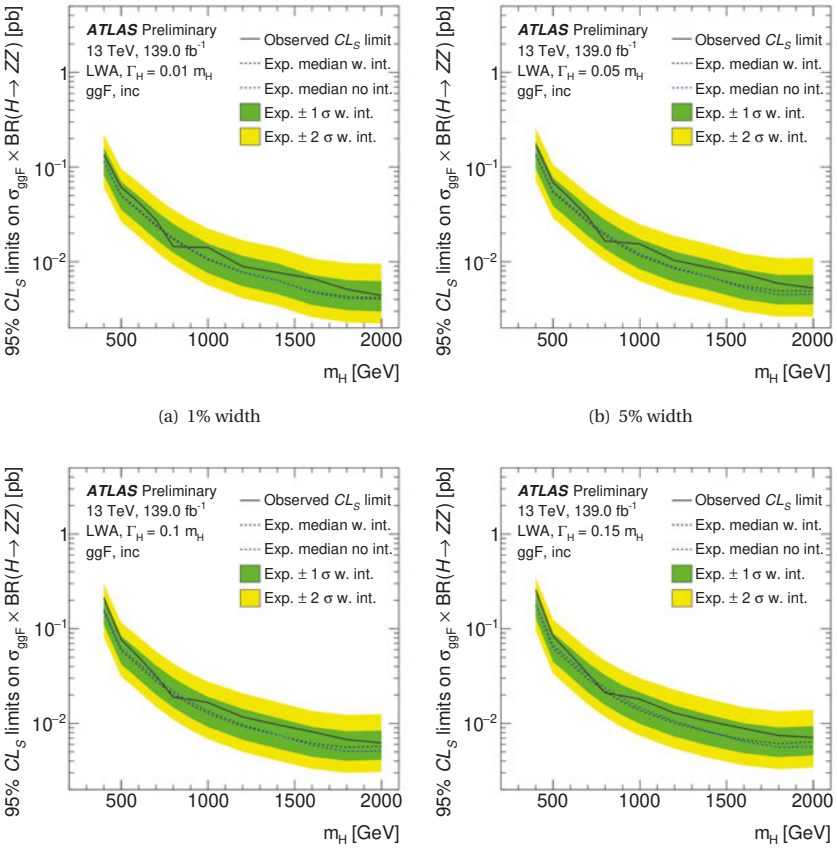

(a) 1% width

(b) 5% width

(c) 10% width

(d) 15% width

Figure 6.30: Expected and observed upper limits on the production cross-section times branching fraction to ZZ pair of a large-width heavy Higgs with a width of (a) 1%, (b) 5%, (c) 10% and (d) 15% of its mass.

Interference effects between LWA signal, 125 GeV Higgs and $ggZZ$ background are modelled using the methods described in detail in Chapter 4.3. Separate templates for the interference and signal only distributions are used as inputs, and the signal plus interference distribution is parametrised as $\mathrm{S+I} = \mu \cdot \mathrm{S} + \sqrt{\mu} \cdot \mathrm{I}$, where μ is the parameter of interest, and I the sum of both interference histograms. In this way, both the changing shape and overall normalisation of S+I compared to S is recalculated for changing μ during the limit setting.

Figure 6.30 shows the observed and expected limits for a large-width heavy Higgs, where the

width is equal to different percentages of its mass. Only the limits derived at mass points where the Γ_H =15% m_H samples exist are shown. The expected limits with uncertainties and the observed limits include the interference modelling. For comparison the median expected limit without interference modelling is also shown.

Comparing to the NWA limits, as shown in Figure 6.31, the LWA limits are between 15% to 60% higher, for widths of 1% and 15% respectively. The effect is largest at the low mass points, where the broadening width has a noticeable impact on the signal acceptance due to the harsh $E_{\mathrm{T}}^{\mathrm{miss}}$ cut and also on the m_{T} shape resolution. At the very high mass points the m_{T} binning in the sensitive region is so coarse that the effect of the broadening width has less impact on the limits. It should be noted however that comparing the NWA and LWA is not a fair comparison, as the NWA also uses events from the VBF category while the LWA does not.

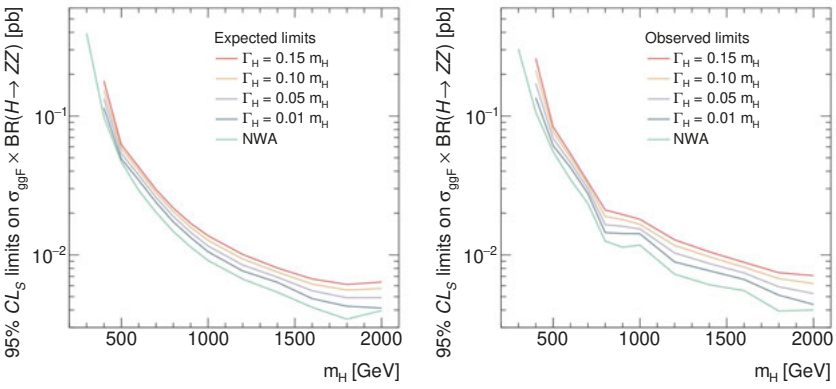

(a) Expected limits

(b) Observed limits

Figure 6.31: Comparison of limits for the different heavy Higgs width scenarios for (a) the expected and (b) the observed limits.

On the whole, the impact of including the interference is relatively minor - much smaller than the 1σ uncertainty on the expected limits. To gain a better understanding of the impact of the interference effects, Figure 6.32 shows a direct comparison of the median expected limits with and without interference. The relative difference shown in the bottom panel is defined as $(\mathrm{limit}_{\mathrm{w.\ int.}} - \mathrm{limit}_{\mathrm{no\ int.}})/\mathrm{limit}_{\mathrm{no\ int.}}$. If it is below 0, the limit with interference is lower - and therefore better - than that without.

As expected, the impact of the interference effects increases with increasing width, from a maximum of 4% at the 1% width to 10% impact at the 15% width point. Moreover, it is dependent on the signal mass: For low mass points the limit improves with interference, for the very high masses it worsens. This effect is consistent with the results of the LWA analysis in the $\ell\ell\ell\ell$ channel. It can be explained by the fact that at low masses the interference has an enhancing effect -

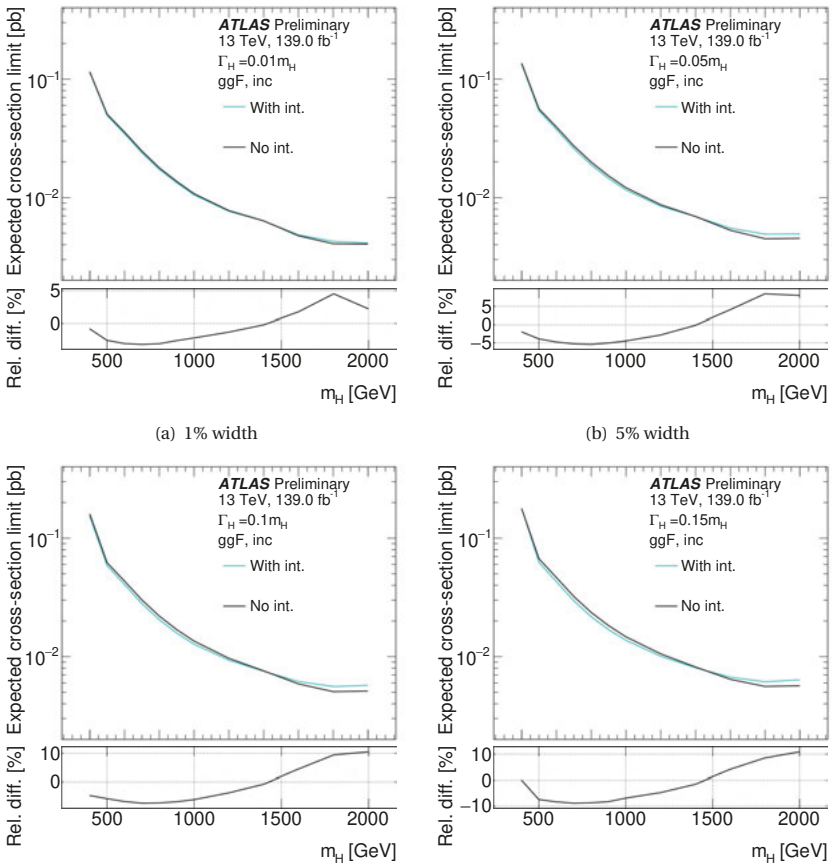

(a) 1% width

(b) 5% width

(c) 10% width

(d) 15% width

Figure 6.32: Comparison of expected median limits with and without interference effects, for a heavy Higgs with a width of (a) 1%, (b) 5%, (c) 10% and (d) 15% of its mass. The bottom panel shows the difference between the limit with and the limit without, normalized to the limit without interference.

the S+I/S ratio is larger than 1 - as evident in Figure 6.33. While the S+I/S ratio takes into account only the impact on the total signal yields, the interference also affects the m_T shape. Specifically, the interference depletes the low m_T side of the signal peaks, as visualized by the example distributions in Chapter 4.3, but enhances the high m_T side. This leads to better a separation of the S+I distribution from the backgrounds. Therefore even if the S+I/S ratio is below 1 the observed limit including the interference can still be better than the limit without interference. This is explains why the crossing point between the limits with and without interference is not at the same same

as where the S+I/S ratio crosses 1, but higher.

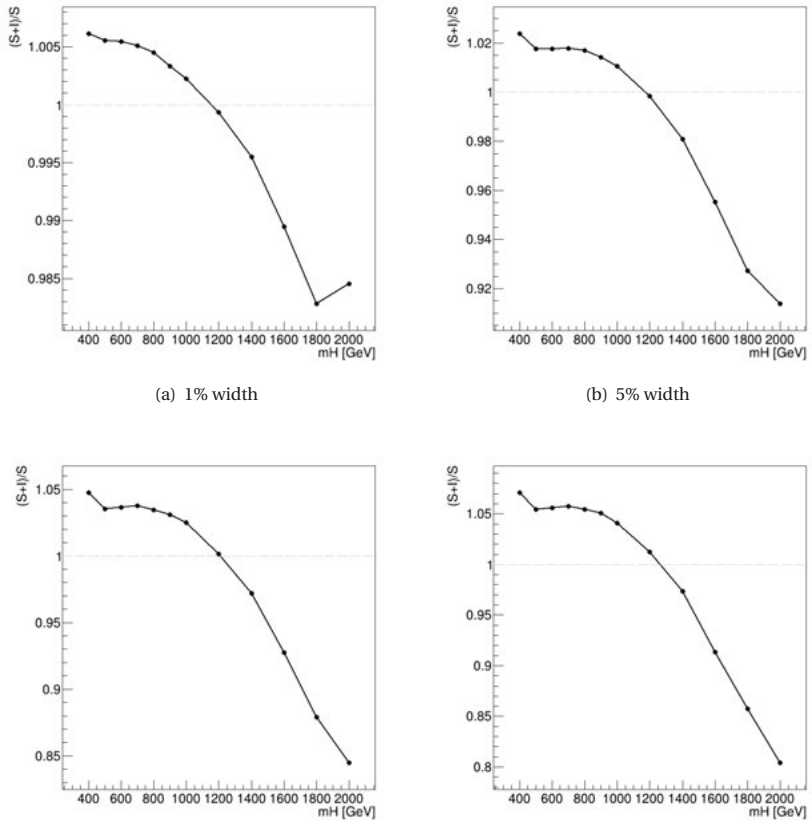

(a) 1% width

(b) 5% width

(c) 10% width

(d) 15% width

Figure 6.33: Ratio of overall signal plus interference yields (S+I) over signal only yields (S) versus the signal masses. All signals are normalized to the expected limit when not including the interference modelling.

6.5 Combination of the $ZZ \to \ell\ell\nu\nu$ with the $ZZ \to \ell\ell\ell\ell$ results

To increase the sensitivity the $ZZ \to \ell\ell\nu\nu$ results are combined with those of a similar search in the $ZZ \to \ell\ell\ell\ell$ channel, where ℓ denotes an electron or muon [140]. The analyses in both channels have different strengths: While the $\ell\ell\ell\ell$ final state is fully reconstructible with an excellent

resolution of the observable $m_{\ell\ell\ell\ell}$ and subject to relatively low background contamination, it is a rare process due to the small branching ratio BR($ZZ \to \ell\ell\ell\ell$). In comparison, the resolution of the $ZZ \to \ell\ell\nu\nu$ observable m_{T} is not as good, and the levels of backgrounds are higher, but the BR($ZZ \to \ell\ell\nu\nu$) is around six times higher. Especially at very high mass values the $ZZ \to \ell\ell\ell\ell$ channel is limited by the available statistics, and the $ZZ \to \ell\ell\nu\nu$ channel provides better sensitivity. This will become more evident in the combined results presented in Chapter 6.5.3. Before discussing the combined results, Chapter 6.5.1 gives a brief overview of the $ZZ \to \ell\ell\ell\ell$ analysis and Chapter 6.5.2 explains how $\ell\ell\nu\nu$ results with a fine mass granularity were obtained as inputs to the combination.

6.5.1 Overview of the $ZZ \to \ell\ell\ell\ell$ analysis

Signal modelling

A key feature of the $ZZ \to \ell\ell\ell\ell$ final state is that resonances in the $m_{\ell\ell\ell\ell}$ spectrum can be described by analytic parametrizations. For the high mass signals, this means that while MC samples are generated at some mass points, with the same setup as in the $ZZ \to \ell\ell\nu\nu$ search, any intermediate signal mass point can be obtained from an analytic function, whose parameters are derived from a fit to the MC distributions.

In the case of a narrow-width heavy Higgs signal, the intrinsic width of the truth line shape is negligible compared to the detector resolution. Thus, the $m_{\ell\ell\ell\ell}$ distribution is fully described by the detector resolution function, which is modelled here as the sum of a Crystal-Ball and a Gaussian function that share the same central value, but have different resolution parameters. This function is fitted to all signal $m_{\ell\ell\ell\ell}$ distributions from MC simulation to derive the values of its free parameters at each of these mass points. To obtain the $m_{\ell\ell\ell\ell}$ distribution at any mass point, the derived parameters are interpolated in m_H using simple polynomials. Figure 6.34 illustrates the analytic NWA signal parametrization with an example: the $m_{\ell\ell\ell\ell}$ distributions of the three mass points $m_H = 300\,\mathrm{GeV}, 600\,\mathrm{GeV}$ and $900\,\mathrm{GeV}$ (shown as dots) are each fitted with the detector resolution model (shown as the dashed lines at those masses) and intermediate mass points are then derived in steps of 100 GeV (shown as the intermediate dashed lines). Although the example shows the distributions normalized to unit area, also the yield of each signal is obtained from the parametrization. Using the analytic parametrization method introduces a bias of up to 3% on the signal yield, which is taken into account as a systematic uncertainty. The bias is estimated by

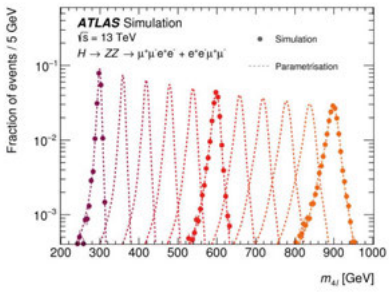

Figure 6.34: Example NWA signal $m_{\ell\ell\ell\ell}$ distributions illustrating the analytic signal parametrization. The signals at $m_H = 300, 600, 900\,\mathrm{GeV}$ are used as inputs to the fit with which all intermediated points are derived.

comparing the results of the analytic parametrization with the original MC distribution at a given mass.

For the large-width heavy Higgs signals, the lineshape of the signal cannot be neglected with respect to the detector resolution. An analytic description of the LWA lineshape was already discussed in Chapter 4.1 for the $\ell\ell\nu\nu$ case, and is analogous for the $\ell\ell\ell\ell$ channel. To obtain the reconstructed $m_{\ell\ell\ell\ell}$ distribution for a large-width signal, this truth lineshape is convolved with the same detector resolution function as used to model the NWA case.

Event selection and categorization

As the $ZZ \to \ell\ell\ell\ell$ channel is a very clean final state, with few background processes contributing, but very rare, the event selection in this channel consists of fairly loose requirements. In comparison to the $ZZ \to \ell\ell\nu\nu$ analysis, no targeted kinematic selections suppressing specific backgrounds need to be made. Instead the aim is to keep the signal acceptance as high as possible, to maximize the event yield.

	Selection criterion	
	Electrons	**Muons**
$\|\eta\|$ acceptance	$\|\eta\| < 2.47$	$\|\eta\| < 2.7$
Cosmic cuts	d_0 significance < 5	d_0 significance < 3
	$\|z_0 \cdot \sin(\theta)\| < 0.5\,\text{mm}$	$\|z_0 \cdot \sin(\theta)\| < 0.5\,\text{mm}$
Identification	Likelihood ID	All muon types
	Loose working point	Loose working point
Isolation	FixedCutPFlowLoose working point	FixedCutPFlowLoose working point
p_{T} threshold	$p_{\text{T}} > 7\,\text{GeV}$	$p_{\text{T}} > 5\,\text{GeV}$

Table 6.15: Lepton selection criteria in the $H \to ZZ \to \ell\ell\ell\ell$ analysis of the full run II data.

Specifically, this also means a looser set of selection criteria for the leptons, as given in Table 6.15. Although the impact parameter and isolation requirements are the same as in the $\ell\ell\nu\nu$ analysis, all other criteria are less stringent. For both electrons and muons, only a *loose* identification is required, and muons without a successful combined refit of ID and MS track are allowed. Moreover, the p_{T} threshold for both electrons and muons is significantly lower.

Jets are reconstructed and selected in the same way as in the $ZZ \to \ell\ell\nu\nu$ analysis.

Table 6.16 gives an overview of the event selection criteria. The same selection is also used in SM $H \to ZZ \to \ell\ell\ell\ell$ analyses, e.g [163]. Events are recorded using a combination of triggers based on the presence of one, two or three leptons. The efficiency of this requirement reaches up to 98% . Next, the main goal of the event selection criteria is to identify the most likely $H \to ZZ \to \ell\ell\ell\ell$ candidate. At least one lepton quadruplet consisting of two same-flavour, opposite-sign (SFOS) pairs is required. The highest p_{T} leptons in such a quadruplet have to be above a certain threshold, and no more than one calorimeter-tagged or stand-alone muon is allowed in

	Selection criterion
Trigger	Combination of single-, di- and trilepton triggers
$ZZ \to \ell\ell\ell\ell$ candidate	At least one quadruplet consisting of two same-flavour, opposite sign lepton pairs
	Leading three leptons with $p_{\mathrm{T}} > 20, 15, 10\,\mathrm{GeV}$
	At most one calorimeter-tagged or stand-alone muon
Leading lepton pair	SFOS lepton pair with invariant mass m_{12} closest to m_Z
	$50 < m_{12} < 106\,\mathrm{GeV}$
Subleading lepton pair	SFOS lepton pair with invariant mass m_{34} second closest to m_Z
	$50 < m_{34} < 115\,\mathrm{GeV}$
Separation in pairs	$\Delta R(\ell, \ell') > 0.1$
J/Ψ veto	$m_{ll} > 5\,\mathrm{GeV}$ in all possible SFOS lepton pairs
Common vertex	Tracks of all four leptons compatible with originating from one vertex
Resolve ambiguity	Select $ZZ \to \ell\ell\ell\ell$ candidate with highest selection efficiency and matrix element

Table 6.16: Lepton selection criteria in the $H \to ZZ \to \ell\ell\ell\ell$ analysis of the full run II data.

it. The lepton pair with an invariant mass closest to m_Z is selected as the leading pair, and the one second closest as the subleading pair. Each pair must be compatible with the m_Z pole mass. It is further required that all leptons in the quadruplet are well separated from each other. In case it is possible to find a lepton pair with invariant mass below 5 GeV, the event is rejected to veto events with J/Ψ decays. To confirm the hypothesis that the event is consistent with a $H \to ZZ \to \ell\ell\ell\ell$ decay, the tracks of all leptons in the quadruplet must be compatible with a common vertex. This is imposed by making specific requirements on the χ^2 of the tracks to vertex fit, maintaining at least 99% signal efficiency. Finally, with the above selection there is still potential for ambiguity in the event, especially if additional leptons are present. First, it is possible that multiple quadruplets with different flavour combinations fulfil the above criteria. In such a case only the one with the highest (expected) efficiency is kept, following the ordering $4\mu, 2e2\mu, 4e$. If however there are still multiple quadruplets fulfilling all requirements, the matrix element at leading order is calculated for each one of them and only the one with the highest probability is kept.

Depending on the signal mass, the acceptance of the $ZZ \to \ell\ell\ell\ell$ event selection is between 25% to 30%, mostly limited by the lepton reconstruction and selection requirements, which have an efficiency between 30% and 40%.

To improve the $m_{\ell\ell\ell\ell}$ resolution, FSR photons are identified in the calorimeter and added to the $Z \to \ell\ell$ candidate following the methods described in [7]. The FSR corrected $Z \to \ell\ell$ momenta are then entered into a Z-mass constrained kinematic fit, to minimize the mass resolution.

As is done in the $ZZ \to \ell\ell\nu\nu$ analysis, the selected events are split into separate categories, depending on whether they are more compatible with the ggF or VBF production mode. However, in the $ZZ \to \ell\ell\ell\ell$ analysis two different strategies are employed: for the narrow-width heavy Higgs analysis the categorization is done based on multivariate classifiers, but for the large-width

heavy Higgs analysis it is based on simple selection cuts very similar to the categorization used in the $\ell\ell\nu\nu$ analysis. Only the mulivariate-classifier is described in the following, the details of the cut-based categorization can be found in [140].

Multivariate-based event categorization In the multivariate analysis, separate classifiers are constructed for the two production modes. Both employ a dedicated Deep Neural Network (DNN) with different input variables - the only shared input variable is the invariant four lepton mass, $m_{\ell\ell\ell\ell}$. The general architecture is similar to that used in [163]. While the VBF-classifier DNN is based on jet related variables, such as the p_{T} and η of the jets or the invariant mass and p_{T} of the di-jet system, the ggF-classifier uses the properties of the four lepton system such as its transverse momentum and η, as well as angular variables of the four leptons in the Higgs rest frame. Both networks are trained on the narrow-width heavy Higgs signal MC samples in the mass range from 200 GeV to 1400 GeV as well as the ZZ background. The event categorization strategy is then as follows:

- The base event selection summarized in Table 6.16 is applied.
- All events passing the selection that have at least two jets are used as inputs to the VBF-classifier. If the output of the VBF-classifier DNN of an event is above 0.8, the event is sorted into the VBF-like category.
- All events that fail the above (either the jet or VBF-classifier selection), are used as inputs to the ggF-classifier. If the output of the ggF-classifier DNN of an event is above 0.5, it is sorted into the ggF-like category.
- All events that fail the above are sorted into the *rest* category.

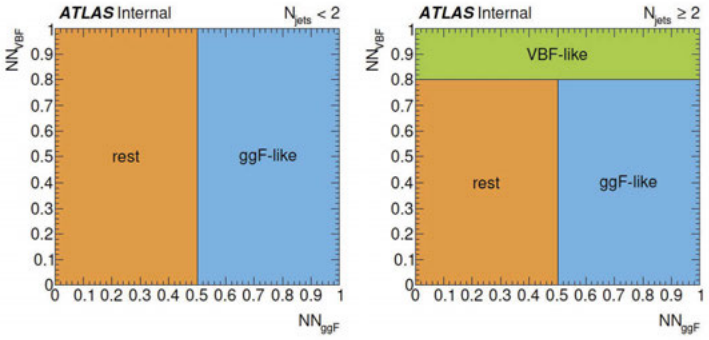

Figure 6.35: Event categorization scheme employed in the multi-variate $ZZ \to \ell\ell\ell\ell$ analysis. Based on the outputs of the VBF-classifier, $\mathrm{NN}_{\mathrm{VBF}}$, and the ggF-classifier, $\mathrm{NN}_{\mathrm{ggF}}$ [140].

This scheme is illustrated in Figure 6.35. Events in the ggF-like category are further split according to the lepton flavours, into the $4\mu, 2e2\mu, 4e$ channels, but the VBF-like and rest category events

of all lepton channels are combined to keep sufficient statistics.

As the multivariate-classifiers are trained on characteristics of specific signal samples, employing this categorization can lead to a model dependence. For this reason, the final results for the NWA Higgs analysis are also presented with the cut-based strategy in [6], but are not discussed in this thesis.

Backgrounds

In the $ZZ \to \ell\ell\ell\ell$ analysis SM non-resonant ZZ production accounts for as much as 97% of the total background. The ZZ total yield in the signal region is estimated from the observed data in the same way as in the $ZZ \to \ell\ell\nu\nu$ analysis, using the normalisation factor μ_{ZZ}. To decrease the statistical uncertainties arising from the finite MC samples, an analytical parametrization approach is used to obtain smoothed $m_{\ell\ell\ell\ell}$ shapes of the $q\bar{q}ZZ$, $qqZZjj$ EW and $ggZZ$ backgrounds. This is done by fitting an empirical function to the signal region $m_{\ell\ell\ell\ell}$ spectra derived from MC simulation. The fit function consists of two terms: The first term describes the low mass region up to the on-shell ZZ production threshold at $2 \cdot m_Z$ and is parametrized with a *Beta prime distribution*. The second term describes the slope along high $m_{\ell\ell\ell\ell}$ values beyond this threshold, and is parametrized with the exponential of a Beta prime distribution (with different parameters). A heavyside step function is used to describe the transition between the two regions. This functional form is described in detail in [6] and [140]. Figure 6.36 shows an example

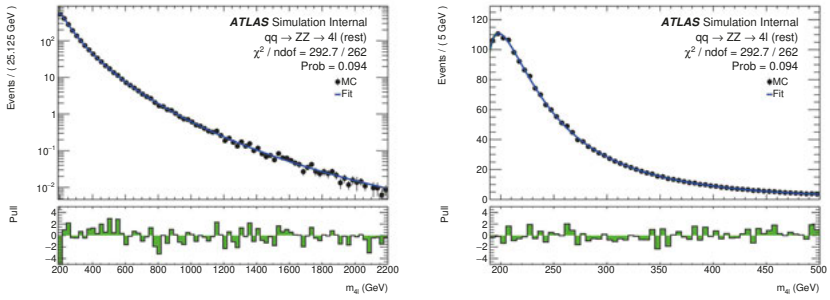

(a) 190 GeV < $m_{\ell\ell\ell\ell}$ < 2.2 TeV (b) 190 GeV < $m_{\ell\ell\ell\ell}$ < 500 GeV

Figure 6.36: Example fit to illustrate the analytic ZZ background parametrization in the $ZZ \to \ell\ell\ell\ell$ analysis, for $q\bar{q}ZZ$ events in the *rest* category. The total fitted range is shown in (a) and (b) presents a zoomed in view of the low $m_{\ell\ell\ell\ell}$ region [140].

of what the fit result looks like, to illustrate the $m_{\ell\ell\ell\ell}$ shape. The uncertainties on the post-fit values of all fit parameters are propagated and a corresponding background parametrization shape uncertainty is built from them.

In addition, there are minor backgrounds arising from Z+jets and $t\bar{t}$, as well as $t\bar{t}V$ and VVV events. Each of them only contributes at the percent-level. A data-driven approach is used to correct the yields of Z+jets and $t\bar{t}$ events using dedicated control regions. The method is common to all ATLAS $H \to ZZ \to \ell\ell\ell\ell$ analyses and described in detail in e.g [163, 164] and [165]. Analogously to the $ZZ \to \ell\ell\nu\nu$ analysis, the $t\bar{t}V$ and VVV contributions are grouped as the *other* background in the following. This background is fully based on MC simulation.

Systematic uncertainties

	Experimental sources				
Process	**Reconstruction**	**Data-driven**	**Luminosity**	**Parametrization**	**Theory**
Signal	✓	-	✓	✓	✓
ZZ	✓	✓	-	✓	✓
Z+jets, $t\bar{t}$	✓	✓	-	-	-
Others	✓	-	✓	-	-

Table 6.17: Overview of systematic uncertainty sources considered for each process in the $ZZ \to \ell\ell\ell\ell$ analysis.

An overview of all sources of systematic uncertainties on each process in the $ZZ \to \ell\ell\ell\ell$ analysis is given in Table 6.17. In general this is analogous to the $ZZ \to \ell\ell\nu\nu$ analysis, with the addition of systematic uncertainties arising from the analytic parametrizations of the signals and ZZ background, as discussed above. Due to the floating normalisation of the ZZ background in the final fit, only uncertainties on the ZZ shapes and relative $q\bar{q}ZZ$- $ggZZ$ acceptance need to be considered, as already detailed in 6.3.3.

In terms of reconstruction uncertainties, the same sources as in the $ZZ \to \ell\ell\nu\nu$ analysis are considered and estimated with the same methods. Only the experimental uncertainties on the total yields or acceptances are propagated, as the shape effects can be neglected. Ranking the experimental uncertainty sources by their (pre-fit) impact the picture is similar to the $\ell\ell\nu\nu$ analysis. In the ggF categories lepton reconstruction efficiency uncertainties play a leading role, but typically have small with impacts between 1% and 2%. Reconstruction uncertainties in the VBF categories are larger with impacts from 10% to 15% and the jet flavour composition and energy resolution being dominant.

The parametrization uncertainties on the signal acceptances are of the order of a few percent, depending on the category, and the impact of reconstruction uncertainties on the parametrization results is found to be negligible. In contrast, the shape uncertainties on the ZZ background

parametrization are significant, with impacts up to 40% especially in the high $m_{\ell\ell\ell\ell}$ regions.

Theory uncertainties from PDF choice, QCD scale and the parton shower model are evaluated for the signal and ZZ background processes. The approach follows that used in the $ZZ \to \ell\ell\nu\nu$ analysis. The impact of theory uncertainties on the signal acceptance is generally small, ranging from 0.2% to 5% depending on the category. Shape effects of the theory uncertainties on the signals can be neglected. For the ZZ backgrounds however, the shape uncertainties are sizeable, with variations up to 10% to 40% in the high $m_{\ell\ell\ell\ell}$ regions. PDF uncertainties on the ZZ yields are in the range of 1% to 3%, QCD scale uncertainties contribute between 3% and 30% and the parton showering uncertainties have impacts from 4% to 40%, all depending on the category. In general, the largest impacts are found for the VBF category.

6.5.2 Adding intermediate points in $ZZ \to \ell\ell\nu\nu$

As described above, the analytic parametrization of heavy Higgs signals in the $\ell\ell\ell\ell$ analysis allows to describe the $m_{\ell\ell\ell\ell}$ distribution at any signal and thus to obtain the cross-section limit with a very fine granularity of signal masses - even for signals for which no simulated events were generated. In contrast, the $\ell\ell\nu\nu$ only limits were so far only extracted for signal masses where simulate samples are available. To provide $\ell\ell\nu\nu$ inputs with higher granularity for the combined results, different interpolation techniques are used to obtain the m_{T} shapes, acceptances and systematic uncertainties for additional, intermediate mass points, as explained in the following.

NWA heavy Higgs

To decide which mass intervals are appropriate for the NWA Higgs signals, Figure 6.37 shows the m_{T} distributions of all ggF and VBF signals where simulated samples exist in their respective signal region category. Ideally, the limits should be set in mass intervals that are not (significantly) smaller than the resolution of the signals at each point. With this in mind, and also taking into account the coarse binning at high m_{T}, the following step size is chosen for the NWA interpretation:

- 20 GeV steps on the range from 300 GeV to 1 TeV of m_H
- 100 GeV steps on the range from 1 TeV to 2 TeV of m_H

At each of these mass points, a full fit using the signal and background m_{T} distributions including all systematic uncertainties will be performed, in the same way it is done for signal masses where simulated samples exist. The intermediate signal mass points are obtained with the following methods:

- First, the m_{T} shapes of the intermediate signal points are obtained using the *moment morphing* technique [142]. The technique is validated by comparing the *morphed* shape pre-

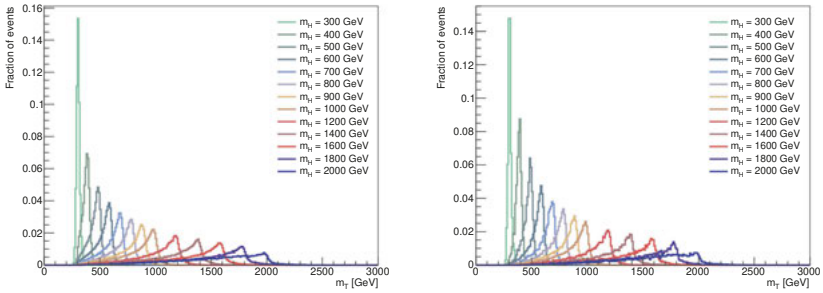

(a) ggF category (b) VBF category

Figure 6.37: m_{T} distributions of the NWA signal samples in the signal region. For (a) the ggF signals in the ggF category and (b) the VBF signals in the VBF category.

diction to the original MC distribution. Figure 6.38 shows this for the example of $m_H = 900$ GeV. Good agreement between the original and morphed shape is evident.

- Next, the signal acceptance is interpolated using a third order spline interpolation method [166], as shown in Figure 6.39.
- Last, the acceptance uncertainties on the signals are interpolated using simple spline-based linear interpolation [167]. An example each is shown in Figure 6.40 for a leading impact experimental and theoretical uncertainty. Since the impact of signal systematics on the results is minor, this interpolation is sufficiently precise.

LWA heavy Higgs

For the large-width analysis, the following granularity is chosen for the limits:

- 20 GeV steps on the range from 300 GeV to 1 TeV of m_H
- 100 GeV steps on the range from 1 TeV to 1.4 TeV of m_H
- 200 GeV steps on the range from 1.4 TeV to 2 TeV of m_H

Due to the broarder signal peak coarser granularity for very high signal masses, above 1.4 TeV is chosen here. As described previously, in Chapter 4.1, LWA signals can be obtained at any given mass point using the signal-to-signal analytic reweighting based on propagator ratios. Both the m_{T} shape and total signal yield at intermediate mass points are obtained in this way. For the LWA signals the same interpolated signal acceptance uncertainties as for the NWA signals are used, assuming that the impact of systematic uncertainties is the same for all widths.

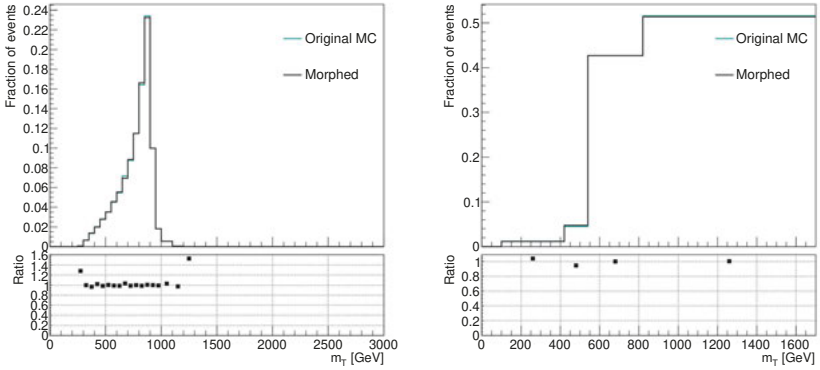

(a) ggF category (b) VBF category

Figure 6.38: Validation of the moment morphing technique: The signal at 900 GeV is obtained from the morphing using all other signals as inputs and then compared to its original MC m_{T} distribution. For (a) the ggF signal in the ggF category and (b) the VBF signal in the VBF category.

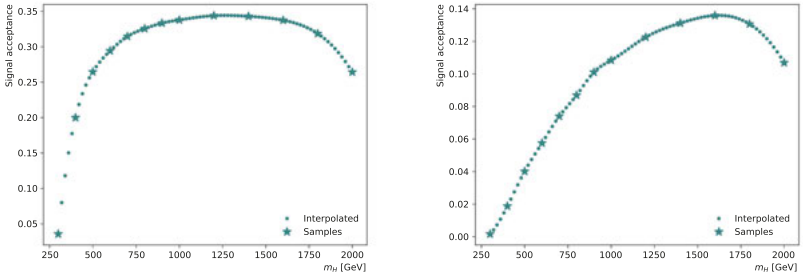

(a) ggF category (b) VBF category

Figure 6.39: Interpolation of the signal acceptances for (a) the ggF signals in the ggF category and (b) the VBF signals in the VBF category.

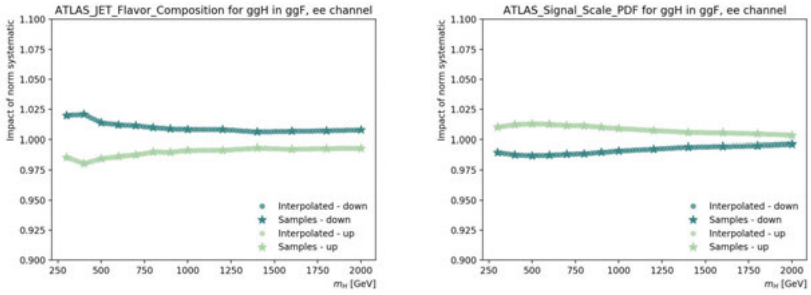

(a) Experimental uncertainty example

(b) Theory uncertainty example

Figure 6.40: Interpolation of the signal acceptance uncertainties arising from (a) the Jet Flavour composition and (b) the QCD scale uncertainty.

6.5.3 Results of the $ZZ \to \ell\ell\nu\nu$ and $ZZ \to \ell\ell\ell\ell$ combination

For the final statistical interpretation, all regions of the $ZZ \to \ell\ell\nu\nu$ and $ZZ \to \ell\ell\ell\ell$ analyses are used in a combined, simultaneous likelihood fit, following the approach explained in Chapter 4.5. With the DNN-based event categorisation of $\ell\ell\ell\ell$ events used for the NWA analysis there are in total nine regions - four from the $\ell\ell\nu\nu$ channel and five from the $\ell\ell\ell\ell$ channel. The large-width Higgs interpretation uses only the ggF category events from both channels and the cut-based $\ell\ell\ell\ell$ categorization, consisting of a total of five regions.

In the combined fit, individual ZZ normalisation factors μ_{ZZ} are used for the two different final states. Although the sensitivity to constrain μ_{ZZ} in the $\ell\ell\nu\nu$ regions would benefit from one common factor, due to the better separation power between signals and ZZ background in the $\ell\ell\ell\ell$ final state, studies done on Asimov data found that the expected sensitivity between the two cases is similar (cf. [9]). Hence, the μ_{ZZ} are kept separate for $\ell\ell\ell\ell$ and $\ell\ell\nu\nu$ regions as a more conservative option, avoiding problems due to the different selections. Moreover, in the $ZZ \to \ell\ell\ell\ell$ analysis separate normalisation factors μ_{ZZ} are defined for each category. This is possible due to the good mass resolution, and is not feasible for the $\ell\ell\nu\nu$ final state since especially in the VBF category the separation power is too small. In total there are then four different μ_{ZZ} factors in the NWA Higgs setup, and two in the LWA setup.

All experimental uncertainties are treated as fully correlated between the two final states. In contrast, the theory uncertainties are treated as uncorrelated, due to the different definitions of the signal regions.

Region	Total Bkg.	Data
$\ell\ell\nu\nu$, ggF, $ee\nu\nu$	1342 ± 52	1323
$\ell\ell\nu\nu$, ggF, $\mu\mu\nu\nu$	1527 ± 60	1542
$\ell\ell\nu\nu$, VBF, $ee\nu\nu$	8 ± 1	8
$\ell\ell\nu\nu$, VBF, $\mu\mu\nu\nu$	9 ± 2	10
$\ell\ell\ell\ell$, ggF, 4μ	284 ± 12	271
$\ell\ell\ell\ell$, ggF, $2e2\mu$	480 ± 20	493
$\ell\ell\ell\ell$, ggF, $4e$	192 ± 8	191
$\ell\ell\ell\ell$, VBF, incl.	19 ± 5	19
$\ell\ell\ell\ell$, rest, incl.	2300 ± 51	2301
Total	6161 ± 98	6158

Table 6.18: Post-fit observed and expected total background yields and their uncertainties in all regions of the $ZZ \to \ell\ell\nu\nu$ and $ZZ \to \ell\ell\ell\ell$ combination.

A fit to the observed data under the background only-hypothesis is performed with the combined setup. Table 6.18 shows the resulting total expected background yields compared to the observed data yields in each region. Here, the are ZZ yields are scaled with the best fit value of the respective normalisation factor, which are as follows:

$$\mu_{ZZ}(\ell\ell\nu\nu, \text{All}) = 1.06 \pm 0.06$$
$$\mu_{ZZ}(\ell\ell\ell\ell, \text{ggF}) = 1.07 \pm 0.05$$
$$\mu_{ZZ}(\ell\ell\ell\ell, \text{VBF}) = 0.89 \pm 0.31$$
$$\mu_{ZZ}(\ell\ell\ell\ell, \text{Rest}) = 1.12 \pm 0.03$$

Within all regions the background only prediction and observed data as shown in Table 6.18 are compatible within two standard deviations. No excess is seen in either final state. This is also apparent from the post-fit m_{T} and $m_{\ell\ell\ell\ell}$ distributions shown in Figure 6.41 and 6.42, respectively.

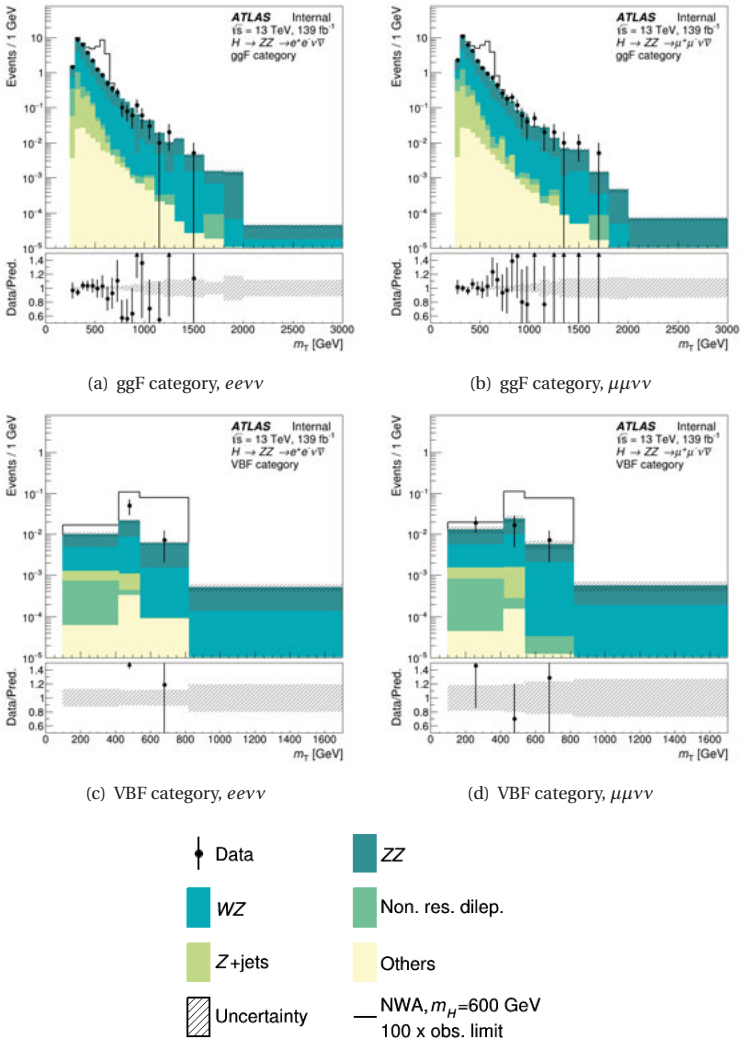

(a) ggF category, $eevv$

(b) ggF category, $\mu\mu\nu\nu$

(c) VBF category, $eevv$

(d) VBF category, $\mu\mu\nu\nu$

Figure 6.41: Post-fit expected and observed transverse mass distributions for the full run II data in the $ZZ \to \ell\ell\nu\nu$ regions after a combined fit to all $ZZ \to \ell\ell\nu\nu$ and $ZZ \to \ell\ell\ell\ell$ regions.

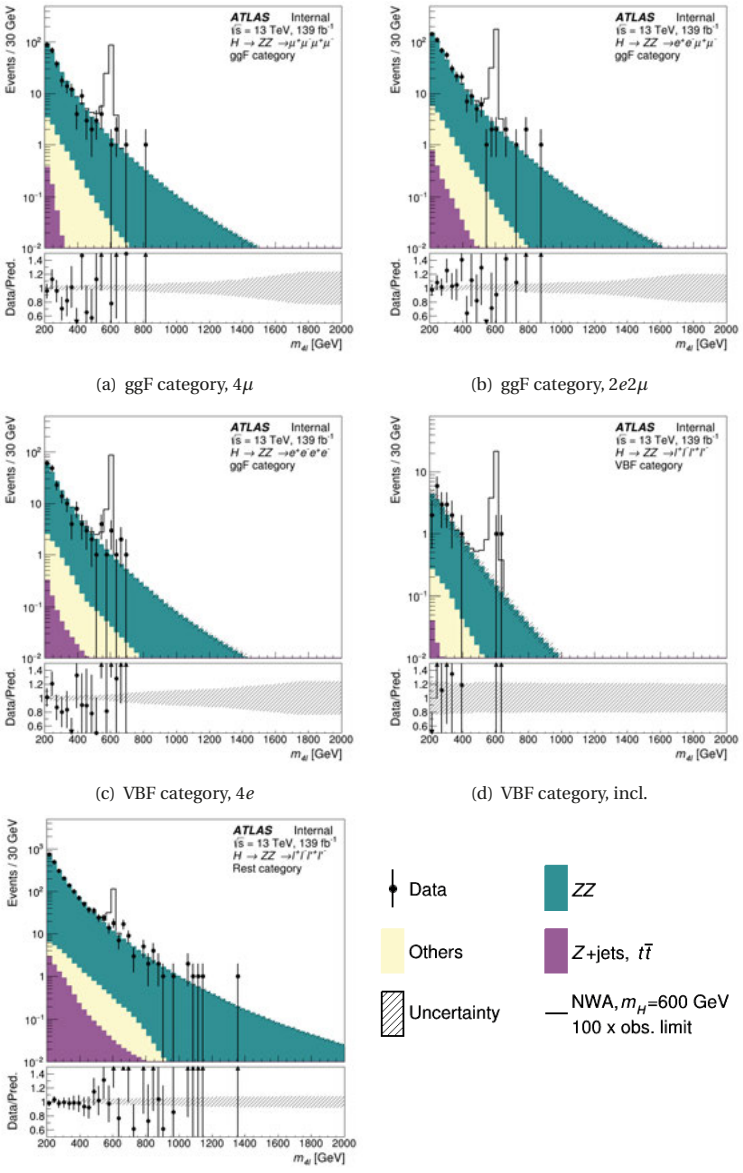

(a) ggF category, 4μ

(b) ggF category, $2e2\mu$

(c) VBF category, $4e$

(d) VBF category, incl.

(e) Rest category, incl

Figure 6.42: Post-fit expected and observed transverse mass distributions for the full run II data in the $ZZ \to \ell\ell\ell\ell$ regions after a combined fit to all $ZZ \to \ell\ell\nu\nu$ and $ZZ \to \ell\ell\ell\ell$ regions.

NWA heavy Higgs interpretation

Figure 6.43 shows the upper limits on the production cross-section times branching ratio, $\sigma \cdot \mathrm{BR}(H \to ZZ)$, of a narrow-width heavy Higgs derived from the combined $ZZ \to \ell\ell\nu\nu$ and $ZZ \to \ell\ell\ell\ell$ results, separately for ggF and VBF production.

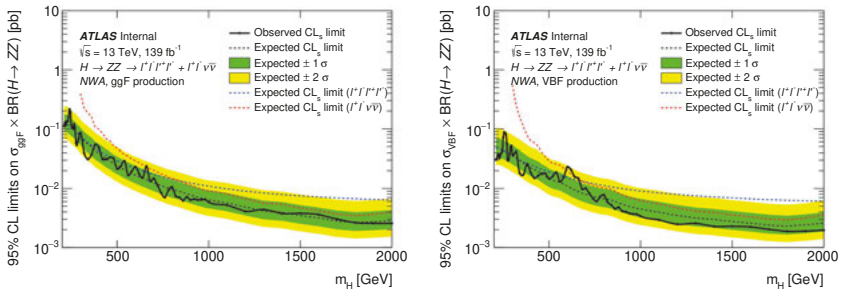

(a) ggF production (b) VBF production

Figure 6.43: Expected and observed upper limits on the production cross-section times branching fraction to ZZ pair of a narrow-width heavy Higgs in (a) ggF and (b) VBF production mode, using the full run II data.

Here, the cross-section limits are determined in the intervals of m_H as given in Chapter 6.5.2, employing the $\ell\ell\nu\nu$ interpolation techniques described there as well. The $\ell\ell\ell\ell$ intermediate mass points are obtained from the analytic parametrization described in Chapter 6.5.1. All connecting lines are purely for visualization. The search range starts at m_H = 200 GeV, using only $ZZ \to \ell\ell\ell\ell$ inputs for the first 100 GeV as the $ZZ \to \ell\ell\nu\nu$ has no sensitivity below 300 GeV due to the $E_{\mathrm{T}}^{\mathrm{miss}}$ cut. On the range from 200 GeV to 300 GeV the $ZZ \to \ell\ell\ell\ell$ limits are derived in intervals of 5 GeV.

The observed limit agrees with the expected limit within two standard deviations across the whole mass range. There are however deviations with 1.5 to 2σ local significance at around m_H =240 and m_H =700 GeV, in both production modes. Both of them originate only from events in the $\ell\ell\ell\ell$ channel - a mass of 240 GeV is outside of the $\ell\ell\nu\nu$ sensitivity range, and the $\ell\ell\nu\nu$ only limits at m_H =700 GeV show no excess (cf. Figure 6.28). Moreover, these minor excesses are only observed in the 2015 and 2016 data - their local significances in the analysis of this data only were above 2σ [5], but decreased with the addition of the 2017 and 2018 data. They were therefore not confirmed by the full run II data analysis, and are likely caused by fluctuations or a specific mismodelling only affecting that subset of the data. It is therefore concluded that no clear evidence for a new resonance is found.

For comparison, Figure 6.43 shows also the individual expected limits from the $\ell\ell\nu\nu$ and $\ell\ell\ell\ell$ final states only. As anticipated, the $\ell\ell\ell\ell$ analysis drives the sensitivity for low masses below $\approx$ 700 GeV, due to its good mass resolution. At higher masses, the $\ell\ell\nu\nu$ analysis provides better

sensitivity, due to the increased data statistics. Combining the two analyses therefore maximizes the potential of the search.

To evaluate the impact of uncertainties on the combined results, Table 6.19 shows an overview of the different uncertainty sources at three example masses. The most important point to note is that compared to the data statistical uncertainty, the impact of systematic uncertainties is limited. While the data statistical uncertainty is always larger than 50%, the total impact of systematic uncertainties is only around 15%. In addition, the five highest ranking (by impact) systematic uncertainty sources are shown in each case. They vary with signal mass hypothesis and production mode. At low masses, uncertainties from the $\ell\ell\ell\ell$ analysis are more relevant, and at high masses the ranking is dominated by $\ell\ell\nu\nu$ uncertainties. This is in accordance with the respective sensitivity of each final state. Similar trends as already seen in the $\ell\ell\nu\nu$ analysis are apparent: leading uncertainties originate mostly from the ZZ modelling and the Z+jets and non-resonant dilepton background estimation, which exhibit the largest relative uncertainties in this analysis. In the VBF category jet reconstruction related uncertainties are more relevant. In summary, the full run II search is still far from being limited by systematic uncertainties, and would benefit further from an even larger dataset.

(a) $m_H = 300$ GeV

ggF production		VBF production	
Uncertainty source	**1σ in %**	**Uncertainty source**	**1σ in %**
Full uncertainty	55	Full uncertainty	60
Data statistics	53	Data statistics	58
Total Systematics	15	Total Systematics	15
$\ell\ell\ell\ell$, ZZ parametrization	5	Common, Jet Flavour Composition	3
$\ell\ell\nu\nu$, Z + jets estimate (sys.)	3	$\ell\ell\ell\ell$, $q\bar{q}ZZ$ QCD scale	3
$\ell\ell\ell\ell$, signal parton showering	2	$\ell\ell\ell\ell$, ZZ parametrization	2
$\ell\ell\nu\nu$, non-resonant dilepton estimate (stat.)	2	Common, Jet energy scale	2
$\ell\ell\nu\nu$, $q\bar{q}ZZ$ EW corrections	2	Common, Luminosity	2

(b) $m_H = 600$ GeV

ggF production		VBF production	
Uncertainty source	**1σ in %**	**Uncertainty source**	**1σ in %**
Full uncertainty	57	Full uncertainty	63
Data statistics	54	Data statistics	61
Total Systematics	18	Total Systematics	16
$\ell\ell\nu\nu$, $q\bar{q}ZZ$ EW corrections	5	$\ell\ell\nu\nu$, ZZ QCD scale	9
$\ell\ell\nu\nu$, $q\bar{q}ZZ$ QCD scale	3	Common, Jet energy resolution (NP1)	6
$\ell\ell\nu\nu$, Z + jets estimate (sys.)	3	$\ell\ell\nu\nu$, ZZ parton showering	4
$\ell\ell\ell\ell$, $q\bar{q}ZZ$ PDF	2	$\ell\ell\nu\nu$, $q\bar{q}ZZ$ EW corrections	3
$\ell\ell\nu\nu$, non-resonant dilepton estimate (stat.)	2	Common, Jet energy resolution (NP5)	2

(c) $m_H = 1$ TeV

ggF production		VBF production	
Uncertainty source	**1σ in %**	**Uncertainty source**	**1σ in %**
Full uncertainty	59	Full uncertainty	59
Data statistics	57	Data statistics	58
Total Systematics	15	Total Systematics	11
$\ell\ell\nu\nu$, $q\bar{q}ZZ$ EW corrections	9	$\ell\ell\nu\nu$, $q\bar{q}ZZ$ parton showering	9
$\ell\ell\nu\nu$, $q\bar{q}ZZ$ parton showering	6	$\ell\ell\nu\nu$, $q\bar{q}ZZ$ EW corrections	5
$\ell\ell\nu\nu$, $q\bar{q}ZZ$ QCD scale	6	$\ell\ell\nu\nu$, $q\bar{q}ZZ$ QCD scale	3
$\ell\ell\nu\nu$, Z + jets estimate (sys.)	2	Common, Jet Flavour Composition	2
$\ell\ell\nu\nu$, $q\bar{q}ZZ$ PDF	2	Common, Jet energy scale	2

Table 6.19: Uncertainty impacts on the expected narrow-width heavy Higgs signal yields for three different example masses, when normalized with the corresponding expected upper cross-section limit. The data statistical uncertainty as well as total systematic uncertainty and the leading five systematic uncertainties are shown.

2HDM interpretation

The exclusion limits of the NWA heavy Higgs search are translated into exclusion contours in the parameter space of a specific Two Higgs doublet model (2HDM) by comparing the specific cross-section prediction at a given point in 2HDM parameter space with the observed and expected limits from the search. An explanation of this 2HDM and its parameters is given in Chap-

ter 1.2.2.

The 2HDM interpretation is only valid under the assumption that the additional Higgs boson in question has a negligible width as well as negligible interference. Therefore it can only be made for low mass points. Figure 6.44 shows the exclusion contours in the $\tan\beta$ versus $\cos(\alpha-\beta)$ plane for a type-I or type-II 2HDM for a mass of m_H = 200 and 300 GeV. At the 200 GeV mass point only the $ZZ \to \ell\ell\ell\ell$ analysis contributes, but the 300 GeV result includes the contribution from the $ZZ \to \ell\ell\nu\nu$ analysis.

Since the coupling of the heavy Higgs boson to a ZZ pair is proportional to $\cos(\alpha-\beta)$ in the 2HDM assumption, the $\cos(\alpha-\beta) = 0$ region cannot be excluded by $H \to ZZ$ searches. Furthermore, in this so-called alignment limit, the 125 GeV Higgs would be indistinguishable from the SM Higgs, despite actually being part of an extended Higgs sector. This would mean that additional heavy Higgs bosons would exist, but could not be found by the search presented here. As can be seen, there is still parameter space allowed aside from this possibility, although not very much, especially in the m_H = 200 GeV case.

LWA heavy Higgs interpretation

Figure 6.45 shows the combined cross-section limits on the ggF production of a heavy Higgs with a width of 1% to 15% of its mass. The interference effects that arise at large-width are included in all results, following the modelling techniques described in Chapter 4.3.

Here, the same effects as discussed previously are seen again: the larger the width the less stringent the limit. In addition, the statistical fluctuations smoothen out with increasing width as well. Furthermore, the turning point at which the $\ell\ell\nu\nu$ analysis becomes more sensitive moves to lower masses with increasing width. This is as expected, since with increasing intrinsic signal width the effect of the different resolutions (m_{T} vs. $m_{\ell\ell\ell\ell}$) becomes less relevant and the higher $ZZ \to \ell\ell\nu\nu$ branching ratio then dominates.

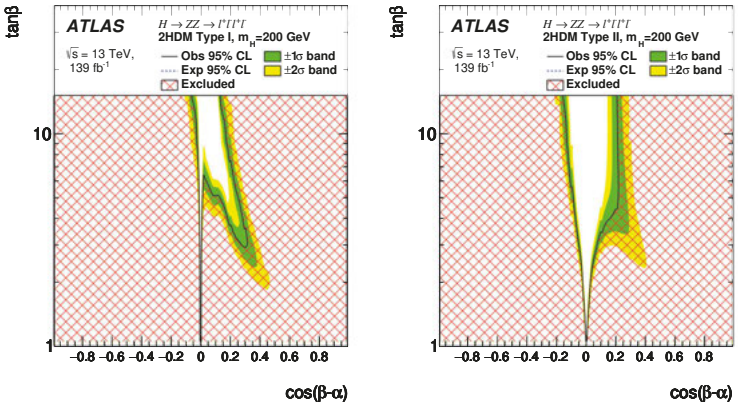

(a) $m_H = 200$ GeV, Type-I

(b) $m_H = 200$ GeV, Type-II

(c) $m_H = 300$ GeV, Type-I

(d) $m_H = 300$ GeV, Type-II

Figure 6.44: Exclusion limits in the $\tan\beta$ versus $\cos(\alpha - \beta)$ plane for a Type-I - (a) and (c) - or Type-II - (b) and (d) - 2HDM, for $m_H = 200$ and 300 GeV respectively. The hatched area is excluded by the observed data.

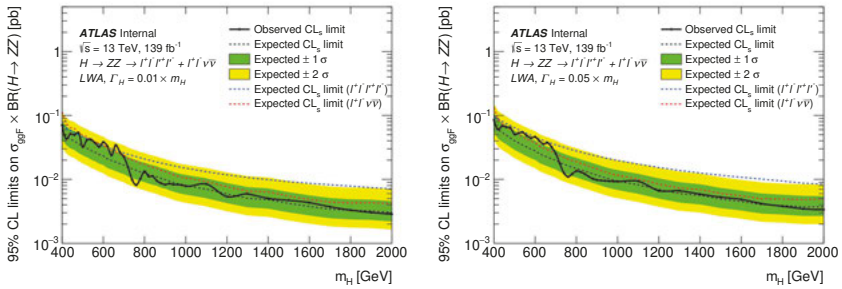

(a) 1% width

(b) 5% width

(c) 10% width

(d) 15% width

Figure 6.45: Expected and observed upper limits on the production cross-section times branching fraction to ZZ pair of a large-width heavy Higgs with a width of (a) 1%, (b) 5%, (c) 10% and (d) 15% of its mass.

Conclusion and outlook

Conclusion

This thesis presents a search for a BSM heavy Higgs boson decaying into a pair of Z bosons, using pp-collision data with $\sqrt{s}$ = 13 TeV recorded with ATLAS during the LHC's second run from 2015 to 2018. The main focus is the search in the $H \to ZZ \to \ell\ell\nu\nu$ channel where the Z boson pair further decays into two electrons or muons accompanied by two neutrinos.

Although the $\ell\ell\nu\nu$ final state is not fully reconstructible due to the neutrinos escaping detection, it offers good sensitivity in the mass range above m_H = 700 GeV due to the large branching ratio of the Z boson to decay to neutrinos. The experimental observable of the $\ell\ell\nu\nu$ channel is the transverse mass, m_{T}. For the official ATLAS results the $\ell\ell\nu\nu$ search is combined with the heavy Higgs search in the $\ell\ell\ell\ell$ channel. Due to its clean signature and excellent mass resolution the $\ell\ell\ell\ell$ channel dominates the sensitivity at lower Higgs masses, below 700 GeV. Together the $\ell\ell\nu\nu$ and $\ell\ell\ell\ell$ channel searches cover a mass range from 200 GeV to 2 TeV, when using the full run II dataset. Results were extracted for different hypothesis for the width of the heavy Higgs: in addition to an analysis assuming the narrow-width approximation (NWA), a large-width analysis (LWA) where the width ranges up to 15% of m_H was performed. In the large-width analysis, a dedicated modelling of the interference effects between heavy Higgs signal and SM Higgs as well as ZZ background was implemented.

No significant deviations with respect to the SM backgrounds were observed and therefore no evidence for any kind of the considered heavy Higgs bosons was found. To quantify the results, upper limits at 95% confidence level on the heavy Higgs production cross-section (including its branching ratio to ZZ) were set for each signal hypothesis using the CL_s method. The observed upper limits in the $\ell\ell\nu\nu$ channel, using the full run II dataset, range from 305 (400) fb for a mass of m_H = 300 GeV to 4-5 (3-4) fb for signal masses above 1.4 TeV in the ggF (VBF) production mode of the NWA analysis. For a heavy Higgs with a large width only the ggF production mode was considered. Here, the observed limits range from 260 fb for a heavy Higgs boson with a mass of 400 GeV and a width of 15% to 4 fb for Higgs bosons with masses above 1.4 TeV and a width of 1%. The LWA interference effects were found to affect the limits by less than one standard deviation.

These results present a significant improvement over the previous $\ell\ell\nu\nu$ analysis - also discussed in this thesis - that was only based on the 2015+16 data: with the full run II dataset, the mass range could be extended from 1.2 TeV to 2 TeV and the exclusion limits improved by a factor 3-4 in the ggF category and by a factor 4-8 in the VBF category of the NWA analysis, depending on the heavy Higgs mass. Several analysis improvements such as the reoptimization of the event

selection and the usage of the m_{T} shape information also in the VBF category lead this result, as from the increase in data statistics alone an improvement with factor 2 is expected.

Even with these improvements, the full run II analysis is still largely limited by statistics. Leading systematic uncertainties in the $\ell\ell\nu\nu$ channel arising from the estimation of the Z+jets background and theory uncertainties on the dominant ZZ background contribute in the range of 10-15% uncertainty, while the data statistical uncertainty is between 55-60%, depending on the specific signal hypothesis. This means that more data will allow for further significant improvement of the search results.

By combining the $\ell\ell\nu\nu$ with the $\ell\ell\ell\ell$ results, the exclusion limits were further improved by a factor 2 to 4 in the low mass range where the $\ell\ell\ell\ell$ channel is more sensitive, and by a factor 1.2 to 2 in the higher mass range where the $\ell\ell\nu\nu$ channel is more sensitive. An interpretation of these limits on heavy Higgs boson production cross-sections in terms of a specific Two Higgs Doublet Model (2HDM) was presented using the $\ell\ell\ell\ell + \ell\ell\nu\nu$ combined results for several Higgs masses. From this interpretation a significant fraction of the 2HDM parameter space was excluded.

In summary, with the full run II results presented here, a heavy Higgs boson with a mass between 200 GeV and 2 TeV that decays to a pair of Z bosons is severely constrained.

Where else to find a heavy Higgs boson?

As summarized above, the results presented in this thesis put a strong bound on the possibility for a heavy Higgs boson that can decay to Z bosons to exist in the considered mass range from 200 GeV to 2 TeV. However this is a very specific corner of phase space and does not necessarily tell us much about the overall probability for heavy Higgs bosons to exist - they may just be hiding somewhere else. Therefore, several other results about BSM Higgs bosons are briefly reviewed here. Two possibilities to look for signs of a heavy Higgs are considered: First, direct searches, such as the $H \to ZZ$ searches presented here, look for a heavy Higgs boson within a specific mass range and decaying into a certain final state, usually with few assumptions on the underlying BSM theory. Such direct searches are performed in many different decay channels, and with many different assumptions on the heavy Higgs boson. While searches for charged heavy Higgs bosons also exist [168], the focus in this section is on searches for a neutral heavy Higgs boson. Second, precision measurements of the cross-section and couplings of the 125 GeV Higgs boson present a complementary strategy to search for evidence of theories that predict the existence of heavy Higgs bosons and can be used to constrain the parameter space of specific models, such as 2HDMs.

Other direct searches involving bosonic decays of the heavy Higgs Aside from the $H \to ZZ$ decay, another possible decay of the heavy Higgs boson that might exhibit a high branching ratio at high masses is the $H \to WW$ channel (cf. Figure 1.5). For example, a search for a heavy, scalar resonance in the $WW \to e\nu\mu\nu$ final state using the 2015+16 ATLAS data of $\mathscr{L}$ = 36.1 fb^{-1} is presented in [169]. This final state is similar to the $\ell\ell\nu\nu$ channel, and this $WW \to e\nu\mu\nu$

search also uses the transverse mass of the final state leptons and missing transverse energy $E_{\mathrm{T}}^{\mathrm{miss}}$ as the discriminating variable. The selection of $H \to WW$ candidate events is based on kinematic variables such as the lepton transverse momenta, the dilepton invariant mass, the pseudorapidity difference between the two leptons and the transverse mass of the $W \to \ell\nu$ candidates. Major backgrounds originate from SM WW production and processes involving top quarks, such as $t\bar{t}$ and tW events, and are estimated from data using dedicated control regions. The top backgrounds are suppressed by a b-jet veto. Also in this $H \to WW$ search no evidence of a heavy Higgs boson is found in the covered mass range, which reaches from 200 GeV to 5 TeV. The results are interpreted as constraints on several different signal models: upper limits on the production cross-section of a heavy Higgs are set under the NWA as well as for large widths of 5, 10 and 15% of m_H. In both cases the ggF and VBF production are considered separately. The ggF NWA limits range from 6400fb for m_H =200 GeV to 8fb for m_H =4 TeV. In the large-width analysis, interference effects were found to have only minor impact on the limits and were thus neglected. Here, the ggF limits range from 5200 fb to 20 fb for heavy Higgs masses of 200 GeV and 4 TeV respectively and a width of 15% of m_H. Compared to the full run II $H \to ZZ$ searches presented in this thesis, the $H \to WW$ search in [169] results in significantly less stringent limits on the heavy Higgs production cross-section but is able to cover a larger mass range.

Another bosonic channel to search for a neutral BSM Higgs boson is the diphoton final state. A $H \to \gamma\gamma$ high mass search using the full run II ATLAS data can be found in [170], and this channel is also sensitive at low masses, below the 125 GeV mass of the discovered Higgs boson [171]. Finally, if the masses of the BSM Higgs bosons are large enough, Higgs to Higgs decays become possible. Promising examples of such channels are resonance searches in the di-Higgs production [172] and the possible decay of a heavy, CP-even BSM Higgs H to a lighter, CP-odd BSM Higgs A and a Z boson [173]. None of these searches have found statistically significant deviations from the SM.

Direct searches involving fermionic decays of the heavy Higgs As previously discussed (cf. Chapter 1.2.2) it is possible that the coupling between a BSM Higgs boson and the bosons of the SM is suppressed. This is the case for example near the alignment limit of 2HDMs, where neither direct searches for heavy Higgs bosons in bosonic channels nor precision measurements of the light Higgs are able to exclude the existence of additional Higgs bosons. To experimentally probe this region of parameter space, searches in fermionic channels are the key. Such fermionic Higgs decays also offer an additional advantage: whereas the decay of the CP-odd BSM Higgs A to the weak vector bosons is forbidden (at tree level), its decay to fermions is allowed. Therefore searches in the $t\bar{t}$ and $\tau\tau$ final state look for both a CP-even heavy Higgs H and a CP-odd heavy Higgs A.

The $A/H \to t\bar{t}$ analysis presents a particular challenge: here the heavy Higgs signal interferes strongly with the $gg \to t\bar{t}$ background and there is no interference with the light Higgs largely cancelling it, as the decay of the 125 GeV Higgs to a top quark pair is energetically not possible. The interference with the $gg \to t\bar{t}$ background therefore deforms the invariant mass distribution of the signal. Instead of a resonance peak, the signal plus interference distributions takes a peak-dip structure - with positive yields only in bins below the resonance mass, and negative yields (i.e.

depleting the background) in bins above it. The latest $A/H \to t\bar{t}$ results ATLAS published used the run I data [174] and observed no deviation from the SM across a mass range from 500 GeV to 750 GeV, while CMS has more recently published a $A/H \to t\bar{t}$ search with the 2015+16 run II data covering a mass range from 400 GeV to 750 GeV, and several different width assumptions [175]. This CMS search observed a moderate signal-like excess for CP-odd Higgs bosons with a mass at the lower bound of the search range with the largest deviation found for a heavy Higgs boson with m_A = 400 GeV and a width of 4% of its mass having a local (global) significance of 3.5 (1.9) σ. Although this is intriguing, missing higher order corrections in the modelling of the dominant SM $t\bar{t}$ background may be able to account for this discrepancy.

The $A/H \to \tau\tau$ searches are particularly promising candidates to constrain SUSY parameter space, as in e.g. the MSSM the heavy Higgs decay to τ-lepton pairs is enhanced. Recent results from ATLAS [176], using the full run II data, have not found any evidence of heavy Higgs bosons in a mass range from 200 GeV to 2.5 TeV.

125 GeV Higgs precision measurements Measuring the couplings of the 125 GeV Higgs boson also allows to constrain the parameter space of specific models, such as the specific 2HDM previously discussed. In this 2HDM, the coupling strengths of the light Higgs boson h to all SM particles are modified by a certain factor, e.g. by $\sin(\beta-\alpha)$ for the coupling to vector bosons, over what the SM predicts. A recent result from ATLAS, combining the 125 GeV Higgs couplings measurements in the $h \to \gamma\gamma$, $h \to ZZ \to \ell\ell\ell\ell$, $h \to WW$, $h \to \tau\tau$, $h \to b\bar{b}$ and $h \to \mu\mu$ decay channels as well as a search for light Higgs decays to invisible particles and using the full run II dataset is published in [4].

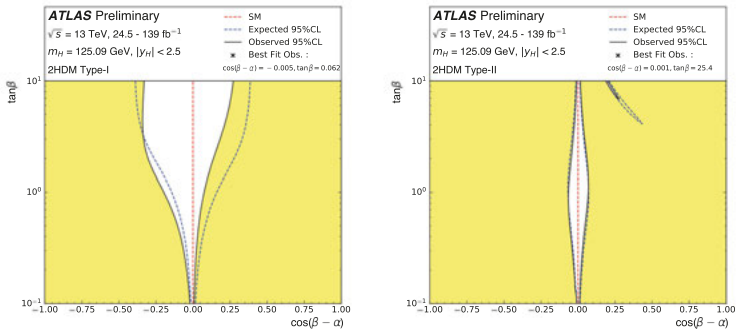

(a) Type-I (b) Type-II

Figure O.1: Exclusion limits in the $\tan\beta$ versus $\cos(\alpha-\beta)$ plane for (a) Type-I and (b) Type-II 2HDMs, based on the measurement of Higgs couplings to SM particles. The hatched area is excluded by the observed data and the dashed red line indicates the alignment limit. From [4].

Figure O.1 shows the 2HDM exclusion limits derived in this context, for type I and type II models. Unlike the 2HDM exclusion limits extracted from the heavy $H \to ZZ$ search shown in Chapter 6.5.3, these limits do not assume a specific Higgs mass, but constrain the 2HDM parameters space in general. The two results are complementary to each other: while the exclusion limits on a type II 2HDM from the couplings analysis are very stringent, the $H \to ZZ$ results from the search for a 200 GeV heavy Higgs are able to exclude a different region of parameter space than the couplings measurement for type I 2HDMs. This complementarity should be considered for future BSM Higgs studies- the results from the couplings analysis may show the way to the most promising regions of parameter space that direct searches may able to cover.

Outlook

This chapter looks into the future, discussing the prospects for the $\ell\ell\nu\nu$ search in particular, and heavy $H \to ZZ$ searches in general, in view of future data taking phases at the LHC. In the near future, a third run of the LHC is planned to start in late 2021. During this run of roughly three years a dataset of around $\mathscr{L} = 300$ fb^{-1} is planned to be collected. After a longer shut down phase, during which the detectors will be upgraded to be able to withstand higher instantaneous luminosities, the High Luminosity LHC (HL-LHC) data taking era will begin in 2027, as per current planning. The HL-LHC will collect a data set of $\mathscr{L}$ =3000 fb^{-1} at a centre-of-mass energy of $\sqrt{s} = 14$ TeV.

Prospects and ideas for the $H \to ZZ \to \ell\ell\nu\nu$ heavy Higgs search in run III

This chapter presents some considerations if, and how, redoing the heavy Higgs search discussed in this thesis with the run III data makes sense. To that end, Figure O.2(a) shows how much sensitivity could be gained by repeating the exact same analysis with a luminosity of 300 fb^{-1}. This simple scaling performed here represents a relatively pessimistic outlook for four reasons: First, it is likely that not only the sensitivity can be improved but that also the covered mass range can be extended with the larger dataset. Second, thanks to the increased statistics it will likely be possible to use a finer binning of the transverse mass observable, improving the expected sensitivity[3]. Third, in the scaling it is assumed that all systematic uncertainties remain the same, although it is likely that they can be decreased in the future - larger datasets used for calibration procedures will allow reducing reconstruction related uncertainties, and advances in theory calculations might provide better accuracy of the major background predictions at higher orders and with smaller theory uncertainties in several years time. Fourth, improvements to the analysis strategy, such as further optimization of the event selection, may be possible, just like 2015-18 data analysis was able to improve upon the analysis of the 2015+16 data.

Nevertheless, the expected increase in sensitivity obtained by repeating the analysis with the run III dataset is between 30% to 40% depending on the mass point, as evidenced in Figure O.2(a).

[3] This is even more relevant for the VBF category, where the m_{T} binning in the run II analysis is still extremely coarse, and hence the comparison is only done for the ggF production cross-section limits here.

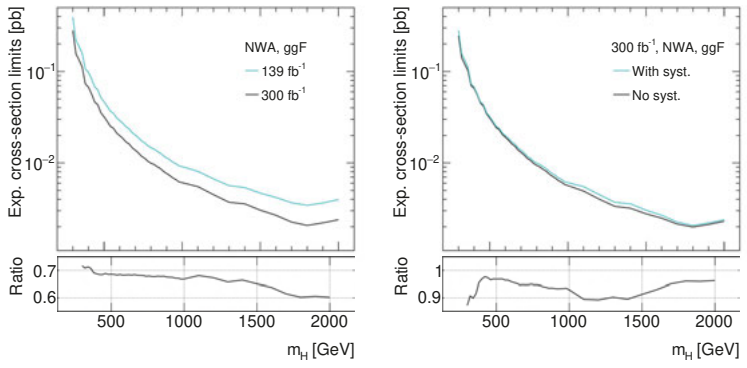

(a) (b)

Figure O.2: Comparison of expected exclusion limits on the ggF, NWA heavy Higgs production : (a) between the run II results, using 139 fb^{-1}, and a simple projection for the run III luminosity of 300 fb^{-1} assuming no other changes to the analysis and (b) between the 300 fb^{-1} expected limits with and without considering systematic uncertainties.

Two effects, pointing the way to areas of further improvement, can be identified: First, the improvement of the limits is significantly smaller at low than at high masses, and it is the smallest for masses below 400 GeV. Second, although the improvement rises with increasing mass, it flattens out for masses above approximately 1.7 TeV. It is therefore crucial to think about what factors are limiting the analysis in these regions.

At low masses, especially below 400 GeV, the available statistics are largest, as the expected background follows an exponentially falling distribution across the mass range considered. Furthermore, the low mass signals largely overlap with the bulk of the expected background, while higher mass signals are more easily separated. In consequence, systematic uncertainties on the background prediction play a bigger role in the low mass range than at higher masses. This is confirmed by Figure O.2(b) comparing the expected limits with and without taking into account systematic uncertainties when scaled to 300 fb^{-1}. The impact of systematics is largest at the low masses, with the limit without systematics at m_H =300 GeV being more than 10% better than the limit with systematics. Recalling the studies on systematic impacts presented in Chapter 6.4.2, leading sources of systematic uncertainties at this mass point arise from the data-driven estimates of the Z + jets and non-resonant dilepton backgrounds. For the non-resonant dilepton background this major uncertainty is the statistical uncertainty on the estimate, due to the limited amount of data statistics in the $e\mu$ control region and hence, this will naturally improve with the increasing dataset. In contrast, the Z + jets estimate is severely limited by its dominant systematic uncertainties. Although these systematic uncertainties are in part also caused by small data statistics, and thus are expected to reduce in the future, it is worthwhile to consider ways in which either the data-driven estimate itself can be made more accurate, or how the impact of this uncertainty on the results could be mitigated. The first may be achieved by following a different

methodology, such as using γ + jets data events to estimate the Z + jets contribution. Advantages of this technique are a large data sample, as well as the possible cancellation of systematic uncertainties on the MC predictions due to using the ratio of Z + jets over γ + jets events to reweight γ + jets to Z + jets events. The implementation of this method has been studied for the ATLAS full run II $\ell\ell\nu\nu$ search in [177], finding comparable results to the sideband method applied for the results presented here, also in terms of uncertainties. The γ + jets method is also used for the Z + jets background estimate in a comparable high mass $\ell\ell\nu\nu$ search performed by CMS [178]: using only the 2015+16 data this results in a total uncertainty on the Z + jets background in the $\ell\ell\nu\nu$ channel of 20-50%, smaller than the 30-80% Z + jets uncertainty achieved by the full run II search presented in this thesis. Hence, studying further improvements to the γ + jets method may be a promising option. Aside from this approach, it may also be possible to reduce the impact of Z + jets uncertainties on the results: one way would be to further optimize the event selection cuts to suppress this background even further, but another route may be to classify signal region events into more than the current two categories. With the 300 fb^{-1} dataset, there should be sufficient statistics to split the ggF category further into a 0-jet category and one (or more) category for events with more than one jet. In the 0-jet category, the Z + jets background contribution should be virtually absent, hence such a category could be very powerful for low signal masses. This categorization approach is already used successfully in the CMS search [178].

Although at high masses the search is largely limited by the available data statistics, another limiting factor is the decreasing signal acceptance at very high masses, notably beyond 1.6 TeV (cf. Figure 6.11). It was already hypothesized in Chapter 6.1.5 that the signal acceptance at such high masses is strongly limited by the efficiency of the lepton isolation requirement - the higher the mass of the heavy Higgs, the more boosted the decaying Z boson and thus the smaller the distance between the two leptons.

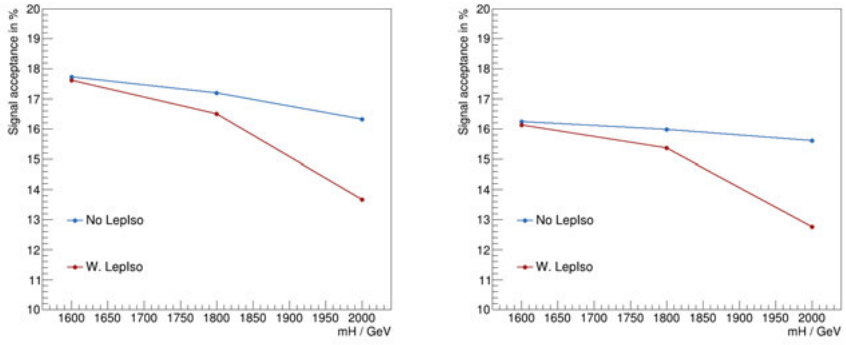

(a) $eevv$ channel (b) $\mu\mu\nu\nu$ channel

Figure O.3: Signal acceptances with and without the lepton isolation requirement for NWA, ggF heavy Higgs signals at three highest signal masses simulated, in (a) the $eevv$ and (b) the $\mu\mu\nu\nu$ flavour channel.

Figure O.3 confirms this hypothesis: the acceptances for the three highest mass signal samples are compared between the nominal event selection and the event selection without the lepton isolation requirement. If the efficiency of the lepton isolation cut could be brought close to 100%, most of the lost signal acceptance for these masses could be regained. Therefore, studying further improvements of the lepton isolation selection, especially for the case of two close-by signal leptons, will be crucial for future searches, that aim to extend the search to even higher masses.

As already indicated in the discussion, the kinematics of signal events are actually very strongly dependent on the signal mass. However, in the analyses presented here a single set of cut values on several kinematic variables is used for all signal masses considered. Every cut value is usually optimized considering only one, or few, signal masses, and therefore it is likely not optimal for all other signal masses. Figure O.4 illustrates this effect with two examples: the distributions of the missing transverse energy, as well as the angular distance between the two leptons are compared for all considered Higgs masses in the NWA analysis.

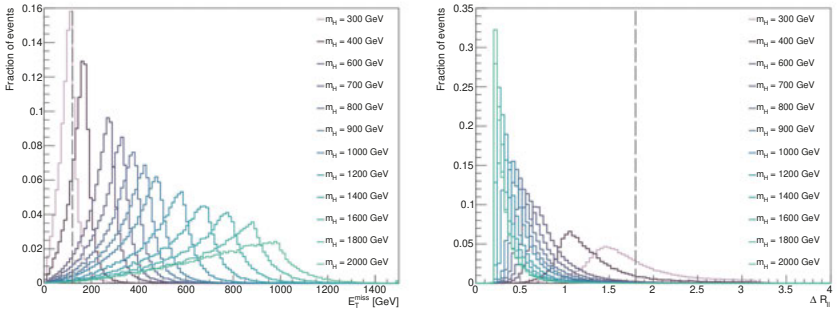

(a) $E_{\mathrm{T}}^{\mathrm{miss}}$ (b) $\Delta R_{\ell,\ell}$

Figure O.4: Comparison of two kinematic event selection variables for different masses of a ggF, NWA heavy Higgs, showing (a) the missing transverse energy and (b) the angular distance between the signal two leptons. The cut value used in the $\ell\ell\nu\nu$ analysis is indicated by the dashed grey line.

Clearly, it is difficult to find a common ground between the low and high mass signals - the latter have much larger $E_{\mathrm{T}}^{\mathrm{miss}}$ and much smaller $\Delta R_{\ell,\ell}$ than the former. A promising route to improvement is therefore the ability to have mass-dependent selection cuts, e.g. lower $E_{\mathrm{T}}^{\mathrm{miss}}$ but higher $\Delta R_{\ell,\ell}$ cut values at lower signal masses. Such mass-dependent criteria would likely improve the results across the full mass range - looser cuts for the low masses will greatly benefit the signal acceptances in this range, while tighter cuts for the higher masses would lead to better background suppression in that range. Although such an approach may be more laborious to implement, it would really let us exploit the full potential of the $\ell\ell\nu\nu$ data.

Finally, the full run II $\ell\ell\ell\ell$ analysis also briefly presented in this thesis has already proven the added value of multi-variate classifiers, such as neural networks, for the event categorization.

Such classifiers could bring a comparable benefit to the $\ell\ell\nu\nu$ channel, if used for the event selection and categorization.

Prospects for heavy Higgs $H \to ZZ$ searches at the HL-LHC

To look further into the future, analysis projections for a heavy Higgs search in $H \to ZZ$ at the HL-LHC are available from ATLAS [179] and CMS [180].

The ATLAS projection studies only the $\ell\ell\ell\ell$ channel, searching a mass range from 200 GeV to 1 TeV, and assumes that the width of the Higgs boson follows the SM Higgs prediction (cf. Figure 1.5). Interference effects with the ZZ background are taken into account in this study as an additional uncertainty, while the interference between heavy and 125 GeV Higgs is not included. Under these conditions, the expected upper limits using the $\mathscr{L} = 3000\text{fb}^{-1}$ of expected HL-LHC data are found to reach down to $\mathcal{O}(0.01)$fb on the ggF cross-section and to $\mathcal{O}(0.001)$fb on the VBF cross-section. Thus, despite considering only the $\ell\ell\ell\ell$ channel - the ZZ decay with the smallest branching ratio - these projected results improve what has been found in the run II analysis by orders of magnitude, simply due to the huge increase in the amount of data. Based on the findings presented in this thesis, combining the $\ell\ell\ell\ell$ with the more abundant $\ell\ell\nu\nu$ channel should offer further significant improvement of the limits, especially in the very high mass range - under the assumption that it is possible to perform a $\ell\ell\nu\nu$ analysis of comparable sensitivity at the HL-LHC. Due to the increase in pile-up (up to $\mathcal{O}(200)$ average interactions per beam crossing) this may not be straightforward, as the reconstruction of the missing transverse energy will become more challenging under such conditions. Another aspect in which the HL-LHC search may offer better sensitivity than quantified in the current official projections is due to the choice in interference modelling: including interference effects only as a systematic uncertainty impacts the sensitivity negatively, while the studies presented in this thesis found that the total effect of *both* the interference with the ZZ background and the 125 GeV Higgs may actually enhance the sensitivity to a heavy Higgs boson (depending on the heavy Higgs mass). With increasing statistics and thus decreasing statistical uncertainties, the large-width heavy Higgs search will become more sensitive to the impact of interference effects. To continue such studies in the future it will likely be necessary to also model the interference effects in VBF production events, which are currently not considered in the $H \to ZZ$ search for a large-width heavy Higgs.

In contrast to the ATLAS study, the CMS projection focusses on the $\ell\ell qq$ channel, as previous $H \to ZZ$ searches at CMS have identified this channel as the most sensitive for masses above 700 GeV[4]. The mass range considered is then also different from the ATLAS case, spanning from 700 GeV to 3 TeV. Only narrow-width Higgs bosons are considered, so interference effects between heavy Higgs signal and backgrounds do not play a role. Moreover, two different scenarios for the systematic uncertainties are compared in the CMS study, but the difference in upper limits between the two is found to be minor. This indicates that the $\ell\ell qq$ search in such high mass regions will *still* be limited by statistics even with $\mathscr{L} = 3000\text{fb}^{-1}$. Clearly this is an indication that it is useful to include additional ZZ decay channels in future searches, e.g. also the fermionic

[4] This means that the expected HL-LHC sensitivity presented in the CMS study is not directly comparable to the results presented in this thesis.

$\ell\ell\nu\nu$ and $\ell\ell\ell\ell$ channels studied in this thesis, to further decrease statistical uncertainties and improve the sensitivity.

A Trigger menus

Data taking period	Trigger selection	
	Single electron	Single muon
2015	e24_lhmedium_L1EM18VH OR e60_lhmedium OR e120_lhloose	mu20_iloose_L1MU15 OR mu50
2016	e24_lhtight_nod0_ivarloose OR e60_lhmedium_nod0 OR e140_lhloose_nod0	mu24_ivarmedium OR mu50
2016, after 1×10^{34} cm^{-2}s^{-1}	e26_lhtight_nod0_ivarloose OR e60_lhmedium_nod0 OR e140_lhloose_nod0	mu26_ivarmedium OR mu50
2017	e26_lhtight_nod0_ivarloose OR e60_lhmedium_nod0 OR e140_lhloose_nod0	mu26_ivarmedium OR mu50
2018	e26_lhtight_nod0_ivarloose OR e60_lhmedium_nod0 OR e140_lhloose_nod0	mu26_ivarmedium OR mu50

Table A.1: Trigger menus used in the analyses presented here: Lowest unprescaled single lepton triggers per data-taking year.

B Kinematic distributions

This appendix shows the distributions of all kinematic variables used for the event selection in the $H \to ZZ \to \ell\ell\nu\nu$ analysis of the full run II dataset of $\mathscr{L}$ = 139 fb^{-1}. All distributions are shown at pre-selection level, right after the requirement for the invariant dilepton mass to be within 15 GeV of the Z boson mass. Here, the expected backgrounds are taken directly from MC, with no further corrections applied. As an example, a narrow-width heavy Higgs boson with m_H = 600 GeV produced in ggF is shown. Only statistical uncertainties are shown.

- Figure B.1 shows the di-lepton invariant mass, $m_{\ell\ell}$.
- Figure B.2 shows the missing transverse energy, using PFlow jets, $E_{\mathrm{T}}^{\mathrm{miss}}$.
- Figure B.3 shows the angular separation between the two selected leptons, $\Delta R_{\ell\ell}$
- Figure B.4 shows the angle between the selected di-lepton and the missing transverse energy, $\Delta\phi(Z, E_T^{\mathrm{miss}})$
- Figure B.5 shows minimal angle between the missing transverse energy and any jet with $p_{\mathrm{T}} > 100\,\mathrm{GeV}$, $\min(\Delta\phi(jet, E_T^{\mathrm{miss}}))$.
- Figure B.6 shows the $E_{\mathrm{T}}^{\mathrm{miss}}$ significance.
- Figure B.7 shows the number of b-tagged jets in the event.
- Finally, Figures B.8 and B.9 show the dijet invariant mass, m_{jj}, and pseudo-rapidity difference, $|\Delta\eta_{jj}|$, as used to isolate VBF-type events.

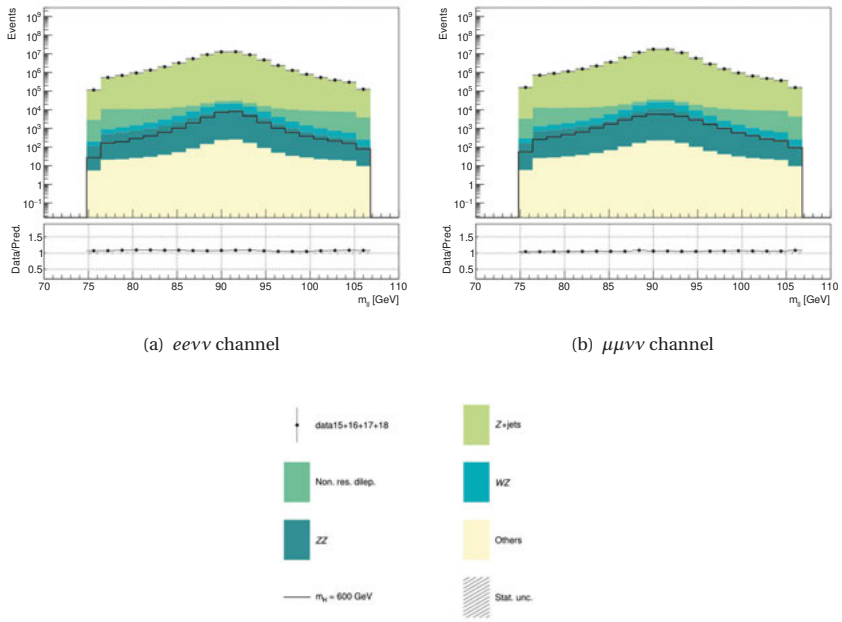

(a) $ee\nu\nu$ channel

(b) $\mu\mu\nu\nu$ channel

Figure B.1: Di-lepton invariant mass, $m_{\ell\ell}$, distributions for events passing pre-selection including the Z mass requirement for the full run II dataset corresponding to $\mathscr{L} = 139$ fb^{-1}.

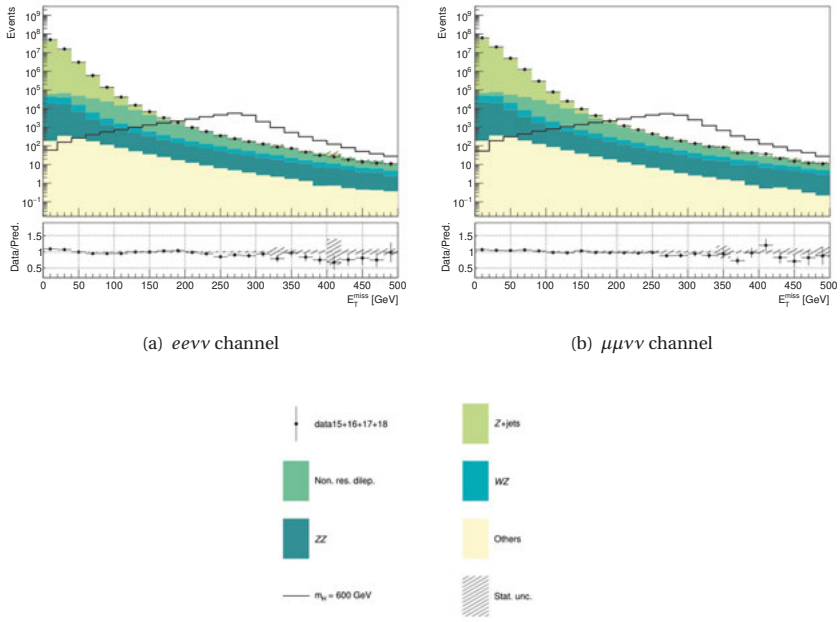

(a) $ee\nu\nu$ channel

(b) $\mu\mu\nu\nu$ channel

Figure B.2: Missing transverse energy, $E_{\mathrm{T}}^{\mathrm{miss}}$, distributions for events passing pre-selection including the Z mass requirement for the full run II dataset corresponding to $\mathscr{L}$ = 139 fb^{-1}.

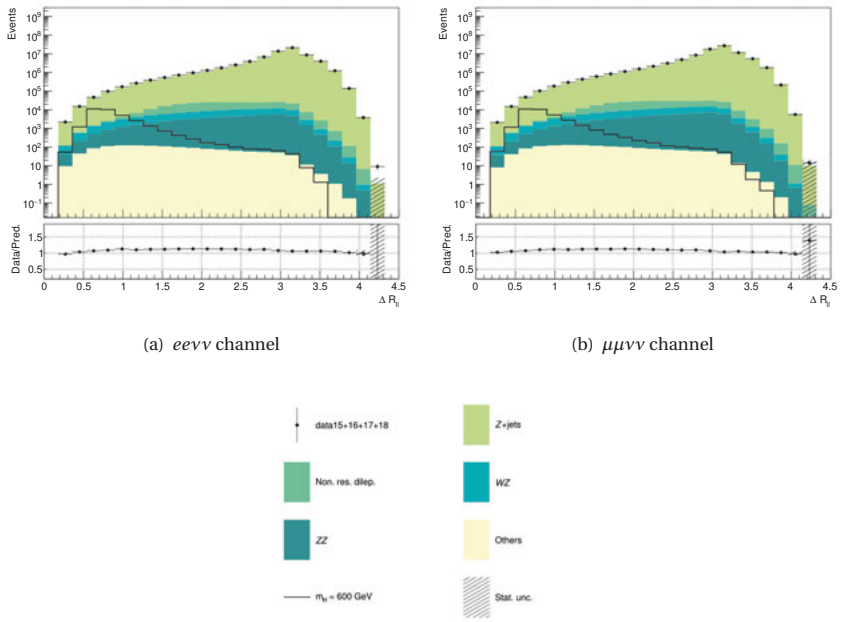

(a) *eevv* channel

(b) *μμvv* channel

Figure B.3: Angular separation between the two selected leptons, $\Delta R_{\ell\ell}$, distributions for events passing pre-selection including the Z mass requirement for the full run II dataset corresponding to $\mathscr{L}$ = 139 fb^{-1}.

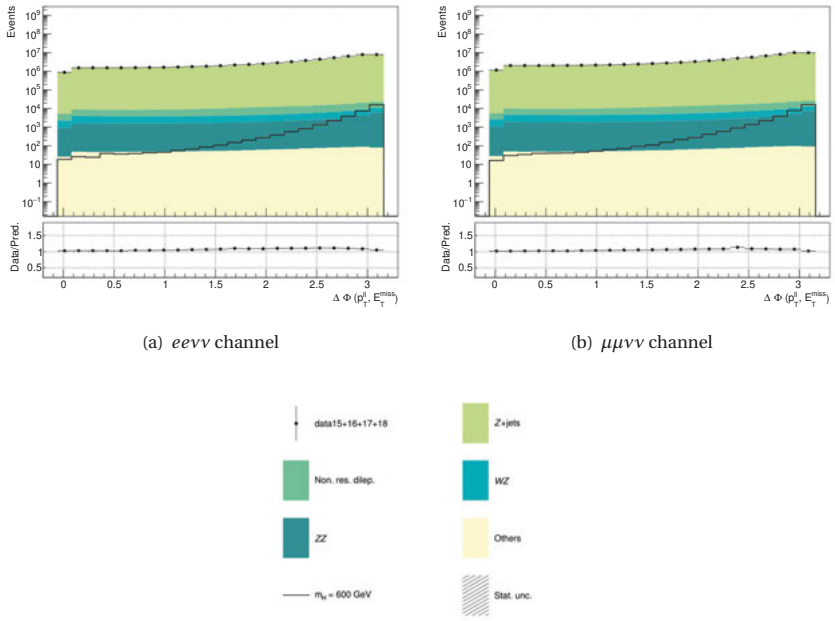

(a) $ee\nu\nu$ channel

(b) $\mu\mu\nu\nu$ channel

Figure B.4: Angular separation between the selected di-lepton and the missing transverse energy, $\Delta\phi(Z, E_T^{\text{miss}})$, distributions for events passing pre-selection including the Z mass requirement for the full run II dataset corresponding to $\mathscr{L}$ = 139 fb^{-1}.

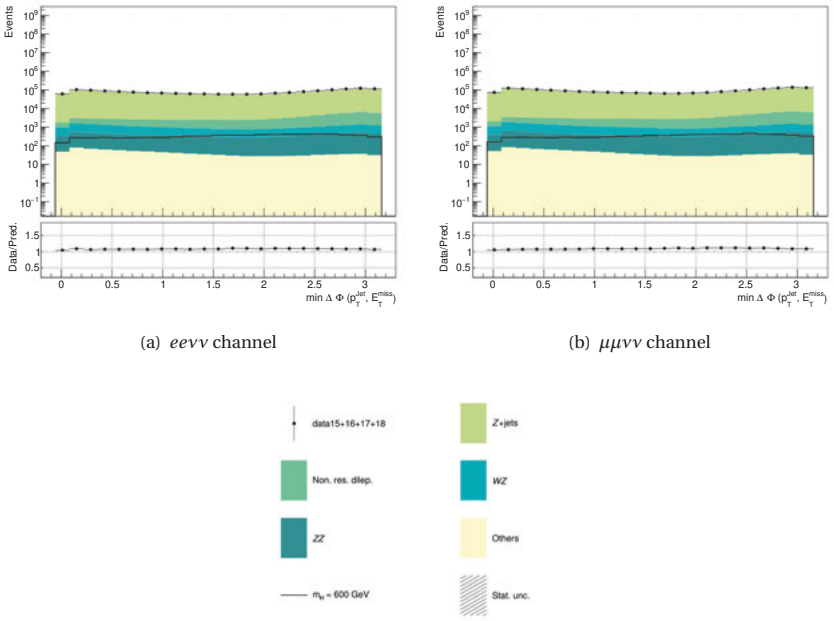

(a) *eevv* channel

(b) $\mu\mu\nu\nu$ channel

Figure B.5: Minimum angular separation between the missing transverse energy and any jet with pT > 100 GeV, $\min(\Delta\phi(jet, E_T^{\text{miss}}))$, distributions for events passing pre-selection including the Z mass requirement for the full run II dataset corresponding to $\mathscr{L}$ = 139 fb^{-1}.

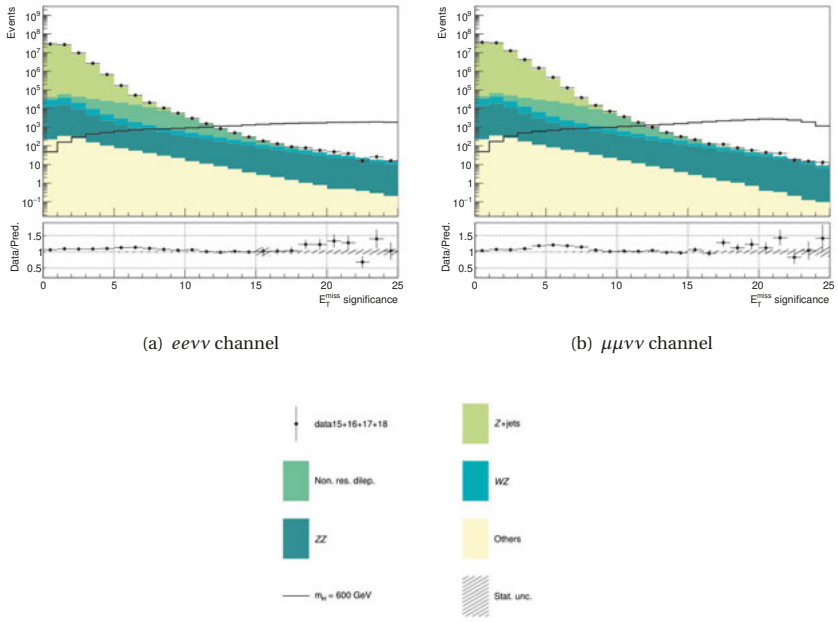

(a) $ee\nu\nu$ channel

(b) $\mu\mu\nu\nu$ channel

Figure B.6: $E_{\mathrm{T}}^{\mathrm{miss}}$ significance distributions for events passing pre-selection including the Z mass requirement for the full run II dataset corresponding to $\mathscr{L}$ = 139 fb^{-1}.

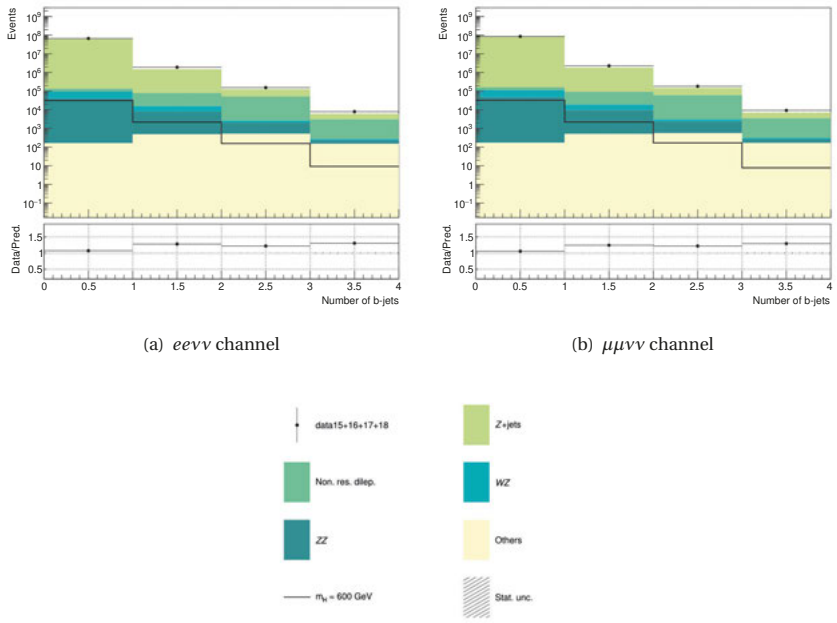

(a) *eevv* channel

(b) $\mu\mu\nu\nu$ channel

Figure B.7: Number of b-tagged jets distributions for events passing pre-selection including the Z mass requirement for the full run II dataset corresponding to $\mathscr{L}$ = 139 fb^{-1}.

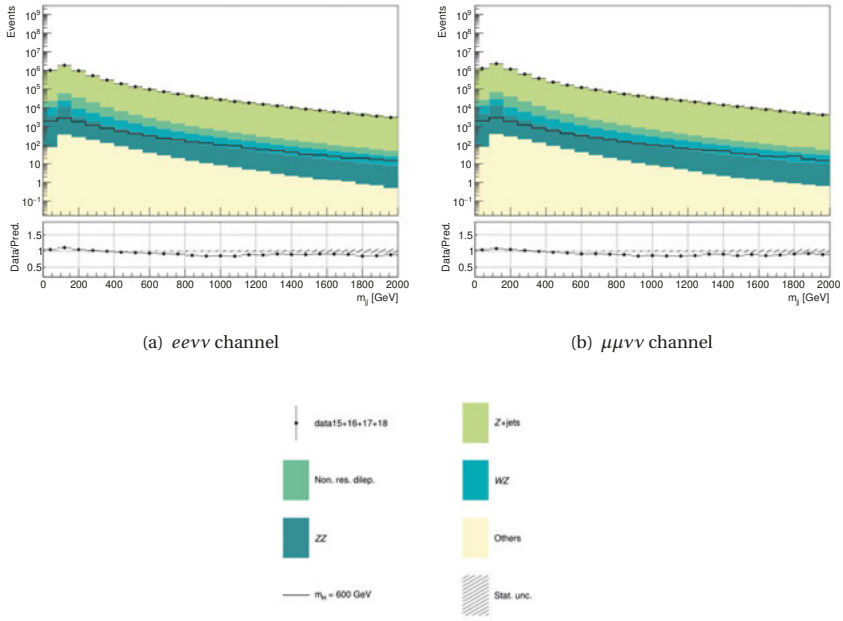

(a) $ee\nu\nu$ channel

(b) $\mu\mu\nu\nu$ channel

Figure B.8: Di-jet invariant mass, m_{jj}, distributions for events passing pre-selection including the Z mass requirement for the full run II dataset corresponding to $\mathscr{L}$ = 139 fb^{-1}.

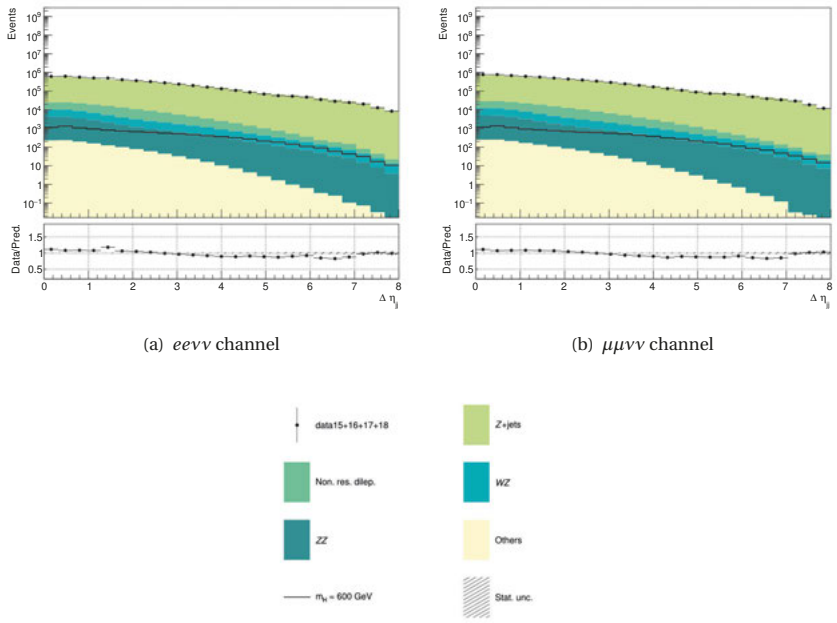

(a) *eevv* channel

(b) *μμνν* channel

Figure B.9: Di-jet pseudo-rapidity difference, $|\Delta\eta_{jj}|$, distributions for events passing pre-selection including the Z mass requirement for the full run II dataset corresponding to $\mathscr{L} = 139$ fb^{-1}.

Bibliography

[1] L. Evans and P. Bryant. "LHC Machine". In: *Journal of Instrumentation* 3.08 (Aug. 2008). DOI: 10.1088/1748-0221/3/08/s08001.

[2] ATLAS Collaboration. "Observation of a new particle in the search for the Standard Model Higgs boson with the ATLAS detector at the LHC". In: *Physics Letters B* 716.1 (Sept. 2012), pp. 1–29. ISSN: 0370-2693. DOI: 10.1016/j.physletb.2012.08.020.

[3] CMS Collaboration. "Observation of a new boson at a mass of 125 GeV with the CMS experiment at the LHC". In: *Physics Letters B* 716.1 (Sept. 2012), pp. 30–61. ISSN: 0370-2693. DOI: 10.1016/j.physletb.2012.08.021.

[4] ATLAS Collaboration. "A combination of measurements of Higgs boson production and decay using up to 139 fb^{-1} of proton–proton collision data at $\sqrt{s}$ = 13 TeV collected with the ATLAS experiment". Tech. rep. CERN, Aug. 2020.

[5] ATLAS Collaboration. "Search for heavy ZZ resonances in the $\ell^+\ell^-\ell^+\ell^-$ and $\ell^+\ell^-\nu\bar{\nu}$ final states using proton–proton collisions at $\sqrt{s}$ = 13 TeV with the ATLAS detector". In: *The European Physical Journal C* 78.4 (Apr. 2018). ISSN: 1434-6052. DOI: 10.1140/epjc/s10052-018-5686-3.

[6] ATLAS Collaboration. "Search for heavy resonances decaying into a pair of Z bosons in the $\ell^+\ell^-\ell'^+\ell'^-$ and $\ell^+\ell^-\nu\bar{\nu}$ final states using 139 fb^{-1} of proton-proton collisions at $\sqrt{s}$ = 13 TeV with the ATLAS detector". 2020. arXiv: 2009.14791 [hep-ex].

[7] ATLAS Collaboration. "Search for an additional, heavy Higgs boson in the $H \to ZZ$ decay channel at $\sqrt{s} = 8$ TeV in pp p collision data with the ATLAS detector". In: *The European Physical Journal C* 76.1 (Jan. 2016). ISSN: 1434-6052. DOI: 10.1140/epjc/s10052-015-3820-z.

[8] E. van der Poel. "Muon performance studies in ATLAS towards a search for the Standard Model Higgs boson". PhD thesis. Universiteit van Amsterdam, 2012.

[9] C. Geng, Y. Wu, B. Stapf, G. Barone, A. Gabrielli, A. Schaffer. "Search for heavy resonances in the $H' \to ZZ \to \ell\ell\nu\nu$ channel with proton-proton collisions at $\sqrt{s}$ = 13 TeV for 2015-2018 data with the ATLAS detector". Tech. rep. CERN, Nov. 2018.

[10] D. J. Griffiths. "Introduction to elementary particles; 2nd rev. version". New York: Wiley, 2008.

[11] M.Merk, I. van Vulpen, and W. Hulsbergen. "Particle Physics 1, Lecture notes for the first year master course onthe electroweak part of the Standard Model". 2018.

[12] W. Hollik. "Quantum field theory and the Standard Model". In: *2009 European School of High-Energy Physics*. Dec. 2010. arXiv: 1012.3883 [hep-ph].

[13] A. Djouadi. "The anatomy of electroweak symmetry breaking". In: *Physics Reports* 457.1-4 (Feb. 2008), pp. 1–216. ISSN: 0370-1573. DOI: 10.1016/j.physrep.2007.10.004.

[14] W. Buchmüller and C. Lüdeling. "Field Theory and Standard Model". In: *2005 European School of High-Energy Physics* (Sept. 2006), pp. 1–54. DOI: 10.5170/CERN-2006-014.1.

[15] M. Tanabashi et al. "Review of Particle Physics". In: *Phys. Rev. D* 98 (3 Aug. 2018). DOI: 10.1103/PhysRevD.98.030001.

[16] E. Noether. "Invariante Variationsprobleme". In: *Nachrichten von der Gesellschaft der Wissenschaften zu Göttingen, Mathematisch-Physikalische Klasse* (1918), pp. 235–257.

[17] M. Gell-Mann. "Symmetries of Baryons and Mesons". In: *Phys. Rev.* 125 (3 Feb. 1962), pp. 1067–1084. DOI: 10.1103/PhysRev.125.1067.

[18] S.L. Glashow. "Partial Symmetries of Weak Interactions". In: *Nucl. Phys.* 22 (1961), pp. 579–588. DOI: 10.1016/0029-5582(61)90469-2.

[19] S. Weinberg. "A Model of Leptons". In: *Phys. Rev. Lett.* 19 (21 Nov. 1967), pp. 1264–1266. DOI: 10.1103/PhysRevLett.19.1264.

[20] A. Salam. "Weak and Electromagnetic Interactions". In: *Conf. Proc. C* 680519 (1968), pp. 367–377. DOI: 10.1142/9789812795915_0034.

[21] F. Englert and R. Brout. "Broken Symmetry and the Mass of Gauge Vector Mesons". In: *Phys. Rev. Lett.* 13 (9 Aug. 1964), pp. 321–323. DOI: 10.1103/PhysRevLett.13.321.

[22] P. W. Higgs. "Broken Symmetries and the Masses of Gauge Bosons". In: *Phys. Rev. Lett.* 13 (16 Oct. 1964), pp. 508–509. DOI: 10.1103/PhysRevLett.13.508.

[23] P. W. Higgs. "Broken symmetries, massless particles and gauge fields". In: *Phys. Lett.* 12 (1964), pp. 132–133. DOI: 10.1016/0031-9163(64)91136-9.

[24] G. S. Guralnik, C. R. Hagen, and T. W. B. Kibble. "Global Conservation Laws and Massless Particles". In: *Phys. Rev. Lett.* 13 (20 Nov. 1964), pp. 585–587. DOI: 10.1103/PhysRevLett.13.585.

[25] L. Reina. "TASI 2004 Lecture Notes: Higgs Boson Physics. Higgs Boson Physics". Tech. rep. FSU-HEP-2005-12-30. Dec. 2005.

[26] J. Goldstone, A. Salam, and S. Weinberg. "Broken Symmetries". In: *Phys. Rev.* 127 (3 Aug. 1962), pp. 965–970. DOI: 10.1103/PhysRev.127.965.

[27] J. R. Ellis. "Higgs Physics". 2013. arXiv: 1312.5672 [hep-ph].

[28] C. Rovelli. "Notes for a brief history of quantum gravity". In: *9th Marcel Grossmann Meeting on Recent Developments in Theoretical and Experimental General Relativity, Gravitation and Relativistic Field Theories (MG 9)*. June 2000, pp. 742–768. arXiv: gr-qc/0006061.

[29] L. Randall and R. Sundrum. "Large Mass Hierarchy from a Small Extra Dimension". In: *Physical Review Letters* 83.17 (Oct. 1999), pp. 3370–3373. ISSN: 1079-7114. DOI: 10.1103/physrevlett.83.3370.

[30] K. Freese. "Review of Observational Evidence for Dark Matter in the Universe and in upcoming searches for Dark Stars". In: *EAS Publ. Ser.* 36 (2009), pp. 113–126. DOI: 10.1051/eas/0936016. arXiv: 0812.4005 [astro-ph].

[31] V. C. Rubin and W. K. Ford Jr. "Rotation of the Andromeda Nebula from a Spectroscopic Survey of Emission Regions". In: *Astrophys. J.* 159 (1970), pp. 379–403. DOI: 10.1086/150317.

[32] D. Clowe et al. "A direct empirical proof of the existence of dark matter". In: *Astrophys. J. Lett.* 648 (2006), pp. L109–L113. DOI: 10.1086/508162. arXiv: astro-ph/0608407.

[33] Y. Fukuda et al. "Evidence for Oscillation of Atmospheric Neutrinos". In: *Phys. Rev. Lett.* 81 (8 Aug. 1998), pp. 1562–1567. DOI: 10.1103/PhysRevLett.81.1562.

[34] Q. R. Ahmad et al. “Direct Evidence for Neutrino Flavor Transformation from Neutral-Current Interactions in the Sudbury Neutrino Observatory”. In: *Phys. Rev. Lett.* 89 (1 June 2002). DOI: 10.1103/PhysRevLett.89.011301.

[35] T. D. Lee. “A Theory of Spontaneous *T* Violation”. In: *Phys. Rev. D* 8 (4 Aug. 1973), pp. 1226–1239. DOI: 10.1103/PhysRevD.8.1226.

[36] R. D. Peccei and H. R. Quinn. “CP Conservation in the Presence of Pseudoparticles”. In: *Phys. Rev. Lett.* 38 (25 June 1977), pp. 1440–1443. DOI: 10.1103/PhysRevLett.38.1440.

[37] J. E. Kim. “Light Pseudoscalars, Particle Physics and Cosmology”. In: *Phys. Rept.* 150 (1987), pp. 1–177. DOI: 10.1016/0370-1573(87)90017-2.

[38] G.C. Branco et al. “Theory and phenomenology of two-Higgs-doublet models”. In: *Physics Reports* 516.1-2 (July 2012), pp. 1–102. ISSN: 0370-1573. DOI: 10.1016/j.physrep.2012.02.002.

[39] J. F. Gunion et al. “The Higgs Hunter’s Guide”. Vol. 80. 2000.

[40] D. de Florian et al. “Handbook of LHC Higgs Cross Sections: 4. Deciphering the Nature of the Higgs Sector”. In: (Oct. 2016). DOI: 10.23731/CYRM-2017-002. arXiv: 1610.07922 [hep-ph].

[41] J. F. Gunion and H. E. Haber. “CP-conserving two-Higgs-doublet model: The approach to the decoupling limit”. In: *Physical Review D* 67.7 (Apr. 2003). ISSN: 1089-4918. DOI: 10.1103/physrevd.67.075019.

[42] S. L. Glashow and S. Weinberg. “Natural conservation laws for neutral currents”. In: *Phys. Rev. D* 15 (7 Apr. 1977), pp. 1958–1965. DOI: 10.1103/PhysRevD.15.1958.

[43] E. A. Paschos. “Diagonal neutral currents”. In: *Phys. Rev. D* 15 (7 Apr. 1977), pp. 1966–1972. DOI: 10.1103/PhysRevD.15.1966.

[44] S. Dimopoulos and H. Georgi. “Softly Broken Supersymmetry and SU(5)”. In: *Nucl. Phys. B* 193 (1981), pp. 150–162. DOI: 10.1016/0550-3213(81)90522-8.

[45] E. Witten. “Dynamical Breaking of Supersymmetry”. In: *Nucl. Phys. B* 188 (1981), p. 513. DOI: 10.1016/0550-3213(81)90006-7.

[46] J. R. Ellis et al. “Supersymmetric Relics from the Big Bang”. In: *Nucl. Phys. B* 238 (1984). Ed. by M.A. Srednicki, pp. 453–476. DOI: 10.1016/0550-3213(84)90461-9.

[47] R. Catena and L. Covi. “SUSY dark matter(s)”. In: *The European Physical Journal C* 74.5 (May 2014). ISSN: 1434-6052. DOI: 10.1140/epjc/s10052-013-2703-4.

[48] D. Z. Freedman, P. van Nieuwenhuizen, and S. Ferrara. “Progress toward a theory of supergravity”. In: *Phys. Rev. D* 13 (12 June 1976), pp. 3214–3218. DOI: 10.1103/PhysRevD.13.3214.

[49] J. R. Ellis. “Supersymmetry for Alp Hikers”. In: (Mar. 2002). DOI: 10.5170/CERN-2002-002.157.

[50] J. F. Gunion. “A Simplified Summary of Supersymmetry”. In: (Apr. 1997). DOI: 10.1063/1.52979.

[51] S.P. Martin. “A Supersymmetry Primer”. In: *Advanced Series on Directions in High Energy Physics* (July 1998), pp. 1–98. ISSN: 1793-1339. DOI: 10.1142/9789812839657_0001.

[52] C. Csaki. “The Minimal supersymmetric standard model (MSSM)”. In: *Mod. Phys. Lett. A* 11 (1996), p. 599. DOI: 10.1142/S021773239600062X. arXiv: hep-ph/9606414.

[53] V. Sanz and J. Setford. “Composite Higgs Models after Run 2”. In: *Adv. High Energy Phys.* 2018 (2018), p. 7168480. DOI: 10.1155/2018/7168480. arXiv: 1703.10190 [hep-ph].

[54] O. Witzel. “Review on Composite Higgs Models”. arXiv: 1901.08216 [hep-lat].

[55] ATLAS Collaboration. “A strategy for a general search for new phenomena using data-derived signal regions and its application within the ATLAS experiment”. In: *The European Physical Journal C* 79.2 (Feb. 2019). ISSN: 1434-6052. DOI: 10.1140/epjc/s10052-019-6540-y.

[56] LHC Higgs Cross Section Working Group. URL: https://twiki.cern.ch/twiki/bin/view/LHCPhysics/LHCHXSWG.

[57] ATLAS Collaboration. “Constraints on off-shell Higgs boson production and the Higgs boson total width in $ZZ \to 4\ell$ and $ZZ \to 2\ell 2\nu$ final states with the ATLAS detector”. In: *Phys. Lett. B* 786 (2018), pp. 223–244. DOI: 10.1016/j.physletb.2018.09.048. arXiv: 1808.01191 [hep-ex].

[58] M. Hoffmann. “The Search for a Heavy Higgs Boson in the $H \to ZZ$ Decay Channels with the ATLAS Detector at the LHC”. Theses. Université Paris-Saclay, Oct. 2016.

[59] The ATLAS Collaboration. “The ATLAS Experiment at the CERN Large Hadron Collider”. In: *Journal of Instrumentation* 3.08 (Aug. 2008), S08003–S08003. DOI: 10.1088/1748-0221/3/08/s08003.

[60] S. Myers and E. Picasso. “The design, construction and commissioning of the CERN large Electron–Positron collider”. In: *Contemporary Physics* 31.6 (1990), pp. 387–403. DOI: 10.1080/00107519008213789.

[61] E. Mobs. “The CERN accelerator complex - August 2018”. In: (). General Photo. URL: https://cds.cern.ch/record/2636343.

[62] The CMS Collaboration. “The CMS experiment at the CERN LHC”. In: *Journal of Instrumentation* 3.08 (Aug. 2008). DOI: 10.1088/1748-0221/3/08/s08004.

[63] The LHCb Collaboration. “The LHCb Detector at the LHC”. In: *Journal of Instrumentation* 3.08 (Aug. 2008). DOI: 10.1088/1748-0221/3/08/s08005.

[64] The ALICE Collaboration. “The ALICE experiment at the CERN LHC”. In: *Journal of Instrumentation* 3.08 (Aug. 2008). DOI: 10.1088/1748-0221/3/08/s08002.

[65] K. Wille. “The physics of particle accelerators: An introduction”. 2000.

[66] T. S. Pettersson and P. Lefèvre. “The Large Hadron Collider: conceptual design”. Tech. rep. CERN-AC-95-05-LHC. Oct. 1995.

[67] ATLAS Collaboration. “LuminosityPublicResultsRun2”. URL: https://twiki.cern.ch/twiki/bin/view/AtlasPublic/LuminosityPublicResultsRun2#Luminosity_summary_plots_for_201.

[68] ATLAS Collaboration. “Measurement of the Inelastic Proton-Proton Cross Section at $\sqrt{s} =$ 13 TeV with the ATLAS Detector at the LHC”. In: *Physical Review Letters* 117.18 (Oct. 2016). ISSN: 1079-7114. DOI: 10.1103/physrevlett.117.182002.

[69] The TOTEM Collaboration. “First measurement of elastic, inelastic and total cross-section at $\sqrt{s} = 13$ TeV by TOTEM and overview of cross-section data at LHC energies”. 2018. arXiv: 1712.06153 [hep-ex].

[70] LHCb Collaboration. “Measurement of the inelastic pp cross-section at a centre-of-mass energy of 13 TeV”. In: *Journal of High Energy Physics* 2018.6 (June 2018). ISSN: 1029-8479. DOI: 10.1007/jhep06(2018)100.

[71] ATLAS Collaboration. “The ATLAS Simulation Infrastructure”. In: *Eur. Phys. J. C* 70 (2010), pp. 823–874. DOI: 10.1140/epjc/s10052-010-1429-9. arXiv: 1005.4568 [physics.ins-det].

[72] ATLAS Collaboration. “ATLAS inner detector: Technical Design Report, Vol. 1”. Technical Design Report ATLAS. CERN, 1997.

[73] ATLAS Collaboration. “ATLAS inner detector: Technical design report. Vol. 2”. Technical Design Report ATLAS. Apr. 1997.

[74] K. Potamianos. “The upgraded Pixel detector and the commissioning of the Inner Detector tracking of the ATLAS experiment for Run-2 at the Large Hadron Collider”. Tech. rep. ATL-PHYS-PROC-2016-104. 15 pages, EPS-HEP 2015 Proceedings. CERN, Aug. 2016.

[75] M. Capeans et al. “ATLAS Insertable B-Layer Technical Design Report”. Tech. rep. CERN-LHCC-2010-013. ATLAS-TDR-19. Sept. 2010.

[76] N. Wermes and G. Hallewel. “ATLAS pixel detector: Technical Design Report”. Technical Design Report ATLAS. CERN, 1998.

[77] A. Abdesselam and T. Akimoto. “The Barrel Modules of the ATLAS SemiConductor Tracker”. Tech. rep. ATL-INDET-PUB-2006-005. CERN, July 2006. DOI: 10.1016/j.nima.2006.08.036.

[78] R. Nisius. “End-cap modules for the ATLAS SCT”. In: *Nuclear Instruments and Methods in Physics Research Section A: Accelerators, Spectrometers, Detectors and Associated Equipment* 530.1-2 (Sept. 2004), pp. 44–49. ISSN: 0168-9002. DOI: 10.1016/j.nima.2004.05.045.

[79] C. Leroy and P. G. Rancoita. “Principles of Radiation Interaction in Matter and Detection, 2nd Edition”. In: (2009). DOI: 10.1142/6872.

[80] “ATLAS liquid-argon calorimeter: Technical Design Report”. Technical Design Report ATLAS. CERN, 1996.

[81] “ATLAS tile calorimeter: Technical Design Report”. Technical Design Report ATLAS. CERN, 1996.

[82] “ATLAS muon spectrometer: Technical design report”. 1997.

[83] G. Barone et al. “Momentum resolution improvements with the inclusion of the Alignment Errors On Track”. Tech. rep. ATL-COM-PHYS-2018-826. CERN, June 2018.

[84] A. Ruiz-Martinez and the ATLAS Collaboration. “The Run-2 ATLAS Trigger System”. Tech. rep. ATL-DAQ-PROC-2016-003. CERN, Feb. 2016. DOI: 10.1088/1742-6596/762/1/012003.

[85] “ATLAS level-1 trigger: Technical Design Report”. Technical Design Report ATLAS. CERN, 1998.

[86] P. Jenni et al. “ATLAS high-level trigger, data-acquisition and controls: Technical Design Report”. Technical Design Report ATLAS. CERN, 2003.

[87] J. Pequenao and P. Schaffner. “How ATLAS detects particles: diagram of particle paths in the detector”. Jan. 2013. URL: https://cds.cern.ch/record/1505342.

[88] T. Herrmann et al. “LHC International Masterclasses Webpage”. URL: https://atlas.physicsmasterclasses.org/en/wpath_teilchenid1.htm.

[89] ATLAS Collaboration. “Electron reconstruction and identification in the ATLAS experiment using the 2015 and 2016 LHC proton–proton collision data at $\sqrt{s} = 13$TeV”. In: *The European Physical Journal C* 79.8 (Aug. 2019). ISSN: 1434-6052. DOI: 10.1140/epjc/s10052-019-7140-6.

[90] ATLAS Collaboration. “Electron and photon performance measurements with the ATLAS detector using the 2015–2017 LHC proton-proton collision data”. In: *Journal of Instru-*

mentation 14.12 (Dec. 2019), P12006–P12006. ISSN: 1748-0221. DOI: 10.1088/1748-0221/14/12/p12006.

[91] W. Lampl et al. "Calorimeter Clustering Algorithms: Description and Performance". Tech. rep. ATL-LARG-PUB-2008-002. CERN, Apr. 2008.

[92] ATLAS Collaboration. "Topological cell clustering in the ATLAS calorimeters and its performance in LHC Run 1". In: *The European Physical Journal C* 77.7 (July 2017). ISSN: 1434-6052. DOI: 10.1140/epjc/s10052-017-5004-5.

[93] ATLAS Collaboration. "Performance of the ATLAS track reconstruction algorithms in dense environments in LHC Run 2". In: *The European Physical Journal C* 77.10 (Oct. 2017). ISSN: 1434-6052. DOI: 10.1140/epjc/s10052-017-5225-7. URL: http://dx.doi.org/10.1140/epjc/s10052-017-5225-7.

[94] T. Cornelissen et al. "The new ATLAS track reconstruction (NEWT)". In: *J. Phys.: Conf. Ser.* 119 (2008). DOI: 10.1088/1742-6596/119/3/032014.

[95] T. Cornelissen et al. "The global χ^2 track fitter in ATLAS". In: *Journal of Physics: Conference Series* 119.3 (July 2008). DOI: 10.1088/1742-6596/119/3/032013.

[96] ATLAS Collaboration. "Improved electron reconstruction in ATLAS using the Gaussian Sum Filter-based model for bremsstrahlung". Tech. rep. ATLAS-CONF-2012-047. CERN, May 2012.

[97] ATLAS Collaboration. "Electron and photon energy calibration with the ATLAS detector using 2015–2016 LHC proton-proton collision data". In: *Journal of Instrumentation* 14.03 (Mar. 2019). ISSN: 1748-0221. DOI: 10.1088/1748-0221/14/03/p03017.

[98] ATLAS Collaboration. "Electron efficiency measurements with the ATLAS detector using the 2015 LHC proton-proton collision data". Tech. rep. ATLAS-CONF-2016-024. CERN, June 2016.

[99] S. H. Abidi et al. "Event selection and background estimation in the $H \to ZZ \to 4l$ channel at $\sqrt{s}$ = 13 TeV- Final Run 2 Analysis". Tech. rep. ATL-COM-PHYS-2018-1710. CERN, Dec. 2018.

[100] The ATLAS Collaboration. "Muon reconstruction performance of the ATLAS detector in proton–proton collision data at $\sqrt{s}$=13 TeV". In: *The European Physical Journal C* 76.5 (May 2016). ISSN: 1434-6052. DOI: 10.1140/epjc/s10052-016-4120-y.

[101] ATLAS Collaboration. "Muon reconstruction and identification efficiency in ATLAS using the full Run 2 pp collision data set at $\sqrt{s}$ = 13 TeV". Tech. rep. ATLAS-CONF-2020-030. CERN, Aug. 2020.

[102] S. Rettie. "Muon identification and performance in the ATLAS experiment". Tech. rep. ATL-COM-PHYS-2018-839. CERN, June 2018.

[103] G. Artoni et al. "Support Note for 2015 Muon Combined Performance Paper ". Tech. rep. ATL-COM-PHYS-2015-1149. Support note for ATL-COM-PHYS-2015-1564. CERN, Sept. 2015.

[104] M. Cacciari, G. P. Salam, and G. Soyez. "The anti-ktjet clustering algorithm". In: *Journal of High Energy Physics* 2008.04 (Apr. 2008). ISSN: 1029-8479. DOI: 10.1088/1126-6708/2008/04/063.

[105] ATLAS Collaboration. "Jet reconstruction and performance using particle flow with the ATLAS Detector". In: *The European Physical Journal C* 77.7 (July 2017). ISSN: 1434-6052. DOI: 10.1140/epjc/s10052-017-5031-2.

[106] ATLAS Collaboration. "EM+JES and PFlow Pile-Up jet rate - LHCP 2017". May 2017. URL: https://atlas.web.cern.ch/Atlas/GROUPS/PHYSICS/PLOTS/JETM-2017-006/.

[107] ATLAS Collaboration. "Jet energy scale and resolution measured in proton-proton collisions at $\sqrt{s}$ = 13 TeV with the ATLAS detector". 2020. arXiv: 2007.02645 [hep-ex].

[108] ATLAS Collaboration. "Tagging and suppression of pileup jets with the ATLAS detector". Tech. rep. ATLAS-CONF-2014-018. CERN, May 2014.

[109] ATLAS Collaboration. "Performance of pile-up mitigation techniques for jets in pp collisions at $\sqrt{s}$ = 8 TeV using the ATLAS detector". In: *The European Physical Journal C* 76.11 (Oct. 2016). ISSN: 1434-6052. DOI: 10.1140/epjc/s10052-016-4395-z.

[110] N. Bartosik. "Associated top-quark-pair and b-jet production in the dilepton channel at $\sqrt{s}$ = 8 TeV as test of QCD and background to tt+Higgs production". PhD thesis. Universität Hamburg, 2015.

[111] ATLAS Collaboration. "ATLAS b-jet identification performance and efficiency measurement with $t\bar{t}$ events in pp collisions at $\sqrt{s}$ = 13 TeV". In: *The European Physical Journal C* 79.11 (Nov. 2019). ISSN: 1434-6052. DOI: 10.1140/epjc/s10052-019-7450-8.

[112] ATLAS Collaboration. "$E_{\mathrm{T}}^{\mathrm{miss}}$ performance in the ATLAS detector using 2015-2016 LHC p-p collisions". Tech. rep. ATLAS-CONF-2018-023. CERN, June 2018.

[113] ATLAS Collaboration. "Expected performance of missing transverse momentum reconstruction for the ATLAS detector at $\sqrt{s}$ = 13 TeV". Tech. rep. ATL-PHYS-PUB-2015-023. CERN, July 2015.

[114] ATLAS Collaboration. "Performance of missing transverse momentum reconstruction with the ATLAS detector using proton–proton collisions at $\sqrt{s}$ = 13 TeV". In: *The European Physical Journal C* 78.11 (Nov. 2018). ISSN: 1434-6052. DOI: 10.1140/epjc/s10052-018-6288-9.

[115] "Missing transverse energy performance in 2017 data". URL: https://atlas.web.cern.ch/Atlas/GROUPS/PHYSICS/PLOTS/JETM-2017-011/.

[116] M. Dobbs and J. B. Hansen. "The HepMC C++ Monte Carlo Event Record for High Energy Physics". Tech. rep. ATL-SOFT-2000-001. CERN, June 2000.

[117] "CTEQ Parton Distribution Functions". Website. URL: https://www.physics.smu.edu/scalise/cteq/#PDFs.

[118] "NNPDF Collaboration". Website. URL: http://nnpdf.mi.infn.it/.

[119] The NNPDF Collaboration et al. "Parton distributions from high-precision collider data". 2017. arXiv: 1706.00428 [hep-ph].

[120] J. M. Campbell, J. W. Huston, and W. J. Stirling. "Hard interactions of quarks and gluons: a primer for LHC physics". In: *Reports on Progress in Physics* 70.1 (Dec. 2006), pp. 89–193. ISSN: 1361-6633. DOI: 10.1088/0034-4885/70/1/r02.

[121] S. Agostinelli et al. "GEANT4–a simulation toolkit". In: *Nucl. Instrum. Meth. A* 506 (2003), pp. 250–303. DOI: 10.1016/S0168-9002(03)01368-8.

[122] P. Nason and G. Zanderighi. "W^+W^-, WZ and ZZ production in the POWHEG-BOX-V2". In: *The European Physical Journal C* 74.1 (Jan. 2014). ISSN: 1434-6052. DOI: 10.1140/epjc/s10052-013-2702-5.

[123] H. Lai et al. "New parton distributions for collider physics". In: *Physical Review D* 82.7 (Oct. 2010). ISSN: 1550-2368. DOI: 10.1103/physrevd.82.074024.

[124] T. Sjöstrand, S. Mrenna, and P. Skands. "A brief introduction to PYTHIA 8.1". In: *Computer Physics Communications* 178.11 (June 2008), pp. 852–867. ISSN: 0010-4655. DOI: 10.1016/j.cpc.2008.01.036.

[125] P. Golonka and Z. Was. "PHOTOS Monte Carlo: a precision tool for QED corrections in Z and W decays". In: *The European Physical Journal C* 45.1 (Jan. 2006), pp. 97–107. ISSN: 1434-6052. DOI: 10.1140/epjc/s2005-02396-4.

[126] T. Riemann. "The Z Boson Resonance Parameters". Tech. rep. DESY-97-001. DESY, Sept. 1997.

[127] W. Wetzel. "Electroweak Radiative Corrections for e+ e- —> mu+ mu- at LEP Energies". In: *Nucl. Phys. B* 227 (1983), pp. 1–30. DOI: 10.1016/0550-3213(83)90139-6.

[128] W. Verkerke and D. Kirkby. "The RooFit toolkit for data modeling". arXiv: physics/0306116 [physics.data-an].

[129] T. Sjöstrand et al. "An introduction to PYTHIA 8.2". In: *Computer Physics Communications* 191 (June 2015), pp. 159–177. ISSN: 0010-4655. DOI: 10.1016/j.cpc.2015.01.024.

[130] J. Alwall et al. "The automated computation of tree-level and next-to-leading order differential cross sections, and their matching to parton shower simulations". In: *Journal of High Energy Physics* 2014.7 (July 2014). ISSN: 1029-8479. DOI: 10.1007/jhep07(2014)079.

[131] N. Kauer, C. O'Brien, and E. Vryonidou. "Interference effects for $H \to WW \to l\nu qq$ and $H \to ZZ \to llqq$ searches in gluon fusion at the LHC". 2015. arXiv: 1506.01694 [hep-ph].

[132] E. Bothmann et al. "Event generation with Sherpa 2.2". In: *SciPost Physics* 7.3 (Sept. 2019). ISSN: 2542-4653. DOI: 10.21468/scipostphys.7.3.034.

[133] R. D. Ball et al. "Parton distributions for the LHC run II". In: *Journal of High Energy Physics* 2015.4 (Apr. 2015). ISSN: 1029-8479. DOI: 10.1007/jhep04(2015)040.

[134] F. Caola et al. "QCD corrections to ZZ production in gluon fusion at the LHC". In: *Physical Review D* 92.9 (Nov. 2015). ISSN: 1550-2368. DOI: 10.1103/physrevd.92.094028.

[135] ATLAS Collaboration. "Measurement of ZZ production in the $\ell\ell\nu\nu$ final state with the ATLAS detector in pp collisions at $\sqrt{s} = 13$ TeV". In: *Journal of High Energy Physics* 2019.10 (Oct. 2019). ISSN: 1029-8479. DOI: 10.1007/jhep10(2019)127.

[136] ATLAS Collaboration. "Multi-Boson Simulation for 13 TeV ATLAS Analyses". Tech. rep. ATL-PHYS-PUB-2016-002. 2016.

[137] R. Gavin et al. "FEWZ 2.0: A code for hadronic Z production at next-to-next-to-leading order". In: *Computer Physics Communications* 182.11 (Nov. 2011), pp. 2388–2403. ISSN: 0010-4655. DOI: 10.1016/j.cpc.2011.06.008.

[138] ATLAS Collaboration. "Studies on top-quark Monte Carlo modelling for Top2016". Tech. rep. ATL-PHYS-PUB-2016-020. CERN, Sept. 2016.

[139] N. Kauer and C. O'Brien. "Heavy Higgs signal-background interference in $gg \to VV$ in the Standard Model plus real singlet". In: *JHEP* 10 (2015), p. 022. DOI: 10.1140/epjc/s10052-015-3586-3. arXiv: 1502.04113v4 [hep-ph].

[140] S. H. Abidi et al. "Searches for heavy Higgs bosons in the four-lepton decay channel with the ATLAS detector using 140 fb^{-1} of $\sqrt{s} = 13$ TeV data". Tech. rep. ATL-COM-PHYS-2018-1697. CERN, Dec. 2018.

[141] H. Okawa et al. "Search for a Higgs boson in the $H \to ZZ \to \ell\ell\nu\nu$ Channel". Tech. rep. ATL-COM-PHYS-2014-270. CERN, Apr. 2014.

[142] M. Baak et al. “Interpolation between multi-dimensional histograms using a new non-linear moment morphing method”. In: *Nuclear Instruments and Methods in Physics Research Section A: Accelerators, Spectrometers, Detectors and Associated Equipment* 771 (2015), pp. 39–48. ISSN: 0168-9002. DOI: https://doi.org/10.1016/j.nima.2014.10.033.

[143] J. Neyman, E. S. Pearson, and K. Pearson. “IX. On the problem of the most efficient tests of statistical hypotheses”. In: *Philosophical Transactions of the Royal Society of London. Series A, Containing Papers of a Mathematical or Physical Character* 231.694-706 (1933), pp. 289–337. DOI: 10.1098/rsta.1933.0009.

[144] S. S. Wilks. “The Large-Sample Distribution of the Likelihood Ratio for Testing Composite Hypotheses”. In: *Ann. Math. Statist.* 9.1 (Mar. 1938), pp. 60–62. DOI: 10.1214/aoms/1177732360.

[145] A. L. Read. “Modified frequentist analysis of search results (the CL_s method)”. In: CERN-OPEN-2000-205 (2000). DOI: 10.5170/CERN-2000-005.81.

[146] G. Cowan et al. “Asymptotic formulae for likelihood-based tests of new physics”. In: *The European Physical Journal C* 71.2 (Feb. 2011). ISSN: 1434-6052. DOI: 10.1140/epjc/s10052-011-1554-0.

[147] F. Cascioli et al. “ZZ production at hadron colliders in NNLO QCD”. In: *Physics Letters B* 735 (July 2014), pp. 311–313. ISSN: 0370-2693. DOI: 10.1016/j.physletb.2014.06.056.

[148] S. Gieseke, T. Kasprzik, and J. H. Kühn. “Vector-boson pair production and electroweak corrections in HERWIG++”. 2014. arXiv: 1401.3964 [hep-ph].

[149] K. Melnikov and M. Dowling. “Production of two Z-bosons in gluon fusion in the heavy top quark approximation”. In: *Physics Letters B* 744 (May 2015), pp. 43–47. ISSN: 0370-2693. DOI: 10.1016/j.physletb.2015.03.030.

[150] C. S. Li et al. “Soft gluon resummation in the signal-background interference process of $gg(\to h^*) \to ZZ$”. In: *JHEP* 08 (2015). DOI: 10.1007/JHEP08(2015)065.

[151] B. Abbott et al. “Measurement of the W boson mass”. In: *Physical Review D* 58.9 (Sept. 1998). ISSN: 1089-4918. DOI: 10.1103/physrevd.58.092003.

[152] ATLAS Collaboration. “Electron efficiency measurements with the ATLAS detector using 2012 LHC proton-proton collision data”. In: *Eur. Phys. J. C* 77 (2017), p. 195. DOI: 10.1140/epjc/s10052-017-4756-2. arXiv: 1612.01456 [hep-ex].

[153] ATLAS Collaboration. “Performance of the ATLAS Trigger System in 2015”. In: *Eur. Phys. J.* C77.5 (2017), p. 317. DOI: 10.1140/epjc/s10052-017-4852-3. arXiv: 1611.09661 [hep-ex].

[154] ATLAS Collaboration. “Monte Carlo Calibration and Combination of In-situ Measurements of Jet Energy Scale, Jet Energy Resolution and Jet Mass in ATLAS”. Tech. rep. ATLAS-CONF-2015-037. CERN, Aug. 2015.

[155] ATLAS Collaboration. “Jet Calibration and Systematic Uncertainties for Jets Reconstructed in the ATLAS Detector at $\sqrt{s} = 13$ TeV”. Tech. rep. ATL-PHYS-PUB-2015-015. CERN, July 2015.

[156] ATLAS Collaboration. “Calibration of the performance of b-tagging for c and light-flavour jets in the 2012 ATLAS data”. Tech. rep. ATLAS-CONF-2014-046. CERN, July 2014.

[157] W. Buttinger. "Using Event Weights to account for differences in Instantaneous Luminosity and Trigger Prescale in Monte Carlo and Data". Tech. rep. ATL-COM-SOFT-2015-119. CERN, May 2015.

[158] ATLAS Collaboration. "Luminosity determination in pp collisions at $\sqrt{s} = 8$ TeV using the ATLAS detector at the LHC". In: *The European Physical Journal C* 76.12 (Nov. 2016). ISSN: 1434-6052. DOI: 10.1140/epjc/s10052-016-4466-1.

[159] ATLAS Collaboration. "Object-based missing transverse momentum significance in the ATLAS detector". Tech. rep. ATLAS-CONF-2018-038. CERN, July 2018.

[160] S. Kallweit et al. "NLO QCD+EW predictions for $2\ell 2\nu$ diboson signatures at the LHC". In: *Journal of High Energy Physics* 2017.11 (2017), p. 120.

[161] ATLAS Collaboration. "Luminosity determination in pp collisions at $\sqrt{s} = 13$ TeV using the ATLAS detector at the LHC". Tech. rep. ATLAS-CONF-2019-021. CERN, June 2019.

[162] J. Butterworth et al. "PDF4LHC recommendations for LHC Run II". In: *Journal of Physics G: Nuclear and Particle Physics* 43.2 (Jan. 2016). ISSN: 1361-6471. DOI: 10.1088/0954-3899/43/2/023001.

[163] ATLAS Collaboration. "Higgs boson production cross-section measurements and their EFT interpretation in the 4ℓ decay channel at $\sqrt{s} = 13$ TeV with the ATLAS detector". 2020. arXiv: 2004.03447 [hep-ex].

[164] ATLAS Collaboration. "Measurement of the Higgs boson coupling properties in the $H \to ZZ* \to 4\ell$ decay channel at $\sqrt{s} = 13$ TeV with the ATLAS detector". In: *Journal of High Energy Physics* 2018.3 (Mar. 2018). ISSN: 1029-8479. DOI: 10.1007/jhep03(2018)095.

[165] ATLAS Collaboration. "Measurement of inclusive and differential cross sections in the $H \to ZZ* \to 4\ell$ decay channel in pp collisions at $\sqrt{s} = 13$ TeV with the ATLAS detector". In: *Journal of High Energy Physics* 2017.10 (Oct. 2017). ISSN: 1029-8479. DOI: 10.1007/jhep10(2017)132.

[166] "TSpline3 Class Reference". https://root.cern.ch/doc/master/classTSpline3.html. Accessed: 2020-05-19.

[167] "Function description of scipy's slinear interpolation". https://docs.scipy.org/doc/scipy/reference/generated/scipy.interpolate.interp1d.html. Accessed: 2020-05-19.

[168] H. Ohman. "Charged Higgs boson searches in ATLAS and CMS." Tech. rep. ATL-PHYS-PROC-2016-137. CERN, Sept. 2016. DOI: 10.22323/1.276.0085.

[169] ATLAS Collaboration. "Search for heavy resonances decaying into WW in the $e\nu\mu\nu$ final state in pp collisions at $\sqrt{s} = 13$ TeV with the ATLAS detector". In: *The European Physical Journal C* 78.1 (Jan. 2018). ISSN: 1434-6052. DOI: 10.1140/epjc/s10052-017-5491-4.

[170] ATLAS Collaboration. "Search for resonances decaying to photon pairs in 139 fb^{-1} of pp collisions at $\sqrt{s} = 13$ TeV with the ATLAS detector." Tech. rep. ATLAS-CONF-2020-037. CERN, Aug. 2020.

[171] ATLAS Collaboration. "Search for resonances in the 65 to 110 GeV diphoton invariant mass range using 80 fb^{-1} of pp collisions collected at $\sqrt{s} = 13$ TeV with the ATLAS detector". Tech. rep. ATLAS-CONF-2018-025. CERN, July 2018.

[172] ATLAS Collaboration. "Combination of searches for Higgs boson pairs in pp collisions at $\sqrt{s}$=13TeV with the ATLAS detector". In: *Physics Letters B* 800 (Jan. 2020). ISSN: 0370-2693. DOI: 10.1016/j.physletb.2019.135103.

[173] CMS Collaboration. "Search for new neutral Higgs bosons through the H → ZA → $\ell^+\ell^-$b$\bar{\text{b}}$ process in pp collisions at $\sqrt{s}$ = 13 TeV". In: *Journal of High Energy Physics* 2020.3 (Mar. 2020). ISSN: 1029-8479. DOI: 10.1007/jhep03(2020)055.

[174] ATLAS Collaboration. "Search for Heavy Higgs Bosons A/H decaying to a top quark pair in pp collisions at $\sqrt{s}$=8 TeV with the ATLAS detector". In: *Physical Review Letters* 119.19 (Nov. 2017). ISSN: 1079-7114. DOI: 10.1103/physrevlett.119.191803.

[175] CMS Collaboration. "Search for heavy Higgs bosons decaying to a top quark pair in proton-proton collisions at $\sqrt{s}$ = 13 TeV". In: *Journal of High Energy Physics* 2020.4 (Apr. 2020). ISSN: 1029-8479. DOI: 10.1007/jhep04(2020)171.

[176] ATLAS Collaboration. "Search for Heavy Higgs Bosons decaying into two tau leptons with the ATLAS detector using pp collisions at $\sqrt{s}$=13 TeV". In: *Physical Review Letters* 125.5 (July 2020). ISSN: 1079-7114. DOI: 10.1103/physrevlett.125.051801.

[177] D. Krasnopevtsev et al. "Study of $\ell\ell + E_T^{miss}$ with proton-proton collisions at $\sqrt{s}$ = 13 TeV in the HZZ group: introduction of common analysis strategies". Tech. rep. ATL-COM-PHYS-2018-1528. CERN, Nov. 2018.

[178] A. M. Sirunyan et al. "Search for a new scalar resonance decaying to a pair of Z bosons in proton-proton collisions at $\sqrt{s}$ = 13 TeV". In: *Journal of High Energy Physics* 2018.6 (June 2018). ISSN: 1029-8479. DOI: 10.1007/jhep06(2018)127.

[179] ATLAS Collaboration. "Beyond Standard Model Higgs boson searches at a High-Luminosity LHC with ATLAS". Tech. rep. ATL-PHYS-PUB-2013-016. CERN, Oct. 2013.

[180] M. Cepeda et al. "Higgs Physics at the HL-LHC and HE-LHC". 2019. arXiv: 1902.00134 [hep-ph].

Summary

Heavy Higgs Hunting

A search for a heavy Higgs boson decaying to a pair of Z bosons with the ATLAS detector

Particle physics strives to answer the very fundamental questions about the universe that have likely been asked since the beginning of critical thinking, such as what all matter is made of. We know nowadays that matter is made of atoms, that atoms consist of nucleons and electrons and that nucleons are made of quarks. Our current best understanding of the world of elementary particles like electrons and quarks is summarized in an elegant mathematical model called the Standard Model of Particle Physics (SM). Throughout the past decades, the SM has passed many experimental tests of its predictions with flying colours, making it a huge success. To experimentally probe the physics of particle dynamics and interactions which happen at the microscopic scale, we need to study processes that happen at very high energies, similar to how we need a very powerful microscope to see something as tiny as an atom. This can be achieved with high energy colliders, such as the *Large Hadron Collider* (LHC). As of today, the LHC is the world's most powerful particle accelerator, colliding protons that travel at nearly the speed of light and reaching centre-of-mass energies of $\sqrt{s} = 13$ TeV.

The discovery of a Higgs boson by the LHC experiments ATLAS [2] and CMS [3] in 2012 is the SM's latest success, shedding light on a previously unconfirmed aspect of the theory: in its initial formulation, all particles of the SM are massless, in stark contrast to reality. It is the interaction with an additional field - the Higgs field, giving rise to the Higgs boson - that allows particles to acquire mass in the (Brout-Englert)-Higgs mechanism of electroweak symmetry breaking. Nevertheless, the discovery of a Higgs boson is by no means an end to all questions on this matter. For example, we now know that electroweak symmetry breaking happens, but we do not know why it should happen the way it does. Other observations the SM is unable to explain include the existence of dark matter and the asymmetry between matter and antimatter in the universe. Answers to such questions come in the form of Beyond the Standard Model (BSM) theories, many of which predict the existence of more than one Higgs boson. For example, Two Higgs Doublet Models (2HDMs) postulate five Higgs bosons with different properties - two neutral, CP-even ones that may be of very different mass, one neutral, CP-odd Higgs and two charged Higgses. Although the lack of new particle discoveries after the Higgs boson and high precision measurements of the Higgs properties have significantly narrowed the parameter space available to many theories, there is so far no definite answer to the question of whether the Higgs boson is the only one of its kind.

This open question motivates the experimental search for a heavy BSM Higgs boson decaying to a pair of Z bosons presented in this thesis. By "heavy", we mean here that the mass of the BSM Higgs boson is larger than that of the already discovered Higgs at 125 GeV, and in particular, that its mass is large enough for the two Z bosons to be on-shell, i.e. $m_H > 2\ m_Z$. The mass range of the presented searches therefore spans from 200 GeV to 2 TeV. Different scenarios for the heavy Higgs boson width are probed: an analysis under the narrow-width approximation (NWA) and a large-width analysis (LWA) are performed. While the narrow-width analysis studies the heavy Higgs production in both gluon-gluon fusion (ggF) and vectorboson fusion (VBF), the large-width analysis considers only ggF production. Four distinct Higgs width scenarios are studied in the LWA and interference effects between the heavy, large-width Higgs and the Higgs at 125 GeV as well as the background from the $ggZZ$ process are included.

The pièce de résistance of this thesis is the analysis of the $H \to ZZ \to \ell\ell\nu\nu$ channel using the full run II data of $\mathscr{L}$=139 fb^{-1} collected by ATLAS from 2015 through 2018. Compared to the similar $ZZ \to \ell\ell\ell\ell$ decay channel, the $ZZ \to \ell\ell\nu\nu$ channel offers higher statistics due to the higher branching ratio of the Z boson decaying to neutrinos, but a worse mass resolution because the neutrinos in the $\ell\ell\nu\nu$ final state escape detection. Their total transverse momentum is measured only indirectly through the missing transverse energy, $E_{\mathrm{T}}^{\mathrm{miss}}$.

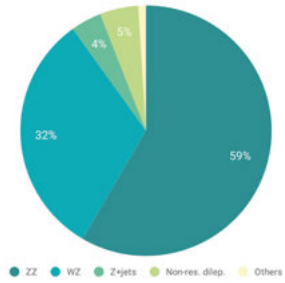

(a) Background composition

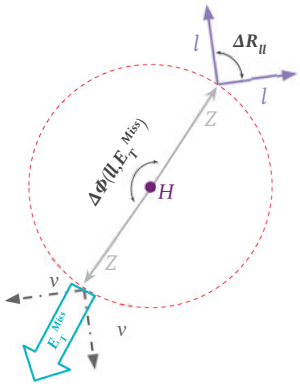

(b) Expected signal kinematics

Figure S.1: (a) Background composition in the $\ell\ell\nu\nu$ signal region and (b) sketch of the expected kinematics of a signal event.

There are several other physics processes - some of which very abundant at the LHC - that result in the same $\ell\ell\nu\nu$ final state and are therefore backgrounds to the search that need to be suppressed in order to find a (possibly small) signal in the data. Figure S.1(a) shows the composition of the expected background in the $\ell\ell\nu\nu$ analysis of the 2015-18 data. The picture is dominated by the non-resonant SM production of boson pairs, specifically ZZ and WZ pairs. A dedicated event selection, which exploits the expected signal kinematics, is used to reject events that are more likely to be background than signal. This selection is based on the assumption that, in most cases, the heavy Higgs boson is produced (approximately) at rest, leading to a large angle between the $Z \to \ell\ell$ and $Z \to \nu\nu$ decays, and a small angle between the two leptons of the $Z \to \ell\ell$ decay, as illustrated in Figure S.1(b). Furthermore, the $Z \to \nu\nu$ decay is reconstructed as a significant amount of $E_{\mathrm{T}}^{\mathrm{miss}}$. Selection criteria on these three observables, amongst others, define the signal region. To enhance the sensitivity, the signal region is split into two categories: one that is enriched in VBF-produced heavy Higgs events and one that is in enriched in ggF events.

While the WZ, Z+jets and non-resonant dilepton background contributions are estimated using data from control regions orthogonal to the signal region, the dominant ZZ background is so similar to the signal that the signal region itself can be used to constrain its total yield. Data-driven estimates of the major backgrounds are important in order to ascertain that no mismodelling of the backgrounds occurs, which could be interpreted as the false presence of a signal.

To enhance the search sensitivity, the statistical interpretation uses the distribution of the transverse mass observable, m_{T}, defined as

$$m_{\mathrm{T}}^2 \equiv \left(\sqrt{m_Z^2 + |\vec{p}_{\mathrm{T}}^{\,\ell\ell}|^2} + \sqrt{m_Z^2 + |\vec{E}_{\mathrm{T}}^{\,\mathrm{miss}}|^2}\right)^2 - \left(\vec{p}_{\mathrm{T}}^{\,\ell\ell} + \vec{E}_{\mathrm{T}}^{\,\mathrm{miss}}\right)^2.$$

where m_Z is the mass of the Z boson and $\vec{p}_{\mathrm{T}}^{\,\ell\ell}$ denotes the transverse momentum vector of the lepton pair. Figure S.2 shows the m_{T} distribution for an example heavy Higgs signal and all backgrounds in simulation, as well as the data distribution, in the two lepton flavour channels of the ggF category. By using the m_{T} distribution, the fit can exploit the difference in shape between the peaking signal and exponentially falling background.

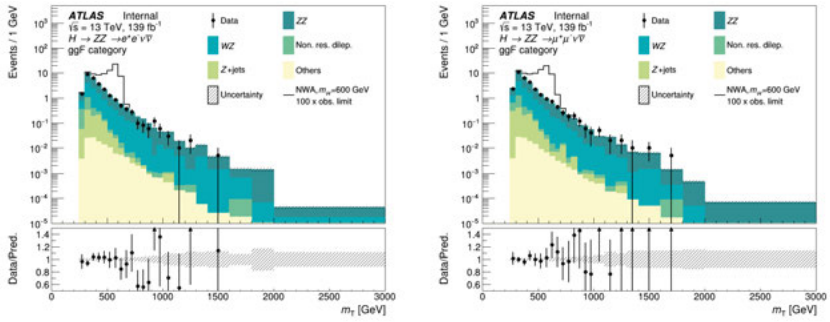

(a) ggF category, $eev\nu$ (b) ggF category, $\mu\mu\nu\nu$

Figure S.2: Expected and observed transverse mass distributions for the full run II data in (a) the ggF category, $eev\nu$ channel, (b) the ggF category, $\mu\mu\nu\nu$ channel. An example heavy Higgs signal with a mass of $m_H = 600$ GeV and a narrow-width is shown, scaled to 100 times the observed upper limit on its production cross-section. The last bin includes all events beyond the boundary.

No significant deviation from the SM expected backgrounds is observed in the 2015-18 data, hence no evidence for a heavy Higgs boson is found. Given the absence of a signal excess, exclusion limits are set on the respective production cross-section (including the branching ratio to ZZ) of the various Higgs boson hypotheses using the CL_s method at 95% confidence level. These upper limits quantify how much signal could still exist in nature without being incompatible with the observed data. Using the full 2015-18 data in the $\ell\ell\nu\nu$ final state, the upper limits on the ggF production cross-section of a narrow-width heavy Higgs range from approximately 305 fb to 4 fb for masses from 300 GeV to 2 TeV.

Due to several improvements of the analysis, such as reoptimizing the event selection and exploiting the transverse mass distribution also in the VBF category, these full run II results present a factor 3-8 improvement over the previously published $\ell\ell\nu\nu$ results that used only the 2015+16 data of $\mathscr{L}$=36.1 fb^{-1}, which are also presented in this thesis. This improvement is significantly better than the factor 2 that was expected from the increase in data volume alone.

To enhance the sensitivity of the search even further, the $\ell\ell\nu\nu$ results are combined with the results of a similar search in the $\ell\ell\ell\ell$ channel. The $\ell\ell\ell\ell$ channel analysis is conceptually different from the $\ell\ell\nu\nu$ analysis; the $H \to ZZ \to \ell\ell\ell\ell$ decay is relatively rare, so only a small number of events is expected, yet it is also a very clean channel with small backgrounds and an excellent mass resolution.

The two analyses therefore have different strengths, as seen in Figure S.3(a), which shows the upper limits of the NWA ggF analysis for both channels. At low masses, the $\ell\ell\ell\ell$ channel dominates the sensitivity, whereas at high masses, the $\ell\ell\nu\nu$ channel becomes more sensitive due to its larger statistics. The combination of both channels is thus a perfect partnership.

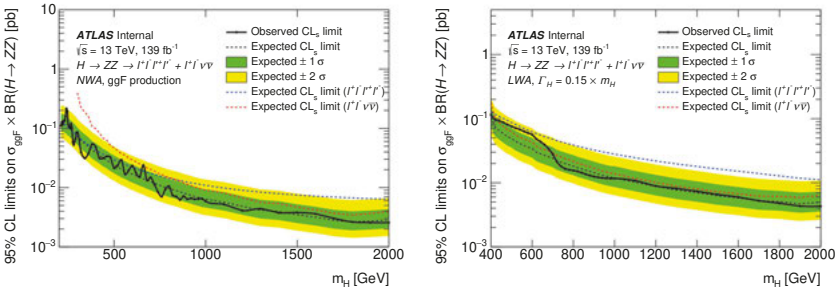

(a) Narrow-width (b) 15% width

Figure S.3: Expected and observed upper limits on the ggF production cross-section times branching fraction to ZZ pair of (a) a narrow-width heavy Higgs and (b) a large width heavy Higgs with a width 15% of its mass.

Figure S.3(b) shows the upper limits for a heavy Higgs boson which has a width of 15% of its mass. These large-width limits are up to a factor 2 worse than the narrow-width limits at the same mass, as the broader signal peak is less easily separated from the background and hence harder to exclude.

It should be noted that the impact of systematic uncertainties on the results is small in comparison to the data statistical uncertainty. The latter corresponds to between 55% and 65%, while the total impact of systematic uncertainties ranges from 10% to 15% depending on the signal hypothesis. Leading sources of systematic uncertainties are theory uncertainties on the modelling of the ZZ background in both the $\ell\ell\ell\ell$ and $\ell\ell\nu\nu$ channel, and experimental uncertainties arising from the data-driven estimates of the Z + jets and non-resonant dilepton backgrounds in the $\ell\ell\nu\nu$ channel. Because the search is limited by the available data statistics, adding new data

from future LHC runs will allow for further improvement of the limits and extension of the mass range.

Finally, an interpretation of the upper limits in terms of the specific 2HDM with five Higgs bosons is also presented, using the combined $\ell\ell\nu\nu$ and $\ell\ell\ell\ell$ results. In this context, the heavy Higgs searched for in this thesis corresponds to one of the neutral, CP-even Higgses of such theories, while the low-mass, CP-even Higgs is assumed to be the already discovered Higgs at 125 GeV. With the full 2015-18 results, a large region of 2HDM parameter space for heavy Higgs masses between 200 and 400 GeV is excluded by this interpretation.

In conclusion, the results from run II severely constrain the possibility of a heavy Higgs boson with a mass between 200 GeV and 2 TeV that decays to a pair of Z bosons. If such a heavy Higgs exists, it likely has a very different signature, or an even higher mass, than studied here, and is thus hiding out of sight.

Samenvatting

Deeltjesfysica heeft als doel het beantwoorden van de fundamentele vragen over het universum, die al sinds het onstaan van kritisch denken gevraagd worden, zoals waar alle materie van gemaakt is. We weten tegenwoordig dat materie gemaakt is van atomen, dat atomen bestaan uit nucleonen en elektronen, en dat nucleonen gemaakt zijn uit quarks. Ons huidige beste begrip van de wereld van elementaire deeltjes zoals elektronen en quarks is samengevat in een elegant wiskundig model genaamd het Standaardmodel van de deeltjesfysica (SM). In de laatste decennia heeft het Standaardmodel vele experimentele toetsen van zijn voorspellingen met vlag en wimpel doorstaan, wat het een doorslaand succes maakt. Om de fysica van deeltjesdynamiek en microscopische interacties experimenteel te testen, moeten we processen bestuderen die gebeuren bij zeer hoge energie, vergelijkbaar met hoe we een krachtige microscoop nodig hebben om iets zo klein als een atoom te kunnen zien. Dit kan gedaan worden met een hoge-energie deeltjesversneller, zoals de *Large Hadron Collider* (LHC). Op dit moment is de LHC de krachtigste deeltjesversneller in de wereld, waarin protonen met een snelheid van bijna de lichtsnelheid op elkaar gebotst worden met een energie van tot $\sqrt{s} = 13$ TeV.

De ontdekking van een Higgsboson door de LHC experimenten ATLAS [2] en CMS [3] in 2012 is het meest recente success van het Standaardmodel, wat een eerder onbevestigd aspect van de theorie aantoonde: in zijn originele omschrijving waren alle deeltjes van het Standaardmodel massaloos, wat niet met de realiteit overeen bleek te komen. Het is de interactie met een additioneel veld - het Higgsveld, waaruit het Higgsboson ontstaat - dat deeltjes de mogelijkheid geeft om massa te verkrijgen in het (Brout-Englert-)Higgsmechanisme van de breking van de elektrozwakke wisselwerking. Ondanks dit is de ontdekking van een Higgsboson in geen geval het einde van alle vragen over dit onderwerp. We weten nu bijvoorbeeld dat breking van elektrozwakke wisselwerking gebeurt, maar dit verklaart niet waarom het op déze manier gebeurt. Andere observaties die het SM niet kan verklaren zijn onder andere het bestaan van donkere materie en de asymmetrie tussen materie en antimaterie in het universum. Antwoorden op zulke vragen komen in de vorm van Buiten-het-Standaardmodel (BSM) theorieën, vele van welke voorspellen dat er meer dan één Higgsboson bestaat. Zogenoemde *Two Higgs Doublet Models* (2HDMs) voorspellen vijf Higgsbosonen met verschillende eigenschappen: twee neutrale, CP-even bosonen die mogelijk zeer verschillende massa hebben, één neutrale CP-oneven Higgs en twee geladen Higgsen. Alhoewel er geen nieuwe deeltjes ontdekt zijn sinds het Higgsboson en hoge-precisiemetingen van de Higgseigenschappen de parameterruimte van vele theorieën significant versmald hebben, is er tot nu toe nog geen definitief antwoord op de vraag of het Higgsboson de enige van zijn soort is.

Deze open vraag is motivatie voor de experimentele zoektocht naar een zwaar BSM-Higgsboson dat vervalt in een Z boson-paar welke in dit proefschrift gepresenteerd wordt. Met "zwaar"wordt

hier bedoeld dat de massa van het BSM Higgsboson groter is dan die van de eerder ontdekte Higgs op 125 GeV, en specifiek dat zijn massa groot genoeg is voor de twee Z bosons om *on-shell* te zijn, d.w.z. $m_H > 2\,m_Z$. Daarom hebben de gepresenteerde zoektochten een massabereik van 200 GeV tot 2 TeV.

Verschillende scenarios voor de zware Higgsboson-breedte worden onderzocht: een analyse onder de smalle-breedte-benadering (NWA) en een grote-breedte-analyse (LWA) worden uitgevoerd. Waar de NWA de productie van zware Higgs in zowel gluon-gluonfusie (ggF) en vectorbosonfusie (VBF) bestudeert, kijkt de LWA enkel naar ggF productie. Vier unieke Higgsbreedtescenarios worden onderzocht in de LWA en interferentie-effecten tussen de zware grote-breedte Higgs en de 125 GeV Higgs alsook de $ggZZ$ achtergrond worden meegenomen.

De pièce de résistance van dit proefschrift is de analyse van het $H \to ZZ \to \ell\ell\nu\nu$-kanaal gebruikmakend van de volledige Run 2 data van $\mathscr{L}$=139 fb^{-1} die van 2015 tot 2018 door ATLAS verzameld is. In vergelijking tot het vergelijkbare $ZZ \to \ell\ell\ell\ell$-kanaal, biedt het $ZZ \to \ell\ell\nu\nu$-kanaal hogere statistiek door de hogere branching ratio van het verval van Z boson in neutrinos, maar een slechtere massaresolutie omdat de neutrinos in de $\ell\ell\nu\nu$-eindtoestand aan detectie ontsnappen. Hun totale transversale momentum wordt alleen indirect gemeten door de missende transversale energie, $E_{\mathrm{T}}^{\mathrm{miss}}$.

Er zijn verschillende andere fysische processen, waarvan sommige in overvloed bij de LHC, die resulteren in dezelfde $\ell\ell\nu\nu$-eindtoestand en daardoor achtergronden bij de zoektocht zijn die moeten worden onderdrukt zodat een (mogelijk klein) signaal in de data gevonden kan worden. Figuur S.1(a) toont de compositie van de verwachte achtergrond in de $\ell\ell\nu\nu$-analyse van de 2015-2018 data. De afbeelding wordt gedomineerd door de niet-resonante SM-productie van bosonparen, specifiek ZZ- en WZ-paren. Een gerichte eventselectie, die gebruik maakt van de verwachte signaalkinematica, wordt gebruikt om events te weigeren die naar alle waarschijnlijkheid geen signaal, maar achtergrond zijn. Deze selectie is gebaseerd op de aanname dat, in de meeste gevallen, het zware Higgsboson (ongeveer) in rust wordt geproduceerd, wat leidt tot een grote hoek tussen de $Z \to \ell\ell$- en $Z \to \nu\nu$-vervallen, en een kleine hoek tussen de twee leptonen van het $Z \to \ell\ell$-verval, zoals geïllustreerd in Figuur S.1(b). Verder wordt het $Z \to \nu\nu$-verval gereconstrueerd als een significante hoeveelheid

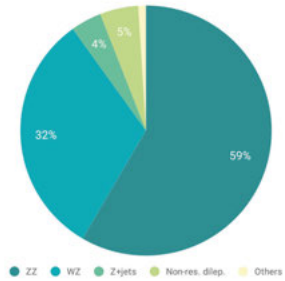

(a) Achtergrondcompositie

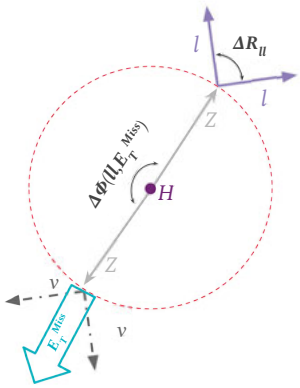

(b) Verwachte signaalkinematica

Figuur S.1: (a) Achtergrondcompositie in de $\ell\ell\nu\nu$-signaalregio en (b) schets van de verwachte kinematica van een signaalevent.

$E_{\mathrm{T}}^{\mathrm{miss}}$. Selectiecriteria over deze drie observeerbaren definieëren onder andere de signaalregio. Om de gevoeligheid te vergroten, wordt de signaalregio in twee categorieën gesplitst: één die verrijkt is in VBF-geproduceerde zware-Higgs-evenementen, en één die is verrijkt in ggF-evenementen.

Terwijl de WZ-, Z+jets- en non-resonant dilepton-achtergrondtoevoegingen worden geschat gebruikmakend van data uit controleregio's orthogonaal aan de signaalregio, lijkt de dominante ZZ-achtergrond zo sterk op het signaal dat de signaalregio zelf kan worden gebruikt om haar totale opbrengst in te schatten. Datagedreven schattingen van de belangrijkste achtergronden zijn essentieel om zeker te zijn dat geen mismodellering van de achtergronden ontstaat, welke zouden kunnen worden geïnterpreteerd als de valse aanwezigheid van een signaal.

Om de zoekgevoeligheid van het signaal te versterken, gebruikt de statistische interpretatie de distributie van de transversale massa-observabele, m_{T}, gedefinieërd als

$$m_{\mathrm{T}}^2 \equiv \left(\sqrt{m_Z^2 + |\vec{p}_{\mathrm{T}}^{\,\ell\ell}|^2} + \sqrt{m_Z^2 + |\vec{E}_{\mathrm{T}}^{\,\mathrm{miss}}|^2}\right)^2 - \left(\vec{p}_{\mathrm{T}}^{\,\ell\ell} + \vec{E}_{\mathrm{T}}^{\,\mathrm{miss}}\right)^2$$

waar m_Z de massa is van de Z boson en $\vec{p}_{\mathrm{T}}^{\,\ell\ell}$ de transversale momentumvector van het leptonenpaar beschrijft. Figuur S.2 toont de m_{T}-distributie van een voorbeeld zware-Higgssignaal en alle achtergronden in simulatie, alsook de data-distributie, in de twee lepton-flavour-kanalen van de ggF-categorie. Door gebruik te maken van de m_{T}-distributie kan de fit profiteren van het verschil in vorm tussen het piekende signaal en de exponentieel vallende achtergrond.

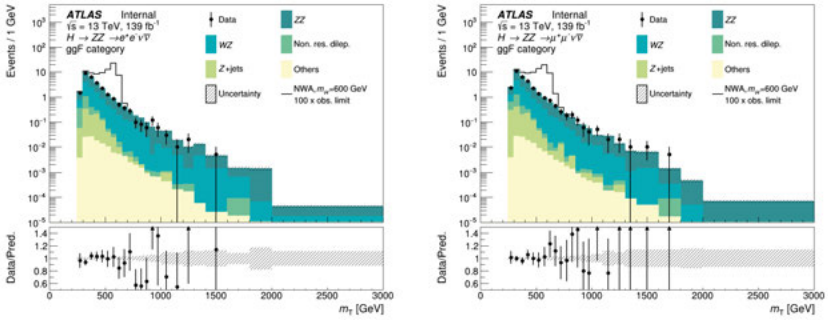

(a) ggF-categorie, $eevv$

(b) ggF-categorie, $\mu\mu vv$

Figuur S.2: Verwachte en geobserveerde transversale massadistributies voor de volledige Run II data in (a) de ggF-categorie, $eevv$-kanaal, (b) de ggF-categorie, $\mu\mu vv$-kanaal. Een voorbeeld zware-Higgssignaal met een massa van m_H = 600 GeV en een smalle-breedte is getoond, geschaald tot 100 maal de geobserveerde bovengrens op zijn productiedoorsnede. De laatste bak bevat alle events voorbij de limiet.

In de 2015-2018 data is geen significante afwijking van de SM verwachte achtergronden is geobserveerd, en dus is er geen bewijs voor een zwaar Higgsboson gevonden. Gegeven de afwezigheid van een signaaloverschot, worden exclusielimieten gezet op de respectievelijke productiedoor-

snede (inclusief de branching ratio naar ZZ) van de verscheidene Higgsboson-hypotheses gebruikmakend van de CL_s-methode met 95% betrouwbaarheid. Deze bovengrenzen kwantificeren hoeveel signaal kan bestaan in de natuur zonder incompatibel te zijn met de geobserveerde data. Gebruikmakend van de volledige 2015-18 data in de $\ell\ell\nu\nu$-eindtoestand, is het bereik van de bovenlimieten van de ggF productiedoorsnede van een smalle-breedte Higgs van ongeveer 305 fb tot 4 fb bij massa's van 300 GeV tot 2 TeV.

Door verschillende verbeteringen van de analyse, zoals het heroptimiseren van de eventselectie en ook in de VBF categorie gebruik te maken van de transversale massadistributie, presenteren deze volledige Run II-resultaten een factor drie tot acht verbetering over de eerder gepubliceerde $\ell\ell\nu\nu$-resultaten die enkel de 2015+2016 data van $\mathcal{L}$=36.1 fb^{-1} gebruikten, welke ook gepresenteerd worden in dit proefschrift. Deze verbetering is significant groter dan de factor twee die verwacht werd door enkel de vergroting van het datavolume.

Om de gevoeligheid van de zoektocht nog verder te verbeteren, worden de $\ell\ell\nu\nu$-resultaten gecombineerd met de resultaten van een vergelijkbare zoektocht in het $\ell\ell\ell\ell$-kanaal. De analyse van het $\ell\ell\ell\ell$-kanaal is conceptueel anders dan de $\ell\ell\nu\nu$-analyse; het $H \to ZZ \to \ell\ell\ell\ell$-verval is relatief zeldzaam, waardoor een kleine hoeveelheid evenementen wordt verwacht, maar het is ook een erg schoon kanaal met kleine achtergronden en een excellente massaresolutie.

De twee analyses hebben daarom verschillende sterkten, zoals te zien in Figuur S.3(a), dat de bovenlimieten van de NWA-ggF-analyse voor beide kanalen toont. Bij lage massa's domineert het $\ell\ell\ell\ell$-kanaal de gevoeligheid, in tegenstelling tot bij hoge massa's waar het $\ell\ell\nu\nu$-kanaal gevoeliger wordt door de grotere statistieken. De combinatie van beide kanalen is daardoor een perfect samenspel.

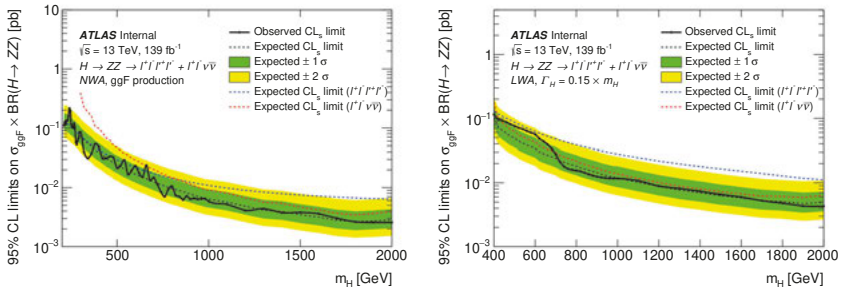

(a) Smalle-breedte

(b) 15% breedte

Figuur S.3: Verwachte en geobserveerde bovengrenzen van de ggF-productiedoorsnede van (a) een smalle-breedte Higgs en (b) een grote-breedte zware Higgs met een breedte van 15% van zijn massa.

Figuur S.3(b) toont de bovenlimieten voor een zware Higgsboson met een breedte van 15% van zijn massa. Deze grote-breedte-limieten zijn tot een factor twee slechter dan de smalle-breedte-limieten met dezelfde massa, omdat de bredere signaalpiek niet eenvoudig gescheiden kan worden van de achtergrond en daardoor moeilijker uit te sluiten is.

Het moet gezegd worden dat de impact van de systematische onzekerheden op de resultaten klein is in vergelijking met de statistische onzekerheid. De laatstgenoemde komen overeen tot tussen 55% en 65%, terwijl de volledige impact van systematische onzekerheden varieert van 10% tot 15%, afhankelijk van de signaalhypothese. Leidende bronnen van systematische onzekerheden zijn theorie-onzekerheden over het modelleren van de ZZ-achtergrond in zowel de $\ell\ell\ell\ell$- en $\ell\ell\nu\nu$-kanalen, en experimentele onzekerheden die onstaan uit de datagedreven schattingen van de Z+jets- en non-resonant dilepton-achtergronden in het $\ell\ell\nu\nu$-kanaal. Omdat de zoektocht gelimiteerd is tot de beschikbare data-statistieken, zal het toevoegen van nieuwe data uit toekomstige LHC-runs verdere verbetering van de limieten en uitbreiding van het massabereik mogelijk maken.

Tot slot wordt een interpretatie van de bovenlimieten ten aanzien van het specifieke 2HDM met vijf Higgsbosonen gepresenteerd, gebruikmakend van de gecombineerde $\ell\ell\nu\nu$- en $\ell\ell\ell\ell$-resultaten. In deze context komt de zware Higgs, die in dit proefschrift gezocht wordt, overeen met één van de neutrale, CP-even Higgsen van zulke theorieën, tegelijkertijd wordt aangenomen dat de lage-massa, CP-even Higgs de al ontdekte Higgs van 125 GeV is. Met de volledige 2015-18 resultaten wordt een grote regio van de 2HDM-parameterruimte voor zware Higgs-massa's tussen 200 en 400 GeV uitgesloten door deze interpretatie.

Samenvattend is duidelijk dat de resultaten van Run II de mogelijkheid van het bestaan van een zwaar Higgsboson met een massa tussen 200 GeV en 2 TeV dat vervalt in een paar van Z-bosonen aanzienlijk begrenzen. Als zo'n zware Higgs bestaat, heeft het naar alle waarschijnlijkheid een totaal andere signatuur of een nog grotere massa dan hier bestudeerd, en is daarom niet zichtbaar.

Zusammenfassung

Die Teilchenphysik als Disziplin strebt danach die grundlegenden Fragen über das Universum zu beantworten, die vermutlich seit Anbeginn des kritischen Denkens gestellt werden, zum Beispiel die Frage danach woraus alle Materie besteht. Heutzutage wissen wir, dass Atome aus Nukleonen und Elektronen aufgebaut sind, und dass Nukleonen wiederum aus Quarks bestehen. Unser aktueller Erkenntnisstand der Welt der Elementarteilchen, so wie Quarks und Elektronen es sind, ist in einem eleganten mathematischen Modell namens *Standardmodell der Teilchenphysik* (SM) zusammengefasst. Im Laufe der letzten Jahrzehnte hat das Standardmodell viele experimentelle Tests mit Bravour bestanden und ist so zu einem der grössten Erfolge der Teilchenphysik geworden. Um die Physik der mikroskopischen Wechselwirkungen von Elementarteilchen experimentell erforschen zu können, müssen hochenergetische Prozesse studiert werden, ähnlich wie ein sehr starkes Mikroskop gebraucht wird um etwas so kleines wie ein Atom zu sehen. Teilchenbeschleuniger wie der Large Hadron Collider (LHC) ermöglichen dies. Zum heutigen Zeitpunkt ist der LHC der leistungsstärkste Teilchenbeschleuniger der Welt und dort kollidieren Protonen, die auf nahezu Lichtgeschwindigkeit beschleunigt werden mit einer Schwerpunktsenergie von derzeit $\sqrt{s} = 13$ TeV.

Die Entdeckung eines Higgs-Bosons durch die LHC Experimente ATLAS [2] und CMS [3] in 2012 ist der jüngste Erfolg des Standardmodells und bestätigte einen bis dahin nur postulierten Aspekt der Theorie experimentell: In der ursprünglichen Formulierung sind alle Teilchen des Standardmodells masselos, was mit der Realität nicht vereinbar ist. Erst durch die Interaktion mit einem zusätzlichen Feld - dem Higgs-Feld, welches das Higgs-Boson hervorbringt - erlangen die Elementarteilchen ihre Masse durch die spontane Symmetriebrechung der elektroschwachen Wechselwirkung, auch (Brout-Englert)-Higgs-Mechanismus genannt. Nichtsdestotrotz stellt die Entdeckung eines Higgs-Bosons kein Ende aller Fragen zu dieser Thematik dar. So ist zum Beispiel jetzt bestätigt, dass elektroschwache Symmetriebrechung geschieht, aber nicht warum diese so geschehen sollte wie sie es tut. Zudem gibt es andere Beobachtungen die mit dem Standardmodell nicht erklärbar sind, zum Beispiel die Existenz von dunkler Materie und die beobachtete Asymmetrie zwischen Materie und Antimaterie in unserem Universum. Antworten auf solche Fragen geben so genannte *Beyond the Standard Model* (BSM) Theorien, also Theorien die über das Standardmodell hinaus gehen. Viele solcher BSM Theorien sagen die Existenz von mehreren Higgs-Bosonen voraus - so postulieren zum Beispiel die sogenannten *Two Higgs Doublet Models* (2HDMs) fünf Higgs-Bosonen, zwei davon elektrisch neutral und CP-gerade aber möglicherweise mit sehr unterschiedlichen Massen, und zusätzlich ein elektrisch neutrales aber CP-ungerades Higgs-Boson sowie zwei elektrisch geladene Higgs-Bosonen. Obwohl seit dem Higgs-Boson keine weiteren neuen Teilchen entdeckt wurden und Präzisionsmessungen der Eigenschaften des Higgs-Bosons die Möglichkeiten vieler BSM Theorien bereits stark einschränken, ist die Frage

ob das entdeckte Higgs-Boson das einzige seiner Art ist noch nicht abschliessend beantwortet.

Diese offene Frage motiviert die in dieser Arbeit vorgestellte experimentelle Suche nach einem schweren, BSM Higgs-Boson, das in ein Paar von Z-Bosonen zerfällt. Im Speziellen ist mit »schwer« hier gemeint, dass die Masse des BSM Higgs-Bosons grösser ist als die des bereits entdeckten Higgs-Bosons mit 125 GeV und insbesondere gross genug, dass die beiden Z-Bosonen *on-shell* produziert werden, d.h. $m_H > 2\ m_Z$. Die Suche umfasst daher Massen zwischen 200 GeV und 2 TeV. Verschiedene Szenarien für die Zerfallsbreite des schweren Higgs-Bosons werden untersucht: Sowohl eine Analyse unter der *narrow-width approximation* (NWA) unter der die intrinsische Breite vernachlässigbar ist, als auch eine *large-width analysis* (LWA) werden durchgeführt. Während unter der NWA sowohl die Higgs-Produktion durch Gluon-Gluon-Fusion (ggF) als auch durch Vektorboson-Fusion (VBF) berücksichtigt werden, betrachtet die LWA nur die ggF-Produktion. In der LWA werden vier verschiedene spezifische Annahmen zur Zerfallsbreite untersucht und Interferenzeffekte zwischen dem schweren Higgs und dem leichten Higgs mit 125 GeV Masse sowie dem $ggZZ$ Untergrund werden explizit miteinbezogen.

Das Herzstück dieser Arbeit stellt die Analyse des $H \to ZZ \to \ell\ell\nu\nu$ Zerfallskanals mit den *full run II* Daten von $\mathcal{L}$=139 fb^{-1}, welche durch ATLAS in den Jahren 2015 bis 2018 aufgenommen wurden, dar. Im Vergleich zum ähnlichen $H \to ZZ \to \ell\ell\ell\ell$ Zerfallskanal, bietet der $H \to ZZ \to \ell\ell\nu\nu$ Kanal aufgrund der höheren Zerfallswahrscheinlichkeit des $Z \to \nu\nu$ Zerfalls eine bessere statistische Grundlage, aber eine schlechtere Massenauflösung, da die produzierten Neutrinos nicht direkt gemessen werden können. Nur eine indirekte Messung des totalen transversalen Impulses der Neutrinos ist durch die sogenannte *fehlende Transversalenergie*, $E_{\mathrm{T}}^{\mathrm{miss}}$, möglich.

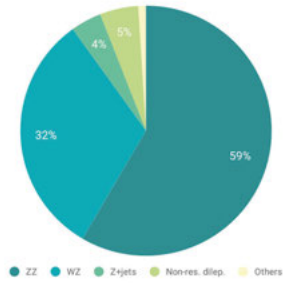

(a) Zusammensetzung des Untergrunds

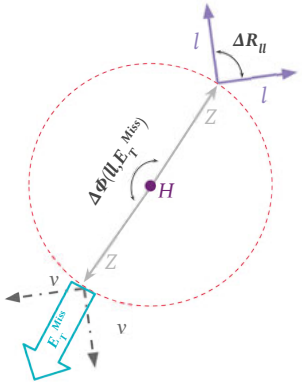

(b) Erwartete Signal Kinematik

Abbildung S.1: (a) Zusammensetzung des Untergrunds in der $\ell\ell\nu\nu$ Signalregion und (b) Skizze der erwarteten Kinematik eines Signalereignisses.

Mehrere andere Prozesse resultieren in demselben $\ell\ell\nu\nu$-Endzustand wie das gesuchte Signal und einige dieser Prozesse passieren im Überfluss am LHC. Diese Prozesse stellen den sogenannten Untergrund der Suche dar, den es zu reduzieren gilt, damit ein (möglicherweise sehr kleines) Signal in den Daten gefunden werden kann. Abbildung S.1(a) zeigt die Zusammensetzung des erwarteten Untergrunds in der $\ell\ell\nu\nu$-Analyse der 2015-18 Daten. Die nicht-resonante SM Produktion von Vektorbosonpaaren, speziell ZZ und WZ, dominiert das Bild. Mithilfe einer Ereignisselektion, die

sich die erwartete Kinematik von Signalereignissen zu Nutze macht, können Ereignisse die mit höherer Wahrscheinlichkeit Untergrund als Signal sind von der Analyse ausgeschlossen werden. Diese Selektion basiert auf der Annahme, dass das Higgs-Boson in den meisten Fällen (ungefähr) in Ruhe produziert wird, was zu einem grossen Winkel zwischen den $Z \to \nu\nu$- und $Z \to \ell\ell$-Zerfällen und einem kleinen Winkel zwischen den beiden Leptonen des $Z \to \ell\ell$-Zerfalls führt, wie in Abbildung S.1(b) illustriert. Ausserdem wird der $Z \to \nu\nu$-Zerfall als signifikante fehlende Transversalenergie rekonstruiert. Auswahlkriterien basierend auf unter anderem diesen drei Grössen definieren die Signalregion. Um die Sensitivität der Suche zu erhöhen wird diese Signalregion in zwei Kategorien eingeteilt: eine die hauptsächlich VBF-produzierte Ereignisse enthält, und eine für ggF-Ereignisse.

Während die Untergrundsbeiträge durch WZ-, Z+jets- und nicht-resonante Dilepton-Produktion mittels zur Signalregion orthogonaler Kontrollregionen bestimmt werden können, ist der dominante ZZ-Untergrund dem Signal so ähnlich, dass die Daten in der Signalregion selbst genutzt werden können um die Gesamtanzahl von ZZ-Ereignissen abzuschätzen. Solche *data-driven* Methoden zur Bestimmung des Untergrunds sind essentiell, um mögliche Fehlmodellierungen auszuschliessen, da solche als die falsche Anwesenheit eines Signals interpretiert werden könnten.

Zur weiteren Erhöhung der Sensitivität, wird für die statistische Auswertung die Verteilung der *transversalen Masse*, m_{T}, ausgenutzt, welche definiert ist als

$$m_{\mathrm{T}}^2 \equiv \left(\sqrt{m_Z^2 + |\vec{p}_{\mathrm{T}}^{\,\ell\ell}|^2} + \sqrt{m_Z^2 + |\vec{E}_{\mathrm{T}}^{\,\mathrm{miss}}|^2}\right)^2 - \left(\vec{p}_{\mathrm{T}}^{\,\ell\ell} + \vec{E}_{\mathrm{T}}^{\,\mathrm{miss}}\right)^2.$$

wobei m_Z für die Masse des Z-Bosons steht und $\vec{p}_{\mathrm{T}}^{\,\ell\ell}$ den gesamten Transversalimpulsvektor des Leptonpaares beschreibt. Abbildung S.2 zeigt die m_{T}-Verteilungen eines Beispielsignals und aller Untergründe in Simulation sowie die Datenverteilung, für die zwei möglichen Leptonkombinationen $ee\nu\nu$ und $\mu\mu\nu\nu$ in der ggF-Kategorie. Die Benutztung dieser Verteilungen erhöht die Sensitivität, da sich so das peakende Signal vom exponentiell fallenden Untergrund unterscheiden lässt.

In den 2015-18 Daten wird keine signifikante Abweichung vom Standardmodell gemessen, also kein neues, schweres Higgs-Boson gefunden. Stattdessen werden sogenannte *Ausschlusslimits*, also obere Grenzwerte, der entsprechenden Produktionswirkungsquerschnitte für die verschiedenen Higgs-Szenarien bestimmt. Dazu wird die CL_s-Methode mit einer Sicherheit von 95% genutzt. Solche Ausschlusslimits geben an, wie viel Signal in der Natur existieren könnte ohne mit den beobachteten Daten inkompatibel zu sein. Mit den 2015-18 Daten im $\ell\ell\nu\nu$-Endzustand reichen die oberen Grenzen des ggF-Wirkungsquerschnittes für ein schweres Higgs-Boson mit vernachlässigbarer Breite von etwa 305 fb bis 4 fb für Massen von 300 GeV bis 2 TeV.

Aufgrund von mehreren Verbesserungen der Analyse, so zum Beispiel der Reoptimisierung der Ereignisselektion und das Ausnutzen der m_{T}-Verteilungen auch in der VBF-Kategorie, stellen diese Ergebnisse eine Verbesserung von Faktor drei bis acht über die vohergehend veröffentlichen $\ell\ell\nu\nu$-Ergebnisse mit den 2015+16 Teildaten von $\mathcal{L}$=36.1 fb^{-1} dar, die ebenfalls in dieser Arbeit präsentiert werden. Insbesondere ist diese Verbesserung signifikant grösser als der Faktor zwei, der allein durch das Vergrössern des Datenvolumens zu erwarten wäre.

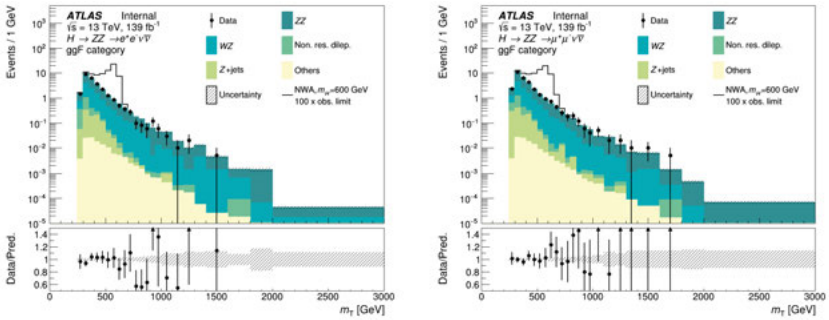

(a) ggF-Kategorie, $eevv$ (b) ggF-Kategorie, $\mu\mu vv$

Abbildung S.2: Erwartete und beobachtete Verteilung der transversalen Masse mit den 2015-18 Daten in (a) der ggF-Kategorie, $eevv$-Kanal, (b) der ggF-Kategorie, $\mu\mu vv$-Kanal. Als Beispiel wird ein Higgs-Signal mit einer Masse von m_H = 600 GeV und vernachlässigbarer Breite gezeigt, das auf einen Wirkungsquerschnitt, der 100 mal dem beobachteten Ausschlusslimit entspricht, skaliert ist. Der letzte *bin* enthält alle Beiträge, die über die Achsenbeschränkung hinausgehen.

Eine weitere Verbesserung wird dadurch erreicht, dass die $\ell\ell vv$-Ergebnisse mit denen einer ähnlichen Analyse im $\ell\ell\ell\ell$-Kanal kombiniert werden. Die $\ell\ell\ell\ell$-Analyse unterscheidet sich konzeptuell von der $\ell\ell vv$-Analyse, da der $H \to ZZ \to \ell\ell\ell\ell$ Zerfall sehr selten ist, sodass in diesem Kanal nur eine geringe Anzahl an Signalereignissen erwartet wird, aber die Untergründe ebenfalls klein sind und dieser Kanal vor allem eine exzellente Massenauflösung bietet.

Die beiden Analysen haben also unterschiedliche Stärken, wie in Abbildung S.3(a) ersichtlich, welche die erwarteten Ausschlusslimits der NWA ggF-Analyse in beiden Kanälen zeigt. Die Sensitivität bei niedrigeren Massen wird vom $\ell\ell\ell\ell$-Kanal dominiert, während der $\ell\ell vv$-Kanal aufgrund seiner grösseren Datenstatistik für höhere Massen empfindlicher wird. Die Kombination der beiden Analysen ist daher eine perfekte Partnerschaft.

Abbildung S.3(b) zeigt die Ausschlusslimits für ein schweres Higgs-Boson mit einer Zerfallsbreite von 15% von seiner Masse. Diese Limits sind bis zu einem Faktor zwei schlechter als die entsprechenden NWA-Limits, da der breitere Signalpeak schwieriger vom Untergrund zu unterscheiden ist und daher auch schwieriger auszuschliessen ist.

Es ist erwähnenswert, dass die Auswirkung von systematischen Unsicherheiten verglichen mit den statistischen Unsicherheiten im Kontext der hier präsentierten Analysen gering ist. So liegt die statistische Unsicherheit je nach Signalhypothese zwischen 55% und 65%, während die systematischen Unsicherheiten in der Summe nur zu 10% bis 15% weiterer Unsicherheit führen. Die wichtigsten Ursachen systematischer Unsicherheiten sind hierbei die ZZ-Modellierungsunsicherheiten theoretischer Natur in sowohl $\ell\ell\ell\ell$- als auch $\ell\ell vv$-Kanal, und experimentelle Unsicherheiten die aus der Bestimmung der Z + jets und nicht-resonanten Dilepton Untergründen im $\ell\ell vv$-Kanal entstehen. Da die Suche noch durch die verfügbare Datenstatistik eingeschränkt

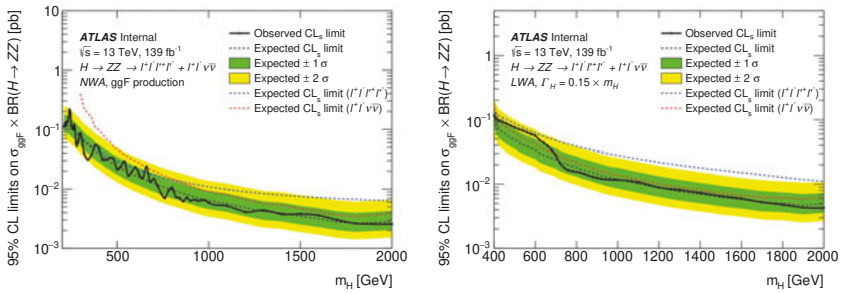

(a) NWA, vernachlässigbare Zerfallsbreite

(b) LWA, Zerfallsbreite von 15% der Masse

Abbildung S.3: Erwartete und beobachtete Ausschlusslimits des Wirkungquerschnittes für die ggF-Produktion eines schweren Higgs-Bosons (inklusive der Zerfallswahrscheinlichkeit in ein ZZ-Paar) mit (a) einer vernachlässigbaren Breite und (b) mit einer Breite von 15% von seiner Masse.

ist, wird das Hinzufügen weiterer Daten aus zukünftigen LHC Betriebsphasen sowohl die weitere Verbesserung der Ausschlusslimits als auch eine Ausbreitung der Massenreichweite erlauben.

Abschliessend wird eine Interpretation der kombinierten $\ell\ell\ell\ell$- und $\ell\ell\nu\nu$-Suchergebnisse im Kontext eines spezifischen 2HDMs präsentiert. Dabei stellt das hier gesuchte, schwere Higgs eines der beiden neutralen, CP-geraden Higgs-Bosonen dieses Modells dar, während das bereits entdeckte Higgs mit 125 GeV Masse als das zweite neutrale, CP-gerade Higgs-Boson interpretiert wird. Mit den 2015-18 Daten lässt sich ein Grossteil des 2HDM-Parameterraumes für schwere Higgs-Massen zwischen 200 GeV und 400 GeV ausschliessen.

Zusammenfassend kann gesagt werden, dass die hier präsentierten Ergebnisse mit den 2015-18 Daten die Möglichkeit, dass ein schweres Higgs-Boson mit einer Masse zwischen 200 GeV und 2 TeV, das in ein Z-Bosonpaar zerfallen kann, existiert, signifikant einschränken. Sollte solch ein schweres Higgs-Boson bestehen, hat es wahrscheinlich eine sehr andere Signatur oder Masse als hier angenommen, und versteckt sich daher ausserhalb des Blickfeldes.

Acknowledgements

"It is good to have an end to journey toward; but it is the journey that matters, in the end.'
— Ursula K. Le Guin, *The Left Hand of Darkness*

And what a journey it has been. Being part of a large scientific collaboration such as ATLAS, with people from all over the world and all kinds of backgrounds working together, is an amazing and humbling experience and I am very lucky to have enjoyed it. The last four(-ish) years that I have spent working on this thesis have been a great experience, though of course not without the occasional struggle. But there have always been so many people ready to support my research effort or me as a person and their support has been invaluable to the completion of this work. For this I would like to express my gratitude in the following, though often a few pretty words don't do justice to just how much their help means to me.

First and foremost I would like to thank Peter and Wouter, for giving me the opportunity to pursue the analysis presented here to begin with, for being my (co-)promoters and for reading through this (not so short!) manuscript and offering many helpful improvements on the text. Working with both of you was a truly inspiring experience and I have learned a lot from it. Peter, thank you so much for your continuous and patient support in my daily work - your readiness to answer any question, your skill at helping solve any problem so quickly and your enthusiasm about physics and helping to fill in "the big picture". Wouter, thank you for all your help, especially during the thesis manuscript finalisation phase, and taking the time to explain things (particularly statistics) so comprehensibly to me even if it meant adding yet another responsibility to your already very busy schedule. Also a big thank you to both of you for advising me on any scientific career path matters and for encouraging me to pursue goals and take opportunities that I likely would not have dared to without your support.

My thanks also go to all the members of the committee - Ivo van Vulpen, Robert Fleischer, Hella Snoek, Patrick Decowski, Eric Laenen, Gerhard Raven and Yusheng Wu - for kindly agreeing to read through all of this thesis. A special thanks to Robert for your support as a C3 member and following my progress throughout the years.

A big thank you to Peter, Ivo, Hella, Michiel and Ash - without our $\ell\ell\nu\nu$ team at Nikhef it would have been much more difficult and less fun to complete this work. Hella and Ivo, I am very grateful to both of you for helping to sort out planning issues and involving yourself to push our analysis forward. Thank you for your support on all levels, Hella, for always being understanding and for taking the responsibility to make our little team work well. Special shout-out to Ivo for coming up with the great, "catchy" thesis title - your deep understanding of complicated matters combined with your talent for explaining them in simple ways continues to amaze me. Michiel, thank you so much for your hard work and dedication throughout the years, your (mostly un-

complaining) acceptance of drudging through the most boring, although extremely vital, tasks, for always keeping a clear, level perspective on things and thus being a steady support. It was a pleasure to work together with you and you contributed significantly to the success of this work. Ash, thank you for lending a helping hand already when you had barely joined the group and for your contagious cheerfulness. I wish both of you all the success in the world for continuing your (PhD) endeavours.

There is one more *Nikheffer* whose academic support was extremely valuable, especially during my first years as a new student, who I owe a big debt of gratitude to: Jochen, ohne deine Hilfe wäre ich so oft so verloren gewesen. Danke für alles!

Drawing the circle wider, I want to thank everyone in the ATLAS $\ell\ell\nu\nu$ team for the pleasurable collaboration: A big thank you goes to Yusheng for coordinating the full run II analysis and always being happy to help with any problem or question I encountered - your explanations have furthered my understanding a great deal and I marvel at your dedication. Thanks also to previous analysis contacts - Cong, Hideki and especially Monica who was so very welcoming and keen to help me on the right path from the very start - and all other team members - Dimitrii, Yuri, Jun, Jing Li, Fang-Ying, Sarah, Kayla, Mariyan, Wen - whose efforts have contributed to the success of the analyses presented here. Along this line I am also grateful to the $H \to ZZ$ conveners whose coordinating and managing role was crucial for making it to the finish line that is the "ATLAS publication of the results" and for their helpful feedback - so thanks to Giacomo, R.D., Andrea, Gaetano and Will. Moreover, thank you also to the $\ell\ell\ell\ell$ team, especially Lailin, Heling and Xiangyang for help with the high mass interpretation, Denys for the interference modelling and Haider for all matters minitree production.

It takes more than just scientific support to succesfully finish a PhD, and in that respect Nikhef is indeed a special place, where one is always made to feel welcome, help is readily given and there is a great community spirit. For their help with all things administrative I am indebted to Ed and Pieter - thank you for making all these bureaucratic things so uncomplicated.

Thank you to all my colleagues and friends at Nikhef and CERN for all the happy coffee breaks, dinners & drinks, movie nights, swimming days at the lake and other fun outings - Alice, Alessio, Anamika, Ann-Kathrin, Antonia, Ash, Brian, Broos, Bryan, Carlo, Carsten, Edwin, Federica, Hannah A., Hannah H., JJ., Jordy, Katya, Koen, Kees, Lucrezia, Lydia, Maddie, Magdalena, Marc, Marcus, Marko, Matteo, Michiel, Naghmeh, Olena, Pepijn, Rahul, Sara, Sonia, Stefano, Terry, Tim, Veronica, Vince. I am pleased to have met you all and lucky to have enjoyed your company.

Many friends - old and new, physics insiders and outsiders - have supported me, lent their ear to my worries and given advice on many occasions while working on this thesis:

Alice, thank you for our conversations (often deep, sometimes not), for sharing experiences and views and your support. Carsten, vielen lieben Dank für die gute Zeit als *office mates* am CERN. Deine Hilfsbereitschaft - sei es Hilfe mit meinen fehlenden Myonen, ein klarer Blick auf schwierige emotionale Lagen oder als Fahrer - schätze ich sehr. Lydia, thank you for all the fun times you organized, for being so welcoming and encouraging from the very beginning and for being such an inspiration in your enthusiasm, skill and dedication. Matteo, thank you for all the enjoyable

talking breaks, for helping me with coding and computing issues, for being supportive in times of anxiety and for your great *bunnysitting* skills.

Hannah H., you are a force of nature - your dedication to, enthusiasm for and understanding of physics are impressive. Thank you so much for being there for me, for pulling me onwards with your drive, and for pushing me when I couldn't be pulled. Olena, thank you for the happy times as house mates in Ferney-Voltaire. Your cheerfulness always brightened the day and I hope you still find many things that you love, *absolutely love*.

Clara, danke dafür, dass du immer ein offenes Ohr und einen guten Rat hast, für dein Feedback zu plotting style und Illustrationsfragen und für deine unerschütterliche Unterstützung. David, danke dafür, dass du dir schon seit Jahren mein Gejammer anhörst, wenn ich wieder irgendein Problem habe, und dass du mir weiterhin so oft mit Physik- und Programmier-Problemen aushilfst - und natürlich für die übertrieben helle Taschenlampe, dank der ich auch nachts von control room shifts mit Freuden nach Hause radeln konnte. Rebecca, danke für dein Zuhören, fürs (Fehler-)Lesen von Teilen dieser Arbeit und schwieriger Emails, und natürlich fürs Teilen von Katzenbildern. And I must thank Quint for proof-reading the summary so carefully and sharing his detailed linguistics knowledge to help me understand the improvements.

Thank you also to my family: Lieben Dank an meine ganze Familie für euer Interesse und eure Unterstützung. En ook bedankt aan familie Seidel voor jullie interesse en steun - dankjewel Marjoke voor het proeflezen van de samenvatting.

Jasper, thank you for translating the summary to Dutch and, you know, for everything.

Abschliessend geht mein grösster Dank an meine Eltern - ohne eure Unterstützung in jedem Aspekt wäre ich nie so weit gekommen. Danke, dass ihr immer für mich da seid!